EXCITED-STATE ACID-BASE & COORDINATION CHEMISTRY OF RUTHENIUM(II) DIIMINES: ASSOCIATION WITH VARIOUS METAL CATIONS

by

José L. Zambrana, Jr.

A dissertation submitted
to the Graduate Faculty in Chemistry
in partial fulfillment of the requirements
for the degree of Doctor of Philosophy,
The City University of New York
2007

ProQuest LLC
789 East Eisenhower Parkway
P.O. Box 1346
Ann Arbor, MI 48106-1346

This manuscript has been read and accepted by the Graduate Faculty in Chemistry in satisfaction of the dissertation requirement for the degree of Doctor of Philosophy.

Harry D. Gafney

12/07/2006
Date

Harry D. Gafney
Chair of Examining Committee

Michael E. Green

12/07/2006
Date

Michael E. Green
Acting Executive Officer

Thomas C. Strekas

Robert Engel

Max Diem

Supervision Committee

City University of New York

Abstract

EXCITED-STATE ACID-BASE & COORDINATION CHEMISTRY

OF RUTHENIUM(II) DIIMINES:

ASSOCIATION WITH VARIOUS METAL CATIONS

by

José L. Zambrana, Jr.

Supervisor: Harry D. Gafney

Ruthenium(II) diimines have been extensively studied for their remarkable photophysical properties. Of particular interest are compounds with peripheral base sites, such as bis(2,2'-bipyridine) (2,3-bis(2-pyridyl) pyrazine) ruthenium(II), $[(bpy)_2Ru(dpp)]^{2+}$, which upon excitation undergoes a metal-to-ligand-charge transfer out onto the dpp ligand, leading to an emissive state and incredible increases in basicity. Quenching by protonation in acidic aqueous solution most likely involves transfer of the proton from the pyridyl ring of the dpp ligand, the site of higher basicity in the ground state, to the pyrazinyl ring in the excited state, the nearby transient site of higher basicity.

Previous work suggested that such changes in basicity could translate into an excited-state coordination

chemistry. For example, the photoinduced reaction of $[(bpy)_2Ru(dpp)]^{2+}$ with $PtCl_6^{2-}$ to form $[(bpy)_2Ru(dpp)PtCl_4]^{2+}$ is thought to involve initial exciplex formation. Reexamination of the excited-state acid-base properties of $[(bpy)_2Ru(dpp)]^{2+}$ reveals an inversion in basicity in the asymmetric, distinct imine nitrogens on the dpp ligand upon excitation. This serves as the basis for association between $[(bpy)_2Ru(dpp)]^{2+}$ and various metal cations, in particular the d^{10} metal cations Ag^+, Cd^{2+}, and Zn^{2+}. Each forms an emissive bimetallic complex where the more well-known quenching mechanisms of energy and electron transfer can be precluded based on energetics and/or the emissivity of the ensuing bimetallic complex. These interactions have been characterized by nuclear magnetic resonance, electronic absorption, and both steady-state and time-resolved emission spectroscopy. Data fit a model based on reversible associational quenching with a degree of diffusional association due to the inversion of imine basicity upon excitation. Thus, distinct, emissive bimetallics are formed, characterized by lower energy transitions and reduced lifetimes, thus strongly implying that in well-chosen systems, excited-state enhanced basicity can lead to heretofore unseen excited-state coordination chemistry.

Acknowledgments

I have been fortunately surrounded by a supportive community of family, friends, lab mates, mentors, and colleagues, without whom I could never have accomplished this great endeavor. I would especially like to offer my deepest gratitude to the following:

My mentor, Dr. Harry Gafney, for his timeless patience, incredible wisdom, encyclopedic knowledge, nurturing mentorship, encouragement, insight, joy, jokes, stories, indomitable spirit, and infectious passion that got me interested in the first place—working with you is one of the best life choices I have ever made;

My parents, José and Evelyn Zambrana, for their unconditional love, undying support, prayers, and financial assistance;

Melissa Sanchez, my sister, and her family, David, Noé, and Emanuel (my godson), for prayers, support, and inspiration;

Cindy Olson, who has been the best cheerleader, the best caretaker, and the best friend a human could possibly have, for her unwavering support at every step—I could not have done this without you and am eternally grateful;

My extended family here in the States, including grandmother Mandy, aunt Olga, uncle Angel, cousin Lena and her family Pete, Ariana (my goddaughter) and Danny, for their support and pride in having the first family member ever complete a doctorate;

Mi familia en Puerto Rico por todo su amor y apollo;

For all my lab mates, past and present, Dr. Edward Look, Dr. Sunil Dehipawalage, Dr. Nathan Stevens, Keeshan Williams, Shanta Amarasinge, Dr. Rolf Dolfinger, Wendy Sanchez, Dr. Chaim Levi, Dr. Rolande Hodel, and Jim Dimitrikapolous, but especially Dr. Charlie Hicks, Elena Ferloni and Dr. Julie Colis who were co-laborers on this project and a constant source of fun, support, and friendship;

Edward McCarthy, for becoming a loving friend along the way of this journey, but who offered unwavering support nevertheless;

My thesis committee for their longsuffering and insight;

The National Science Foundation for a Graduate Research Fellowship;

The National Science Foundation and the AP Fellows Program at The Graduate Center, City University of New York, for a GK-12 Fellowship;

The Louis Stokes Alliance for Minority Participation at CUNY for several Graduate Assistantships and a Dissertation Fellowship, and for the AMP community of scholars;

Dr. Claude Brathwaite, for his steady pushing and encouraging;

The faculty of the Department of Chemistry & Biochemistry of Queens College for insightful conversations and helpful hints along the way, especially Dr. David Locke for use of his HPLC;

My fellow Ph.D. students along the way in other labs at Queens College including Dr. Sharon Lall and Dr. Chandima Abeywickrama—for their collegiality;

Dr. Cherice Evans, along with Xianbo Shi, for considerable help in programming Igor, and for her keen insights;

The community of St. Bartholomew's Church, especially Pam Curry and Robert Zappulla, and former associate rector The Reverend Nancy Hanna, and especially all those of the former Alpha program—for prayers, support and encouragement;

The community of Trinity Lutheran Church, Long Island City, for their support, prayers, and understanding;

My former chemistry teachers who inspired me to study the subject especially Chris Schweiger of Chapel Field Christian High School, and Dr.'s Bernard Piersma, Irmgard Howard, Fred Shannon, and Larry Christensen of Houghton College;

Mr. William Hodgetts, for his love and support for many years;

O. Diane Adebowale and Vivian Mason of the Doctoral Chemistry Office—for their kind and encouraging words and great organization;

My students, past and present;

Molash Alemayehu and Jeanne Deutsch, Queens College Department of Chemistry & Biochemistry secretaries who make working at QC a joy;

The National Academies of Science for a Christine Mirzayan Graduate Science Policy Fellowship;

The Doctoral Student's Council of the Graduate Center;

The Interactive Technology and Pedagogy Certificate Program and Steve Brier—for his keen mind, eloquence, patience, ethics, and respect for process;

and

Dr. Gerald Koeppl, for his kind mentorship, everlasting patience, and helpfulness.

Deo Gratias, Pater, Filio, et Spiritus Sanctus.

Dedication

This dissertation is dedicated to the memory of my grandfathers Nicasio Martinez and Segundo Zambrana whose incredible work ethic in the face of adversity has inspired the generations that have followed them.

Table of Contents

Lists of Tables

Lists of Figures

Symbol Key

Δ	change in
ΔG	free energy change
k	generic rate constant for any relaxation event or the total rate constant for deactivation
τ	generic lifetime for any species, or more commonly, the observed lifetime
H	Hamiltonian operator
ψ	generic electronic wavefunction
E	eigenvalues of electronic energy
p	momentum of particle
x	position of a particle
h	Planck's constant, = 6.626×10^{-34} J · s
π	the constant, 3.14, or the molecular orbital with symmetry above and below the axis the of the bond
t	time
σ	a molecular orbital with symmetry along the axis of a bond
n	a non-bonding molecular orbital
d	the atomic orbitals with azimuthal quantum number $l = 2$
μ	magnetic moment
N	number of unpaired electrons
μ_B	Bohr magneton, = 9.274×10^{-24} J/T
S	sum of spin quantum numbers in a system
m_S	spin quantum number
L	orbital angular momentum
M_L	sum of orbital quantum numbers
m_L	orbital quantum number
S_o	ground state singlet state (electron spins are anti-parallel)
T_o	ground state triplet state (electron spins are parallel)
Σ	molecular wavefunction "sigma"
Π	molecular wavefunction "pi"
c	speed of light, = 2.998×10^{8} m/s
λ	wavelength of light
T_1	first excited state triplet
S_1	first excited state singlet
μ_B	transition dipole moment
ψ^*	wavefunction of the excited state
$\hat{\mu}$	electric dipole moment operator
ε	molar extinction coefficient or absorptivity
P_o	incident radiant power

P_f	power of light transmitted
b	path length
A	absorbance
D	a set of molecules
*D	a set of molecules in the excited state
I	rate of excited state production or emission intensity at an analytical wavelength
I_o	Emission intensity at zero quencher concentration
I_a	rate of light absorbed
η^*	efficiency of excited state production
π^*	anti-bonding π molecular orbital
α	fractional contribution of a first species
β	fractional contribution of a second species
dX	the differential change in a generic quantity X
Q	a quencher
k^o_F	inherent rate constant for fluorescence
k^o_P	inherent rate constant for phosphorescence
τ^o_F	lifetime due only to fluorescence
τ^o_P	lifetime due only to phosphorescence
k_{ST}	rate for intersystem crossing from an excited singlet state to an excited triplet state
k_{TS}	rate for intersystem crossing from an excited triplet state to a ground singlet state
T_n	where n>1, upper excited triplet states
S_n	where n>1, upper excited singlet states
k_{isc}	rate constant for intersystem crossing
$h\nu$	light energy
k_{IC}	rate constant for internal conversion
k_r	radiative rate constant
k_{nr}	non-radiative rate constant
τ_{obs}	specifically, the observed lifetime
τ_o	the calculable inherent radiative lifetime
Φ_{em}	the quantum yield of emission
Φ_{nr}	the quantum yield of non-radiative decay
k_{nr}	rate constant for photochemical reaction
*S	the excited state product of a photochemical reaction
A	detector response to emitted light (observed intensity or area)
A_o	Pre-exponential factor
$[X]_o$	initial concentration of species X
EC	encounter complex
k'_d	the rate constant for diffusion to form an excited state encounter complex
k'_{-d}	rate constant for separation of an excited state encounter complex complex

k_{de}	total rate constant for deactivation of an encounter complex
k_{d}	the rate constant for diffusion of ground state species
k_{-d}	rate constant for separation of a ground state encounter complex
K_{eq}	Association constant in the ground state
K^{*}_{eq}	Association constant in the excited state
k'_{r}	radiative rate constant for encounter complex
k'_{nr}	non-radiative rate constant for encounter complex
k'_{SC}	rate constant for formation of a successor complex from an encounter complex
k'_{o}	sum and non-radiative and radiative rate constants for deactivation of an encounter complex, excluding formation of a successor complex
k'_{de}	total rate constant for deactivation of an encounter complex, including the rate constant for successor complex formation
k''_{r}	radiative rate constant for successor complex
k''_{nr}	non-radiative rate constant for successor complex
k''_{o}	total rate constant for deactivation of a successor complex
τ''_{o}	lifetime of a successor complex
k_{q}	rate constant for quenching
K_{SV}	Stern-Volmer quenching constant
k_{en}	general rate constant for energy transfer
k_{et}	general rate constant for electron transfer
k_{ret}	rate constant for reductive electron transfer
k_{oet}	rate constant for oxidative electron transfer
k_{1}	rate constant for protonation
k_{2}	rate constant for deprotonation
N_{A}	Avogrado's number, = 6.022 x 10^{23} mol^{-1}
ΔH	change in enthalpy
ΔS	change in entropy
ν	frequency, usually in cm^{-1}
T	temperature
pK	(-) log of the equilibrium constant, K
K_{a}	acid dissociation constant
pK_{a}	(-) log of the acid dissociation constant
K^{*}	an excited state equilibrium constant
c_{i}	fractional contribution from the i^{th} component
k_{EX}	rate constant for exciplex formation
k_{-EX}	rate constant for separation of an exciplex
k^{*}_{1}	rate constant for excited state protonation
k^{*}_{2}	rate constant for excited state deprotonation

τ_{EX}	The lifetime of an exciplex
M	A generic metal species
f_i	The fractional concentration of the ith species
p	The overlap ratio of two emissions
φ	Corrected emission intensity
A	First set of pre-exponential values for a biexponential fit
A	Second set of pre-exponential values for a biexponential fit
τ_1	First lifetime in a biexponential decay
τ_2	Second lifetime in a biexponential decay

1. INTRODUCTION

1.A. CONTEXT

The fleeting landscape of electronically excited molecules, being so remarkably distinct from that of the ground state, suggests a new world of chemistry the likes of which chemists have just begun to glimpse over the past half-century. People have been intuitively aware of the power of this "photochemistry" for some time, recognizing that plants harnessed light energy to support life on earth. In 1912 Italian photochemist Giacomo Ciamician recognized that photochemistry could revolutionize the future of energy production–predicting a society entirely based on solar, renewable energy.[1] Although human society is still far off from that vision, chemists are much farther along in understanding processes available to excited states.[i] One key finding is that the structure of a molecule or complex is inextricably linked to its electronic properties, and thus to how it behaves when excited by light.

Early theoretical work in photochemistry focused on organic molecules, which laid the groundwork for more in-

---

[i] Excited state will always mean "electronically" excited state, unless otherwise stated.

depth investigations of inorganic molecules.[ii] Although the quantum mechanics and mathematics of the excited state are the same regardless of distinctions between "organic" or "inorganic" molecules, what is different is that excited states in the latter can additionally arise from states based in d orbitals. This has important consequences not only for the language used to describe the excited states of inorganic molecules, but also more importantly for the possible subsequent excited-state chemical interactions and how quickly such events take place. Any photochemical investigation necessarily asks the question—How fast do these events occur? Nature's spontaneous drive is to reduce the energy of matter, simply stated by:

$$\Delta G < 0 \text{ for any spontaneous reaction,} \qquad (1)$$

where ΔG is the free energy change for the process under consideration. Therefore, the drive of any excited molecule is to spontaneously relax, and to do so efficiently. However, competitive with relaxation are other possible chemical pathways not available in the ground state. Whether or not the excited molecule travels along one of

[ii] The earliest recordings of chemical photosensitivity concern inorganic molecules—silver halides being known since at least the 1700's, and ferric oxalate recorded in 1831 by Johann Wolfgang Döbereiner (1780-1849).[2]

the these pathways is dependent upon whether or not it can do so quickly enough before the molecule relaxes by other means. The issue of how long-lived is the excited state can be related to the average "lifetime", in seconds, of a set of molecules. The inverse lifetime would then be the number of molecules relaxing per second. For any relaxation event, whose "quickness" or "rate" is related to a defined rate constant, k, the event will be a significant relaxation pathway if

$$k > \frac{1}{\tau} , \qquad (2)$$

where τ is the average lifetime of the excited molecules. The elucidation of rate constants for various processes then becomes critical to understanding what can and does happen in the excited state. The question addressed here is whether a rarely observed process, excited-state coordination, is possible in the system presented, and what mitigating factors impact this process. Evidence presented will support the very real possibility of transient excited-state coordination as an excited state mechanism.

1.B. THE NATURE OF ELECTRONICALLY EXCITED MOLECULES

1.B.1. WAVEFUNCTIONS

In 1925, Ernest Schrödinger presented a deceptively

simple equation that describes the quantum mechanical energies of a system:

$$H\psi = E\psi, \tag{3}$$

where H is the Hamiltonian operator acting on ψ, the wavefunction of electrons, to yield a set of eigenvalues of the energies, E.[3] In reality, solutions of the equation are daunting, and in cases of more than one electron, exact solutions are impossible because the interaction energy between electrons cannot be perfectly defined. This is complicated by Heisenberg's Uncertainty Principle,[4] which places limits on the information that can be absolutely known about an electron according to the equations:

$$\Delta \rho \Delta x \geq \frac{h}{4\pi}, \text{ and} \tag{4}$$

$$\Delta E \Delta t \geq \frac{h}{4\pi}, \tag{5}$$

where h is Planck's constant, Δx is the uncertainty in the position of the electron, $\Delta \rho$ the uncertainty in the momentum of the electron at position x, ΔE is the uncertainty in the energy, and Δt is the uncertainty in the time when E is measured. Suffice it to say, getting a handle on the energy levels has required some carefully formulated theories and approximations. One pervasive and useful simplification is the Born-Oppenheimer

approximation,[5] which assumes that the molecular wavefunction can be separated into contributions from nuclear and electron motion, giving:

$$\Psi_{\text{molecule}} = \psi_{\text{electronic motion}}\,\psi_{\text{nuclear motion}}. \qquad (6)$$

In essence, because electrons, by virtue of their near weightlessness, move much faster than nuclei, the nuclei can be considered to be fixed with respect to electronic motion. Thus, looking at the electronic wavefunction alone, two successful theories are germane to this discussion: molecular orbital theory (MO) and ligand field theory.

1.B.2. MOLECULAR ORBITAL AND LIGAND FIELD THEORY

In MO theory, the wavefunction of a molecule is described as the superposition of linearly combined atomic orbitals, resulting in the same number of *molecular* orbitals, having energies similar to, greater than, and lower than those atomic orbitals. Some combinations give rise to bonding orbitals with lower energy, designated as "σ" & "Π": others give rise to non-bonding orbitals designated "n" of similar energy to that of the atomic orbitals: and, anti-bonding orbitals of higher energy are designated as "σ^*" & "Π^*". σ bonds are molecular bonding orbitals with electron density cylindrically symmetrical

along the bond axis, and Π bonds have electron density symmetrical above and below the plane of symmetry that defines the axis of the bond.[iii] Whereas bonding orbitals suggest a region of common electron density (delocalized), anti-bonding orbitals, by their nature often result in polarization of electron density (localization). The Pauli Exclusion principle[6,7] still requires that each MO be populated with no more than two electrons, while the Aufbau principle[8] requires that the orbitals are filled from the MO with lowest energy to that with the highest. Since chemical interactions are primarily outer-sphere, one simplification is to look only at the so-called "frontier orbitals"—the highest occupied MO (HOMO) and the lowest unoccupied MO (LUMO). The first electronic excited state then is an electron from the HOMO being promoted to the LUMO.

In metal coordination compounds where ligands coordinate[iv] to a central metal atom or ion, the "frontier orbitals", so to speak, are the d orbitals, so ligand-field theory focuses on their energies only. The degeneracy of the d orbitals is broken when ligands coordinate to the metal thus creating an electronic "ligand" field, causing

---

[iii] Higher order bonding orbitals such as δ bonds are also possible.
[iv] A coordination bond is often described as a ligand donating both electrons to the bonding pair.

electrons in those orbitals involved in bonding to be raised in energy due to electronic repulsion of the ligands, and the others to be concomitantly lowered. The difference between the energies, termed the ligand-field splitting parameter determines the placement of electrons into the d orbitals, *a la* Aufbau. An example of a symmetric octahedral field where two levels of degenerate orbitals are made is given in Figure 1, which shows a strong field case for a d^6 metal. As a consequence of group theory, the low energy three-fold degenerate set is termed t_{2g} and the upper two-fold degenerate set, e_g.

In the d^6 "low spin" configuration, the electrons are paired since the energetic cost of electron pairing is preferred to placing electrons in the higher energy d orbitals. An electronic transition then may involve promotion of an electron from one d orbital in the lower energy set to another in the higher energy set—a d-d transition, designated $e_g \rightarrow t_{2g}$. Where there are unpaired electrons, the spin and orbital angular momenta can give rise to a measurable magnetic moment. In coordination compounds however, the orbital angular momenta of electrons is quenched, or reduced by interactions with the non-spherical ligand field, leaving only the spin angular momenta to contribute to the magnetic moment. This has

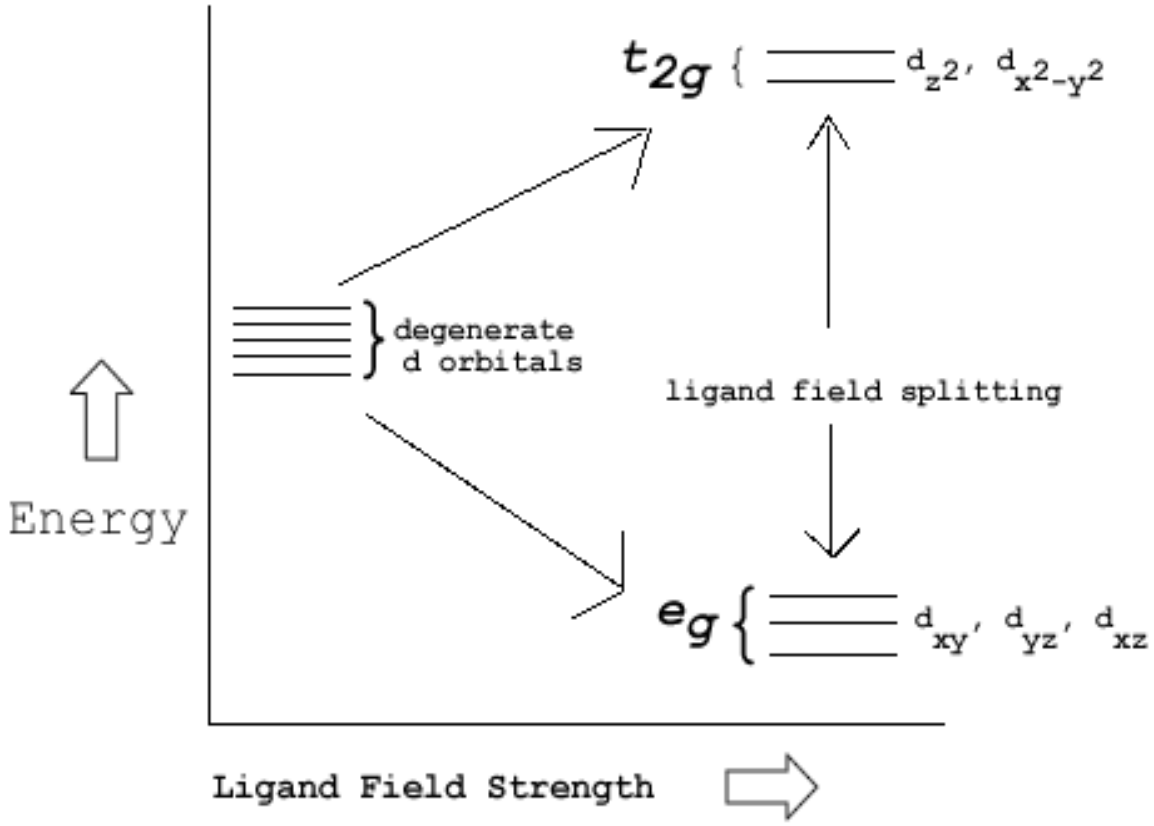

Figure 1. Octahedral ligand field splitting of d orbitals.

allowed the success of ligand field theory to come to light experimentally—the strong/weak field distinction made evident by the measured spin-only magnetic moment, μ, which is related to the number of unpaired electrons *N* by

$$\mu = \left\{ N\left(N+2 \right) \right\}^{1/2} \mu_B \quad , \qquad (7)$$

where μ_B is the Bohr magneton = 9.274 x 10^{-24} J/T. For example, the weak field d^5 system $[Fe(OH_2)_6]^{3+}$ with 5 unpaired electrons has a measured magnetic moment of about 5.9μ_B, comparable with a calculated value of 5.92μ_B.[9]

1.B.3. SPIN STATES

To determine actually the specific frontier orbitals, spin states must now be taken into account since for multi-electron systems, not all collections of various possible spin states are energetically the same due to electron repulsion. For atomic systems, Hund's rules[10,11] state that the lowest energy state is comprised of the least amount of electron spin pairing, or the greatest spin multiplicity, *2S+1*, where

$$S = \sum m_s \qquad (m_s = \text{spin quantum number}) \qquad (8)$$

and the greatest orbital angular momentum (least amount of electron interactions), *L*, where *L* = max of M_L and

$$M_L = \sum m_l \qquad (m_l = \text{orbital quantum number}). \qquad (9)$$

A pair of electrons with anti-parallel spins is termed a singlet state (S_o for the ground state) since it has a spin multiplicity of 1 calculated from $2S+1$, with $S=0$. For parallel spins, the spin multiplicity is 3 ($S=1$)—meaning there are three different vectorial spin arrangements. This is called a triplet state (T_o for the theoretical ground state), and clearly is lower in energy than the singlet state, which has more electronic repulsion. Coupled with symmetry considerations, such spin-state considerations for molecules lead to molecular term symbols (with capitalized wavefunction designations, Σ & Π) that account for the degeneracy, multiplicity, symmetry, and parity of the different states. How atomic term symbols evolve into molecular term symbols based on ligand field symmetry and weak field *vs.* strong field cases can be seen graphically in Tanabe-Sugano diagrams (Figure 2). When the ground state is known, the various transitions to excited states can then be reasoned.

1.C. THE FORMATION OF ELECTRONICALLY EXCITED STATES

With a basic understanding of the various electronic states involved, how then are excited states actually

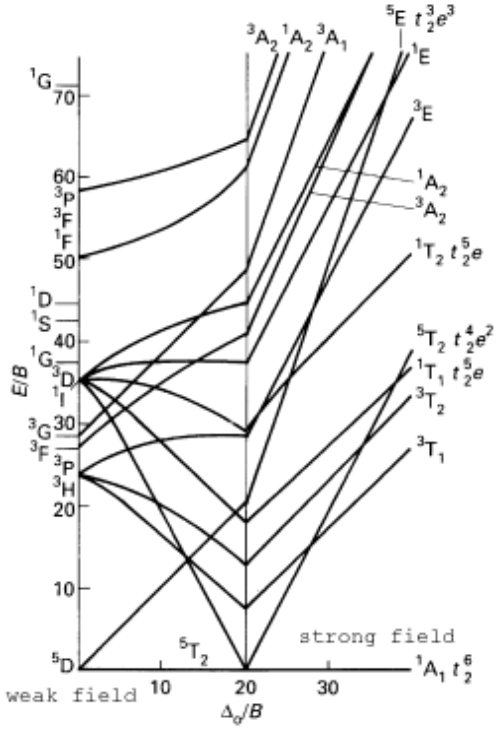

Figure 2. Tanabe-Sugano diagram of a d^6 system.
The plot details the various possible spin states in a d^6 system, based on the strength of the ligand field.

achieved? An excited state is obtained when the appropriate amount of energy is added to the system—most often *via* photonic excitation. When a photon interacts with a molecule, an electron can be promoted to an excited state if the following resonance condition is held:

$$\Delta E = \frac{hc}{\lambda} \tag{10}$$

where ΔE is the energy between the ground state and excited state, h is Planck's constant, c is the speed of light, and λ is the wavelength of light. The energies required to excite an electron correspond to wavelengths of light on the order of 200nm – 700nm, or light in the ultraviolet to visible spectrum. The oscillating electric component of electromagnetic radiation can interact with the electron, passing its energy to the electron and causing it to move to an excited state.

In a collection of molecules, the probability of absorption of photons to achieve an excited state is related to how allowed the transition may be, which is, in a simple estimation, related to the overlap between ground state and excited state wavefunctions. The greater the overlap, the greater the probability of the transition, or in other words, the "easier" it is for the electron to move

from one wavefunction to the other. Therefore, not all transitions suggested by the Tanabe-Sugano diagrams are allowed, but are in fact governed by rules of symmetry, overlap of wavefunctions, spin selection rules and Laporte selection rules (regarding change of parity). Whereas absorption of a photon can excite an electron, it cannot change the relative orientation of electrons' spins, meaning, for "spin-allowed" transitions, the first triplet state, T_1 cannot arise directly from a ground state singlet state S_0 and vice versa. If however, as in the case with heavy atoms, the spin angular momenta can couple with the orbital angular momenta, such "spin-orbit coupling" can both relax the spin selection rule and allow spin-forbidden transitions.

In d-d transitions, centrosymmetric molecules are governed by Laporte selection rules.[12] These require a change of parity that arises from the fact that the intensity of a transition depends upon the strength of a transient electric dipole, or the transition dipole moment, defined as

$$\mu_{fi} = \int \psi^* \hat{\mu} \psi dt \tag{11}$$

where ψ^* is the wavefunction of the excited state, ψ is that of the ground state, and $\hat{\mu}$ is the electric dipole

moment operator. Again, intuitively, overlap between the ground and excited state wavefunctions is essential. A molecule can achieve a Laporte-forbidden transition by reducing its symmetry (Jahn-Teller effect[v]) to cancel the requirement. In all, the allowedness of light absorption is indicated by the extinction coefficient or molar absorptivity (in cases of molar solutions), ε, that indicates how much light is attenuated when passing through a solution. For light of radiant power P_o impinging on a dilute solution, the light will be attenuated by the concentration of absorbing species (c), the path through the absorbing solution (b), and the cross-section for absorption (the extinction coefficient or molar absorptivity ε) yielding the attenuated radiant power of light transmitted, P_f according to the Beer-Lambert law:

$$P_f = P_o e^{-2.303\ \varepsilon bc} . \qquad (12)$$

From the equation's $\frac{P_f}{P_o}$ more common form with the negative log of the transmittance as absorbance (A)

$$A = \varepsilon bc, \qquad (13)$$

---

[v] A molecule of apparent high symmetry may contain a nontotally symmetric vibration as one if its irreducible degenerate representations, and thus adopt nuclear equilibrium positions of lower symmetry to remove the degeneracy. This is referred to as the Jahn-Teller effect.[13]

it is clear that the extinction coefficient has units of L mol^{-1} cm^{-1}. Values for ε_{max} can vary from as little as 10^{-5} for forbidden transitions, to 10^{5} for fully allowed transitions.[14] A set of molecules, D, will become excited, indicated by *D,[vi] based on the rate of excited state production I, according to

$$D \xrightarrow{I} {}^{*}D \qquad (14)$$

where I is the product of the rate of light absorbed, I_a, and the efficiency of production of $^{*}D$, η^{*}.

1.D. BASIC TYPES OF ELECTRONIC TRANSITIONS

With an instrument sensitive to light transmitted through a sample of known concentration at varying wavelengths, a plot of ε vs. wavelength will reveal various electronic transitions of differing types, classified as ligand-centered, metal-centered, or charge-transfer (between the metal and ligand). At higher energies (UV), $n \rightarrow \Pi^{*}$ and $\Pi \rightarrow \Pi^{*}$ transitions are quite strong in organic compounds and in coordination compounds with organic ligands coordinated to the metal. For coordination

---

[vi] The "*" sign is indicative of an electronically excited species, or a quantity relevant to the same.

compounds, symmetry-allowed transitions between d orbitals and Π^* orbitals on attached ligands are of special interest, and in general are referred to as charge transfer bands. "Charge transfer" here refers to the fact that electron density—a region of negative charge—is redistributed amongst spectrally different portions of the complex, usually from one part of the molecule into another, leaving behind an electron-poor region of more positive charge.

Charge transfer transitions lead to more or less charge on attached ligands. The often critical consequences this has on a molecule's interactions with other chemical species—since the "outer" ligands usually are the points of inter-molecular contact—cannot be overstated. In a ligand-ligand transition an excited state electronic orbital may be more extant and energetic, but a bird's-eye view of the overall charge of that portion of the molecule ("moiety"), *per se*, does not change. On the other hand, in a coordination compound with charge transfer states, the metal's d orbitals can serve as either a source of *additional* negative charge or an electron sink.

It is now known that in many cases, an electron can be actually transferred out of the molecule or into the molecule from another species. Ligand-to-metal charge

transfers (LMCT) occur when the transition involves electronic redistribution from the ligand to the unoccupied, usually lower energy metal centered orbitals. *Vice versa*, metal-to-ligand charge transfers (MLCT) involve electronic distribution from the occupied d orbitals to the unoccupied, usually low-energy-lying π^* orbitals centered on the ligand.

Interestingly, it is also possible for two molecules to interact and absorb a photon together. The interaction is weak, and a new absorption band uncharacteristic of the two species appears. Such an "absorption complex" is often charge-transfer in nature.[14] In such cases, the energy of the transition will be lowered with increasing solvent polarity. The wavefunction of the absorption complex with D as a donor and A as an acceptor can be represented as:

$$\Psi_{complex} = \alpha D,A + \beta D^{+}A^{-} \qquad (15)$$

where α and β are the contributions of the "no-bond" electronic configuration and charge-transfer configuration, respectively. Bond formation is weak and may or may not be structurally specific. Also, the excited state may or may not involve the same interaction as that of the ground state. All in all, two fundamental questions are addressed here: First, can a transient electronic reorganization

facilitate peripheral bond formation at the ligand of a coordination complex? And second, to what extent is it dependent on the ground-state interaction?

1.E. GENERAL PROCESSES OF THE EXCITED STATE

With a framework of the nature of the excited state and how it is achieved, once a molecule is excited what happens next? The answer to that question is always contextualized by the drive to achieve a low energy state, *i.e.* the prime directive, so to speak, of the electronically excited molecule is to rid itself of excess energy. In the absence of more added energy, the molecule, or any collection of molecules, will eventually succeed at achieving this goal; the issue is how long will it take and by what means will it be accomplished.

Interestingly though, some molecules may not return to the ground state from which they came, but may, by virtue of the excess energy and alternate landscape of the excited state, follow a pathway to a different ground-state, in essence, undergoing a fundamental chemical change. The chemical change may be a loss or gain of electrons, a change of stereochemistry, bond-formation and/or bond-scission. Bond breaking and bond formation are possible when enough thermal energy is present to overcome the

energy activation barrier in a ground state landscape. "Landscape" refers to the *potential energy* landscape associated with chemical bonds. Since excited state wavefunctions are different from the ground state, the landscape for bond formation and breaking is also different, and thus the products of a photochemically-activated and induced chemical change are often, but not always, themselves quite different. This was dramatically demonstrated and explained in 1965 as pertaining to the thermal vs. photochemical dependence of electrocyclic ring opening and closing of conguated polyenes by Woodward and Hoffmann, summarized in the "Woodward-Hoffmann" rules.[15] With coordination compounds, several years later Adamson[16] described the thermal vs. photochemical dependence of $[Cr(NH_3)_5(NCS)]^{2+}$ aquation: thermal activation leads to $[Cr(NH_3)_5(H_2O)]^{3+}$, but photochemical activation to $[Cr(NH_3)_4(H_2O)(NCS)]^{2+}$. There are many more examples, but clearly, the excited state can facilitate pathways unavailable to ground state molecules.

Although overall photo-induced chemical change is perhaps more interesting, it is certainly not more common. In fact, since an excited molecule is driven to dissipate its energy, there are many ways in which it may do so, and most are much more efficient than chemical change. These

processes are all termed "relaxation" process, and can be divided into those that are inherent to the molecule, or *intra*molecular, and those that are dependent on interactions with other species, or *inter*molecular. All of the possible relaxation processes in essence compete with each other. The rate at which excited molecules relax *via* any particular intramolecular process is a first-order process, only depending upon the concentration of excited species [*D] and the likelihood of relaxing by that process, indicated by a particular rate constant, k, according to

$$\frac{-d[^*\mathrm{D}]}{dt} = k[^*\mathrm{D}] \tag{16}$$

where $-d[^*\mathrm{D}]/dt$ is the rate of disappearance of *D with time. In the case of intermolecular processes, *D must interact with some other species, Q. The more Q, the more the possibility for interaction and relaxation, also called "quenching".[vii] When first-order processes are not explicitly considered, this bimolecular relaxation process is dependent upon the quencher concentration, [Q] according to

---

[vii] The term quenching is used to imply enhanced relaxation of the excited state usually measured by the extinguishing of the emitted light.

$$\frac{-d[{}^{*}\mathrm{D}]}{dt} = k_{q}[\mathrm{Q}][{}^{*}\mathrm{D}] \tag{17}$$

where k_q is the bimolecular rate constant for quenching. Before getting into any complicated mathematics, it is obvious that those intramolecular processes that are inherent to the molecule will dictate the extent to which bimolecular processes will be important, meaning, in general, $k >> k_q$. This is because in solution Q and *D must diffuse to each other for the interaction to occur, and this takes additional time. If certain intramolecular processes are slow and [Q] is high enough, bimolecular processes become quite important.

1.F. INTRAMOLECULAR RADIATIVE RELAXATION PROCESSES

1.F.1. GENERAL CONSIDERATIONS

Given that a molecule is initially excited by absorption of a photon, the most obvious choice of energy release is the reverse, to emit a photon. The oscillating electron may itself generate an oscillating electromagnetic wave, and transfer its energy to it, leading to light output of wavelengths in the ultraviolet to visible spectrum. This luminescent behavior can be distinguished based on the identities of the originating and ending

states. "Fluorescence" occurs between states of the same parentage, the most common example being from an excited singlet state to a singlet ground state (e.g. $S_0 \leftarrow S_1$). "Phosphorescence", on the other hand, is when emission occurs between states of different parentage, the most common being from a triplet excited state to a singlet ground state (e.g. $S_0 \leftarrow T_1$).[viii] Again, in coordination compounds with heavy atoms, the angular momentum of the d electrons can cause spin-orbit coupling that blurs this distinction. Even so, in practical terms, because of the additional time needed for the electron in a triplet state to undergo another spin flip in order to reach the ground state, phosphorescence rates tend to be slower, meaning, phosphorescence tends to last longer than fluorescence. Whether fluorescence or phosphorescence, the "radiative" rate constants of each, k°_{F} and k°_{P} respectively, are inherent to the emitting molecule in question and depend on the likelihood of the molecule releasing energy by generating a photon as opposed to other deactivation methods. By the same token, the inverses of each, $1/k^{\circ}_{F}$ and $1/k^{\circ}_{P}$, are the inherent lifetimes, τ°_{F} and τ°_{P}, in the

---

[viii] Whereas radiation between excited states has been observed experimentally, such as $T_1 \leftarrow T_2$, these processes have such small contributions that they are not considered here.

absence of any other deactivation pathways.

1.F.2. VIBRATIONAL CONSIDERATIONS

One might expect that with discreet energy levels, absorption and emission spectra would be composed of sharp lines. This is only the case with low-pressure gaseous atoms. With molecules, vibrational energy levels are superimposed onto electronic energy levels.[ix] Given that most molecules reside in their ground vibrational states at room temperature, nearly all transitions usually arise from that ground vibrational state. A molecule can be excited to a number of vibrational states within an *excited* electronic state, and coupled with the myriad of states arising from different nuclear positions and collisions, the spectrum will appear quite broad and smooth given the available energy at room temperature, *ca.* 200cm^{-1}. A distribution of possible states yields a near Boltzmann distribution of energy transitions, and thus an almost Gaussian shaped set of transitions.

With a vibrating molecule, the nuclear positions of the atoms are constantly changing. However, because

---

[ix] Rotational energy levels are further superimposed onto vibrational levels, but are not considered here since they are not distinguishable for molecules in solution and have little or no bearing on the behavior of electronic states in such scenarios.

coupling of a photon with an electron in absorption is so fast, the nuclear positions are considered fixed upon excitation—this being referred to as the Franck-Condon Principle.[17] A typical way of conceptualizing this is in Figure 3, where the energy of a ground state and first excited state are plotted verses nuclear coordinate. Since excited states often involve anti-bonding orbitals, the nuclear positions are more separated, meaning, the well is shallow. Excitation into the first excited state produces an excited vibrational level *within* that state since the nuclear coordinates of the two states do not line up. The 0-0 transition between lowest vibrational states within each electronic state is the smallest energy gap, but certainly not the most probable absorption transition. Since absorption produces mostly excited vibrational states within the excited state, there is a strong drive to relax to the lowest vibrational level, which is easily accomplished within a few vibrations. The frequency of vibration is large such that all excited vibrational states can and do relax to the lowest vibrational state (meaning the rate constant for vibrational relaxation is very high) before other processes, such as emission, occur. Within spin states, this kind of relaxation is a form of internal conversion (*vide infra*).

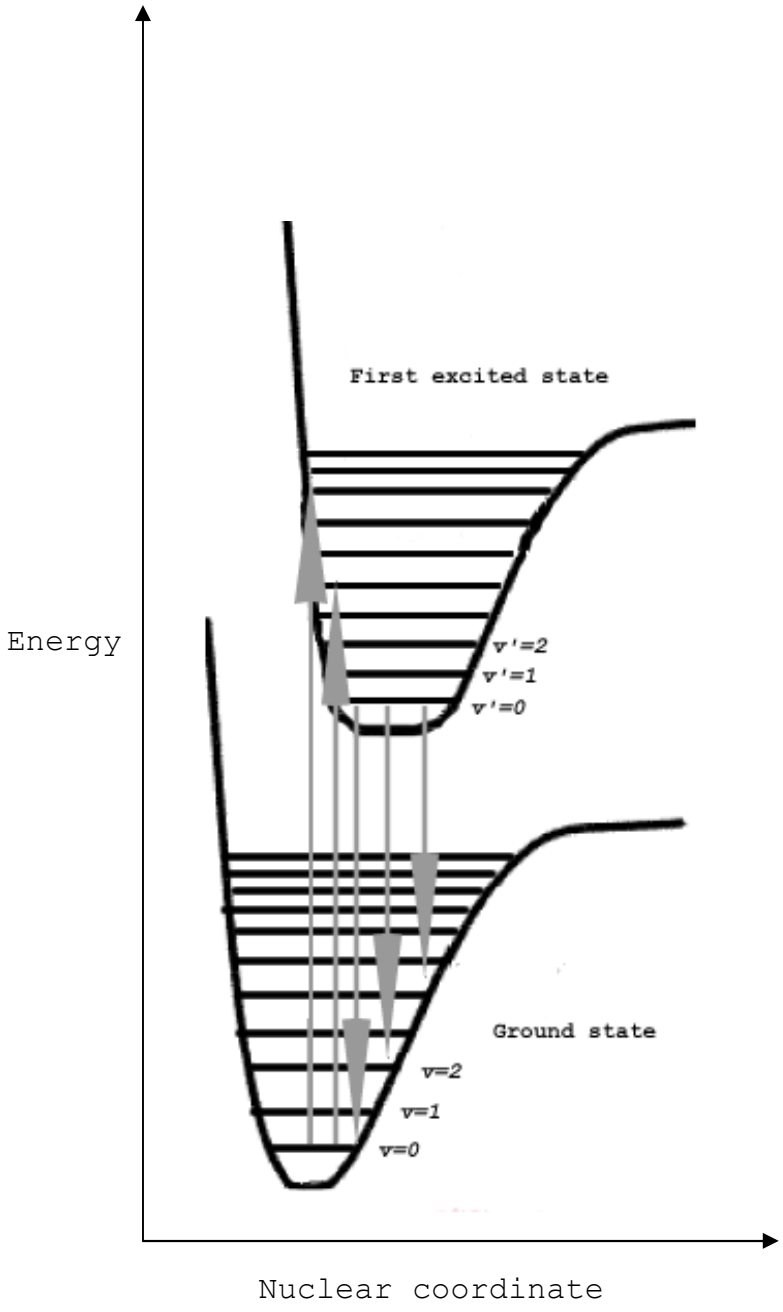

Figure 3. Absorption and emission from vibrational levels within electronic states.

The molecule may then relax, by emission, to any of the number of excited vibrational states within the electronic ground state. Unlike absorption, the 0-0 transition represents the largest energy gap, but not the most common. Since the vibrational spacing within the ground and first excited electronic state are somewhat similar (otherwise, electronic excitation would easily lead to bond dissociation, which it does not), the absorption and emission spectra tend to mirror each other, with their intersection representing the mirror-plane, *i.e.* the 0-0 transition. Since some vibrational (thermal) energy is lost after excitation, the emission spectrum is always lower in energy than the absorption spectrum, and the difference between the maxima, which is a measure of this energy loss, is the Stokes shift.[17] In theory, the spectra should not cross, but occasionally do when circumstances (or intention, as in Coherent anti-Stokes Raman spectroscopy [CARS]) allow absorption or emission from an excited vibrational state.

1.G. INTRAMOLECULAR NON-RADIATIVE RELAXATION PROCESSES

1.G.1. INTERSYSTEM CROSSING

Upon initial excitation into the first singlet state, S_1, a molecule may undergo a spin flip, leading to an

excited triplet state, T_1, which is lower in energy, due to reduced electron-electron repulsion. Additionally, an excited triplet state may undergo a "spin-forbidden" flip to the lower energy singlet ground state, S_0. These spin-relaxation processes are called intersystem crossing. The relevant rate constants for each can be designated $k_{ST,}$ which leaves the molecule in an excited state, and $k_{TS,}$ which deactivates the molecule entirely. In both examples, energy is lost as heat to the surroundings. As previously discussed, coordination complexes with a heavy metal tend to facilitate intersystem crossing due to spin-orbit coupling. The time distinction between fluorescence and phosphorescence, while being a judge of whether the emissive state is a singlet or triplet, also reflects on the amount and rate of intersystem crossing. Since $S_0 \leftarrow T_1$ transitions by intersystem crossing barely compete with other more efficient processes, its contribution is small, and thus the rate of intersystem crossing, k_{isc}, is usually a reflection of $T_1 \leftarrow S_1$ only.

1.G.2. INTERNAL CONVERSION

Excitation into upper spin states such as S_2 and T_2 creates high-energy species. On the order of a vibration, these states can quickly relax to the first excited states,

S_1 and T_1. Indeed, vibrations and vibronic coupling stimulate these *internal conversions*, $T_1 \leftarrow T_n$ and $S_1 \leftarrow S_n$, within a particular spin state, and as discussed before, relaxation to the first excited state levels is quick and efficient, such that radiative processes almost always only occur from the S_1 or T_1 as articulated by Kasha's rules.[18]

Vibronic coupling refers to a breakdown of the Born-Oppenheimer approximation such that the electronic and vibrational wavefunctions are no longer separable, but influence each other. Internal conversion can also occur between the first singlet state and the ground state by vibronic coupling between the two to dissipate the energy as heat (there is no corresponding transition within triplet states since T_0 is meaningless). However, this requires overlap between the *nuclear* wavefunctions of the excited and ground states, meaning, that there is a portion where the potential energy curves of the states come very close. With greater separation of energy between them, the overlap is quite small (energy gap law[x]), and thus transitions between them become Franck-Condon "forbidden" (non-vertical as pertaining to nuclear

---

[x] The Energy Gap Law states that as the difference in energies between states increases, the rate of transfer between them decreases. Thus, internal conversions where the overlap is small are usually slower than intersystem crossings.

configurations). Thus, this process is quite slow compared to other possible relaxation pathways, and by Ermolaev's rule[19] (normally stated in terms of the quantum yields, *vide infra*), the sum of the rate constants for fluorescence and $T_1 \leftarrow S_1$ is nearly equal to the total rate constant for intramolecular deactivation k.

Considering then only processes after the first excited singlet state is produced, the possible deactivation pathways and their rates constants are shown in Scheme 1.

Scheme 1.

Excitation	$h\nu + S_0 \rightarrow S_1$	Rate = $I_a \eta^*$
Internal Conversion	$S_1 \rightarrow S_0$ + heat	Rate = $k_{IC}[S_1]$
Intersystem Crossing	$S_1 \rightarrow T_1$ + heat	Rate = $k_{ST}[S_1]$
Intersystem Crossing	$T_1 \rightarrow S_0$ + heat	Rate = $k_{TS}[T_1]$
Phosphorescence	$T_1 \rightarrow S_0 + h\nu$	Rate = $k^o_P[T_1]$
Fluorescence	$S_1 \rightarrow S_0 + h\nu$	Rate = $k^o_F[S_1]$

Figure 4 is a simple representation, called a Jablonski diagram,[20] of these processes. El Sayed points out that intersystem crossings, being mitigated by a change in orbital angular momentum when there is spin-orbit coupling

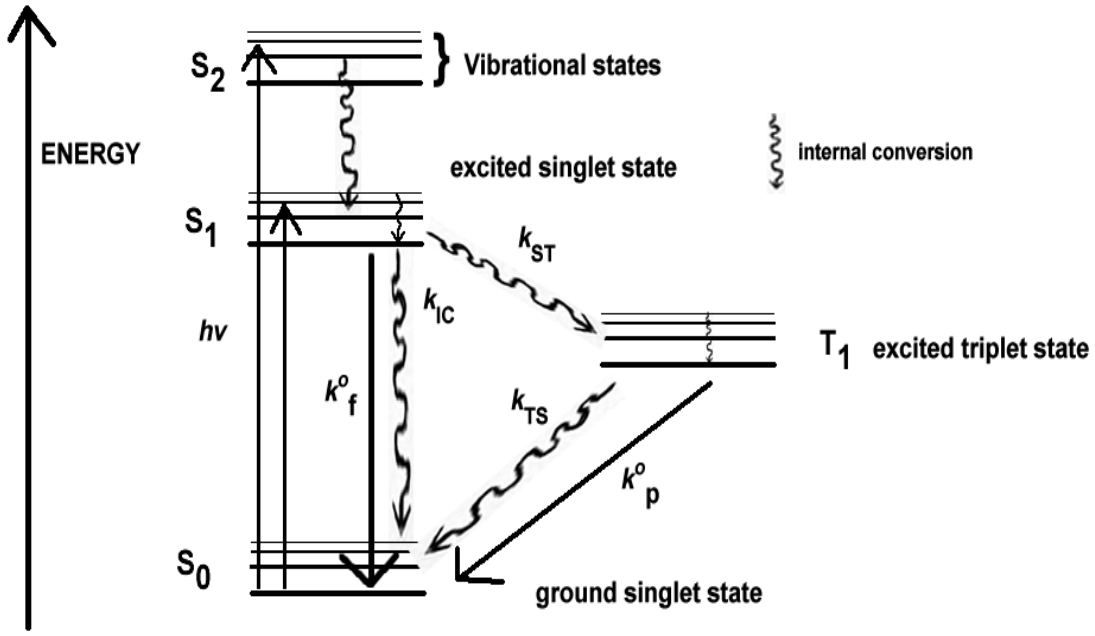

Figure 4. Jablonski diagram.

are faster than internal conversions, where only a change in spin occurs.[21,22]

1.G.3. QUANTUM YIELD OF INTRAMOLECULAR RELAXATION

For purposes here, it becomes helpful and convenient to recall that in coordination complexes with significant spin-orbit coupling, the distinction between T_1 and S_1 can become blurred. To simplify then, radiative and non-radiative relaxation processes can be separated and individual component terms combined yielding *generic* radiative and non-radiative rate constants, k_r + k_{nr} respectively, where

$$k_r = k_P^o + k_F^o \tag{18}$$

and

$$k_{nr} = k_{IC} + k_{ST} + k_{TS} \quad . \tag{19}$$

The *observed* lifetime, τ_{obs} will be the reciprocal sum of all rate constants

$$\tau_{obs} = \frac{1}{(k_r + k_{nr})} \quad , \tag{20}$$

which is distinguishable from the non-observable, but

calculable inherent radiative lifetime,

$$\tau_{\mathrm{o}} = \frac{1}{k_{\mathrm{r}}} \quad . \tag{21}$$

For steady state excitation of D → *D, the rate of excitation (product of light absorbed I_{a} and efficiency of excited state production η^{*}) is equal to the rate of decay, meaning

$$I_{\mathrm{a}}\eta^{*} = \left(k_{\mathrm{r}} + k_{\mathrm{nr}}\right)\left[{}^{*}\mathrm{D}\right] \quad . \tag{22}$$

Therefore, the efficiencies—"quantum yields"—of radiative and non-radiative decay, Φ_{em} and Φ_{nr} respectively, are

$$\Phi_{em} = \frac{k_{\mathrm{r}}}{k_{\mathrm{r}} + k_{\mathrm{nr}}} \tag{23}$$

and

$$\Phi_{nr} = \frac{k_{\mathrm{nr}}}{k_{\mathrm{r}} + k_{\mathrm{nr}}} \quad . \tag{24}$$

Quantum yield can be thought of as the probability that absorption of one photon ("quantum" of light) will lead to a particular radiative or non-radiative event. Since all possible events must be accounted for, it is clear that

$$\Phi_{em} + \Phi_{nr} = 1 \tag{25}$$

and that from experimentally obtainable knowledge of Φ_{em} and τ_{obs} (from here on simply designated τ), the radiative and non-radiative rate constants can be determined from

$$k_{r} = \frac{\Phi_{em}}{\tau} \tag{26}$$

and

$$k_{nr} = \frac{1 - \Phi_{em}}{\tau} \quad . \tag{27}$$

Since a range of wavelengths can produce the same excited state, the Φ_{em} represents the probability that a molecule, once excited, will relax by emission, and is therefore independent of the excitation wavelength, which is often called Vavilov's law (or the Kasha-Vavilov rule).[23,24] In practice, Φ_{em} is proportional to the total area under an emission decay curve, or steady-state emission spectrum. Not included in Scheme 1 and the above discussion is the possibility that given $^{*}S$ has new chemical pathways available to it, $^{*}S$ may by itself undergo a first-order chemical reaction such as a rearrangement, or bond-scission leading to a different (relaxed) product. The rate constant for this photochemical reaction, k_{rx} is folded into k_{nr} as a

non-radiative process, but can be extracted out if significant.

1.G.4. TIME DEPENDENCE OF INTRAMOLECULAR RELAXATION

Integration of (16) with the assumption that $[^*D]=[^*D]_0$ at t=0 gives

$$\ln \frac{[D]_o}{[^*D]} = -kt \tag{28}$$

and furthermore,

$$[^*D]=[*D]_0\, e^{-kt}. \tag{29}$$

If $^*D$ is luminescent, and a detector response A is proportional to $[^*D]$, then the first-order decay of $[^*D]$ is observed as

$$A=A_0\, e^{-t/\tau}, \tag{30}$$

where A_0 is representative of the initial excited state population, and τ is the lifetime, or time required for the concentration to be reduced by 1/e. Normally, a plot of ln (A/A_o) *vs. t* will give a straight line with intercept $-1/\tau$, but a non-linear, two-parameter least-squares fit of the data will directly give both excellent values of A_0 and τ. Again, *k* is the sum of all rate constants for deactivation

(k_r + k_{nr}), so both k_r + k_{nr} can be calculated from (26) and (27) if the quantum yield is known.

1.H. INTERMOLECULAR RELAXATION PROCESSES

1.H.1. GENERAL CONSIDERATIONS

If an excited molecule interacts with any quencher molecule other than a solvent molecule (*vide infra*), it is usually because the two have diffused together, which is complexly dependent upon a number of factors including the charge of each species, their size, and polarizability among other things. Upon diffusion, the two species form an encounter complex (EC), which may fall apart without any net change (diffuse apart), or continue on to some deactivation mechanism according to the following:

$$ {}^{*}D + Q \underset{k'_{-d}}{\overset{k'_{d}}{\leftrightarrows}} \{EC\} \xrightarrow{k_{de}} D + Q, \qquad (31) $$

where k'_d is the rate constant for diffusion, k'_{-d} the rate constant for separation, and k_{de} the rate constant for deactivation. Any deactivation pathway that depends upon the species diffusing together first is said to be "diffusion-limited", meaning $k_{de} \geq k'_d$. It is extremely difficult to determine experimentally rate constants for diffusion and separation; however, both can be

approximately calculated from the Debye-Smoluchowski equation[25-29] and the Eigen equation[30] respectively. It is useful here to distinguish between the rate constants for diffusion and separation when one species is excited, k'_{d} and k'_{-d}, and the rate constants for the corresponding ground-state processes, k_{d} and k_{-d}. In both cases, the ratios of the rate constants of diffusion over separation define the association equilibrium constants in the excited state,

$$K^{*}_{eq} = k'_{d} / k'_{-d}, \tag{32}$$

and ground state,

$$K_{eq} = k_{d} / k_{-d}. \tag{33}$$

The Debye-Smoluchowski and Eigen equations cannot distinguish between the ground-state and excited state equilibrium and rate constants (*i.e.* $K^{*}_{eq}=K_{eq}$ because $k'_{d}=k_{d}$ and $k'_{-d}=k_{-d}$) due to their inherent approximations.[xi] These assumptions include the consideration of only electrostatic interactions between ions treated as rigid spheres, and the disregard of hydrogen bonding interactions. In this limitation, any distinction between ground and excited

---

[xi] This also assumes the charges on the species remains the same before and after the encounter, thus precluding formal electron transfer.

state would result from interactions other than electrostatic, such as covalent bonding. Even so, the equations make clear that diffusion of like-charged species is favored by increasing ionic strength and dielectric constant of the solvent; in conceptual words, the ions will 'drag' less through the solvent.

Figure 5 shows the flow of mechanistic steps and rate constants. The encounter complex, (*D--Q), designated EC in equation (31), can undergo its own radiative and non-radiative decay processes with associated rate constants k'_r and k'_{nr} respectively, and with $k'_o = k'_r$ & k'_{nr}.[xii] However, these processes are normally not considered to be much different from those associated with $^{*}D$, such that $k_r \approx k'_r$, $k_{nr} \approx k'_{nr}$ and their sums are equal, $k_o \approx k'_o$.[31] More importantly, significant interactions between $^{*}D$ and Q can mean the encounter complex continues on, *via* the generic rate constant, k'_{sc}, to a (non-separated) successor complex, of which the possibilities are discussed below and include energy transfer, electron transfer, proton transfer, excimer formation, and exciplex formation. The new rate constant for deactivation, k'_{de} is now the sum of $k'_o + k'_{sc}$,

---

[xii] Relaxation rate constants for a "non-interacting" excited species are distinguished from the primed relaxation rate constants for the encounter complex, and from the doubly primed relaxation rate constants for the successor complex discussed below.

$$k'_{de} = k'_o + k'_{sc}$$

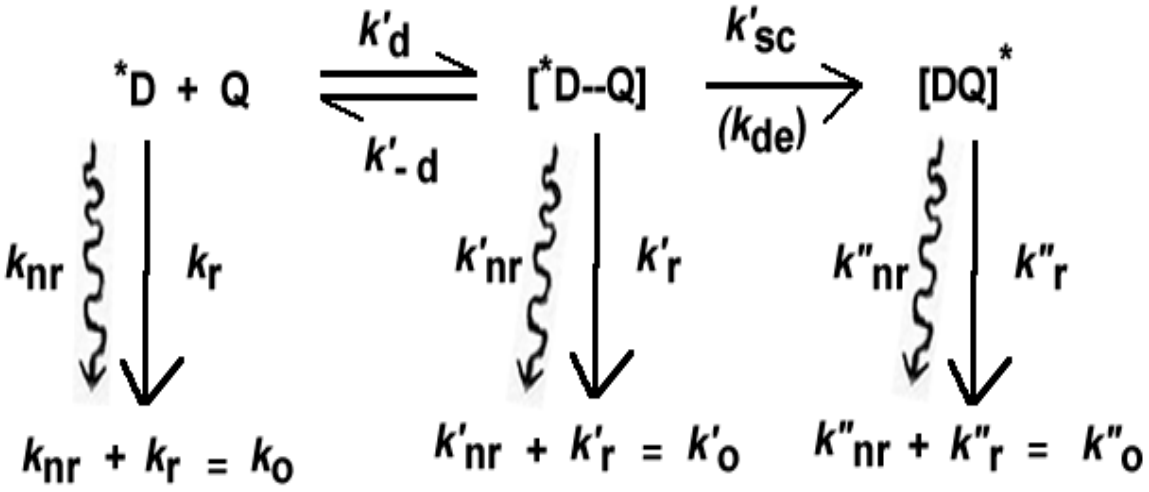

Figure 5. Mechanistic steps and intermolecular relaxation processes.

and the successor complex continues on to other deactivation mechanisms with their own associated rate constants k''_r and k''_{nr} whose sum is $k''_o = 1/\tau''_o$.

1.H.2. KINECTICS OF INTERMOLECULAR RELAXATION

When intermolecular relaxation processes are included, the total rate constant for decay is now

$$k = k_o + k_q[Q], \tag{34}$$

where folded into k_q are k'_d, k'_{-d}, and k'_{sc}. Although (28) and (29) still technically hold, k is actually now a function of and varies with [Q]. (16), (17), and (34) combine to become

$$\frac{-d[^*D]}{dt} = (k_o + k_q[Q])[^*D] \quad . \tag{35}$$

It becomes helpful at this juncture to invoke a steady state approximation, meaning, when there is a constant excitation intensity,

$$\frac{-d[^*D]}{dt} = 0 \quad . \tag{36}$$

Under this assumption,

$$[^{*}\mathrm{D}]_{\text{steady state}} = \frac{I_{\mathrm{a}}\eta^{*}}{k_{\mathrm{o}}} = A_{\lambda}^{\mathrm{o}} \tag{37}$$

when [Q]=0, and

$$[^{*}\mathrm{D}]_{\text{steady state}} = \frac{I_{\mathrm{a}}\eta^{*}}{\left(k_{\mathrm{o}} + k_{\mathrm{q}}[\mathrm{Q}]\right)} = A_{\lambda} \tag{38}$$

at some concentration [Q] and analytical wavelength λ=*1*. Dividing (37) by (38) gives

$$\frac{A_{\lambda}^{\mathrm{o}}}{A_{\lambda}} = 1 + K_{\mathrm{sv}}[\mathrm{Q}] \quad , \tag{39}$$

where

$$K_{\mathrm{SV}} = \frac{k_{\mathrm{q}}}{k_{\mathrm{o}}} = k_{\mathrm{q}}\tau \tag{40}$$

and K_{SV} is called the Stern-Volmer constant. A similar relationship can be derived in the absence and presence of [Q] for the lifetime, yielding

$$\frac{\tau_{\lambda}^{\mathrm{o}}}{\tau_{\lambda}} = 1 + K_{\mathrm{sv}}[\mathrm{Q}] \quad . \tag{41}$$

Plots of $A^{\circ}_{\lambda}/A_{\lambda}$ *vs.* [Q] and $\tau^{\circ}_{\lambda}/\tau_{\lambda}$ *vs.* [Q] that are coincident, linear, and have a slope of K_{SV} indicate the

system follows Stern-Volmer kinetics.[32] K_{SV} is now a measure of the quenching efficiency or ability of [Q] to quench per encounter with *D. When such plots are not coincident and/ or show deviations from linearity, other mechanisms are in play and must be vetted.

It is also clear now that the quenching constant, k_q can be calculated from (31) since the excited state species is deactivated:

$$k_q = \frac{k'_d k_{de}}{k_{de} + k'_{-d}} \quad . \tag{42}$$

In the diffusion limit, $k_{de} >> k'_{-d}$ and thus the reaction will be diffusion controlled since $k_q \sim k'_d$. On the other hand, in the pre-equilibrium limit, $k_{de} << k'_{-d}$, and $k_q = K^*_{eq} k_{de}$. The overall quenching rate will be much lower than the rate of diffusion and will be controlled by the particular mechanism of deactivation, k_{de}. Most systems are nearly-diffusion limited, falling somewhere in between.

When a pulsed light source serves as the excitation, the steady-state approximation is invalid, and the concentrations of intermediate species are time-dependent, requiring the solving of appropriate differential equations with the assumptions that $[^*D] = [^*D]_0$, and $[^*D\text{-}Q] = 0$ when $t = 0$.[31] Thus,

$$\frac{d[^{*}\mathrm{D}]}{dt} = k_{-\mathrm{d}}[^{*}\{\mathrm{DQ}\}] - (k_{\mathrm{o}} + k_{\mathrm{d}}^{'}[\mathrm{Q}])[^{*}\mathrm{D}] \quad , \tag{43}$$

$$\frac{d[^{*}\{\mathrm{DQ}\}]}{dt} = k_{\mathrm{d}}[^{*}\mathrm{D}][\mathrm{Q}] - (k_{-\mathrm{d}}^{'} + k_{\mathrm{de}})[^{*}\{\mathrm{DQ}\}] \quad , \tag{44}$$

$$[^{*}\mathrm{D}]_{t} = c_{1}[^{*}\mathrm{D}]_{\mathrm{o}} e^{-\mathrm{m}_{1}t} + c_{2}[^{*}\mathrm{D}]_{\mathrm{o}} e^{-\mathrm{m}_{2}t} \quad , \tag{45}$$

$$[^{*}\{\mathrm{DQ}\}\ ]_{t} = c_{3}[^{*}\mathrm{D}]_{\mathrm{o}} (e^{-\mathrm{m}_{1}t} - e^{-\mathrm{m}_{2}t}) \quad , \tag{46}$$

where

$$m_{1} = \tfrac{1}{2}(\mathrm{k}_{\mathrm{o}} + k_{\mathrm{de}} + k_{-\mathrm{d}}^{'} + k_{\mathrm{d}}^{'}[\mathrm{Q}]) + \tfrac{1}{2}\mathrm{R}^{\frac{1}{2}} \quad , \tag{47}$$

$$m_{2} = \tfrac{1}{2}(\mathrm{k}_{\mathrm{o}} + k_{\mathrm{de}} + k_{-\mathrm{d}}^{'} + k_{\mathrm{d}}^{'}[\mathrm{Q}]) - \tfrac{1}{2}\mathrm{R}^{\frac{1}{2}} \quad , \tag{48}$$

$$R = (\mathrm{k}_{\mathrm{o}} + k_{\mathrm{de}} + k_{-\mathrm{d}}^{'} + k_{\mathrm{d}}^{'}[\mathrm{Q}])^{2} - 4(k_{\mathrm{o}}k_{-\mathrm{d}}^{'} + k_{\mathrm{o}}k_{\mathrm{de}}^{'} + k_{\mathrm{de}}k_{\mathrm{d}}^{'}[\mathrm{Q}]) \quad ; \tag{49}$$

and,

$$C_{1} = \frac{k_{\mathrm{o}} + k_{\mathrm{d}}^{'}[\mathrm{Q}] - \mathrm{m}_{2}}{\mathrm{m}_{1} - \mathrm{m}_{2}} \quad , \tag{50}$$

$$C_{2} = \frac{m_{1} - k_{\mathrm{o}}^{'} - k_{\mathrm{d}}^{'}[\mathrm{Q}]}{\mathrm{m}_{1} - \mathrm{m}_{2}} \quad , \text{ and} \tag{51}$$

$$C_3 = \frac{(k_o + k_d'[Q] - m_2)(m_1 - k_o' - k_d'[Q])}{k_d'(m_1 - m_2)} \quad . \qquad (52)$$

$^*D$ will exhibit biexponential decay kinetics with $m_2 \rightarrow k_o$ as $[Q] \rightarrow 0$, and $m_2 \rightarrow k_{de}$ as $[Q] \rightarrow \infty$. $[^*\{DQ\}]$ will increase, reach a maximum, and then decrease. The point here is that wisdom would dictate a steady-state approach when possible, given the complexity of the time-dependence.

1.H.3. SOLVENT INTERACTIONS

Once a molecule becomes excited it may interact with other molecules nearby, leading to chemical interaction or some other non-radiative deactivation, or radiative decay. Clearly, the "closest" molecules nearby are the solvent molecules. Given their numbers, their concentration [Q] in (16) can be considered constant, and the dynamic set of solvent molecules surrounding the molecule is often referred to as the "solvent cage". In reality, rather than thinking of an excited molecule interacting with a specific solvent molecule, the solvent serves as a homogenous medium that may enhance or inhibit other relaxation pathways, so that the interactions and decay are "pseudo" first order. The solvent's orientation around chromopore molecules is

equilibrated in the ground state. Upon excitation of the chromophore the solvent must now reorient itself with respect to the redistribution of electronic charge in the chromophore—this process itself costs energy, which is often paid for by the excited molecules (see Marcus theory below). In this respect the solvent becomes an efficient energy sink. Conceptually, as the molecule achieves an excited state, the more extant electronic distribution "pushes" against the solvent cage. Thus, solvents of differing viscosities (viscosity here can be thought of as the resistance to being "pushed") will have differing effects on the non-radiative rate constant. Generally though, all solvents will increase k_{nr} with respect to k_r, so lifetimes in solvents at room temperature are much shorter than in a glass matrix at low temperature, or when the solid form of a chromophore is considered.

Especially in the instance of charge transfers where charge separation in the excited-state occurs, solvents of differing dielectric constants will be able to accommodate this charge separation to varying degrees. Here, the charge transfer is actually coupled to the solvent, and different solvents "tune" the energy gap between the ground state and excited state. For example, the charge-transfer based emission of $Ru(bpy)_2CN_2$ appears at 635 nm in H_2O, but at 680

nm in dimethylformamide.[33]

Another important solvent consideration is that k_q will be a function of ionic strength if D and Q are ions, since their rates of diffusion will vary, as already mentioned. Experimentally, it is critical to maintain the same ionic strength in order to obtain proper values for k_q.

1.H.4. ENERGY TRANSFER

If the quencher has low-lying unfilled orbitals, the excited species or "donor" may deactivate with concurrent activation of the "acceptor" species:

$$^{*}D + A \xrightarrow{k_{en}} D + {}^{*}A, \qquad (53)$$

where k_{en} is the rate constant for energy transfer, and A is the acceptor molecule. The successor complex, D-A* precedes separation. Two general mechanisms of energy transfer are possible: one which depends upon the molecules diffusing together to form an encounter complex first (exchange mechanism or Dexter excitation transfer); and, the other in which at-a-distance Coulombic interaction (dipole-dipole, or Förster energy transfer) stimulates the transfer.[14] For the former, efficient energy transfer will

depend upon a high quantum yield of emission of the donor, a large extinction coefficient of the acceptor, and significant overlap between the emission spectrum of the former and absorption of the latter. If the rate of energy transfer is fast compared to separation of the *DA complex, the rate will be diffusion limited. As stated, a useful predictor of the efficiency of energy transfer is when the absorption spectrum of the acceptor lies to the lower energy side of the donor emission and the two spectra have finite overlap. The acceptor, now in an excited state, must relax and may do so radiatively or non-radiatively. If radiatively, an indication of energy transfer is oftentimes disappearance of the emission from the donor in question, and appearance of an emission characteristic of the acceptor. If non-radiatively, increasing [A] will concurrently cause decreases in emission from *D, and analysis will yield a quenching rate constant near the diffusion limit.

1.H.5. ELECTRON TRANSFER

Another usually diffusion-limited relaxation process and perhaps the most well known is electron transfer. In reductive electron transfer (54) the excited complex donates an electron to the quencher; and, in oxidative

electron transfer (55) the excited chromophore accepts an electron from the quencher:

$$^{*}D + Q \xrightarrow{k_{ret}} D^{+} + Q^{-} \quad (54)$$

$$^{*}D + Q \xrightarrow{k_{oet}} D^{-} + Q^{+}. \quad (55)$$

Again, the successor complexes precede separation. The Nobel-prize winning work of Rudolph Marcus[34] explicated that the rate for electron transfer, k_{et}, depends not only on the degree of closeness of the donor and acceptor and the overlap of their orbitals, but particularly on the free energy change for the reaction (ΔG°) and how it compares to the reorganization energy. The free energy change is directly correlated with the combination of oxidation-reduction (redox) potentials of the species. The reorganization energy is the difference in energy between the minimum ground-state nuclear configuration of the products, and a higher energy state vertical to the minimum ground-state nuclear configuration of the reactants based on the Frank-Condon principle. More simply, since electron transfer happens so quickly, the molecules themselves (*a la* their nuclear configurations & vibrational modes) and the solvent cage must rearrange to accommodate the enormous change in electron distribution. The rate of electron

transfer will be highest when the reorganization energy and free energy change match (*i.e.* the activation energy is zero), but will decrease with increasing driving force greater than the reorganization energy ("Marcus inverted region").

Central to issues discussed here is the fact that electron transfer may occur adiabatically or diabatically[xiii] (without or with loss of heat energy), and with or without loss of excitation energy depending on how competitive the *back* electron transfer process is with other relaxation mechanisms. In diabatic electron transfer, the chromophore has lost its energy (officially a non-radiative relaxation process), and an overall chemical change will take place if the redox pair can separate (*e.g.* photosystems of chlorophyll), or the back reaction will produce the original species. If adiabatic, a fast back-reaction can reform the excited chromophore (such as the triplet state), which can now relax radiatively or non-radiatively. Alternately, without a back reaction, the chromophore relaxes non-radiatively, and the quencher itself can now relax either radiatively (energy transfer) or non-radiatively. After relaxation, the redox pair can separate

---

[xiii] The use of the term "nonadiabatic", with its double negative, is discouraged in favor of "diabatic".[35]

or reform the original species. These possibilities are summarized in Figure 6 for the case of reductive electron transfer. The adiabatic and diabatic cases are limiting: if in reality a forward and back photoinduced electron transfer uses up only a portion of the excitation energy, an excited chromophore of reduced energy may in fact go on to relax radiatively, and the resulting emission spectrum will show a bathochromic shift (red-shift). Whether this occurs or not will depend upon the overall exergonicity of the redox reaction firstly, and then subsequently on the reorganization energy, orbital overlap, and outer-sphere contact distance where transition metal coordination complexes are concerned. It is also important to note that in some instances, electron transfer is energetically best accomplished along with proton transfer, leading to overall hydrogen atom transfer.[36]

1.H.6. PHOTO-INDUCED CHEMICAL REACTION

Much of photochemistry revolves around how photoinduced excited-state manifolds can provide pathways to chemical change. The possibilities include rearrangement, decomposition, oxidation-reduction, substitution, and addition. The question of whether the

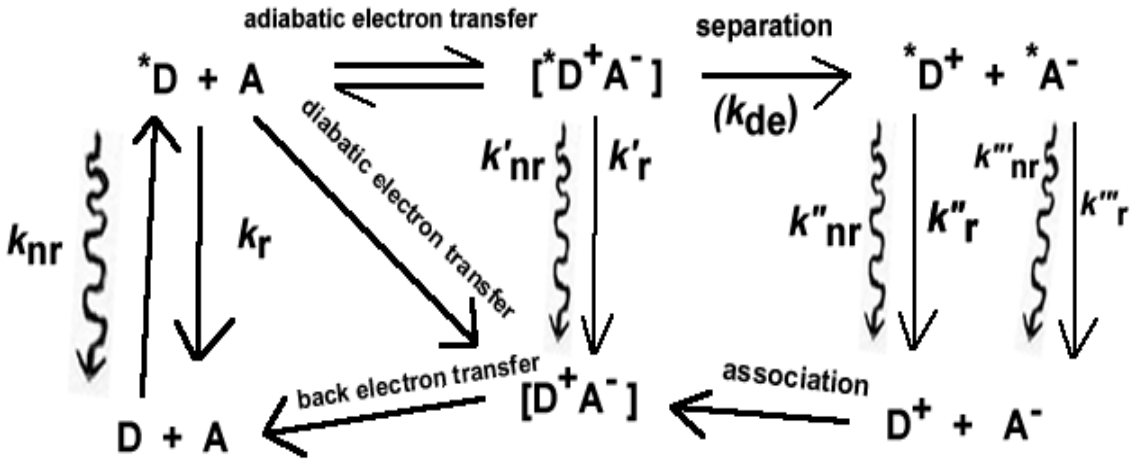

Figure 6. Reductive electron transfer mechanism and relaxation processes.

chemical change is transient or persistent[xiv] revolves around the likelihood of reverse reactions. In most instances there are two determinants of persistent chemical change: 1) if redox or decomposition products can separate; and, 2) if the excited-state interaction represents the rate-determining step and forms a high-energy intermediate that will subsequently undergo another fast mechanistic step to form low energy products, the reverse will be unfavorable, and there will be overall chemical change. A keen example is the case of electron transfer from ruthenium(II) diimines to cobalt(III) compounds elucidated by Gafney & Adamson[37]. The mechanism of electron transfer from excited-state ruthenium to cobalt could be postulated because the initial formation of a reduced Co(II) complex, now substitution-labile, continued on in a second step to form a different (low-energy) chemical species for which the reverse reaction is not favored. Photo-induced persistent chemical change is obviously easier to monitor because the products can usually be detected. Again, the key is separation–either physical or chemical.

[xiv] By "persistent", permanence is implied when the reverse reaction is extremely small.

1.H.7. TRANSIENT CHEMICAL REACTIONS

1.H.7.a. GENERAL CONSIDERATIONS

Transient chemical reactions are much more difficult to elucidate because there needs to be some fast "handle" on the new species. When this is available, evidence will usually point to a specific mechanism. Quenching of an emission is a handle most often used and an electron transfer mechanism will be postulated if the redox potentials are energetically favorable, or an energy transfer mechanism[xv] postulated if the quencher is known to have unfilled states lying to lower energy. Apart from electron transfer, transient chemical reactions involve fundamental change in the *atomic* structure of the chromophore. These reactions include excimer formation, proton transfer (*i.e.* protonation and deprotonation), and exciplex formation.

1.H.7.b. EXCIMER FORMATION

A chromophore in solution may in fact interact with another unexcited chromophore if the concentration is high enough. The excited-state dimer ("excimer") can now relax, radiatively or non-radiatively, then separate in the ground

---

[xv] Energy transfer is not considered a chemical change since the overall atomic or electronic structure is invariant.

state to re-form the monomers. The interaction of the excited molecule with the ground state molecule is stabilizing—the electron can now be further delocalized—and thus, radiative decay will occur from a lower energy. This red-shifted emission then becomes the "handle" of the excimer. Molecules with flat π systems, such as pyrene, often form excimers since the rings can physically 'stack' and thus interact.[14] Excimers are a special case of an excited state complex ("exciplex"), where the quencher is the same species. Thus, the quenching of the original monomer emission now has a bimolecular component and exhibits complex exponential decay kinetics.

1.H.7.c. PROTON TRANSFER

Excited states, by virtue of their localization of charge, are often stronger Brønsted acids or bases. Extensive studies have been performed on excited-state acid-base properties, particularly with organic compounds.[38,39] Protonation or deprotonation may lead directly to relaxation (diabatic proton transfer), or result in a species that then relaxes radiatively and/or non-radiatively (adiabatic proton transfer). If the base and acid forms of a molecule absorb at difference energies, their excited states will also have an energetic difference

and there will be a drive to shift the equilibrium towards the lower excited state. This equilibrium shift is the source of the increased acidity or basicity. Förster[40] devised a more formal explanation, appropriately called the "Förster cycle", which is shown in Figure 7. Consider the protonation of a base,

$$B + H^+ \underset{k_2}{\overset{k_1}{\leftrightharpoons}} BH^+ \tag{56}$$

where the protonated form absorbs at lower energy, both forms emit, and, k_1 and k_2 are the rate constants for protonation and deprotonation respectively. Assuming entropic contributions are minimal, the enthalpy changes and energy transitions can be set equal,

$$N_A(h\nu)_{BH^+} + \Delta H^* = N_A(h\nu)_B + \Delta H \tag{57}$$

and

$$N_A h(\nu_B - \nu_{BH^+}) = \Delta H^* - \Delta H \tag{58}$$

where N_A is Avogadro's number. If ΔS° upon excitation is negligible, and the solutions are dilute enough such that

$$\Delta H^* - \Delta H = \Delta H^{*\circ} - \Delta H^\circ, \tag{59}$$

then

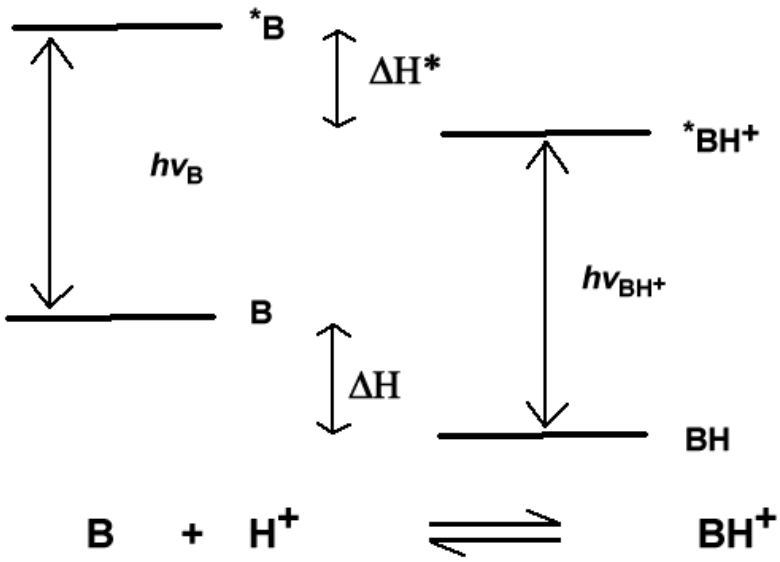

Figure 7. Depiction of the Förster cycle.

$$\Delta H^{*o} - \Delta H^{o} \sim \Delta G^{*o} - \Delta G^{o} = 2.303RT(pK^{*} - pK) \quad (60)$$

since

$$\Delta G^{o} = \Delta H^{o} - T\Delta S^{o} \quad (61)$$

and

$$\Delta G^{o} = (2.303RT)pK. \quad (62)$$

Combining (58), (59), and (60), the change in pK can be estimated from the energy difference in the transitions between the two forms:

$$\Delta pK = 0.00209(\nu_{B} - \nu_{BH}+)/cm^{-1} \quad (63)$$

where ν_{B} and $\nu_{BH}+$ are the 0-0 transitions for the base and acid forms respectively. In practice, emission maxima are easier to identify, so their difference is used to obtain the energy difference. If the ground state pK is known, fairly good estimates of excited state pK^{*} values can be obtained from Förster cycle calculations, or at least a sense of the magnitude and direction of the change.

One assumption built into the aforementioned discussion is that the excited state achieves 'equilibrium', despite its transient nature. This is possible if *both* the basic and acidic excited forms live long enough. More often, one form is short-lived, which poses a problem for Förster cycle determinations and for

emission titrations—the most common method used to obtain pK^* values. Similar to ground state pH titrations based on the Henderson-Hasselbach equation[41,42]

$$\mathrm{p}H = \mathrm{p}K_a + \log\frac{[\mathrm{Base}]}{[\mathrm{Acid}]} \tag{64}$$

where the inflection point is at pH=pK_a, an emission titration involves following the emission of either or both the basic and acidic excited state forms with varying pH. Now the inflection point is where pH=pK^*_a. In order for equilibrium to be reached (as in (2)), either

$$\frac{1}{\tau_{base}} << k_1[H^+] \tag{65}$$

or

$$\frac{1}{\tau_{acid}} << k_2 \tag{66}$$

must hold, meaning the rates of decay must be far less than the rates of protonation, $k_1[H^+]$, and/or deprotonation, k_2 (from equation 56). If one form is shorter-lived, the equilibrium will artificially shift towards replenishing it, by Le Chatelier's principle.[43] Given (65) and/or (66), based on (64),

$$\mathrm{p}H_{\text{inflection}} = \mathrm{p}K_{\mathrm{a}}^{*} + \log\frac{[\tau_{\text{base}}]}{[\tau_{\text{acid}}]}, \qquad (67)$$

and this lifetime correction will give a more realistic $\mathrm{p}K^{*}_{\mathrm{a}}$.[38]

Whereas in some instances, protonation or deprotonation occurs adiabatically without quenching, other times it may result in non-radiative deactivation. Usually, because a proton is a lightweight zero-electron species, the bond is a particularly facile oscillator: vibrating at high frequency, it serves as an efficient energy dissipator. Deprotonation then often facilitates emission (increasing k_{r}) while protonation quenches emission (increasing k_{nr}).

1.H.7.d. EXCIPLEX FORMATION

Given that exciplexes are a theme of this thesis, only some introductory comments will be made at this point. They have been well studied, particularly in organic systems, for some time.[44-46] As stated, an exciplex involves an excited species interacting with a ground state species of different atomic structure. The interaction usually is charge-transfer in nature and stabilizes the complex relative to its constituent parts.[47] The net stabilization

results because the excited electron in the LUMO of one constituent can move into a lower energy LUMO that results from the combinations of LUMOs from both species.[14] The successor complex, now a new electronic species is longer lived in the excited state than the corresponding ground state encounter complex: in other words, the excited state equilibrium constant for association is greater than the ground state counterpart. Traditionally, the constituents have no observable ground-state interactions, and the exciplex exhibits excited-state properties different than those of the constituent components.

Similar to the absorption complex and (15), the wavefunction of an exciplex between an excited *donor* species $^{*}D$ and a ground state *acceptor* species A, assuming no ground-state interaction, can be described as a composite of energy (first two terms) and electron transfer (second two terms) states,[48]

$$\Psi_{\text{exciplex}} = c_1\Psi(^{*}\text{DA}) + c_2\Psi(\text{DA}^{*}) + c_3\Psi(^{\cdot}\text{D}^{+\cdot}\text{A}^{-}) + c_4\Psi(^{\cdot}\text{D}^{-\cdot}\text{A}^{+}). \quad (68)$$

Given the donor/acceptor scheme, c_4 will be negligible and if c_2 is small, the charge transfer (D→A) will be significant enough to result in formalized electron transfer and subsequent separation of the redox products given a solvent of high enough polarity. An exciplex is a

successor complex as described by Figure 5, meaning, it can continue on to its own decay mechanisms. If formal electron-transfer, an emissive exciplex is normally precluded for reasons discussed below. On the other hand, if c_2 is large, subsequent formalized energy transfer can take place, again, precluding an emissive exciplex. However, if c_2 is simply larger than c_3, the overall delocalization can and often does lead to an emissive state. A weak ground-state interaction may "preview" exciplex formation. It is critical to grasp that an exciplex represents a minimum on the excited-state potential energy curve: a radiative, vertical Franck-Condon transition will be to a repulsive, dissociative configuration on the ground-state potential curve. However, if the ground-state configuration is in fact non-dissociative, it suggests the ground and excited state potential curves are similar in shape, and such overlap will encourage radiative transitions *(vide infra*).

Figure 8 shows the mechanistic steps for exciplex formation given weak ground-state association, and exciplex emission. The explicit mechanistic steps of encounter and successor complex formation are simplified into rate constants for exciplex formation and dissociation, k_{EX} and k_{-EX}. The decay kinetics are similar to (43) and (44) with A

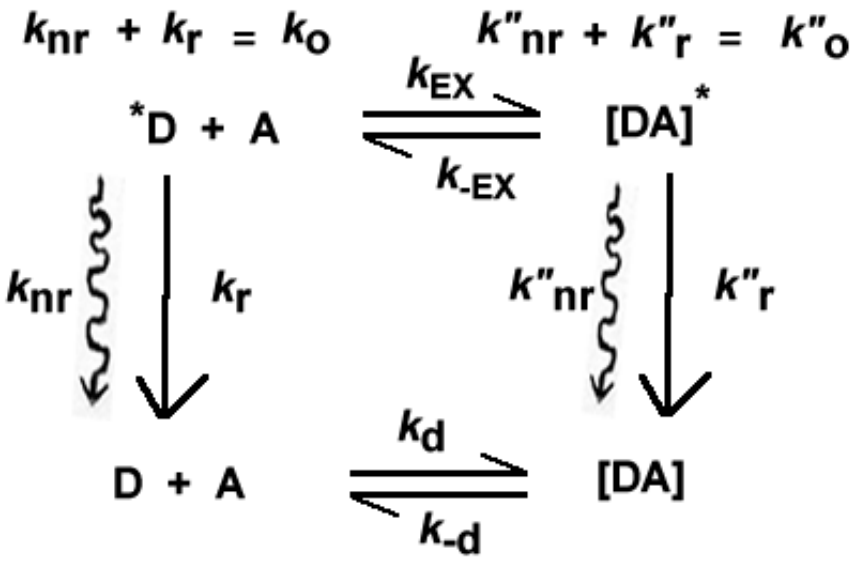

Figure 8. Relaxation processes of exciplexes when there is weak ground-state association.

replacing Q and k_{de}, the rate constant for deactivation, replaced by $k''_r + k''_{nr}$. The solutions, (45)-(52) are therefore the same with these substitutions, and the decay of both species will be biexponential. A closer look reveals that if equilibrium can be reached in the excited state, *i.e.* $k_{EX}[A] >> 1/\tau_{Donor}$ and $k_{-EX} >> 1/\tau_{EX}$, then the excited state equilibrium constant can be obtained from,

$$K^*_{EX} \approx k_{EX} \frac{[A]}{k_{-EX}} \tag{69}$$

and, the observed lifetime of the exciplex is calculated from,

$$\frac{1}{\tau^{EX}_{obs}} = \frac{\dfrac{1}{\tau_{Donor}(k_{-EX} + 1/\tau_{EX})} + k_{EX}[A]}{\dfrac{1}{\tau_{Donor}} + k_{EX}[A]} \tag{70}$$

.

Under steady-state conditions, the exciplex emission must be taken into account. It is helpful to define several quantities:

$$\beta' = A'_1 / \Phi' \tag{71}$$

$$\beta = A_1 / \Phi \tag{72}$$

$$\gamma = \beta' k''_r / \beta k_r, \tag{73}$$

where A'_1 and A_1 are the emission intensities of *(DA) and *D at analytical wavelength $\lambda=1$, Φ' and Φ their quantum yields, and, k''_r and k_r their radiative rate constants. Since $k_r = \Phi_{em}/\tau$ (26), it is clear that

$$\gamma = \frac{A_1' \tau_{\text{Donor}}}{A_1 \tau_{\text{EX}}} \quad . \tag{74}$$

Based on the mechanistic model (31), (37) is combined with (75),

$$[^*\{\text{DA}\}]_{\text{steady state}} = \frac{I_a \eta^* k_q [\text{A}]}{k_o''(k_o + k_q[\text{A}])} \tag{75}$$

to give

$$\frac{A_1^o}{A_1} = \frac{1 + \dfrac{k_q[\text{A}]}{k_o}}{1 + \gamma\left(\dfrac{k_q[\text{A}]}{k_o''}\right)} \quad , \tag{76}$$

which will exhibit negative deviations from linearity.[49,50] When there is no emission from *{DA}, meaning γ=0, (76) reduces to (39), the regular Stern-Volmer equation.

1.H.7.e. STATIC ASSOCATIONAL QUENCHING

When ground-state interactions are detectable, data

analysis can be quite daunting. Here, the ground state equilibrium constant must be considered and it defines the pre-excitation ratios. Two very different systems can result. If the equilibrium constant for association is large, meaning, an isolable product is formed, then the chromophore is irreversibly "pre-quenched", and the form of the Stern-Volmer equation is

$$\frac{A_{\mathrm{l}}^{\mathrm{o}}}{A_{\mathrm{l}}} = 1 + (K_{\mathrm{SV}} + K_{\mathrm{eq}})[\mathrm{Q}] + K_{\mathrm{SV}} K_{\mathrm{eq}} [\mathrm{Q}]^2 \quad , \tag{77}$$

which will exhibit positive deviations from linearity.[47] However, if the process is dynamic and reversible, in accordance with (31), (77) is modified to

$$\frac{A_{\mathrm{l}}^{\mathrm{o}}}{A_{\mathrm{l}}} = \frac{1 + (K_{\mathrm{SV}} + K_{\mathrm{eq}})[\mathrm{A}] + K_{\mathrm{SV}} K_{\mathrm{eq}} [\mathrm{A}]^2}{1 + (1+\gamma)\left(\frac{k_{\mathrm{d}}^{'}[A]}{k_{-\mathrm{d}}^{'} + k_{\mathrm{de}}}\right) + \left(\frac{\gamma\{(k_{\mathrm{o}} + k_{\mathrm{d}}^{'}[\mathrm{A}] K_{\mathrm{eq}}[\mathrm{A}]\}}{k_{-\mathrm{d}}^{'} + k_{\mathrm{de}}}\right)} \tag{78}$$

Equation (78) will instead display negative deviations from linearity and will reach a limiting value of $k_{\mathrm{de}}/k_{\mathrm{o}}\gamma$ at high concentrations of [A]. When the denominator of (78) is unity, it collapses to (77), which is true when [Q] replaces [A], and the rate constants for deactivation are large, meaning $(k'_{-\mathrm{d}} + k_{\mathrm{de}}) >> k'_{\mathrm{d}}[\mathrm{Q}]$ and $k_{\mathrm{de}} >> k_{\mathrm{o}}$. Despite the

mathematical complexity of (78), fitting routines and limiting values can be used to get a sense of the kinetic favorableness of exciplex formation, and the mechanism that best explains the data. With few assumptions, reasonable values for K_{SV}, and K^{*}_{eq} can be extracted.

1.I. TRANSITION METAL EXCIPLEXES

Negative deviations from linearity are common among the few examples of transition metal complex exciplexes (TMCEs). In an enlightening review of TMCEs reported up until 1995, Horváth and Stevenson[48] offer two broad categories: ligand-centered exciplexes and metal-centered exciplexes. The distinction is made between exciplexes that involve coordinatively-saturated, transition metal complexes where the interaction is focused at excited-state orbitals about the ligand, and exciplexes with unsaturated coordination sphere where the excited-state interaction is directly at the metal center. The focus will be on the former, since the discussion here is about coordinatively saturated ruthenium diimines, but one metal-centered exciplex should be highlighted. Nagle and Brennan report exciplex formation between the triplet state of a dimeric platinum complex, $Pt_2(\mu\text{-}\eta^2\text{-}H_2P_2O_5)_4^{4-}$ and Tl^{+}.[51,52] This is noteworthy as a rare example of an exciplex that increases

the metal content of a complex. The same complex was also later shown to form an exciplex with $Au(CN)_2^-$, again involving direct metal-metal interactions.[53] Other rare examples fall under the class of ligand-centered exciplexes, specifically, ligand-metal-cation exciplexes. An early example involving charge-transfer complexes was exciplex formation reported between Re(4,7-diphenyl-1,10-penanthroline)$(CO)_3Cl$ and *N,N*-dimethylaniline (DMA).[54]

More germane to this discussion are the reported exciplex formations between $^*[Ru(bpy)_3]^{2+}$ and Ag^+, and similarly between $^*[Ru(Me_2phen)_3]^{2+}$ and Ag^+. In the initial investigation, an electron transfer mechanism to form Ru (III) and Ag(0) was invoked.[55,56] However, later probative re-investigations by Ayala[57] and Tsubomura[58] rejected this postulate, as there was no evidence of either Ag^0 or transient Ru(III) production (in the transient absorption). Instead Ayala proposed a model with two exciplexes, $^*[Ru(bpy)_3]^{2+}$-Ag^+ and $^*[Ru(bpy)_3]^{2+}$-Ag_2^{2+}, the presence of both being confirmed by Tsubomura using circularly polarized luminescence spectroscopy. With increasing concentration of Ag^+ the emission red-shifted, and the Stern-Volmer analysis showed negative deviations. In a similar study, Lever claimed exciplex interactions with up to 6 Ag^+ cations by $^*Ru(bpz)_3^{2+}$.[59]

TMCEs have also been observed with metal porphyrins, such as palladium α,β,γ,δ-mesotetraphenylporphyrin with *N*-*N*-dimethylaniline,[60] and chloroindium(III) tetraphenyl-pophyrin with methylviologen.[61] In most cases, electron transfer is usually claimed as mediating exciplex formation. Also important, since exciplexes are assumed to have amorphous structures, the actual structural basis of exciplex formation is often only hinted at. In the case of $^{*}[Ru(bpy)_3]^{2+}$ with Ag^{+}, the exciplex is assumed to involve association on top of the aromatic π system, since such interactions are known.[6264] Similarly, a proposed exciplex between $^{*}[Ir(phen)_3]^{2+}$ and $HgCl_2$ is thought to be based on the well-known association of $HgCl_2$ with extended π systems.[65,66] Lever suggests that several Ag^{+} cations interact with the imine nitrogens of $^{*}[Ru(bpz)_3]^{2+}$, and likewise, Kinnaird proffers that Ag^{+} interacts with the cyano group in exciplex formation with $^{*}[Ru(bpy)_2(CN)_2]$.[55] Two immediate questions arise: Why does Ag^{+} tend to form exciplexes? And, when an outer bonding site, like an imine nitrogen, is available does the exciplex structure tend toward covalent bonding interactions, or diffuse association with π system? The combination of ideas of excited-state enhanced basicity and charge-transfer based

exciplex formation is unique to this investigation and discussion.

1.J. RUTHENIUM DIIMINES – GENERAL DISCUSSION

Initial reports[67-69] that ruthenium(II) *tris*-bipyridine[70] $[Ru(bpy)_3]^{2+}$ exhibits charge-transfer luminescence spurred interest in this compound. Amidst an energy crisis in the United States, when the photoredox properties of $[Ru(bpy)_3]^{2+}$ were first suggested by Gafney and Adamson[37] and confirmed by others as well as the elucidation of additional key photophysical properties,[71-81] subsequent intense research has led it to be one of the most studied inorganic transition metal complexes.[33,82-89] The holy grail of solar energy conversion–the light sensitized reduction of water to hydrogen and oxygen gas–is a four-electron process:

$$2H_2O(l) + h\nu \xrightarrow{4e^-} 2H_2(g) + O_2(g). \qquad (79)$$

Given that, researchers explored whether $[Ru(bpy)_3]^{2+}$ could be modified and oligomerized to form a compound with multiple metal centers capable of photosensitized multiple-electron transfer. While some succeeded at synthesizing

ruthenium diimine[xvi] dimers with bridging ligands[90-92] (BL) with the general form $[(bpy)_2Ru\text{-}BL\text{-}Ru(bpy)_2]^{4+}$, none exhibited "long-lived" luminescence[xvii] at room temperature—a desirable property often concomitant with electron transfer ability.

In 1984, Braunstein *et. al.*[93] utilized a previously synthesized ligand,[94] nicknamed dpp for "dipyridyl pyrazine",[xviii] as a bridging ligand (Figure 9) to mimic two attached coordinating bipyridines, capable of bonding to two metals. The resulting dimer $[(bpy)_2Ru(dpp)Ru(bpy)_2]^{4+}$ was the first luminescent polymetallic Ru(II) diimine, and along with the monomer $[(bpy)_2Ru(dpp)]^{2+}$ (both shown in Figure 9) exhibited long-lived luminescence and photoredox properties in room temperature solution similar to that of $[Ru(bpy)_3]^{2+}$. When the versatility of the dpp ligand was realized, its synthetic use was extended to polynuclear oligomers with ruthenium and other polypyridyl ligands,[95-99] supramolecular complexes with ruthenium,[100-103] and complexes with other metals such as osmium,[104,105] iron,[106] copper,[107,108] rhodium,[109] iridium,[110] and rhenium.[111,112] Indeed a host of

---

[xvi] An imine, a.k.a. "Schiff base" is a nitrogen base with sp^2 hybridization, such as in an aromatic ring (e.g. pyridine).

[xvii] "Long-lived luminescence" means in the nanosecond domain, usually >100ns.

[xviii] The proper IUPAC name is 2,3-di(pyridin-2-yl)pyrazine, and often 2,3-dpp is used in the literature to distinguish it from the 2,5-dpp analogue.

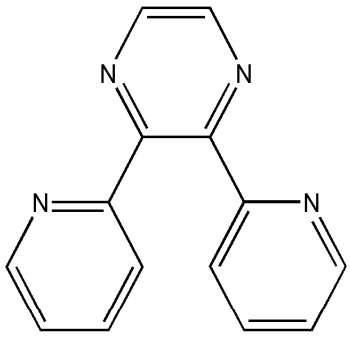

2,3-bis(2-pyridyl)pyrazine
(dpp)

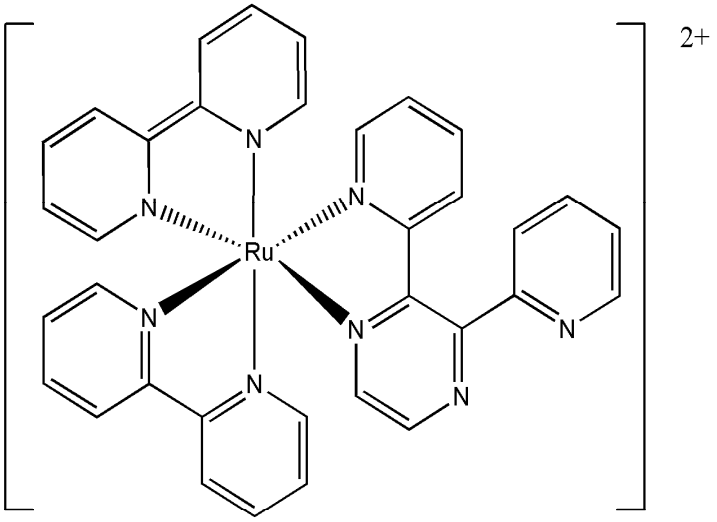

bis(2,2'-bipyridine)(2,3-bis(2-pyridyl)pyrazine)ruthenium(II)
$[\ Ru(bpy)_2(dpp)]^{2+}$

$[(Ru(bpy)_2)_2dpp]^{4+}$

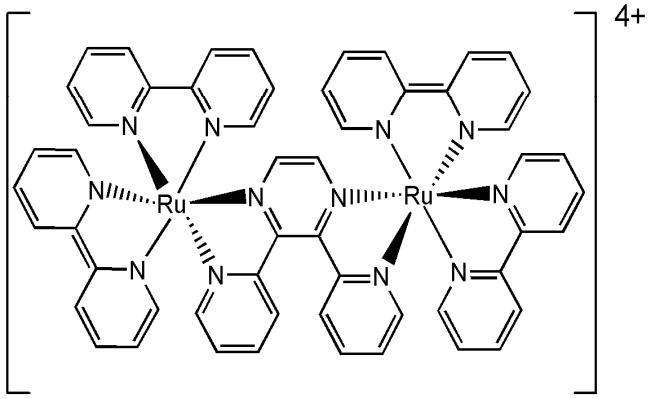

Figure 9. The dpp ligand and related compounds.

various luminescent and photoredox active analogues with differing transition metals, ligands, and numbers of metal centers has been explored.[113] The tris-dpp ruthenium compound,[114] $[Ru(dpp)_3]^{2+}$ has been used as the focal point of a number of interesting dendritic ruthenium-based species.[115-117]

1.K. $[(bpy)_2Ru(dpp)]^{2+}$

1.K.1. Excited-state Enhanced Basicity

We return to *bis*-bipyridyl(2,3-bis(2-pyridyl)pyrazine) ruthenium(II) as the main focus of this discussion. Initial interest in this compound stemmed not only from its remarkable luminescent and photoredox properties similar to $[Ru(bpy)_3]^{2+}$, but mostly from the fact that it exhibited enhanced basicity in the excited state.[118,119] In other words it was postulated, based on certain observations, that the pK_a of $^*[(bpy)_2Ru(dpp)]^{2+}$ (*i.e.* pK^*_a) is greater than the pK_a of $[(bpy)_2Ru(dpp)]^{2+}$. This enhancement[xix] is implied by the Förster cycle (63), and deduced from the excited-state titration's inflection point (section 1.H.7.c., *vide supra*). Since emission from the protonated form could not be observed, proper determination of the pK^*_a by equation

---

[xix] A higher pK_a means the complex is more readily protonated (at a higher pH)—or in other words, a stronger base.

(67) was not possible. The ground state (negatively valued) pK_a was obtained from a UV-VIS titration, but there were conflicting assignments of just which imine was being protonated, which is explored and explained here (*vide infra*).

It is important to note, at this juncture, that pK is a *thermodynamic* parameter, and therefore characteristic of a system at equilibrium. The assignment of a pK^* based on transient species thereby assumes that they attain equilibrium. When one or more excited species in question is so short-lived that the equilibrium assumption is invalid, analyses based on equations (63) and (67) must be questioned. Similar to the aforementioned discussion (section 1.H.1.), the ratios of the *kinetic* steps for protonation and deprotonation must be considered, as in equation (56). For the corresponding excited-state process,

$$ {}^*B + H^+ \underset{k^*_2}{\overset{k^*_1}{\leftrightarrows}} {}^*BH^+. \qquad (80) $$

Consequently, a more basic excited species would mean,

$$ \frac{k^*_1}{k^*_2} > \frac{k_1}{k_2} . \qquad (81) $$

If protonation is solely a diffusion process, then $k^*_1 \approx k_1$ since B and *B are electronic isomers. In this instance,

the issue of differing acidity/basicity between the ground and excited states rests on the relative values of the kinetic deprotonation rate constants k^*_2 and k_2. If the situation is excited-state enhanced basicity, then $k^*_2 < k_2$ and $^*BH^+$ "holds on" to the proton more effectively than BH^+.

Conversely, if both rate constants for deprotonation are fairly similar ($k^*_2 \approx k_2$) then the situation of excited-state enhanced basicity implies that $k^*_1 > k_1$, and therefore $^*B$ "grabs onto" the proton more effectively than B.[xx] Since the rate constants for protonation involve diffusion, this might mean that the perturbation from excitation is enough to produce a species, $^*B$, endowed with properties that increase its "apparent" diffusion ability. In other words, excitation may increase the effective reaction volume of a molecule, causing it to interact more or less with solvent molecules. Even if this were not the situation, the rate constant for protonation, in either the ground or excited state, is a composite of rate constants for diffusion to form an encounter complex, and the rate constant for the

---

[xx] In the terminology of organic chemistry, a similar distinction is often made between "nucleophilicity" and "basicity", the former being the *kinetic* likelihood of a Lewis base reacting with an electrophilic center (usually carbon), and the latter referring to an equilibrium (*thermodynamic*) position. Germane to this discussion, one may defensibly argue that in the situation of short-lived species, since kinetic steps are in question, it is the *nucleophilicity* of the Lewis base being examined, though the end result sought is an implied thermodynamic state.

conversion of the encounter complex into the protonated species. The conversion of the excited-state encounter complex to the protonated species simply, and more likely, may be favored over conversion of the ground-state encounter complex due to factors associated with the charge transfer species. More specifically, increased electron density in the outer and/or bonding region would favor ultimate protonation. This same argument could be used in the "hold on" alternative, where the excited protonated species is less likely to undergo deprotonation, thus reducing the excited state rate constant for deprotonation, k^*_2 relative to the ground state, k_2.

In frameworks where protonation is not primarily diffusion limited, but based on facile transfer from a hydrogen-bonded solvent in close proximity (or a hydrogen bonded proton on another portion of the molecule nearby), again, the "grab on" effect is possible: increased or more extant electron density in the outer and/or bonding region effectively "reaches out" and "grabs onto" the nearby hydrogen bonded proton, resulting in a larger value for k^*_1 relative to k_1. The actual mechanism may involve all or some combination of these possibilities, which would only be observed in increased/decreased rate constants in the excited state. The exercise of detailing these is important

as it lays the groundwork for the discussion on interactions with metal cations. Indeed, the "grab on" and "hold on" analogies help envision what might be otherwise known as the "chelate effect", where rate-limiting monodentate bonding facilitates fast, subsequent bidentate chelation.

1.K.2. Metal Chelation

Chelation by $[(bpy)_2Ru(dpp)]^{2+}$ to other metals was the original idea behind its synthesis: for this reason, the synthesis and investigation of the bimetallic, $[(bpy)_2Ru(dpp)Ru(bpy)_2]^{4+}$ appeared in the original publication.[93] The flexibility of the dpp ligand makes it a particularly versatile metal chelate. Because of the free pyridyl ring, the ligand can twist to accommodate chelation to a number of other metals.[93,98,103,120] It was the conjoining of these two ideas: the excited state enhanced basicity of $[(bpy)_2Ru(dpp)]^{2+}$ *and* its ability to chelate metals that instigated the fundamental question: Can excited-state enhanced basicity facilitate coordination to another metal? Phrased another way, can light be used to increase the metal content of a species? The answer to this question, a qualified "yes", was demonstrated in our lab by Charles Hicks, who showed that the reaction,

$$[(bpy)_2Ru(dpp)]^{2+} + PtCl_6^{2-} \rightarrow [(bpy)_2Ru(dpp)PtCl_4]^{2+} + 2Cl^- \quad (82)$$

is kinetically enhanced photochemically.[121-123] This unique example of a light-facilitated increase in metal content further prompted the question, What is the mechanistic basis of this enhancement? Metals cations with d^{10} configurations, specifically Ag^+, Cd^{2+}, and Zn^{2+} proved to be useful in modeling these interactions because of several propitious properties:

- ✓ All are very soluble in water
- ✓ All lack d states to which energy could be transferred
- ✓ All are diamagnetic, and thus usable in NMR spectroscopy
- ✓ Cd^{2+} and Zn^{2+}, and Ag^+ to some degree, have endergonically unfavorable electron reduction potentials, and thus are less likely to participate in excited-state electron transfer.

The experiment, results and discussion of the interaction of $[(bpy)_2Ru(dpp)]^{2+}$ with these cations as well as H^+ comprise the remainder of this dissertation.

_____

2. EXPERIMENTAL

2.A. SYNTHESIS

2.A.1. Synthesis of $[(bpy)_2Ru(dpp)](NO_3)_2$

The synthesis of $[(bpy)_2Ru(dpp)](NO_3)_2$ was based on a previously published synthesis of $[(bpy)_2Ru(dpp)](PF_6)_2$ with slight modifications.[93] The nitrate form was sought in order to: 1) maximize solubility in water; 2) preclude the precipitation of metal chlorides during titrations; 3) avoid possibly dangerous amine perchlorates[124] by not using the popular ClO_4^- form, and; 4) matching the counter-ion to that of the most readily available and soluble metal salts. The synthesis is shown schematically in Figure 10.

cis-Dichlorobis (2,2'-bipyridine) ruthenium(II) dihydrate, $Ru(bpy)_2(Cl)_2 \cdot 2H_2O$ ($Ru(C_{10}H_8N_2)_2Cl_2 \cdot 2H_2O$, 520.36 g/mol, Sigma-Aldrich, Lot 13227LF), 2,3-bis(2-pyridyl) pyrazine (dpp, $C_{14}H_{10}N_4$, 234.26 g/mol, Sigma-Aldrich, Lot 1181E6,), 200 proof ethanol (Aaper Alcohol, Lot 94B22QA), and ammonium hexaflurophosphate (NH_4PF_6, 163.0025 g/mol, Sigma Aldrich, Lot 62311HO,); reagent grade sodium nitrate ($NaNO_3$, Aldrich, Lot 06226HB), reagent grade silver nitrate ($AgNO_3$, Mallinckrodt, Lot EKZ), and reagent grade acetonitrile (CH_3CN) (J.T. Baker Chemical Company); neutral aluminua (Analtech, Lot 09814MD); and, Dowex 1-X8 (Fluka, Lot 427365/1) were all used as received.

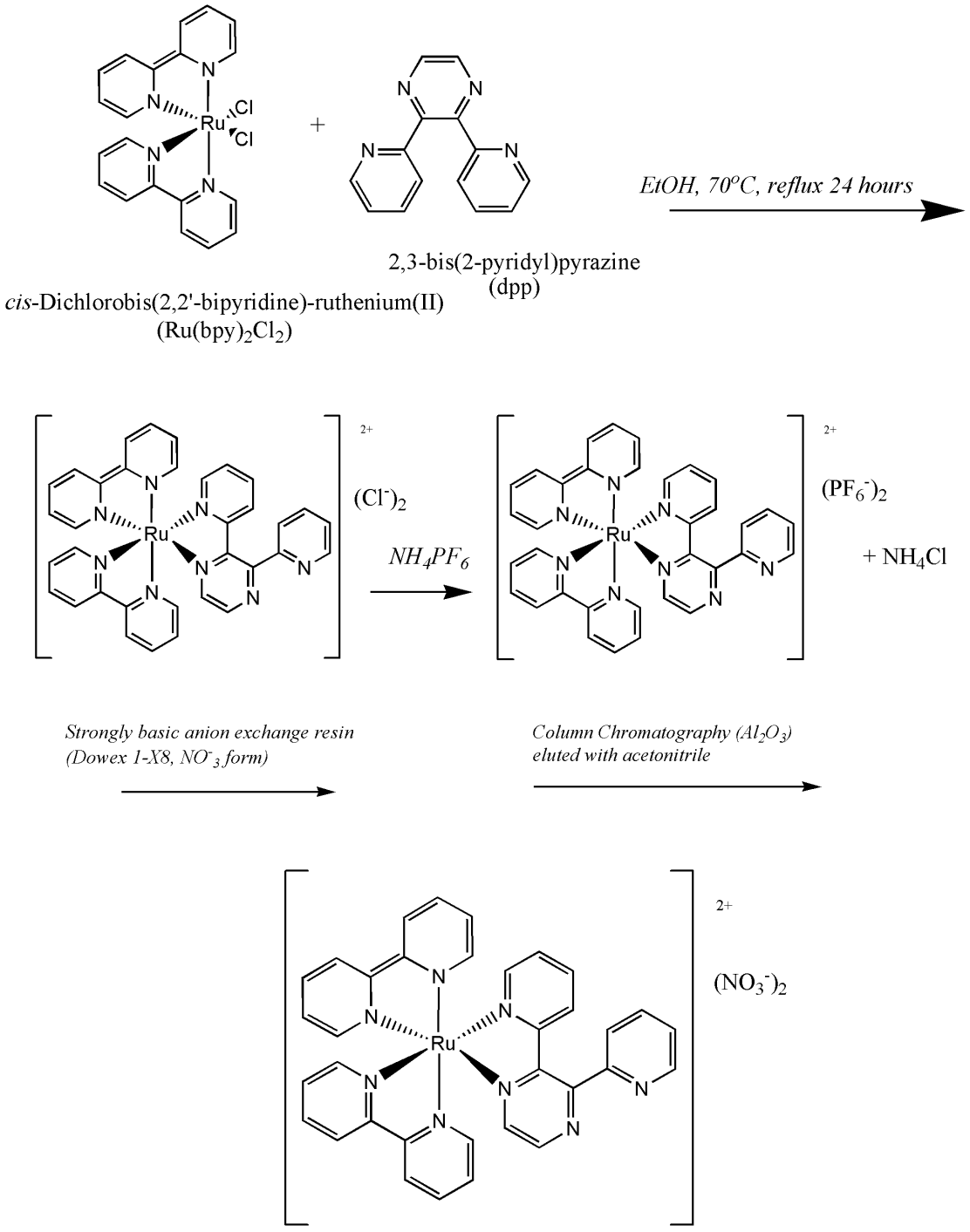

Figure 10. Synthetic scheme of $[(bpy)_2Ru(dpp)](NO_3)_2$.

An equimolar amount of $Ru(bpy)_2(Cl)_2 \cdot 2H_2O$ 520mg, 1.00mmol) and dpp (234mg, 1.00mmol) were refluxed in 100% ethanol at 70°C for 24 hours in a round bottom flask. Heat was removed from the dark red solution. Once it attained room temperature, about 1g of NH_4PF_6 (about 6mmol) was dissolved in a minimum volume of 100% ethanol, and was added dropwise to the solution. An orange precipitate, which immediately formed, was filtered off, and collected.

30ml of Dowex 1-X8, a strongly basic ion-exchange resin, was loaded into a 250mL column, washed with distilled water, then rinsed with 1L 6M sodium nitrate solution until no more Cl^- was detectable in the eluent by testing with a 0.1M solution of $AgNO_3$. The column was finally rinsed several times with distilled water. The precipitate was dissolved in a minimum volume of 25% acetonitrile/water (v/v), charged onto the column, and eluted with the same solvent. To the collected solution is added an equal volume of 95% ethanol (to assist in the evaporation of water), and the solution is evaporated to dryness using a rotovap.

The residue is dissolved in a minimum of acetonitrile, and added to a different column of neutral alumina. In this purification, the first fraction is faintly yellow and contains any remaining unreacted dpp ligand and excess

sodium nitrate. Unreacted starting material ($Ru(bpy)_2(Cl)_2$) remains at the top of the column. The second fraction, which is $[(bpy)_2Ru(dpp)](NO_3)_2$ is collected, and the eluent is removed by evaporation. A third purple-colored fraction is the bimetallic $[(bpy)_2Ru(dpp)Ru(bpy)_2](NO_3)_4$. Yields are in the range of 60%. The absorption spectrum and emission spectrum and lifetime in room temperature aqueous solution agreed with published results.[93]

2.A.2. Synthesis of $[(bpy)_2Ru(dpp)Ru(bpy)_2](NO_3)_4$.

The same synthesis was used for $[(bpy)_2Ru(dpp)Ru(bpy)_2](NO_3)_4$ with a few minor modifications: $Ru(bpy)_2(Cl)_2 \cdot 2H_2O$ was combined with dpp in a 2:1 molar ratio; and, the appropriate fraction was collected off of the alumina column. The absorption spectrum and emission spectrum and lifetime in room temperature aqueous solution agreed with published results.[93]

2.A.3. Synthesis of $[Os(bpy)_3](PF_6)_2$

$[Os(bpy)_3](PF_6)_2$ was prepared according to published methods.[125] The absorption spectrum and emission spectrum and lifetime in room temperature acetonitrile agreed with published results.[125]

2.B. INSTRUMENTAL

2.B.1. UV-VIS Spectroscopy

All ultraviolet-visible (UV-VIS) absorption spectra were obtained on either an AVIV Model 14DS Spectrophotometer, or a Hewlett-Packard Model 8452A Photodiode Array UV-VIS Spectrometer with a deuterium lamp source. Spectral data were exported as .txt files (wavelength, absorbance), and imported into spreadsheet software for further analysis and presentation.

2.B.2. Time-Resolved Emission Spectroscopy

2.B.2.a. Overview

A significant portion of the project involved the setup of an ICCD time-resolved emission spectrometer, which will hence be described in considerable detail. The ICCD camera/spectrograph/laser/timing-generator/source-lamp/computer system used is versatile in that steady-state emission, time-resolved emission, steady-state visible absorbance, and transient-absorbance data can all be obtained, with ease of conversion from one technique to another. A diagram of the setup is shown in Figure 11.

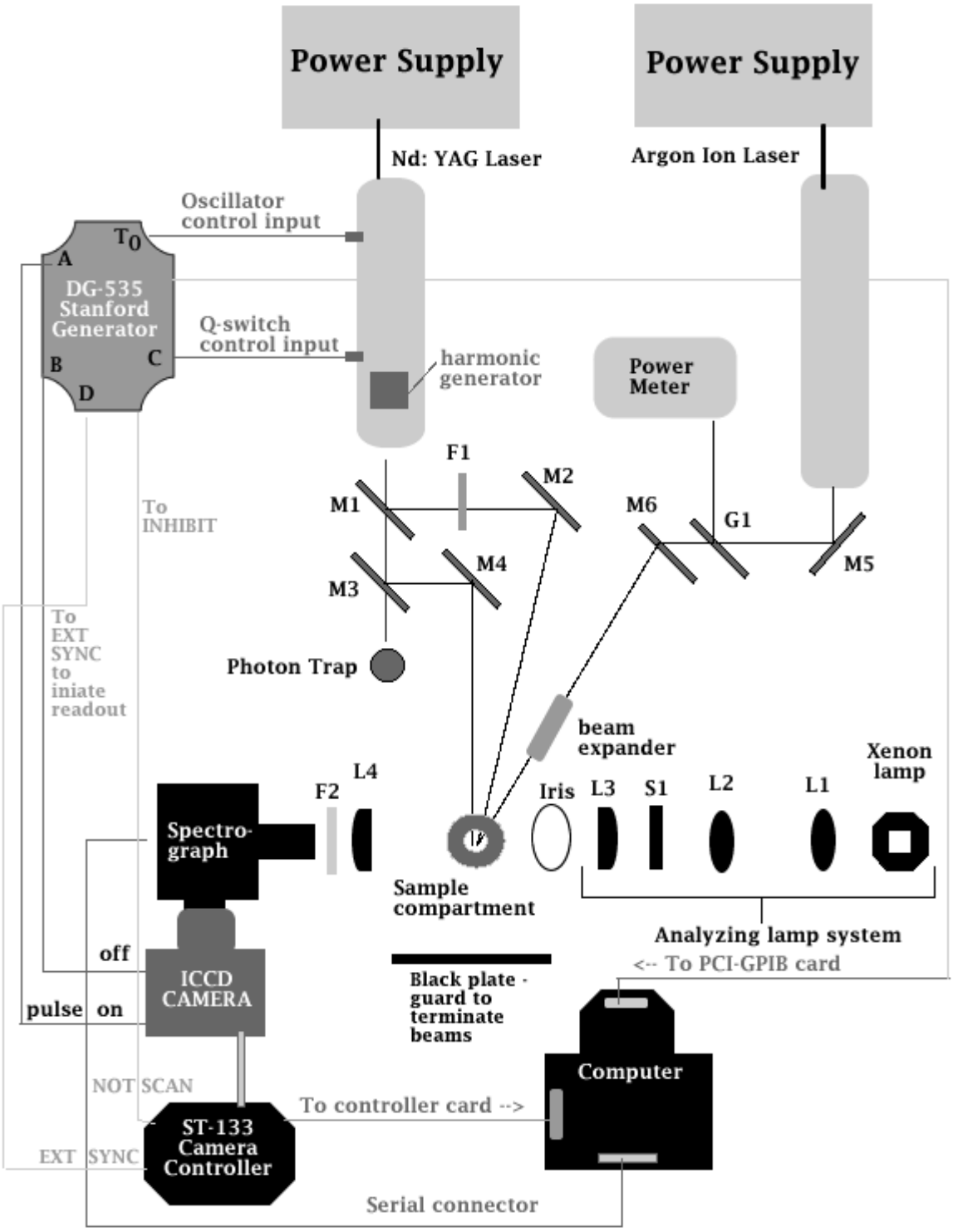

Figure 11. Laser/ICCD camera setup.

2.B.2.b. Laser Systems

Two lasers are used. The first, for time-resolved experiments, is a Quanta Ray DCR-2A Pulsed Nd:YAG (neodymium doped yttrium alumimum garnet) laser fitted with a HG-2 harmonic generator and an amplifier, giving optimum output at 10Hz. The output pulse has a diameter of 6.4mm, and the linewidth at the fundamental, 1064 nanometers (nm), is less than 1 cm^{-1}. The different laser outputs are listed in Table 1.

TABLE 1. Quanta Ray DCR-2A pulsed Nd:YAG laser outputs.

Wavelength (nm)	Pulse Width (ns)	Energy Stability	Pulse Energy (mJ/pulse), oscillator	Pulse Energy (mJ/pulse), amplifier
1064	8-9	+/- 1%	300	800
532	6-7	+/- 3%	150	360
355	5-6	+/- 3%	60	150
266	4-5	+/- 5%	20	60

The oscillator begins the firing sequence in the pulsed laser that is followed by the flashlamps, the Q-switch, and then the pulse. A harmonic generator mixes the 1064-nm fundamental to produce the 532-nm, 355-nm, and 265-nm harmonic wavelengths above it. The 532-nm line is primarily used and occasionally the 355-nm line. The laser can be externally controlled at each stage *via* inputs—at the oscillator, flashlamps, and Q-switched. Both the oscillator and Q-switches are triggered externally in this

system. A variable output timed from the Q-switch can be used to trigger a shutter in the lamp system (Figure 11). The amplifier is rarely employed. A system of dichroic high-energy laser mirrors (Model BSR-31-1537, Lot 64024 to reflect 355 nm, and Model BSR-51-1525, Lot 130938 to reflect 532 nm, CVI Laser Corporation) is employed. The first, M1, reflects primarily the higher energy 355nm light (when in use) to another similar mirror, M2, which points the pulse at the sample compartment. Immediately following the 355-nm mirror is a 532-nm mirror, M3, which similarly reflects the light to another mirror, M4, which points the pulse also at the sample compartment (Figure 11). When one exciting wavelength is in use, the other is blocked. After the 532nm mirror, a 90° elbow of ½" diameter copper tubing serves as a photon trap for the powerful 1064-nm pulse. Both excitation pulses (355 nm or 532 nm) proceed through the sample compartment at close to right angles to the entrance slit of the spectrograph, which is a SpectraPro Model SP-308 (Acton Research Corporation). Since the 532-nm pulse is predominantly used and can damage the camera, a 532-nm holographic notch filter (Model HNF 532.0-1.0, Kaiser Optical Systems, Inc.), F2, is placed before the entrance slit of the spectrograph to block scattering of the laser pulse light from entering. The notch filter has a

spectral bandwidth of 619cm^{-1} about 532.0nm with an optical density of 5.5. It also serves nicely to check the calibration of the spectrograph *(vide infra)*.

The second laser is a Coherent Innova 100-20 Argon Ion Laser. It provides several exciting lines, the one most commonly used being the 488.0nm blue line, which has a maximal output of 6.5W (See Table 2 below). A system of reflective mirrors, M5 & M6 in Figure 11, steers the laser beam to be steered through a beam-expander and onto the sample compartment when needed, which was usually the case for steady-state emission experiments. A glass slide (G1, Figure 11) steers a fraction of the light to a Coherent Model 210 power meter.

TABLE 2. Coherent Innova laser outputs.

Wavelength (nm)	Max Power (W)
457.9	1.4
488.0	6.5
496.5	2.8
501.7	1.7
514.5	8.5

2.B.2.c. ICCD Camera

Until recently, time-resolved measurements were obtained with flash systems that employed time-responsive photomultipliers coupled to oscilloscopes.[49] Since

monochromators were used, only one wavelength could be observed at a time. Arrays used in spectroscopy allowed the simultaneous observation of a range of wavelengths since the light was spatially dispersed, and incident onto an array of detectors which provide the image. A charge coupled device (CCD) is an array of detectors integrated into a single chip. In the CCD, the detectors are a two-dimensional array of pixels, where each pixel can build up a certain amount of charge proportional to the incident light intensity, can be read out and individually digitized. However, since the pixels are static in terms of charge build-up, a different method must be employed for time-resolution. A very fast shutter allows pictures to be taken of an event in time—the pieces are then put together in chronological order to recreate the event: the faster the shutter, the more detailed the picture, *i.e.* better the time resolution.

With an *intensified* CCD, called an ICCD, the intensifier functions not only as an amplifier significantly boosting the signal, but also as a fast shutter to time-resolve the experiments. The intensifier consists of a very sensitive photocathode. When light impinges on it, electrons are ejected (photoelectric effect) and accelerated by an applied voltage between the

photocathode and a microchannel plate. A single electron passing through a microchannel is further accelerated by the applied voltage gradient. As in the dynode chain of a photomultiplier tube, the accelerated electrons strike the walls of the microchannels, ejecting more electrons, which amplify the signal. The ejected electrons then impinge on a phosphor screen which emits light. The emitted light is collected with a fiber optic bundle that is coupled to the CCD. The CCD is mounted on a cold finger and is cooled (Peltier effect) to reduce thermal noise. Since high voltage can be applied and removed quickly, the photocathode of the intensifier can be gated on and off quickly, serving as a fast electronic shutter.

The system used in these experiments (Figure 11) employs a Princeton Instruments PI Max ICCD Camera (Roper Scientific) with a Generation II Intensifier (red enhanced). The CCD array is 1024 pixels wide by 256 pixels high, each pixel being 26 µm x 26 µm, with a well capacity of 500 keV. The 18mm wide intensifier, using 1:1 fiber optic coupling, is bonded to the front of the CCD array which is just over 26mm. 4mm on either side of the intensifier is not illuminated. A gain of 6-8 electrons per photon count is possible, the sensitivity ranging from 1-70 counts depending on the adjustment of the signal gain. The

phosphor screen (P43) has a decay time of 2ms. The intensifier gating on/off ratio is $5x10^6$:1, and can be gated to a window (resolution) of 1.7ns. Jitter is less than 100 ps when the ICCD is cooled to -11°C, which is its normal operating temperature.

The camera controller, a Princeton Instruments Model ST-133 (Roper Scientific), houses the analog-to-digital (A/D) converter, reads the temperature of the CCD array, powers the camera, and is the interface by which the computer controls the camera. The A/D converter can handle 1 megapixel per second at 16 bits. The controller reads out 1 pixel per microsecond (1.024ms to read the entire row of 1024 pixels), and it takes 15 microseconds to move to the next row on the CCD. The camera is connected *via* a serial cable to a high-speed PCI card installed on the computer for data processing and display. Data can be displayed nearly in "real time" with the fast readout, digitizing, and output ability of the controller, coupled with the high-speed serial interface and fast processor of the computer.

2.B.2.d. Computer and Software

A PC with 1000Mhz AMD Athlon Processor, 256MB Ram, 6GB Hard drive, and installed GPIB/PCI Card and High-Speed

Serial PCI Card running Windows XP (SP2) is used to control instrumentation, set experiment parameters, run experiments, process data, and display data. WinSpec32 software package provided by Princeton Instruments (Roper Scientific) serves as the interface, controlling the spectrograph, timing generator, and camera controller. WinSpec32 allows for display of time-resolved data, both emission intensity and transmittance, contains functionalities to convert to absorbance, and can export data files in ASCII format to be imported into spreadsheet software.

2.B.2.e. Spectrograph

Incoming light is dispersed by a SpectraPro 300i series (SP-308) spectrograph (Acton Research Corporation). It has a 0.300 meter focal length, f/4 aperture ratio, and focal plane 27mm wide by 14mm high which extends 1.0” outside at the CCD port for ease of mounting an ICCD camera. Manually adjustable micrometers at the entrance slit and two exit slits (chosen by a motorized mirror) can range from 10μm to 3mm. Light passing through the entrance slit is directed by the entrance mirror onto a back mirror and then onto a triple grating turret, which is driven electronically. Three gratings are mounted on the turret:

the first with 600 grooves/mm is blazed for optimum reflectivity at 500 nm (600/500 shorthand), the second with 150 grooves/mm is blazed for 500 nm (150/500 shorthand), and the third with 150 grooves/mm is blazed for optimum reflectivity at 800nm (150/800 shorthand). The two gratings with 150 grooves/mm allow display of the full spectrum of a typical luminescent compound throughout the visible spectrum. The grating with higher resolution allows focusing in on features of a particular emission. Dispersed light from the grating is then reflected off another back mirror onto the motorized exit mirror which reflects the dispersed light across the ICCD.

The spectrograph comes with its own software and can be used as a monochromator. The spectrograph is connected *via* cable from the RS232 interface to the COM2 port on the computer. The WinSpec32 software is able to control the SP-308, and is used for calibration of the spectrograph. Calibration is accomplished with the line spectrum of an AnaLamp mercury pen lamp, (BHK Corporation, Model # 81-1057-01), with its own power source, (BHK Corporation, Model # 90-0001-01). The lamp also contains argon, and the Ar lines were also used for calibration. Calibration involves assigning wavelength values to each pixel in the

array. To relate pixel number to wavelength, the procedure produces a polynomial equation of the form,

$$\lambda_{nm} = Ax^2 + Bx + C \qquad (83)$$

where "x" is the pixel number, and A, B, and C are rational coefficients.

Confirmation of the grating and calibration is carried out using a combination of a Hamamatsu Xenon Lamp (75 Watt C2177-01) focused onto the entrance slit of the Acton spectrometer (*vide infra*), which is covered by a 532.0nm holographic notch filter. The emission spectrum of a xenon arc lamp is well known for its fairly continuous and even output throughout the visible range.[126] A normalized emission spectra throughout the UV-VIS range is shown in Figure 12. If the lamp output goes through the 532.0nm notch filter, there should be a dip in the spectrum precisely about 532.0nm. The correct grating needs to be confirmed because of occasional faulty communication between the spectrograph and the computer as to which grating is lined up. The 600/500 grating is easy to identify because the spectral distribution (wavelength range) is smaller, thus the dip in the notch filter will be quite wide (Figure 13(top)). Having similar spectral distributions, the 150/500 and 150/800 gratings are

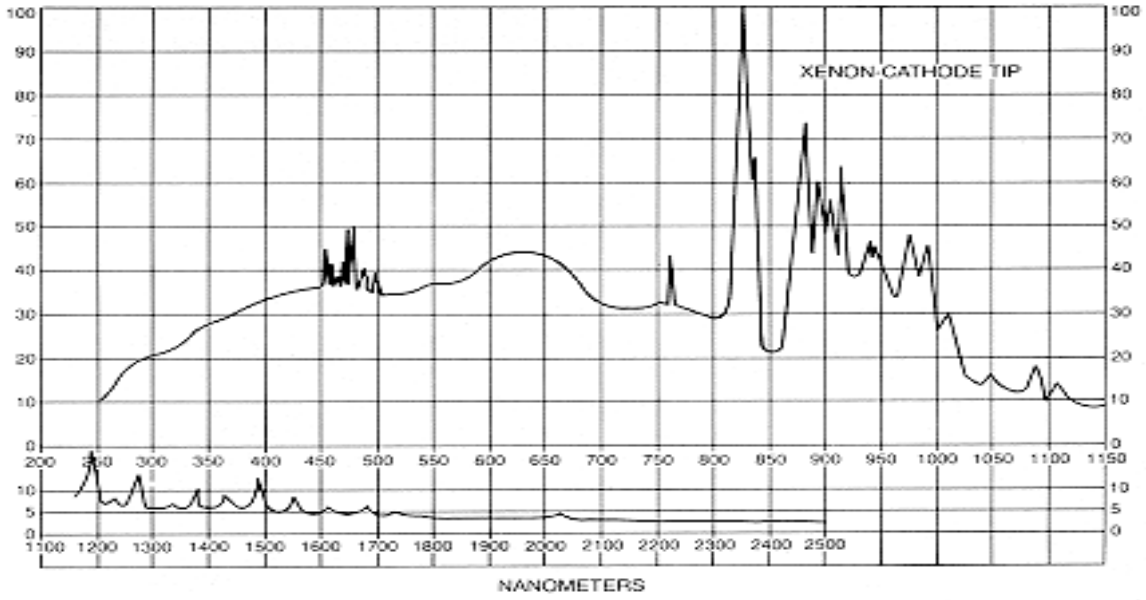

Figure 12. Xenon lamp output.

distinguished by the wavelength dependence of their reflectivity. With the 150/500 grating, the xenon spectrum will be skewed, in terms of intensity, slightly towards 500nm where the output will be greatest, and die off towards the red. Vice versa, the 150/800nm will be skewed towards 800nm, and die off towards the blue. The lack of intensity at 532nm due to the notch filter is an identifying feature in both (Figure 13(bottom)).

2.B.2.f. Lamp & Optics

For steady-state and future transient absorbance measurements, a 75W Xenon lamp (Hamamatsu C2177-01) is directly aligned with the entrance slit of the spectrograph (see bottom of Figure 11). A planoconvex lens (L1, Figure 11) collects and collimates light from the source. A biconvex lens (L2, Figure 11) focuses the collimated light to a point at a Uniblitz Model SD-10 Shutter Drive/Timer (Vincent Associates). The shutter (S1 in Figure 11) can be manually actuated (S1 in Figure 11), or triggered to open with a voltage pulse from the variable Q-switch sync output on the pulse laser. The shutter stays closed to prevent damage to the intensifier and photolysis of the sample, until the light source is needed in the experiment. When opened, the focal point at the shutter expands towards

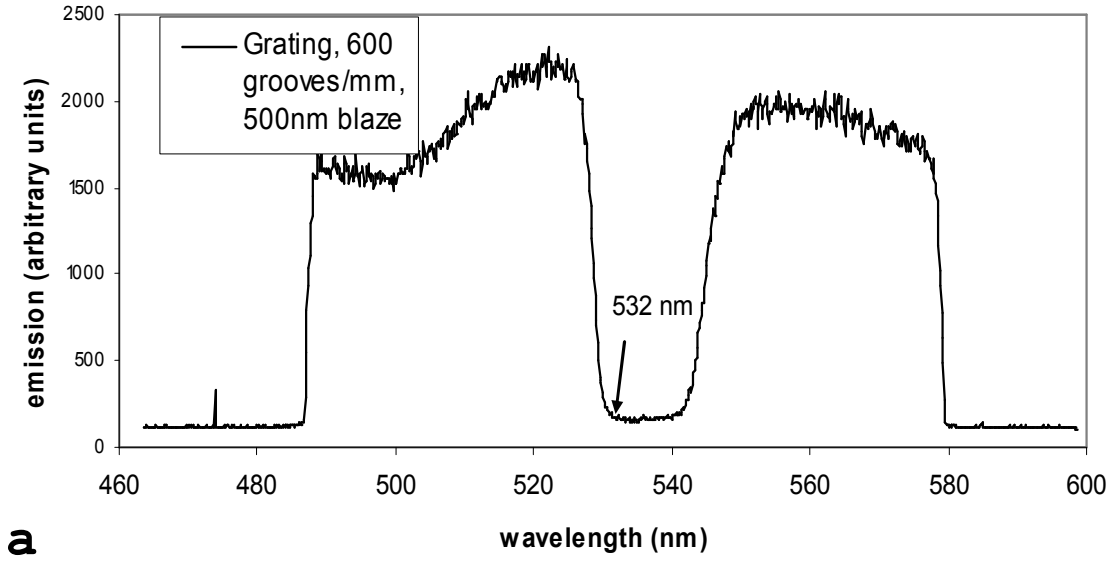

a

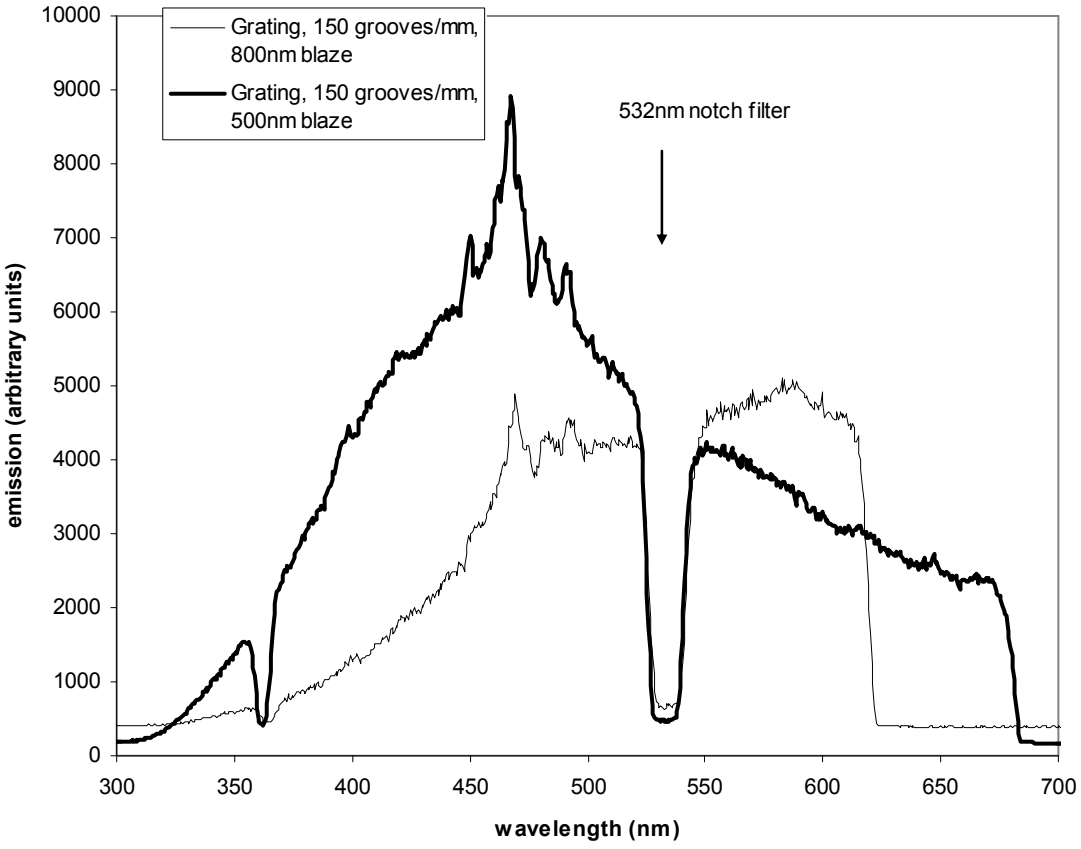

b

Figure 13. Acton spectrograph gratings. (a, top) 600 grooves/mm grating. (b, bottom) 150 grooves/nm gratings with blazes at 500 nm and 800 nm.

another, smaller planoconvex lens (L3, Figure 11) which collimates the light into a beam 8 mm in diameter. This beam then passes through an iris (I1, Figure 11) into the sample compartment. The light passing thorugh the sample then passes through a planoconvex collecting lens (L4, Figure 11) which focuses the light through the last notch filter (F2, Figure 11) onto the entrance slit. In transient absorption experiments, the pulse laser pumps, and the xenon lamp probes the sample.

2.B.2.g. Timing Generator

The sequence of events and their timing is initiated by the computer software and controlled by a Model-DG535 Digital Delay/Pulse Generator (Stanford Research Systems, Inc.) which has a 5 picosecond (ps) resolution. Four delay outputs (2-3 nanosecond rise time) are available, A,B,C,D, or various combinations (AB, -AB, CD, -CD) in addition to time zero T_0, and all can terminate at 50 Ω or high impedance, and deliver a variety of output levels including transistor-transistor logic (TTL, 0 to 4 Vdc, normal or inverted), emitter-coupled logic (ECL, -1.8 to -0.8 Vdc, normal or inverted), nuclear instrumentation module (NIM, -0.8 to 0 Vdc, normal or inverted), and variable (ranging from -3Vdc to +4Vdc). This setup employs

TTL at 4V, normal, terminating in high impedance load. The generator uses a 25ppm crystal oscillator timebase, and RMS jitter from T_0 to any output is 50ps + delay x 10^{-8}. The DG535 can be externally triggered, the insertion delay to T_0 being 85ns, but is not used here.[xxi] It is connected *via* cable from the IEEE488 GPIB (General Purpose Interface Bus) interface to a specially installed GPIB/PCI card from National Instruments. This allows the computer to control the generator and initiate the timing, quickly advancing the time delay as set forth by the WinSpec 32 experiment acquisition parameters.

2.B.2.h. Timing Sequence

A diagram for the timing sequence is provided in Figure 14. When the computer initiates the DG535 (Point 1, Figure 14), the T_0 output pulses the oscillator input on the laser (Point 2, Figure 14). Approximately 210 microseconds after the oscillator fires, the flash lamps of the laser fire (Point 3, Figure 14). The laser Q-switch is

---

[xxi] Early on there was considerable trouble finding a suitable timing sequence. Much effort went into triggering off of one of the laser outputs, the Q-switch output in particular. Because of the insertion delay in the timing generator, it was not possible to "catch" the pulse in time. Because of the age of the laser, the jitter in the other earlier timing outputs made them unreliable. Fortunately, a solution was found using the timing generator to run the laser, and adding resistance to the timing circuit of the Q-switch external output, all of which is described in the next section.

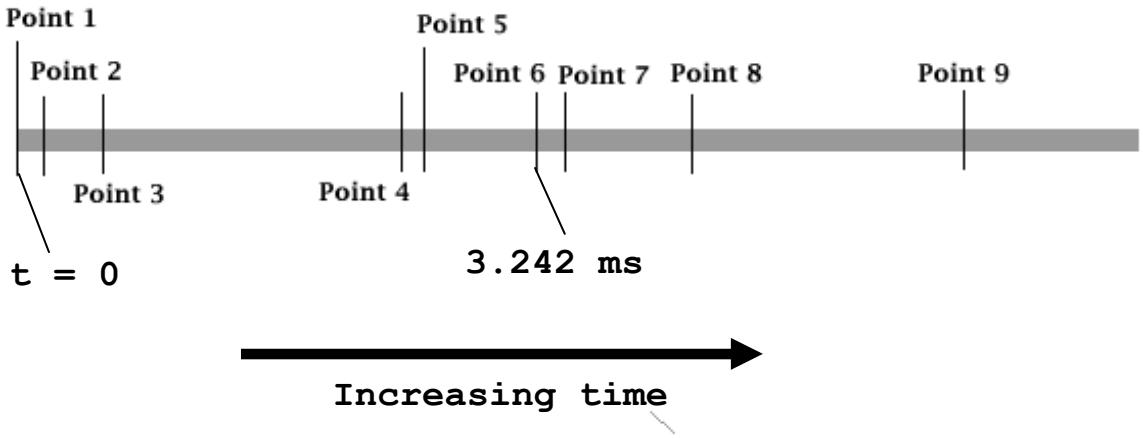

Figure 14. Laser/ICCD Camera timing sequence.

externally controlled by the DG535 through output C (Point 4, Figure 14) which is at a fixed time delay of 3.242 milliseconds from T_0 to achieve the maximum intensity of the laser pulse. Since the laser pulse itself appears approximately 50ns after the Q-switch voltage drops to nominal voltage (Point 5, Figure 14), this affords a clear and convenient starting point for data acquisition, and thus the camera is able to capture data starting just before the pulse is delivered to the sample. Therefore, output A of the DG535 which turns on the camera intensifier (Point 6, Figure 14), is set to start at 3.242ms after T_0, and is advanced forward according to experimental conditions which were usually every 2 ns.

Output B of the DG5335, which turns off the camera intensifier (point 7, Figure 14) occurs at a fixed time delay after Output A. The time between Outputs A and B defines the width of the exposure window, and in turn the time resolution of the camera. As stated above, the intensifier can be gated on and off down to a 1.7-ns window, but a 2-ns window is routinely used as the software is most easily set up for it. Output D is timed to output B (also Point 7, Figure 14) and being connected to the "external sync" input of the camera controller, initiates a readout cycle of the data. Once the controller begins to

readout data (charge) from the CCD array, it sends a signal through the NOT SCAN output to the INHIBIT input on the timing generator (Point 8, Figure 14) which prevents another timing sequence from occurring until readout is complete. The controller A/D converter digitizes the data and sends it to the computer for processing and display (Point 9, Figure 14).

2.B.3. Steady-state Emission Spectroscopy

All steady-state emission spectra were obtained either on a Spectraphysics Model 1692T (Fluorolog-2 emission spectrometer, Jobin Yvex) with two Model 1681 0.22m monochromators, a 450W Xenon lamp (Model 1909 housing), and red-sensitive Hamamatsu photomultiplier detector (R928); or, as previously mentioned, steady-state emission spectra were recorded with the ICCD camera using the argon ion laser as the excitation source.

2.B.4. NMR Spectroscopy

All ^{1}H NMR spectra were obtained on a Bruker Avance DPX400 FT-NMR. Acquisition parameters include: proton frequency at 400.13 MHz, 23 °C, 16 scans, 2 s relaxation delay, 30 µs pulse width, 65k data points, and 20.7 ppm spectral width, and referencing to DSS (0 ppm). Processing

includes deconvolution with a Lorentzian function, and 0.3 Hz line broadening. Two-dimensional ^{1}H-^{1}H COSY spectra were obtained with the following acquisition parameters: proton frequency at 400.13 MHz, 23 °C, 8 scans, 4 s relaxation delay, 12 μs pulse width, and 8.0 ppm spectral width. Data was processed after applying a sinusoidal function.

2.B.5. Examination of Laser Pulses

The ICCD/camera system was first used to examine the pulses of the Nd:YAG laser. To avoid damaging the ICCD camera, a glass slide was used to steer a portion of the pulse towards the spectrograph entrance slit, which was set to 1 um, the smallest possible, identifiable width. The 150/500 grating was used, and the step width of the timing generator was set to 1 ns. Although this in theory does not yield better resolution, since the pulse gate width of the camera is no less than 2 ns, it does provide more data points for a better analysis. The mathematical program IGOR was used to fit the data.

2.C. Characterization of $[(bpy)_2Ru(dpp)](NO_3)_2$

2.C.1. Electronic Spectroscopy

$[(bpy)_2Ru(dpp)](NO_3)_2 \cdot 2H_2O$ was diluted to a concentration of 10^{-4} M in distilled water and analyzed by

UV-VIS, steady-state emission, and time-resolved emission spectroscopy, using quartz cells, distilled water as a blank, and all solutions at room temperature (22°C). Given the known penchant of O_2 to quench $[(bpy)_2Ru(dpp)]^{2+}$,[71] all solutions were deaerated by bubbling with Argon gas for 5 minutes. In all cases, the 150/800 spectrograph grating was employed. For steady-state spectra, the camera background with a closed shutter was obtained and subtracted. This is not normally done with the time-resolved spectrum to allow for the fastest possible processing of data by the ADC. Settings for the Laser/ICCD camera, typical of all emission spectra obtained, are tabulated below (Table 3). For comparison, emission spectra were obtained in ethanol and methanol.

Table 3. Instrument parameters for emission detection.

Instrument parameters	Time-resolved	Steady-state
Slit Width	3 mm	10 µm
Exposure time	N/A	1.00 s
Gate width	2 ns	N/A
Step width	2 ns	N/A
# Spectrum	500	1
Laser Power	Nd:YAG, 70 J	Argon, 4.0W

2.C.2. NMR Spectroscopy

99.9% dueterium oxide (Cambridge Isotope Laboratories, Inc., Lot 2B-198) and 99.9% dueterium oxide with 0.1% v/v DSS (Sigma-Aldrich, Lot 67231KU) were used as received. Several milliliters of D_2O were added to $[(bpy)_2Ru(dpp)](NO_3)_2 \cdot 2H_2O$, and the solution evaporated to dryness in a rotovap. This process was repeated twice in order to replace the waters of crystallization with D_2O. The resulting deuterate, $[(bpy)_2Ru(dpp)](NO_3)_2 \cdot 2D_2O$, was subsequently dissolved in D_2O (with DSS) to a concentration of 10^{-2} M. ^1H NMR confirmed removal of the H_2O, and these solutions were used for the ^1H NMR and 2D ^1H-^1H COSY experiments.

2.D. Acid Titration of $[(bpy)_2Ru(dpp)]^{2+}$

Buffer solutions (Fisher Scientific Chemical Company) at pH 1 (KCl/HCl, Lot 024013), pH 2 (KCl/HCl, Lot 953249-24), pH 3 ($C_8H_5O_4K$/HCl, Lot 936309-24), pH 4 ($C_8H_5O_4K$/HCl, Lot 994080-24), pH 5 ($C_8H_5O_4K$/NaOH, Lot 955144-24), pH 6 (KH_2PO_4/NaOH, Lot 022539-24), pH 7 (KH_2PO_4/NaOH, Lot 050768-24), pH 8 (KH_2PO_4/NaOH, Lot 962227-18), pH 9 (H_3BO_3/KCl/ NaOH, Lot 883771-24), and pH 10 (K_2CO_3/K_3BO_3/KOH, Lot 994163-24); 99.9% D_2O with 0.1% v/v sodium 2,2-dimethyl-2-silapentane-5-sulfonate (DSS) (Sigma-Aldrich, Lot 67231KU);

nitric acid; sulfuric acid; and, deutero-sulfuric acid (D_2SO_4 99.9%, Sigma-Aldrich) were used as obtained. Distilled water was used in all experiments not involving NMR.

A stock solution of $[(bpy)_2Ru(dpp)]^{2+}$ in water was diluted to a concentration of 10^{-5} M, in pH buffer solutions ranging from 8 to 1, and in 1M nitric acid to obtain pH=0.[xxii] Argon gas was bubbled through all solutions for 5 minutes. The ICCD camera was used to obtain the steady-state (488.0 nm excitation) and time-resolved (532 nm excitation) emission spectra. In the case of steady state emissions, any emission from blank buffer solutions was obtained and subtracted. The area under the steady-state spectra was calculated by summing the intensities at all wavelengths. The integration under the three-dimensional time-resolved decays, at all wavelengths and all time intervals utilized Microsoft's Excel program. To simplify the mathematical analysis, decay lifetimes were calculated from a time point following the apparent rise-time due to the build-up of the pulse (See Section 4.A. below for discussion of the rise-time). A special program was written, compiled, and executed in IGOR (Appendix 1) to

[xxii] pH values should not be reported below 1. pH 0 is implied by 1M monoprotic acid. In cases of higher concentrations of acid, the Hammet acidity function, H_o, will be used.

fit exponential decays to each wavelength and plot lifetimes *vs.* wavelength.

$[(bpy)_2Ru(dpp)]^{2+}$ was dissolved separately in D_2O (with DSS) and D_2SO_4 (99.9%), both to concentrations of 0.05M. The D_2SO_4 solution of the complex was added dropwise to the D_2O solution of the complex in the NMR tube, thus keeping the concentration of $[(bpy)_2Ru(dpp)]^{2+}$ constant. Regular ^1H NMR spectra were obtained at various acid concentrations.[xxiii]

To further examine the protonation of $[(bpy)_2Ru(dpp)]^{2+}$, sulfuric acid was used to afford solutions at extremely high $[H^+]$ levels. In these cases, the concentrations of H^+ are reported using the Hammett acidity scale for sulfuric acid,[127] and the protonation equilibrium monitored by absorption spectrosocpy. At pH values between 0 and 1, an additional emission was observed which was more fully examined (*vide infra*). At extremely high $[H^+]$, where the compound is diprotonated to form $[(bpy)_2Ru(dppH_2)]^{4+}$,[118] emission spectra were recorded, but no emission could be detected from this complex.

[xxxiii] Normally acidity is reported as pH. Since the solutions are deuterated, the proper term, "pD" is used although the idea of pH is implied.

2.E. Multiple Emissions from $[(bpy)_2Ru(dpp)]^{2+}$

At very pH an additional emission at higher energy also becomes visible. Its lifetime matched that of the pulse on the laser/ICCD system (*vide infra*), suggesting that a system with faster time-resolution was needed. In these faster experiments, $[(bpy)_2Ru(dpp)]^{2+}$ was dissolved in 1M nitric acid to a concentration of 10^{-3} M and its emissivity observed on a laser/streak camera system in the lab of Professor Robert Alfano, City College of the City University of New York. The sample was excited with the second harmonic, at 400 nm, of a Coherent Mira Modelocked Ti:Sapphire laser outputting 130 femtosecond (fs) pulses of the 800 nm fundamental at a rate of 82 MHz. Luminescence from the sample was collected and focused onto the slit of a streak camera, Model C1587 (Hamamatsu) with a 10ps time resolution, which was triggered by a portion of the laser pulse. Light in the 450nm–750nm range was isolated by use of narrowband filters, and its time dependence recorded. Steady-state emission spectra were still obtainable on the ICCD camera. The dependence of the emission intensity on exciting wavelength was explored using the 458 nm, 488 nm, and 492 nm, and 514 nm lines available from the argon ion laser. Camera gain was set to the maximum and the slits to 1 mm with an exposure time of 1.0 s.

2.F. Association of $[(bpy)_2Ru(dpp)]^{2+}$ with Various Metal Cations

Lead(II) nitrate ($Pb(NO_3)_2$, Fisher, Lot 975492), ferric nitrate nonohydrate ($Fe(NO_3)_3 \cdot 9H_2O$, Fisher, Lot D24352), zinc nitrate hexahydrate ($Zn(NO_3)_2 \cdot 6H_2O$, Fluka, Lot 422837/1), cadmium nitrate tetrahydrate ($Cd(NO_3)_2 \cdot 4H_2O$, Fluka, 37883/1), calcium nitrate tetrahydrate ($Ca(NO_3)_2 \cdot 4H_2O$, General Chemical, Lot 1538), aluminum nitrate nonohydrate ($Al(NO_3)_3 \cdot 9H_20$), Baker, Lot 25831), chromic nitrate nonohydrate ($Cr(NO_3)_3 \cdot 9H_2O$, Baker, Lot 764712), lithium nitrate ($LiNO_3$, Baker), and stannous chloride dihydrate ($SnCl_2 \cdot 2H_2O$, Fisher, Lot 744121) were used as received. $[(bpy)_2Ru(dpp)]^{2+}$ was diluted to concentrations of $2.5x10^{-5}M$ in solutions of different concentrations of metal nitrates to produce the following metal cations in solution: Li^+ (3 M), Ca^{2+} (6 M), Cd^{2+} (5 M), Zn^{2+} (5 M), Cr^{3+} (0.03 M) Pb^{2+} (1.2 M), Al^{3+} (3 M), Fe^{3+} (3 M) and Sn^{2+} (3 M). The bimetallic, $[(bpy)_2Ru(dpp)Ru(bpy)_2]^{4+}$ was also observed for comparison. The resulting absorption, steady state emission, and time-resolved emission spectra were obtained. For absorption and steady-state spectra, the solvent with the particular concentration of metal nitrate was subtracted. All solutions were deaerated by bubbling with argon gas for five minutes. Time-resolved data were fit to

both single and double exponential decays at each emitting wavelength for comparison.

2.G. Quantum Yield Determinations

2.G.1. Theory

Absolute quantum yield determinations require accounting for the total emission from a sample in all directions as compared to the known amount of irradiation. Suffice it to say, such determinations require exceptional equipment and techniques.[128] Whereas determining the amount of absorbed photons is its own challenge, mediated by the fact that light absorbed can come from one direction, determining the total amount of emitted photons in a spherical emission is formidable. Such absolute quantum yield determinations along with the attendant complex detection setups needed are, however, usually unnecessary for routine quantum yield measurements. For the most part, relative quantum yield determinations involve comparing a sample of unknown quantum yield to one of known quantum yield.[129] On the other hand, care must be taken in determining relative quantum yields as error is all too easy.

For determining relative quantum yields, it is critical to note that two solutions with the same

absorbance at a given wavelength can be expected to absorb the same number of photons, thus the ratio of their integrated emission spectrum (which is proportional to the total number of emitted photons), is the same as the ratio of their quantum yields, assuming that concentration effects such as self-quenching[130] and inner filter effects[131] are kept to a minimum. If the solutions are in different solvents, the solvent refractive indices must be accounted for. Choice of a standard is critical and must be made discriminately. The standard and unknown both need to absorb at a common excitation wavelength sufficient to populate the emitting state, and both need to have similar emission profiles with similar emission maximums. Last but not least, the standard must have a well-characterized emission quantum yield as aforementioned.

One common error is to adjust the concentrations of two species so that they have the same absorbance at an exciting wavelength and then compare the areas under their steady-state emission spectra, which is proportional to the quantum yield. This reliance on one data point can, without difficulty, spur poor results. One way to minimize error is to use the gradient method[132] where the ratio of the quantum yields is proportional to the ratio of the gradients of emission *vs.* absorbance. The integrated emission is

determined for a series of samples with varying absorption values at the excitation wavelength, such as 0.02, 0.04, 0.06, 0.08, and 0.1. By keeping all absorption values no greater than 0.1, inner filter effects are kept to a minimum. The quantum yield of the unknown, $\Phi_{unknown}$ can be calculated from (84):

$$\Phi_{unknown} = \Phi_{standard}\left(\frac{\nabla_{unknown}}{\nabla_{standard}}\right)\left(\frac{\eta^2_{unknown}}{\eta^2_{standard}}\right) . \qquad (84)$$

$\Phi_{standard}$ is the quantum yield of the standard, $\nabla_{unknown}$ and $\nabla_{standard}$ the gradients (slope of absorbance *vs.* emission), and $\eta^2_{unknown}$ and $\eta^2_{standard}$ the square of the refractive indices of the respective solvents used at room temperature. The integrated emission intensity vs. absorbance should produce a linear graph with intercept at zero (*i.e.* no absorption = no emission) and a slope equal to the gradient. However, certain spectrometers differ in their ability to reduce noise effects and produce exact absorption values. This requires the obvious, that a given data set be obtained on the same instrument, and also, that the zero-zero point not be forced in the data analysis. In order to obtain the full emission spectra, it is critical to subtract contribution from the specific solvent used as opposed to just using water, and to obtain as much of the

wavelength dependence of the emission as possible by finding the baseline on either side of it. The theory of quantum yield determinations assumes monochromatic light excitation to avoid complications of the wavelength dependence of absorption. Thus, using laser excitation is preferable to employing a broad emission spectrum lamp source with a monochromator, since the actual spectral width depends on the slit entrance, and often a wide slit width is needed to provide enough excitation to observe the emission of dilute species.

2.G.2. Method Development

Tris(2,2′-bipyridyl)dichloro-ruthenium (II) hexa-hydrate ($[Ru(bpy)_3]Cl_2 \cdot 6H_2O$, $RuC_{30}H_{24}N_6 \cdot 6H_2O$, 748.63 g/mol, Sigma Aldrich, Lot 19101CO), and dichlorotris(1,10-phenan-throline)ruthenium(II) hexa-hydrate ($[Ru(phen)_3]Cl_2 \cdot 6H_2O$, $RuC_{36}H_{24}N_6 \cdot 6H_2O$, 712.61 g/mol, Sigma Aldrich, Lot 20504DO) were both used without further crystallization. These along with $[Os(bpy)_3]PF_6$ were used as quantum yield reference standards, with known quantum yields in water and acetonitrile at room temperature.[133]

$[Ru(bpy)_3]Cl_2$ and $[Ru(phen)_3]Cl_2$ were dissolved in distilled water, whereas $[Os(bpy)_3]PF_6$ was dissolved in acetonitrile. $[(bpy)_2Ru(dpp)]^{2+}$ was dissolved in pH 7 buffer

to varying concentrations leading to absorptions at the excitation wavelength, 458 nm or 488 nm, ranging from 0.02 to 0.12 OD in order to avoid inner-filter effects. All solutions were deareated by bubbling with Argon gas for 5 minutes and blank subtracted both while recording absorption spectra and after obtaining emission spectra. The steady-state emission spectra were recorded both on the Fluorolog spectrometer, and with the ICCD camera to compare values, and standardize the method. For the Fluorolog, spectra at 2 nm intervals were recorded with a maximum voltage on the PMT of 950 volts, all slits were set to 8 mm, and acquisition time set to 0.5s. The excitation wavelength was set to 436 nm which gives a stronger emission signal. Since the quantum yield is not wavelength dependent, this served as an additional "test" of whether the argon/ICCD camera system is appropriate for relative quantum yield determinations. For the ICCD system, the entrance slit was set to 250 µm and the 150/800 grating was used. The exposure time was 1.00 s with the camera in the "free run" mode (as opposed to "gated" for time-resolved measurements), and set to a gain of 255. The areas under the steady state curves (510nm-865nm for Fluorolog, 500nm-900 nm for ICCD) were calculated using the built-in area calculator functions in the software programs of each

instrument. Relative quantum yields are obtained by direct comparison of the gradients (slopes) of the emission *vs.* absorption plots (*vide infra*).

Given the difficulty of obtaining reliable quantum yield data, the technique was refined by first cross-standardizing the quantum yields of $[Ru(bpy)_3]^{2+}$ and $[Ru(phen)_3]^{2+}$ in water. Using $[Ru(bpy)_3]^{2+}$, the quantum yields of $[(bpy)_2Ru(dpp)]^{2+}$ in water and $[Os(bpy)_3]^{2+}$ in acetonitrile were determined, allowing both to be used as references for other species.

2.G.3. Quantum Yield Determination of $[(bpy)_2Ru(dpp)]^{2+}$

From the pH titration of $[(bpy)_2Ru(dpp)]^{2+}$ (See 3.C.1. below), it is evident that its quantum yield of emission is highly pH dependent, hence the use of a buffered solution at pH=7. Since when cross-standardizing with $[Ru(bpy)_3]^{2+}$ the quantum yield obtained for $[Os(bpy)_3]^{2+}$ did not match published values,[133] the relative quantum yield of $[(bpy)_2Ru(dpp)]^{2+}$ at pH=7 was determined by direct comparison to $[Ru(bpy)_3]^{2+}$ using both the Fluorolog and the argon/ICCD camera system. Emission areas were integrated from 510-865 nm for the former, and 500-900 nm for the latter. Any anomalous deviations from near Gaussian-shaped emissions at the higher energy tail of $[(bpy)_2Ru(dpp)]^{2+}$

were corrected by matching a template of the emission of $[(bpy)_2Ru(dpp)]^{2+}$ without any bumps with the same maximum intensity.

2.G.4. Quantum Yield Determination of $[Os(bpy)_3]^{2+}$

As mentioned, when the relative quantum yield of $[Os(bpy)_3]^{2+}$ was investigated *vs.* $[Ru(bpy)_3]^{2+}$, the quantum yield obtained was much too low compared to the published value of 0.005.[133] Once the quantum yield of $[(bpy)_2Ru(dpp)]^{2+}$ at pH=7 was confidently determined, it was used as a reference for $[Os(bpy)_3]^{2+}$. In turn, $[Os(bpy)_3]^{2+}$ was used as as an independent reference for $[(bpy)_2Ru(dpp)]^{2+}$ at pH=5.

2.G.5. Quantum Yield of $[(bpy)_2Ru(dppH)]^{3+}$

Because of its low emissivity, the quantum yield determination of the protonated species, $[(bpy)_2Ru(dppH)]^{3+}$ was a distinct challenge. Normally, all instrument parameters must be kept the same. However, the dynamic range of the ICCD camera is not sufficient to observe the emission of $[(bpy)_2Ru(dppH)]^{3+}$ *and* the emission of $[(bpy)_2Ru(dpp)]^{2+}$ at the same instrument settings. There are three ways to increase the signal at the ICCD camera: increasing the entrance slit width, increasing the

intensifier gain, and increasing the exposure time. The slit width needs to be kept to a minimum to maintain the monochromicity of the light. For camera safety, the exposure time is kept to a minimum, which leaves the gain to be varied. At gain levels sufficient to observe the protonated species, emission of the unprotonated will overwhelm the camera. *Vice versa*, at even at low concentrations of $[(bpy)_2Ru(dpp)]^{2+}$ with the gain set to maximum, the emission of $[(bpy)_2Ru(dppH)]^{3+}$ is impossible to see.

One approach was to calibrate the gain settings of the camera. In other words, whereas a gain setting of 200 is needed to observe the emissions of the protonated species with the slits open to 1 mm, the gain needs to be reduced to 73, with the same slit width to observe all of the unprotonated emissions without overwhelming the camera. By measuring the steady-state quantum yield of emission (area under the curve) of $[(bpy)_2Ru(dpp)]^{2+}$ independently at several gain values, a calibration of observed quantum yield *vs.* camera gain could be made. The ratio of the emission areas at two gain settings would correspond to the ratio of relative quantum yields observed at those two gain settings. This ratio can be used to extrapolate the emission area of an emissive species from one gain setting

to another. Thus, although two different camera gain settings were used to observe the emission area *vs.* absorbance gradients of the protonated and unprotonated species, they can be directly compared by use of the calibration curve.

Since such high concentrations of $[(bpy)_2Ru(dppH)]^{3+}$, are needed to perform the quantum yield analysis with OD>1, inner filter effects become significant. Compounded by the extreme low emissivity of $[(bpy)_2Ru(dppH)]^{3+}$, its measured steady-state quantum yield is ± 30%, though still useful.

2.H. Association of $[(bpy)_2Ru(dpp)]^{2+}$ with Ag^+

Given the precedent of Ag^+ to form exciplexes with Ru(II) diimines,[55-57,59] the association of silver cation with $[(bpy)_2Ru(dpp)]^{2+}$ was investigated. This involved examining the $[Ag^+]$ dependence of the absorption, NMR, and steady-state emission spectra of $[(bpy)_2Ru(dpp)]^{2+}$. Solid $AgNO_3$ (Mallinckrodt, Lot EKZ) was used as received. $[(bpy)_2Ru(dpp)]^{2+}$ was diluted to a concentration of 3.17×10^{-5} M in solutions of varying concentrations of $AgNO_3$, from 0 M to 2.0 M. UV-VIS spectra were obtained on the Aviv spectrometer, and emission spectra on the Fluorolog, slits set to 4 mm, excitation at 470 nm. The time-resolved emission of $[(bpy)_2Ru(dpp)]^{2+}$ in higher concentration $[Ag^+]$,

3 M, was also examined in both methanol and water. $LiNO_3$ (General Chemical Company) was used as received to fix the ionic strength and nitrate concentration in aqueous solutions.

For ^1H NMR spectra, $[(bpy)_2Ru(dpp)]^{2+}$ was dissolved to a concentration of 0.008 M in two D_2O solutions, one of which had a $AgNO_3$ concentration of 5 M. To maintain the concentration of $[(bpy)_2Ru(dpp)]^{2+}$, the $Ru/AgNO_3$ solution was titrated into the other, and regular NMR spectra obtained at each step.

2.I. Association of $[(bpy)_2Ru(dpp)]^{2+}$ with Cd^{2+} and Zn^{2+}

Given the preliminary results of the associational study of Cd^{2+} and Zn^{2+} with $[(bpy)_2Ru(dpp)]^{2+}$ (Section 3.F.), a detail examination of the concentration dependence of these ions on the NMR, absorption, steady-state emission, and time-resolved emission spectra of $[(bpy)_2Ru(dpp)]^{2+}$ were accomplished. Additionally, using the relative quantum yield of $[(bpy)_2Ru(dpp)]^{2+}$ in pH 7 buffered solution, the relative quantum yields of the suspected bimetallics, $[(bpy)_2Ru(dpp\text{-}Cd)]^{4+}$ and $[(bpy)_2Ru(dpp\text{-}Zn)]^{4+}$ were obtained in pH=5 buffer solution, using the aforementioned procedures.

Cadmium nitrate tetrahydrate ($Cd(NO_3)_2 \cdot 4H_2O$, Fluka, Lot 377883/1), zinc nitrate hexahydrate ($Zn(NO_3)_2 \cdot 6H_2O$, Fluka, Lot 522837/1) and mercuric nitrate monohydrate ($Hg(NO_3)_2 \cdot H_2O$, Sigma-Aldrich, Lot 230421-50G) were used as received. $[(bpy)_2Ru(dpp)](NO_3)_2$ was diluted to concentrations of 2.5×10^{-5}M in solutions of increasing concentrations of $Cd(NO_3)_2$ and $Zn(NO_3)_2$, first in water, and then in pH 5 buffer solution with $Ca(NO_3)_2$ used to fix the ionic strength of every solution to 5 M $M(NO_3)_2$. All solutions were bubbled with argon gas for 5 minutes. Solutions of the metal cations in water and/or buffer, at the same concentrations were used as blanks. For NMR studies, $Cd(NO_3)_2 \cdot 4H_2O$ and $Zn(NO_3)_2 \cdot 6H_2O$ were dissolved in D_2O, and then dried to dryness with addition of 95 % ethanol. This was repeated several times to obtain the deuterates, $Cd(NO_3)_2 \cdot 4D_2O$ and $Zn(NO_3)_2 \cdot 6D_2O$. $[(bpy)_2Ru(dpp)](NO_3)_2$ was dissolved to 10^{-2} M in D_2O and in D_2O solutions of 5 M $Cd(NO_3)_2$ and $Zn(NO_3)_2$. This ensured that in the titration, the initial $[(bpy)_2Ru(dpp)]^{2+}$ was invariant. Regular ^1H NMR were recorded, referenced to the DSS signal at 0ppm. Lastly, the time-resolved emission spectrum of $[(bpy)_2Ru(dpp)]^{2+}$ in 1M mercuric nitrate solution in 1M nitric acid was also examined for comparison.

---

3. RESULTS

3.A. Examination of Laser Pulses

The time-resolved spectra of the 355 nm and 532nm pulses are shown in Figures 15 and 16 respectively. The frames at maximum intensity were extracted to exhibit the wavelength dependence of the pulses (Figure 17). The time and wavelength dependences of each pulse were fit to Gaussian functions of the form

$$y = y_o + Ae^{\left[-\left(\frac{x-x_o}{width}\right)^2\right]}, \tag{85}$$

where x_o is the center of the curve and *width* is actually the half-width, meaning, the width of the curve at half-the maximal value. The results are tabulated below (Table 4).

Table 4. Nd:YAG Laser pulse characteristics.

	532 nm	355 nm
wavelength center	532.38 nm	354.34 nm
wavelength, full width at half maximum (FWHM)	0.90 nm	0.74 nm
FWHM	9.27 ns	6.67 ns
Expected Width	6-7 ns	5-6 ns
Lifetime	3.5 ns	2.9 ns

The wavelength envelope (center ± FWHM/2) includes the expected wavelength targets of both pulses. Data for the

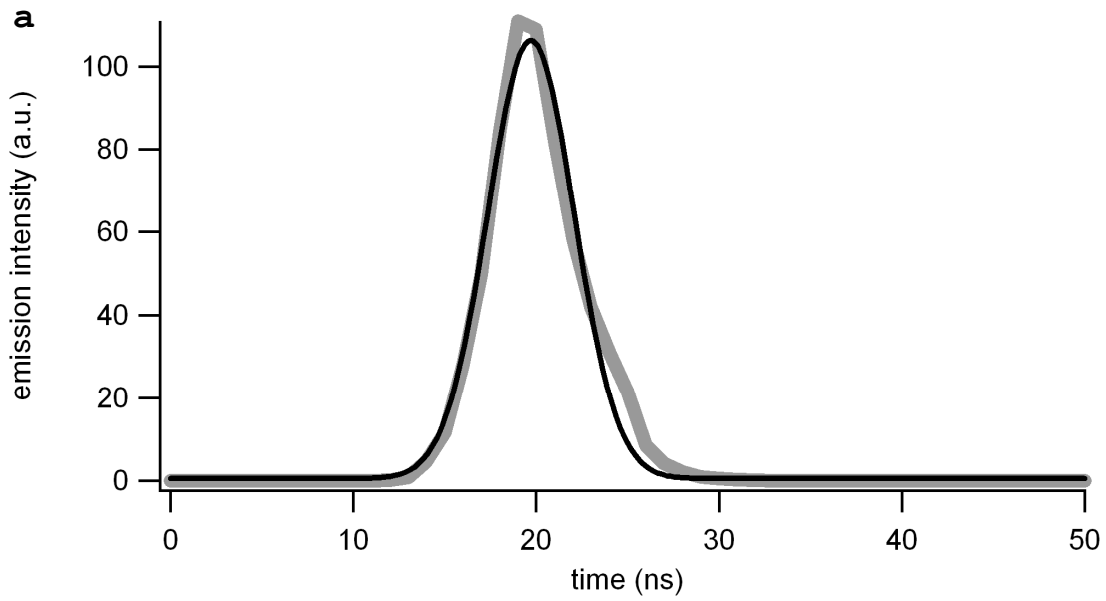

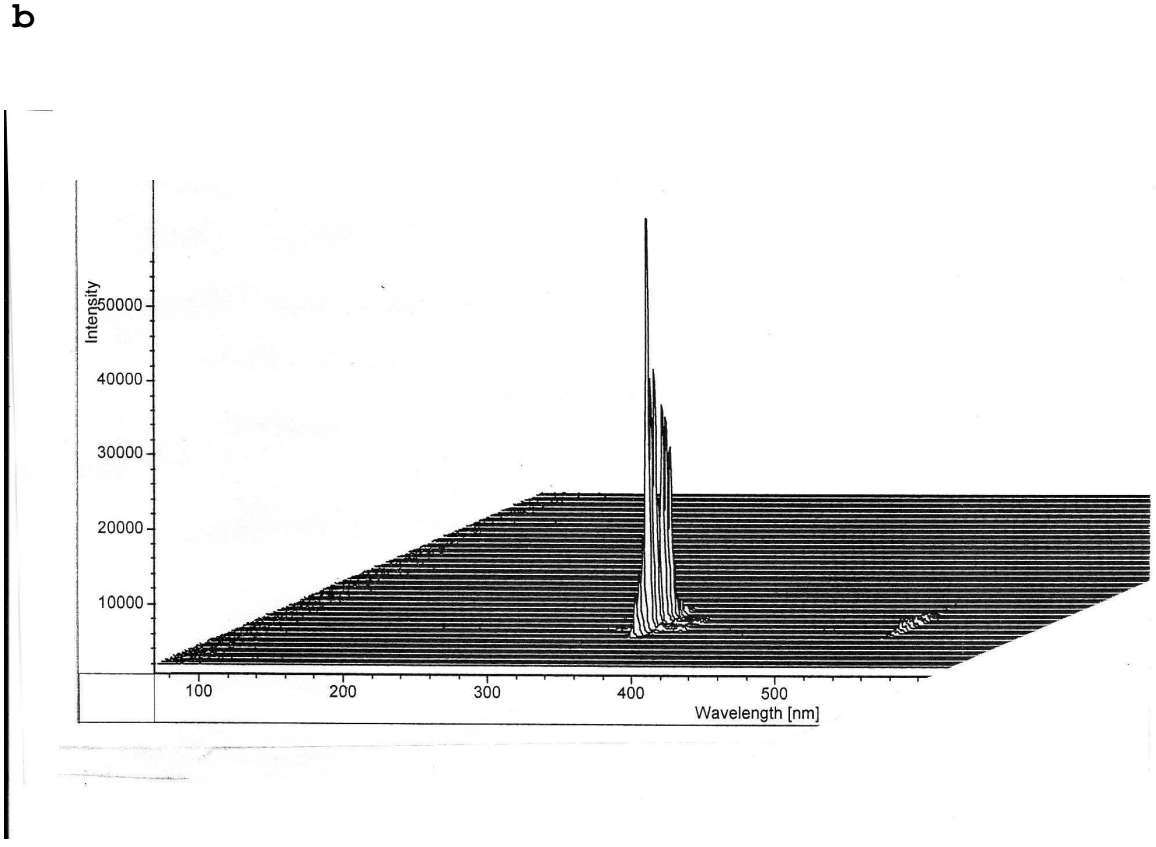

Figure 15. 355nm pulse from the Nd:YAG laser: (a) time-resolved plus fit; (b) 3D time-resolved.

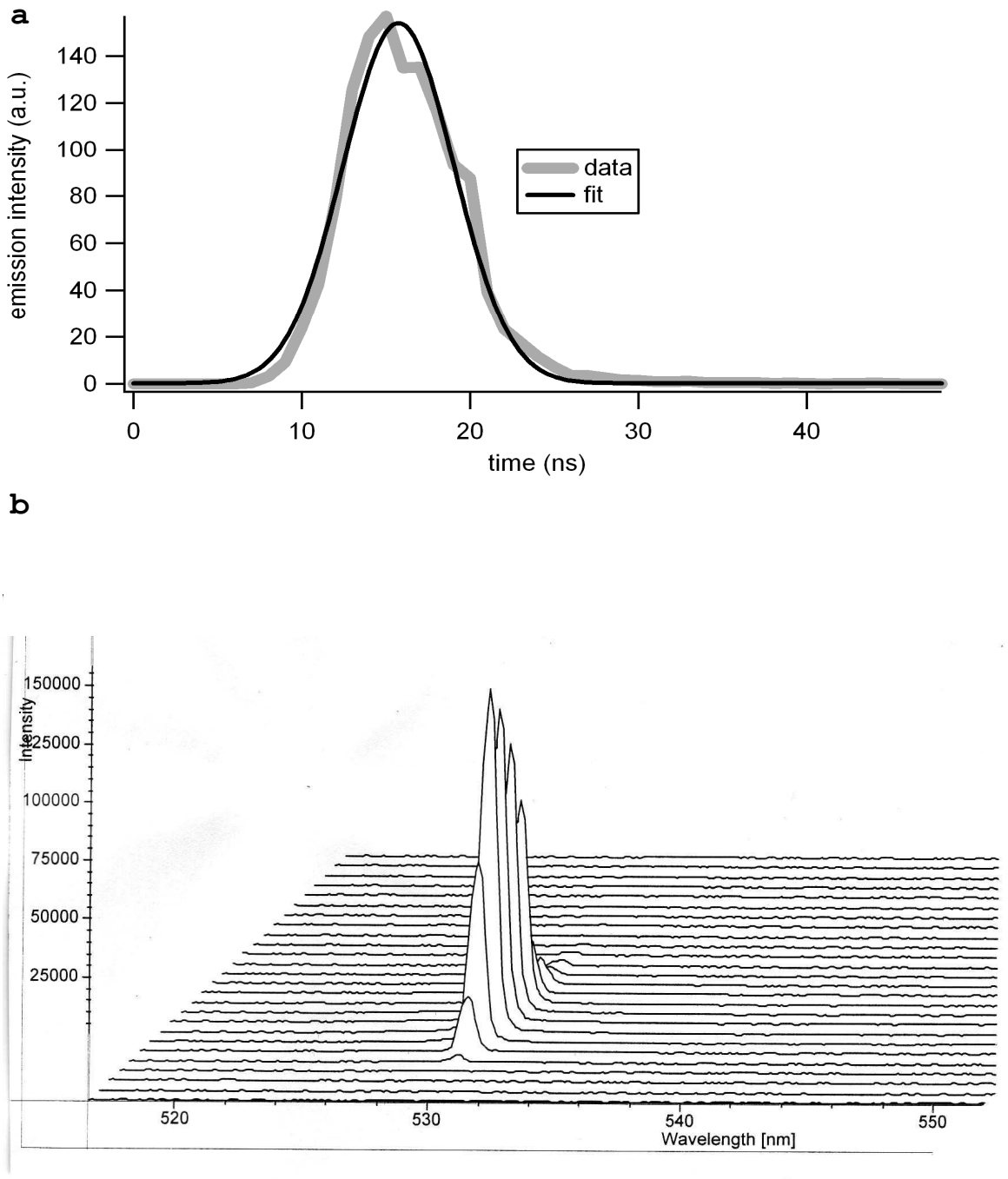

Figure 16. 532nm pulse from the Nd:YAG laser: (a) time-resolved plus fit; (b) 3D time-resolved.

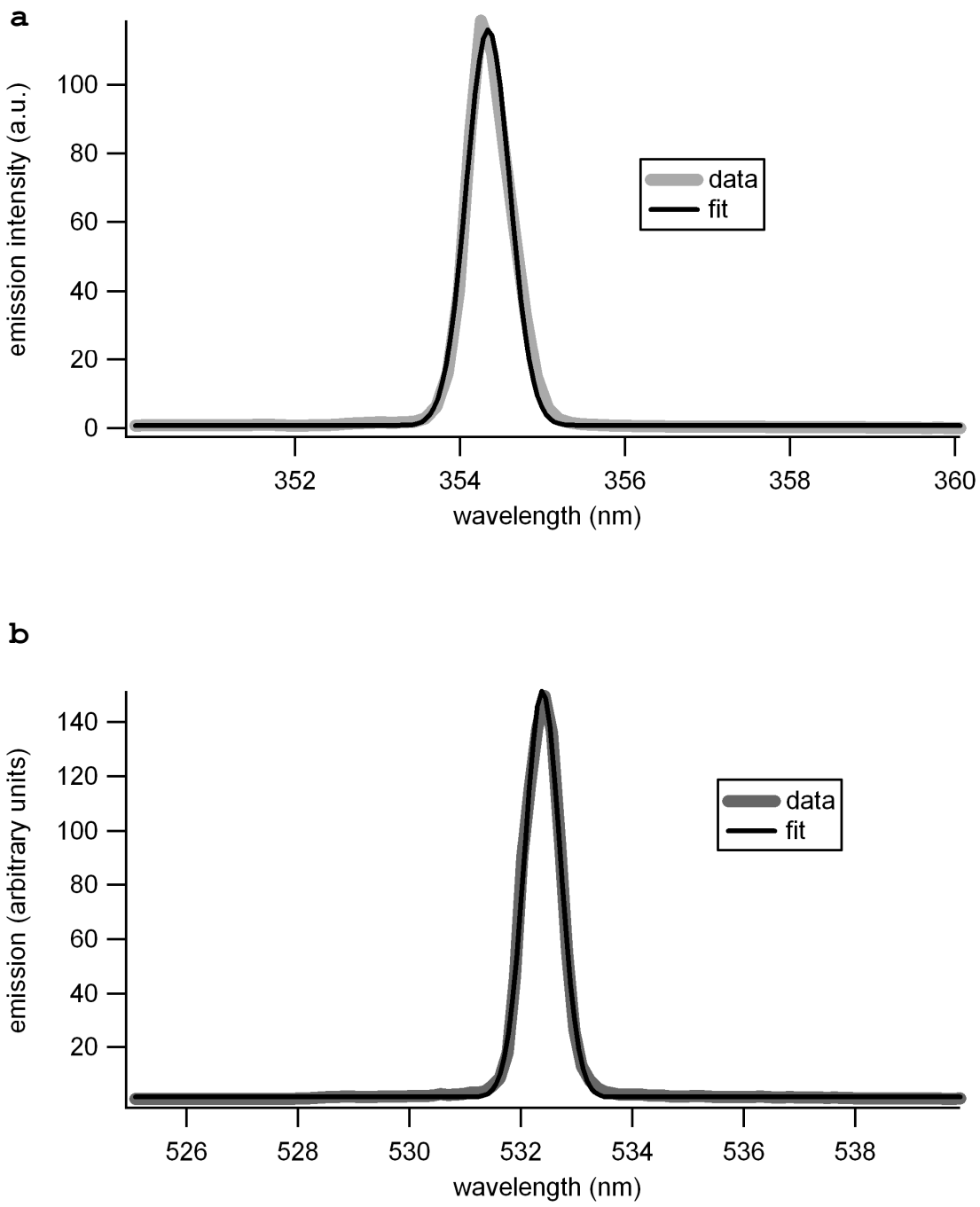

Figure 17. Wavelength dependence of pulses from the Nd:YAG laser: (a) 355 nm pulse, (b) 532nm pulse.

532 nm pulse is expectedly more on target given the blaze of the grating used. When fitting the decay portion of the time-resolved data to single exponential decays, the lifetimes obtained are 2.9 ns and 3.5 ns for the 355 nm and 532 nm pulses respectively. The FWHM obtained are larger than that expected for two possible reasons: first, the age of the pulse laser may have lead to this broadening; and second, the extra width may simply represent the inherent error in the system with gated intensifier widths available only down to 2 ns. Even given so, the 1-3 ns broadening should have minimal effect on examining species with much longer lifetimes.

3.B. Characterization of $[(bpy)_2Ru(dpp)](NO_3)_2$

3.B.1. Electronic Spectroscopy

The electronic spectra of $[(bpy)_2Ru(dpp)]^{2+}$ appear in Figure 18a. Similar to the original published report,[93] two clear MLCT transitions are evident in the 400-500 nm range of the absorption spectrum, at 428 nm, and 476 nm with molar extinction coefficients of 9703 M^{-1} cm^{-1} and 9214 M^{-1} cm^{-1} respectively, the former being slightly higher. A Gaussian fit (Figure 18b), using IGOR, exposes the two MLCT transitions centered at 426 nm and 487 nm. Several, more intense, $\Pi^*\leftarrow\Pi$ transitions are also evident in the UV range.

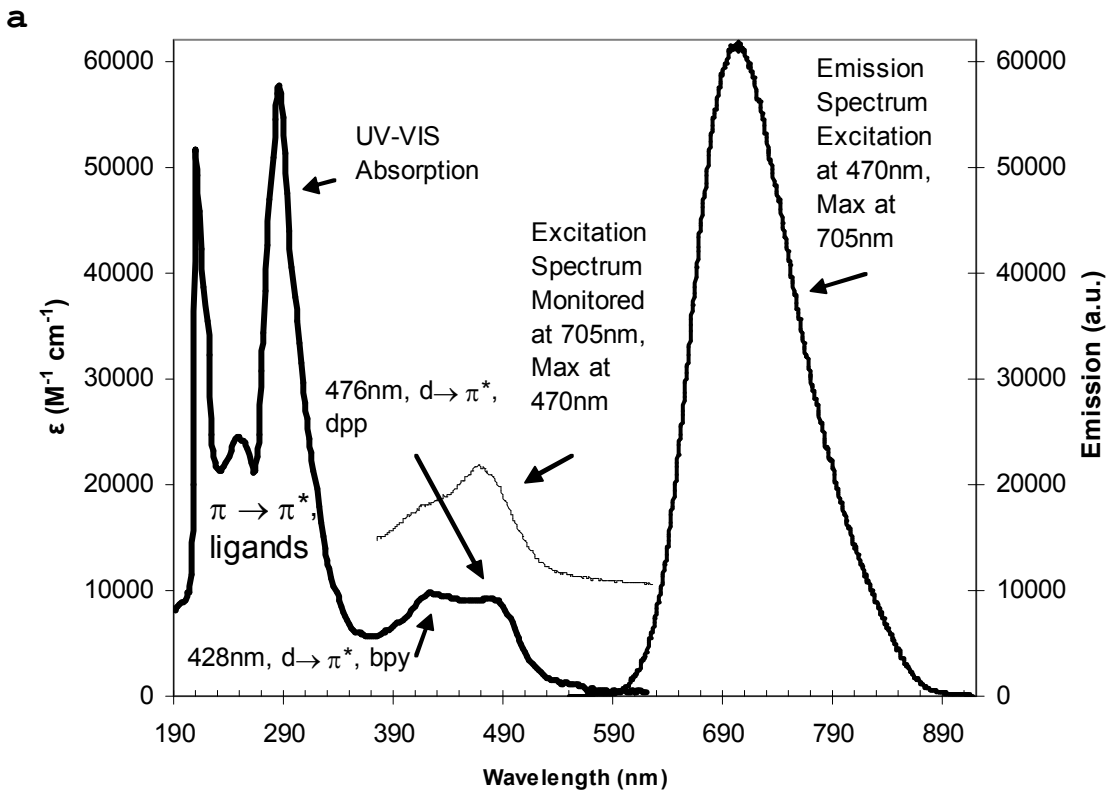

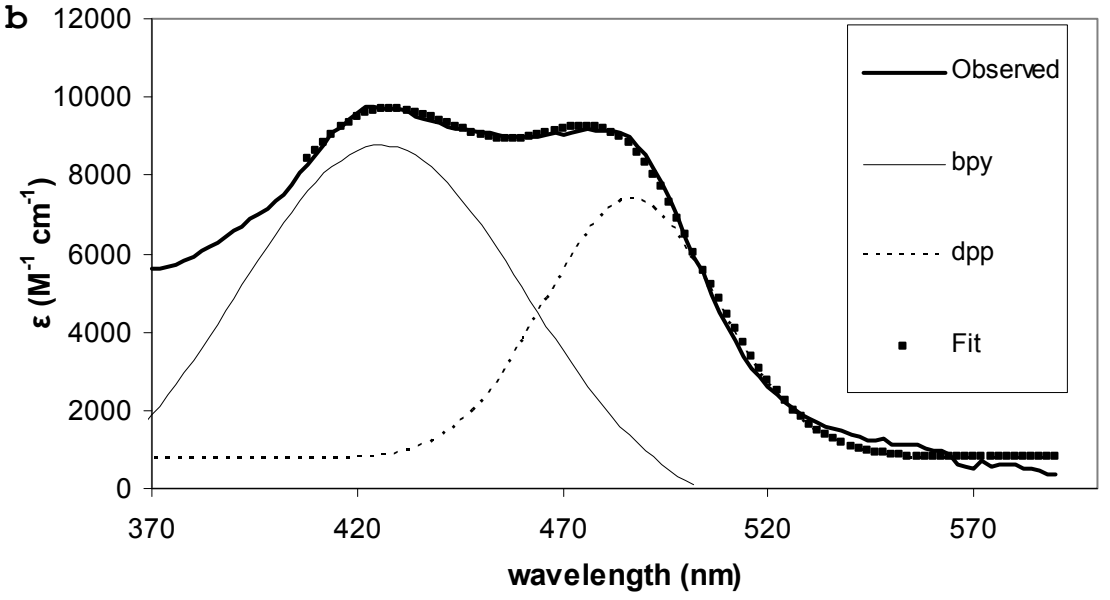

Figure 18. Electronic spectra of $[bpy_2Ru(dpp)]^{2+}$: (a) all spectra, (b) Gaussian fits of MLCT transitions.

The complex yields a broad emission to the red, with a wavelength maximum at 704 nm ± 6 nm in water. The wavelength maximum is longer than that reported elsewhere for the complex in water (690 nm, ClO_4^- form),[119] which is most likely due to the increased red-sensitivity of the ICCD system with the spectrograph grating blazed for maximal reflectivity at 800 nm. The emission is not wavelength dependent: excitation throughout the MLCT transition region consistently results in the 704 nm emission. The excitation spectrum shown confirms that the emission arises solely from the lower energy transition, with maximal excitation occurring at 470 nm. Its assignment is thus $d \leftarrow \Pi^*_{dpp}$.

The time-resolved spectrum of $[(bpy)_2Ru(dpp)]^{2+}$ was carefully examined using the ICCD camera system described above. The full time-resolved three-dimensional spectrum is shown in Figure 19. The trace at the maximum emission intensity (704 nm) going from time zero (T_o) onwards is shown in Figure 20a, which includes the grow-in of the emission. Since population of Ru(II) diimine states is on the order of 100 fs,[134,135] this grow-in is arguably only a function of the pulse profile, which has a finite rise and decay profile (Figure 16). If starting at the initiation of the rise, the entire profile can be fit to a double

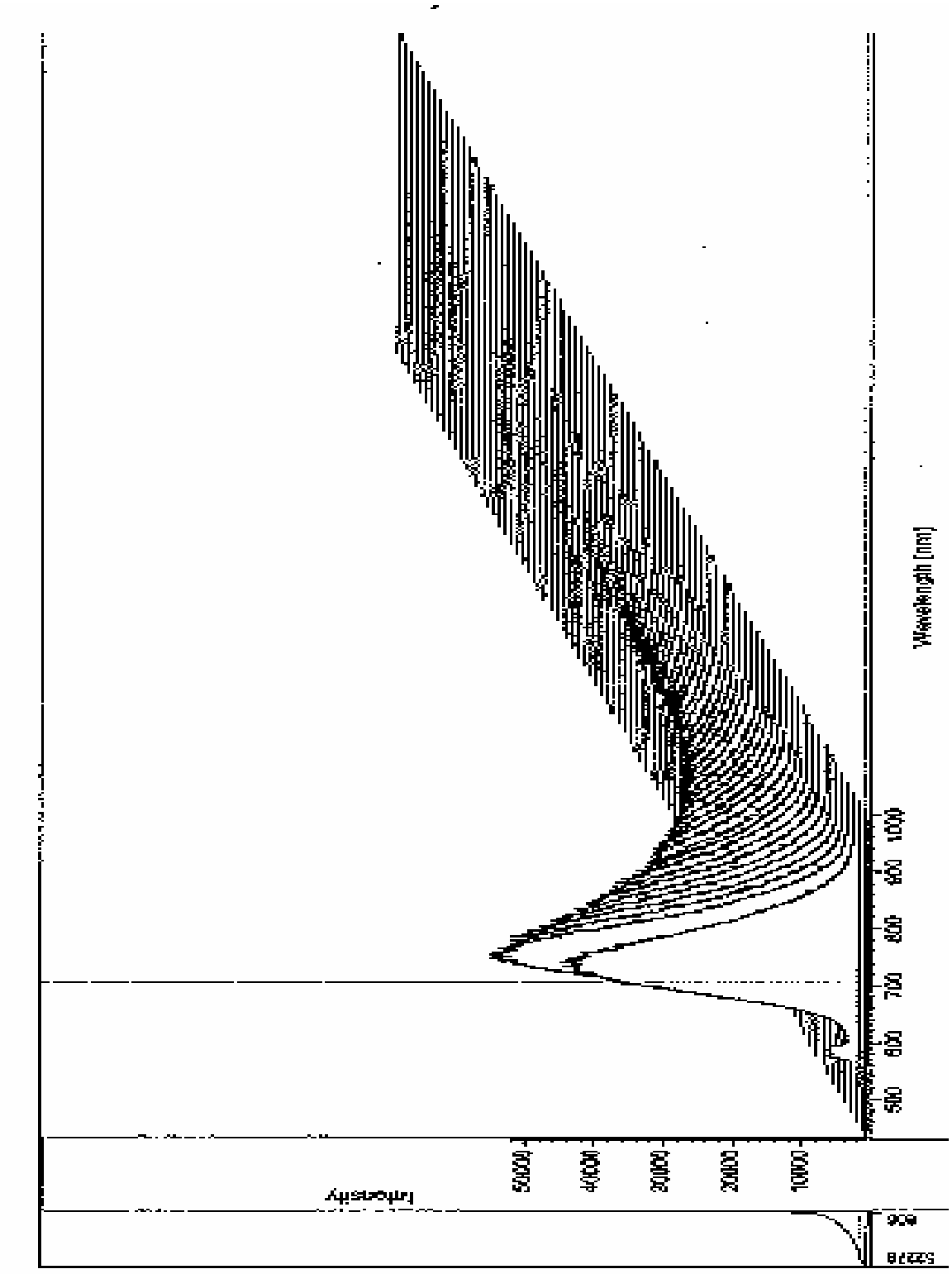

Figure 19. 3D time-resolved emission spectrum of 3 x 10^{-5} M $[bpy_2Ru(dpp)]^{2+}$.

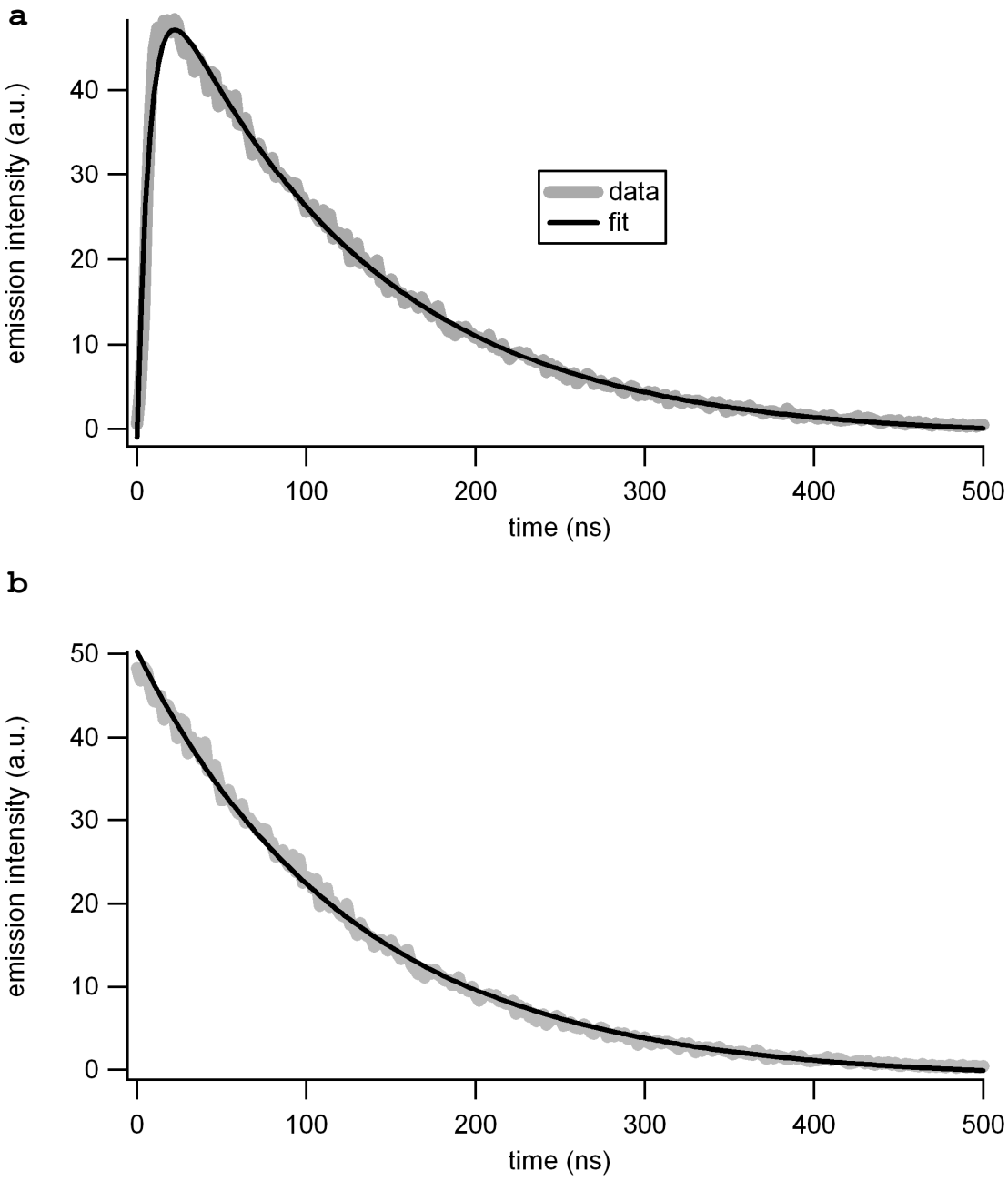

Figure 20. Time-resolved emission spectra of $[bpy_2Ru(dpp)]^{2+}$: (a) full trace with fit, (b) trace from maximum with fit.

exponential equation of the form

$$y = y_o + \left(\frac{k_1}{k_2 - k_1} \right) A\left(e^{-k_1 x} - e^{-k_2 x} \right) , \qquad (86)$$

where k_1 is the rate constant for the rising portion, and k_2 for the decay. The rise-time (analogous to lifetime, but inverted) was 7.5 ± .4 ns, and the decay lifetime 123 ns ± 4 ns. (Errors are reported to two standard deviation). Fitting just the decay portion led to a single exponential decay with a lifetime of 128 ± 2 ns (Figure 20b). Within overall experimental error, these lifetimes are essentially the same. Therefore, fitting just the decay portion will suffice in data analysis.[xxiv] That the lifetime is independent of wavelength can be seen from the plot of decay lifetime as a function of wavelength (Figure 21a). The average lifetime of those calculated is 126 ± 7 ns, nearly exactly that determined from just the one fit at the emission maximum. From these fits, the pre-exponential factors at each wavelength, consistent with a particular, invariant lifetime, can also be plotted (Figure 21a). This, in essence, plots the wavelength dependent spectrum of a

---

[xxiv] Based on this, fitting just the decay portion of the time-resolved spectrum is customary, especially when the lifetime far exceeds the pulse width. This also eases analysis when a double-exponential fit of the decay is required.

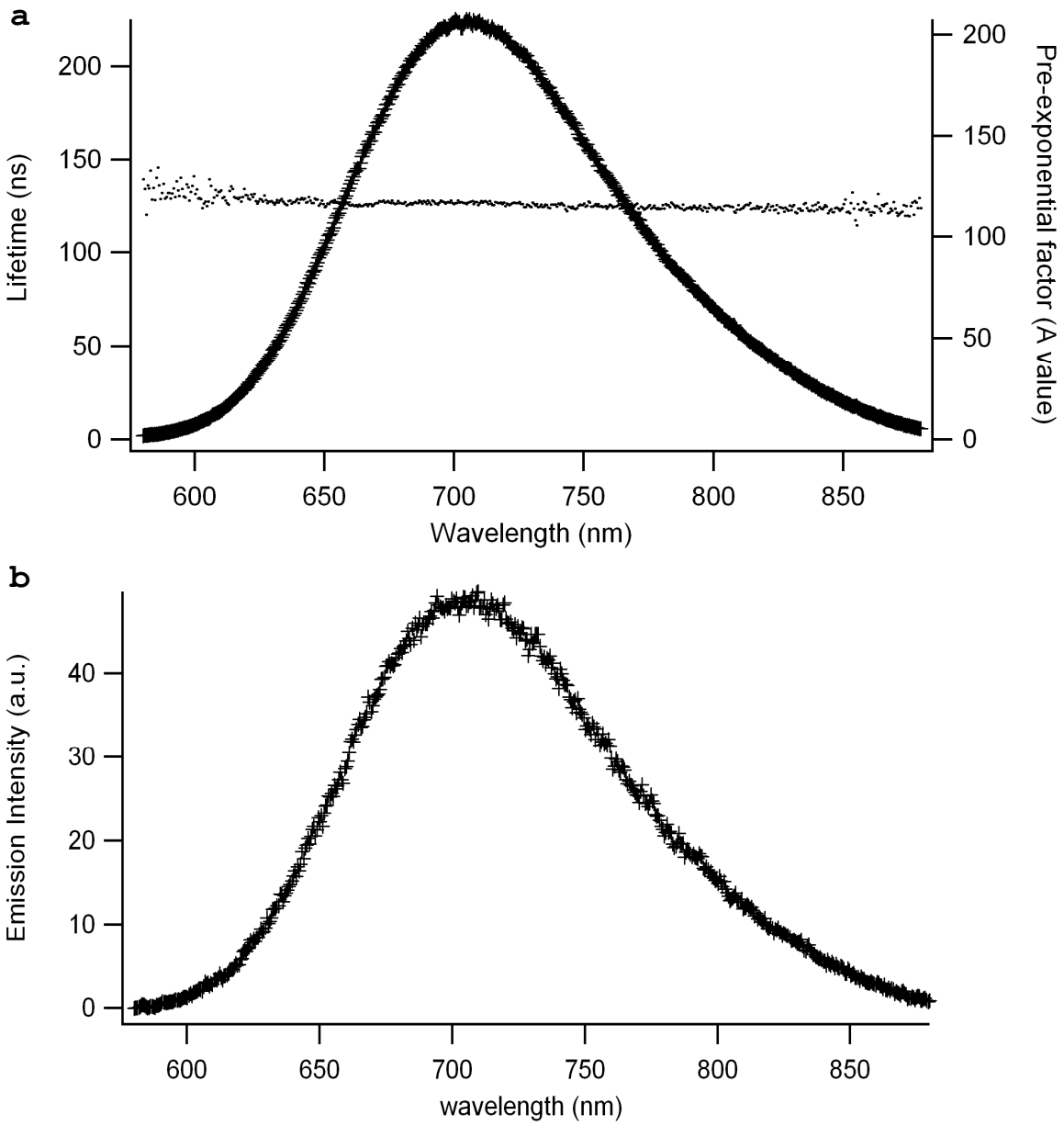

Figure 21. Wavelength dependent emission spectra of $[(bpy)_2Ru(dpp)]^{2+}$: (a) lifetime and pre-exponential factor (A); (b) emission spectrum from maximum frame of lifetime decay.

species with a wavelength-independent lifetime. Taking one frame of the time-resolved data and plotting emission *vs.* wavelength shows the near identical comparison (Figure 21b). Similar plots of the emission of $[(bpy)_2Ru(dpp)]^{2+}$ in ethanol (Figure 22) and methanol (Figure 23) reveal a solvent dependence on the emission maxima and lifetime. The comparison is tabulated below (Table 5).

Table 5. Emission properties of $[(bpy)_2Ru(dpp)]^{2+}$ in different protic solvents

Solvent	Emission maximum (nm)	Average Lifetime (ns)
Water	704	126 ± 7
Methanol	698	150 ± 8
Ethanol	690	219 ± 6

3.B.2. NMR Spectroscopy

The ^{1}NMR of the nitrate form of $[(bpy)_2Ru(dpp)]^{2+}$ in D_2O (referenced to DSS) is shown in Figure 24. The spectrum of the chloride form in acetonitrile has been reported,[136] which is quite similar, but has a few dissimilarities attributable to the solvent differences—the solvent dependency of the proton shifts of 2,2'-bipyridine having been previously reported.[137] Proton-proton correlated spectroscopy (^1H-^1H COSY) was used to assist in making the assignments (Figure 25). There are seven distinct coupled ring systems and a total integration of 26 protons, as

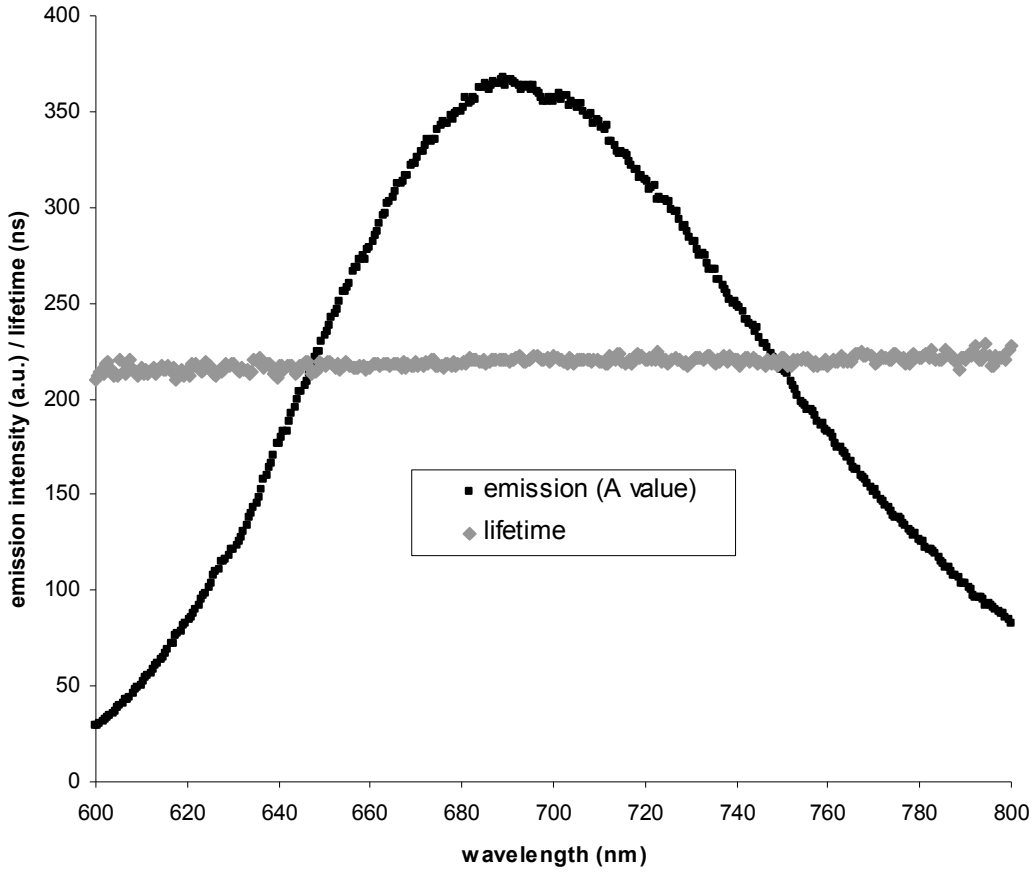

Figure 22: Emission of 3.17 x 10^{-5} M $[(bpy)_2Ru(dpp)]^{2+}$ in ethanol.

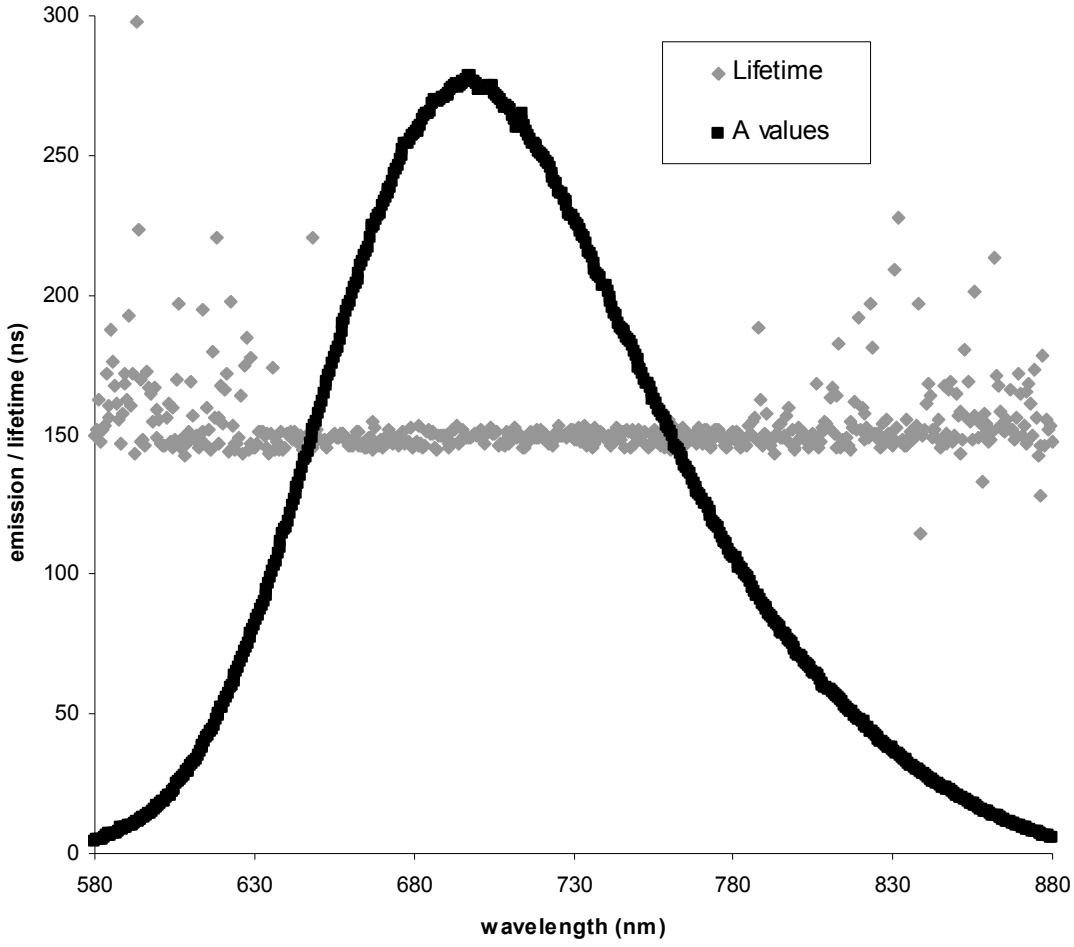

Figure 23: Emission of 3.17 x 10^{-5} M $[(bpy)_2Ru(dpp)]^{2+}$ in methanol.

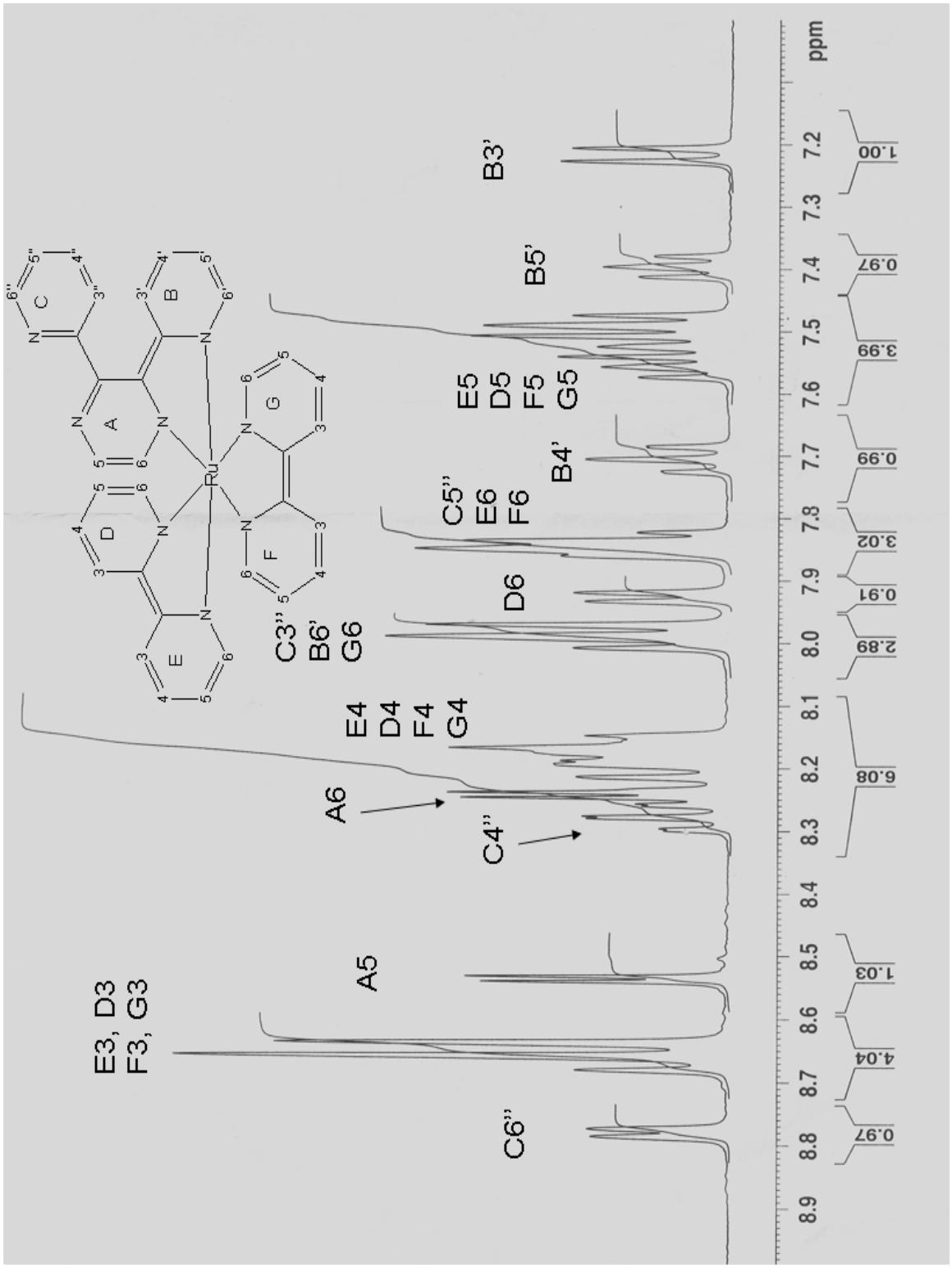

Figure 24. ^{1}H NMR spectrum of 0.01 M $[(bpy)_2Ru(dpp)]^{2+}$ in D_2O.

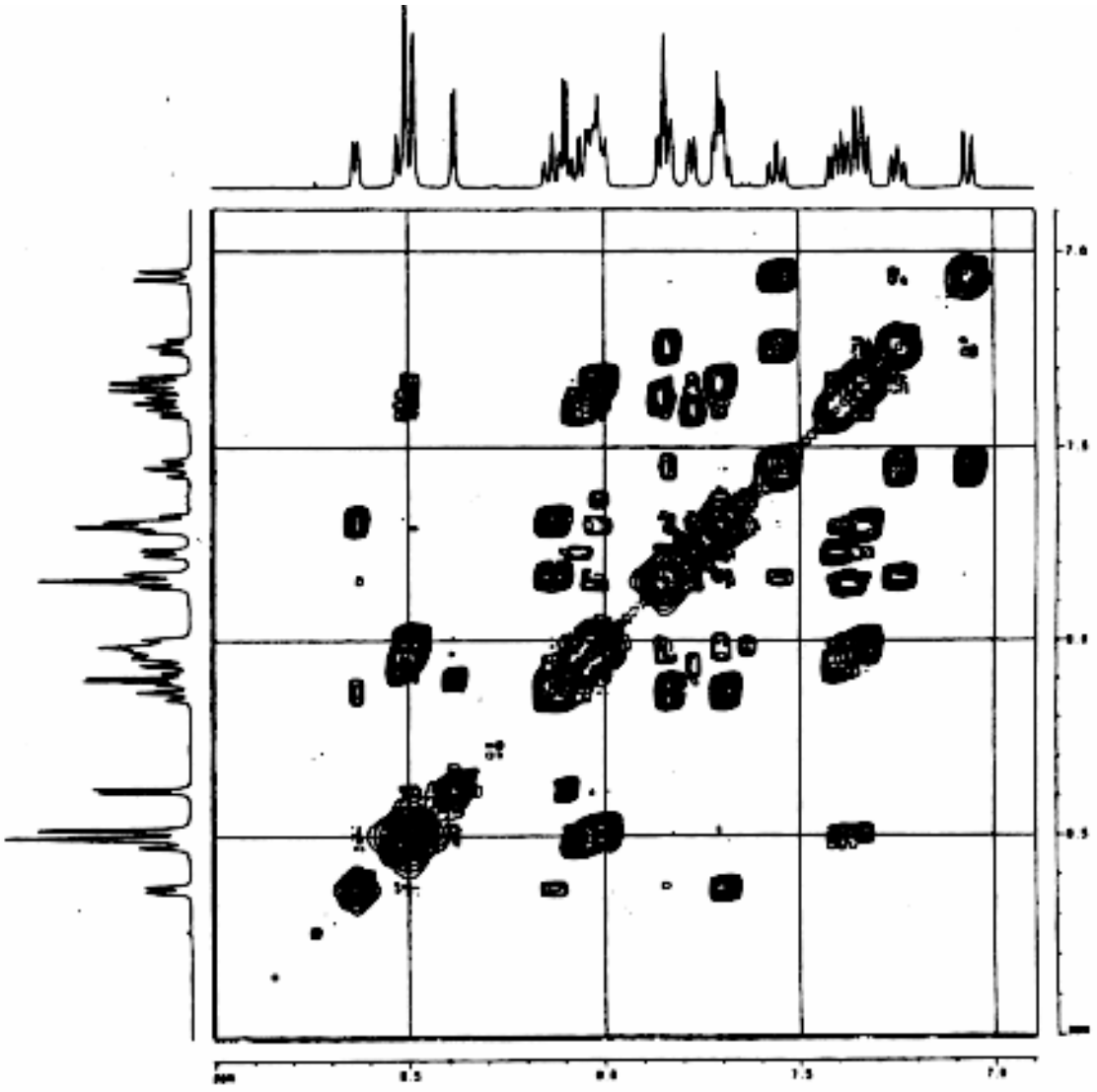

Figure 25. ^{1}H-^{1}H COSY spectrum of 0.01 M $[(bpy)_2Ru(dpp)]^{2+}$ in D_2O.

expected, assuming the integration of one of the extreme doublets, at 8.75 ppm, represents 1 proton. All peaks fall into the traditional aromatic region (6-9 ppm), deshielded from effects due to the +2 charge of the ruthenium metal center. The bipyridine protons, numbered 3 through 6 on rings D through G all fall in clusters, quite close to their assignments in the D3 symmetrical tris complex, $[Ru(bpy)_3]^{2+}$.[138] Table 6 below summarizes this comparison. However, the fact that they are not coincident matches with the structural fact the dpp ligand, when coordinated, creates asymmetry between all the ligands. Further discussion is found in Section 4.A.2.

Table 6. Comparison of 2,2′-bipyridine ^{1}H NMR shifts.

Proton	Chemical shift in $[Ru(bpy)_3]^{2+}$ (ppm)	Chemical shift range in $[(bpy)_2Ru(dpp)]^{2+}$ (ppm)
3	8.9	8.66
4	8.2	8.1-8.2
5	7.55	7.45-7.6
6	7.77	7.8-8.0

3.C. Acid Titration of $[(bpy)_2Ru(dpp)]^{2+}$

3.C.1. Absorption & Emission Spectra

Similar to previous published results,[93,139] the absorption spectrum changes little on going down to pH 0 (Figure 26a). The 422 nm transition increases by about 17%,

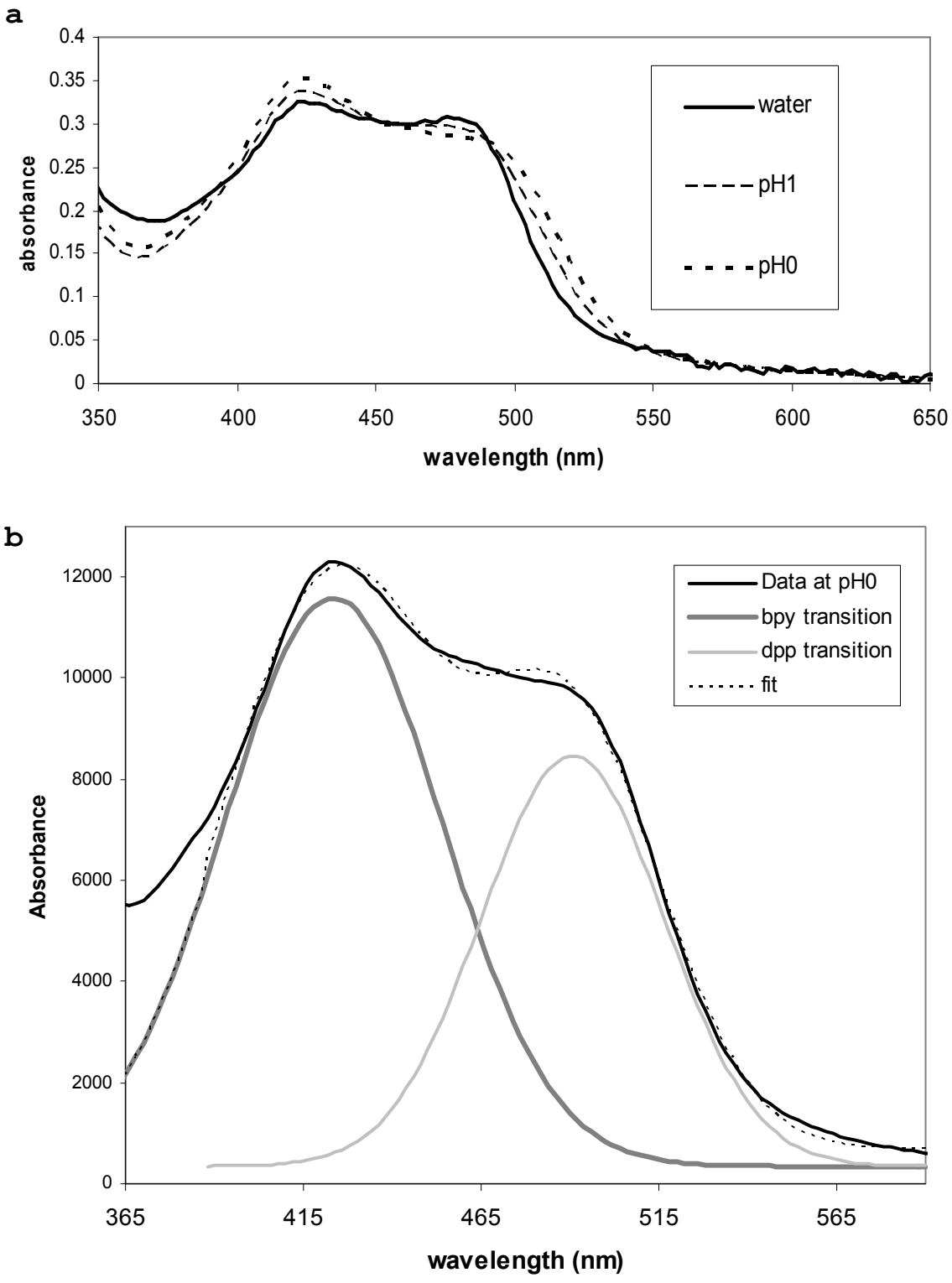

Figure 26. Absorption spectra of pH titration of $[(bpy)_2Ru(dpp)]^{2+}$: (a) spectra; (b) Gaussian fits.

and the 490 nm transition decreases about 10%. The two-Gaussian fit (Figure 26b) shows slight deviations from the data.

The emission of $[(bpy)_2Ru(dpp)]^{2+}$ decreases with decreasing pH significantly (Figure 27). A careful look at the emission at pH 1 shows a red-shift of the emission maximum to 722 nm, and at pH 0, what appears, on first examination, to be a blue shift. Since relative quantum yield was being observed the dynamic range of the ICCD camera at one gain setting is not large (65,536 counts), so these very weak emissions appear quite noisy. Additionally, the Raman water band is slightly attenuated in the sample, so that subtraction of the blank sometimes leads to a dip in the spectrum at 587 nm. Further investigation of these weak emissions at low pH with higher camera gain and chromophore concentration reveal the presence of two emissions *(vide infra)*.

First, it is critical to note the sensitivity of the emission of $[(bpy)_2Ru(dpp)]^{2+}$, which is a weak base, to pH. Differences in the emission are even seen between pH 7 and pH 8. Further investigation of the emission in pH buffers above pH 8 revealed no further differences. A number of parameters were used for comparative analysis of the titration. Here, in addition to calculating the lifetimes

a

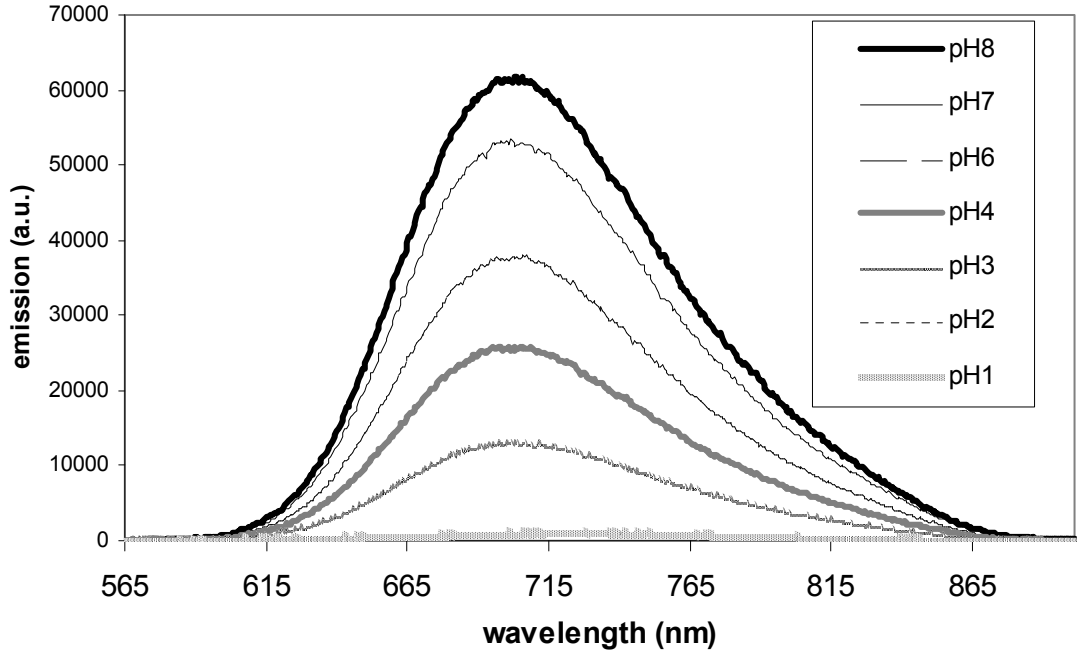

b

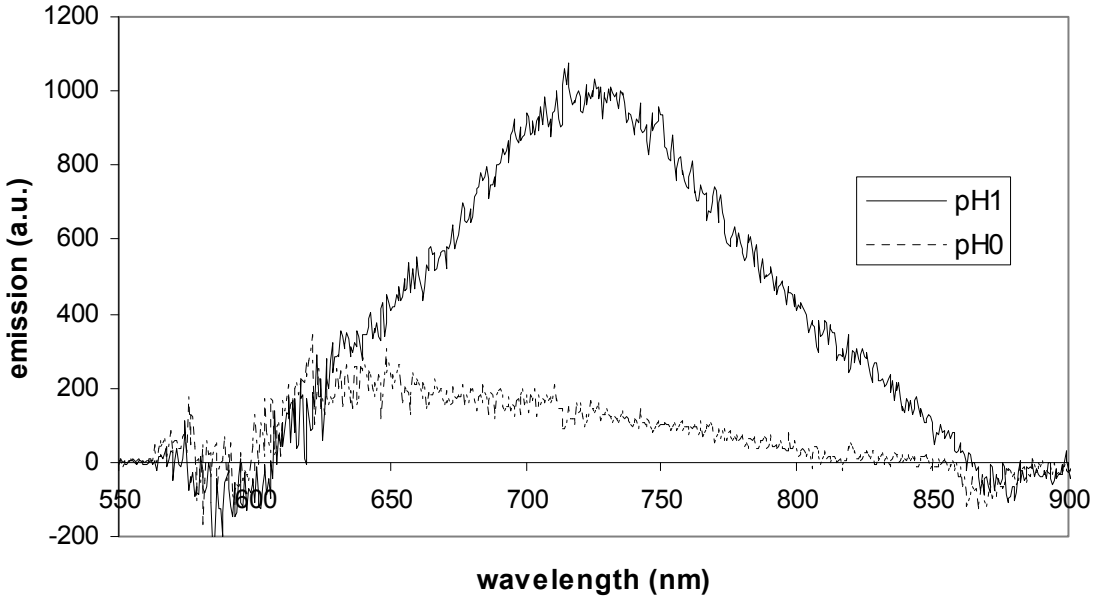

Figure 27. Emission spectra of pH titration of $[(bpy)_2Ru(dpp)]^{2+}$: (a) pH1—pH8; (b) pH0-pH1.

of each solution (τ) and recording the maximum intensities of the steady-state spectra (I, at 702 nm in these cases), the complete area under the steady-state spectrum (A) which represents the relative steady-state quantum yield, and the area under the three-dimensional time-resolved spectra (Φ) which represents the relative quantum yield of the dynamic emission were also calculated. The maximal values at pH 8 (designated $X_\circ$ where X is the symbol of the parameter) were set to 100%, and the percent change was calculated at each data point for each parameter, thus normalizing them to the same scale. The data points are plotted *vs.* pH in Figure 28a, revealing a sigmoid-like shape.

Using Igor's curve fitting function, each plot was fit to a sigmoidal curve of equation:

$$y_{\text{intensity}} = base + \frac{\max}{1 + e^{[(xhalf - x_{pH})/rate]}} \tag{87}$$

where y is the bottom of the curve, max is the top, $xhalf$ is the inflection point, x the pH, and $rate$ the rate of change. One example for $I/I_\circ$ is shown in Figure 28b. Table 7 below tabulates the inflection points from the fits of each data set.

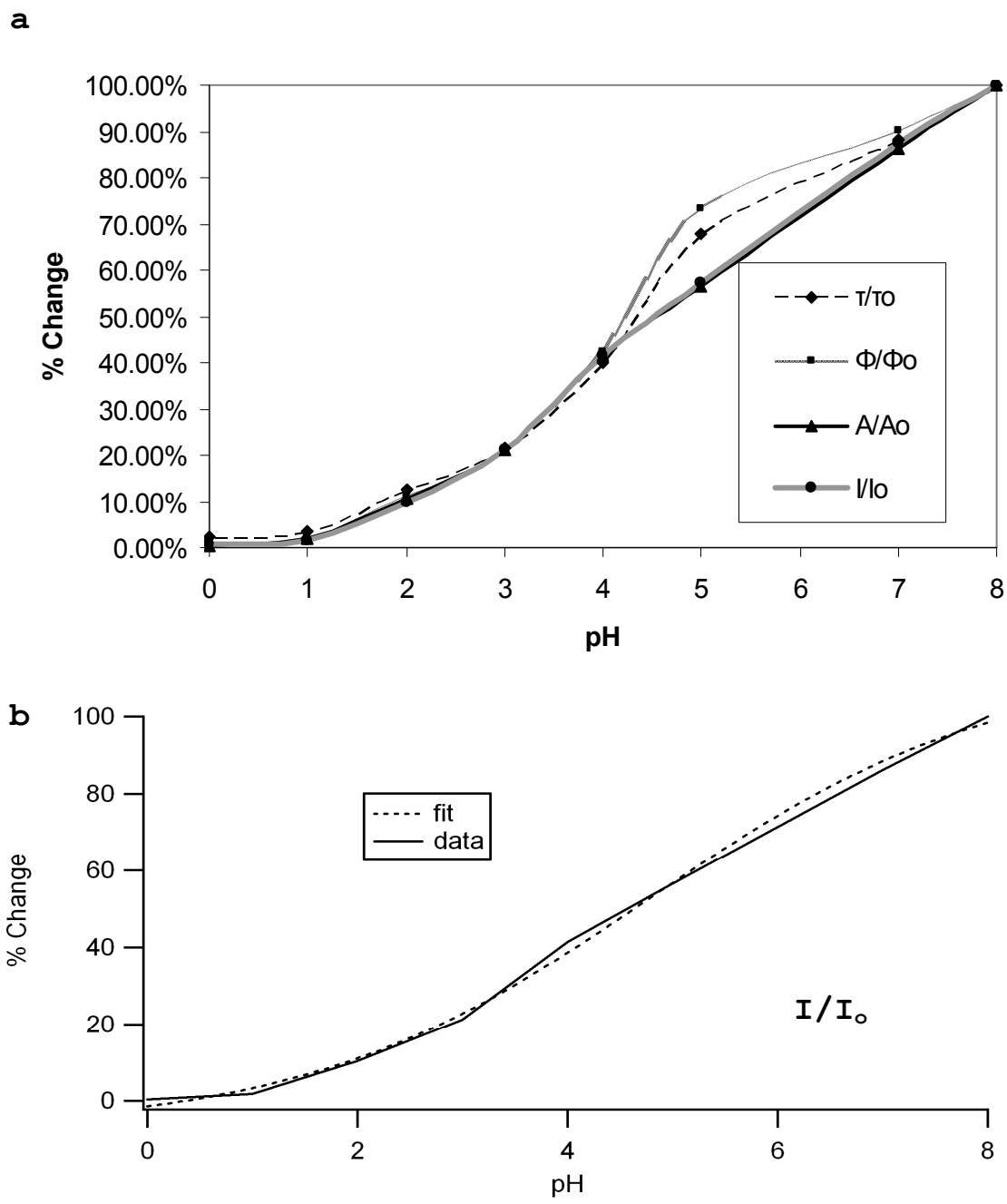

Figure 28. pH titration plot (sigmoid) of 10^{-5} M $[(bpy)_2Ru(dpp)]^{2+}$: (a) τ/τ_o are lifetime ratios, Φ/Φ_o are the total integrated area under the time-dependent curve, A/A_o are the areas under the steady-state emission, and I/I_o the intensities at maximum wavelength; (b) fit for I/I_o.

Table 7. Comparison of inflection points derived from analysis of the emission pH titration of $[(bpy)_2Ru(dpp)]^{2+}$.

Parameter	***p*K*$_a$ (inflection point)**
Lifetime data (τ/τ_o)	4.4 ± .1
Dynamic quantum yield (Φ/Φ_o)	4.2 ± .1
Steady state quantum yield (A/A_o)	4.8 ± .2
Intensity at wavelength max (I/I_o)	4.7 ± .2

The absorption spectra of $[(bpy)_2Ru(dpp)]^{2+}$ going towards very high (sulfuric) acid concentrations is shown in Figure 29a. At Hammett acidity values below -5.00, there is a marked color change in the solution, from light orange to violet. Concurrently, there is a reduction in the 422 nm and 490 nm MLCT transitions, replaced by transitions at 436 nm with an extinction coefficient of 1686 $L \cdot mol^{-1} \cdot cm^{-1}$, and relatively more prominent band at 573 nm, with an extinction coefficient of 1816 $L \cdot mol^{-1} \cdot cm^{-1}$. Presumably the complex is becoming diprotonated. The absorption spectrum alone of $[(bpy)_2Ru(dppH_2)]^{4+}$ is shown in Figure 30a. The low energy band can be fit to two Gaussians, shown in Figure 30b. The new maxima are 520 nm and 580 nm. The ratio of their FWHM values, in cm^{-1} are also 2.17:1, similar to the MLCT absorptions in the unprotonated complex. This suggests that the two MLCT transitions, to bpy and dpp, have red-shifted under this band.

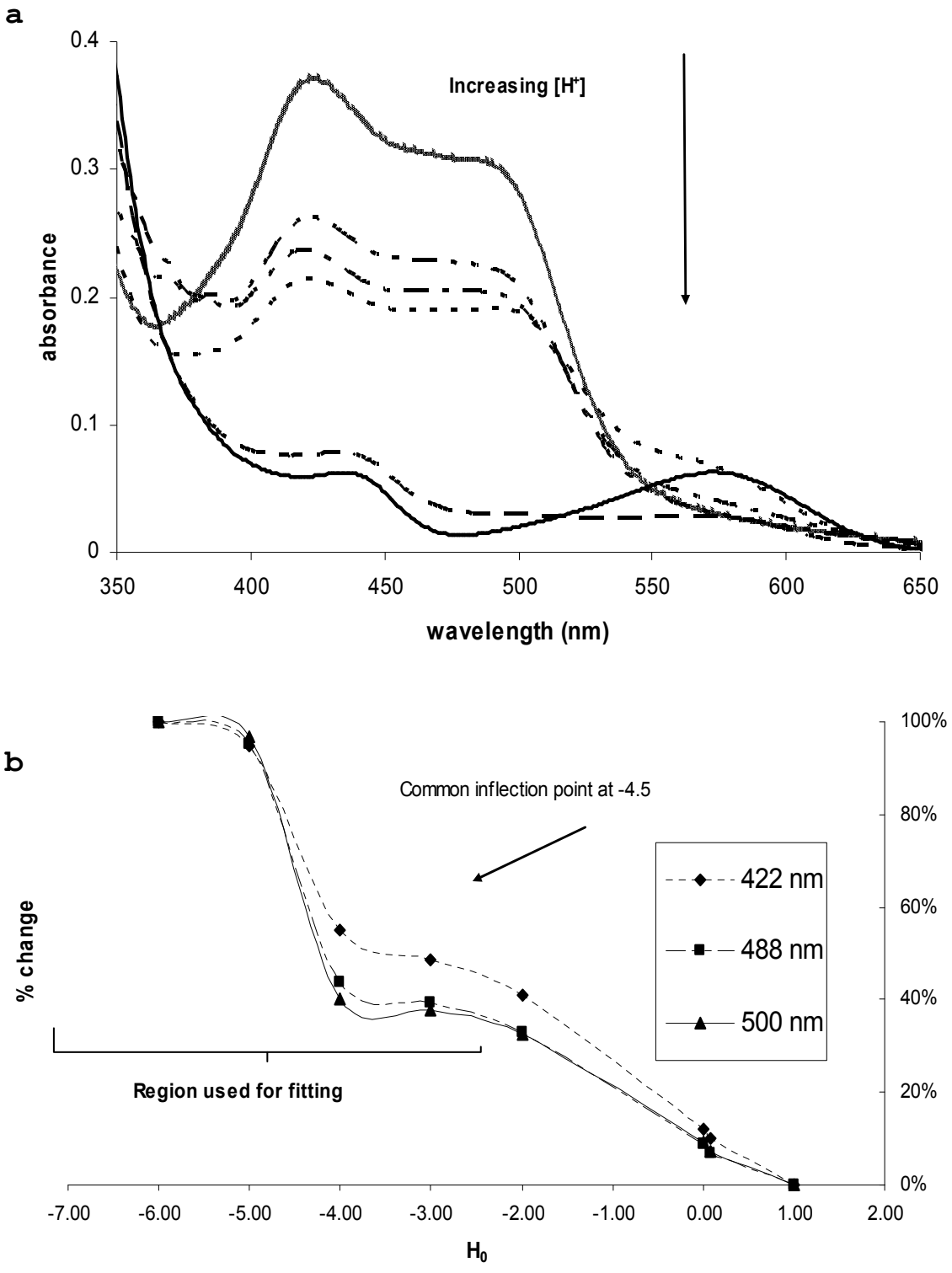

Figure 29. High acid pH titration of $[(bpy)_2Ru(dpp)]^{2+}$: (a) spectra; (b) plots of change in absorbance to obtain pK_a from inflection points.

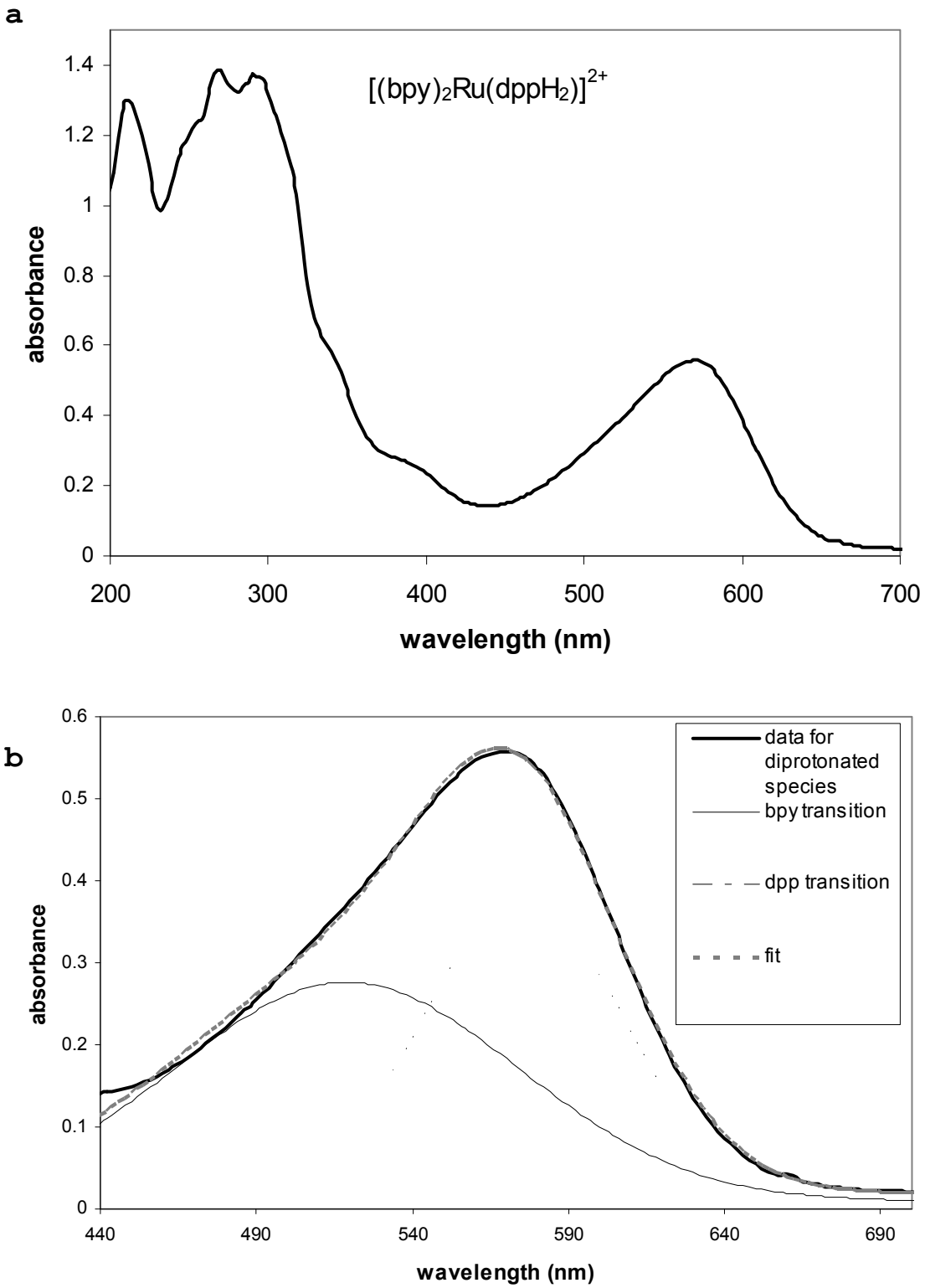

Figure 30. Absorption spectrum of $[(bpy)_2Ru(dppH_2)]^{4+}$: (a) spectrum; (b) Gaussian fits of $[(bpy)_2Ru(dppH_2)]^{4+}$ MLCT.

It is possible to estimate the pK_a for protonation from the inflection of the titration curve. Figure 29b shows the change in absorbance at three different wavelengths, 420 nm, 488 nm, and 500 nm. Again, using IGOR and fitting the high acid concentration portion to a sigmoidal equation (87), the inflection point at each curve agree to an average value of -4.50 ± .07. The suspected previous inflection point implied at higher H_o is most likely a leftover of the titration curve resulting from the first protonation (*vide infra*).

3.C.2. NMR of $[(bpy)_2Ru(dppH)]^{2+}$

The titration with acid led to several shifting peaks in the NMR spectra (Figure 31). Specifically, downfield shifts are observed with protons B3′, C3″, C4″, C5″, and C6″. The primary changes involve protons on the free pyridyl dpp ligand. One proton on the coordinated pyridine ligand, B3′, is also affected. Because of its sensitivity to structural change, NMR has been routinely used to probe equilibrium constants for association.[140-146] Similar to the theoretical basis for calculating equilibrium constants from UV-VIS data,[137] the equilibrium constant can be extracted from various linear plots of change vs. concentration. Assuming a single protonation step, the acid

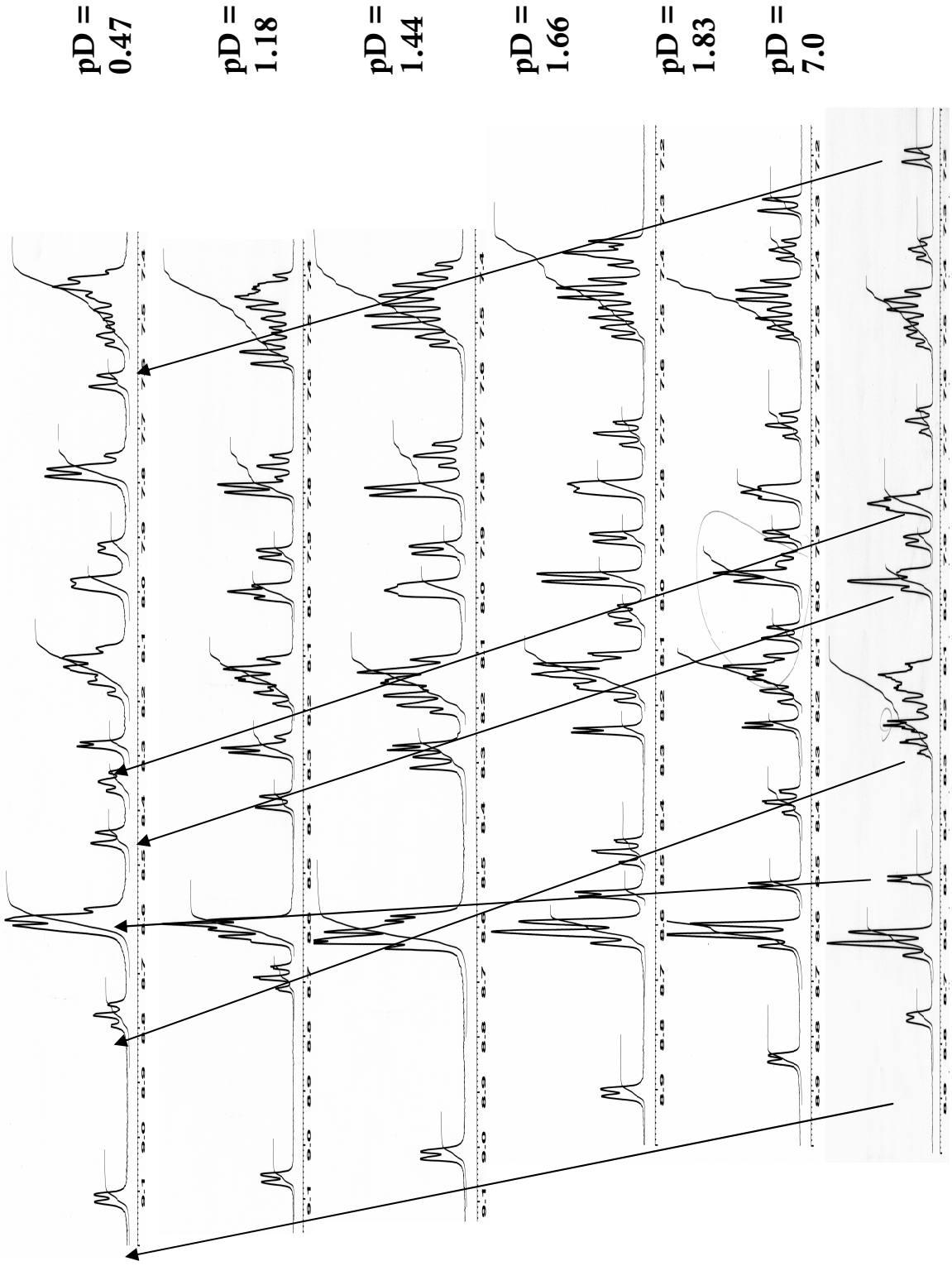

Figure 31. NMR spectra of pD titration of $[(bpy)_2Ru(dpp)]^{2+}$.

dissociation constant, K_a, is probed for the reaction:

$$[(bpy)_2Ru(dppH)]^{3+} \leftrightarrow [(bpy)_2Ru(dpp)]^{2+} + [H^+] \qquad (88)$$

where

$$K_a = \frac{\{[(bpy)_2Ru(dpp)]^{2+}\}\{[H]^+\}}{\{[(bpy)_2Ru(dpp)]^{2+}\}} \quad . \qquad (89)$$

For NMR, an equation can be derived (Appendix 2) that gives the change in chemical shift, $\Delta\delta$, as a function of *initial* reactant concentrations[xxv]

$$\Delta\delta_{observed} = \left[\left(\delta_{bound} - \delta_{free}\right)\right] * \frac{1}{2\left[H^+\right]_o} * \left[\left(\left[H^+\right]_o + [Ru]_o + K_a\right) - \sqrt{\left(\left[H^+\right]_o + [Ru]_o + K_a\right)^2 - 4[Ru]_o\left[H^+\right]_o}\right] \qquad (90)$$

where δ_{free} is the initial chemical shift, and $[M]_o$ and $[H^+]_o$ are the initial metal and proton concentrations. The observed change is plotted *vs.* initial proton concentration (negative inverse log of pH), and the data fit to equation (90) using non-linear least-squares regression to two parameters, K_a and δ_{bound}, the chemical shift at 100% protonation. The two-parameter fit is preferred over linear

---

[xxv] With a probe on the actual product concentrations, the equation is much simpler.

plots since it is inherently more sensitive to slight variations in the data and will yield better values of K_a. The fits to equation (90) of the chemical shift data for the four free pyridyl protons are shown in Figure (32). The pK_a and δ_{bound} values are tabulated below (Table 8).

Table 8. pK_a and δ_{bound} values from fits of NMR data.

Proton	δ_{free} (observed)	δ_{bound} (calculated)	pK_a (calculated)
B3′	7.17	7.68	1.515
C3″	7.97	7.84	1.491
C4″	8.27	8.86	1.522
C5″	7.82	8.44	1.512
C6″	8.76	9.18	1.563

The average pK_a is 1.52 ± .03. A plot of chemical shift vs. pD (pH) for these five shifting peaks, yields a common inflection point at 1.52 showing virtual agreement on the pK_a value for the protonation (Figure 33).

3.D. Multiple Emissions from $[(bpy)_2Ru(dpp)]^{2+}$

As previously mentioned, at pH 1, another emission at higher energy becomes evident coupled with the red-shifted emission. It becomes more prominent at pH 0. The emission is broad with a maximum around 620 nm. The relative intensities of the two simultaneous emissions, at 620 nm and at 735 nm are responsive to the excitation wavelength:

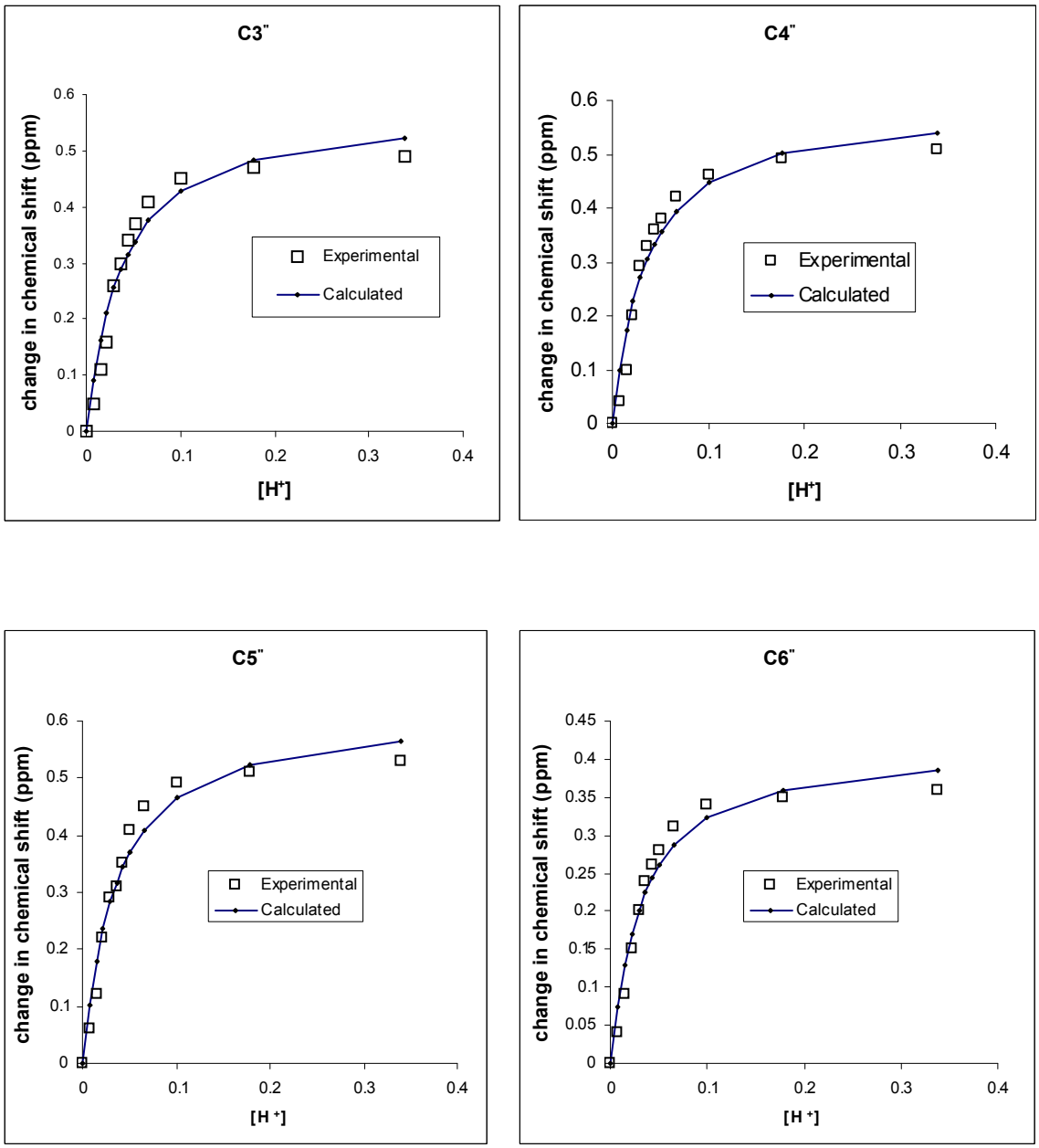

Figure 32. Fits of NMR spectra of pD titration of $[(bpy)_2Ru(dpp)]^{2+}$.

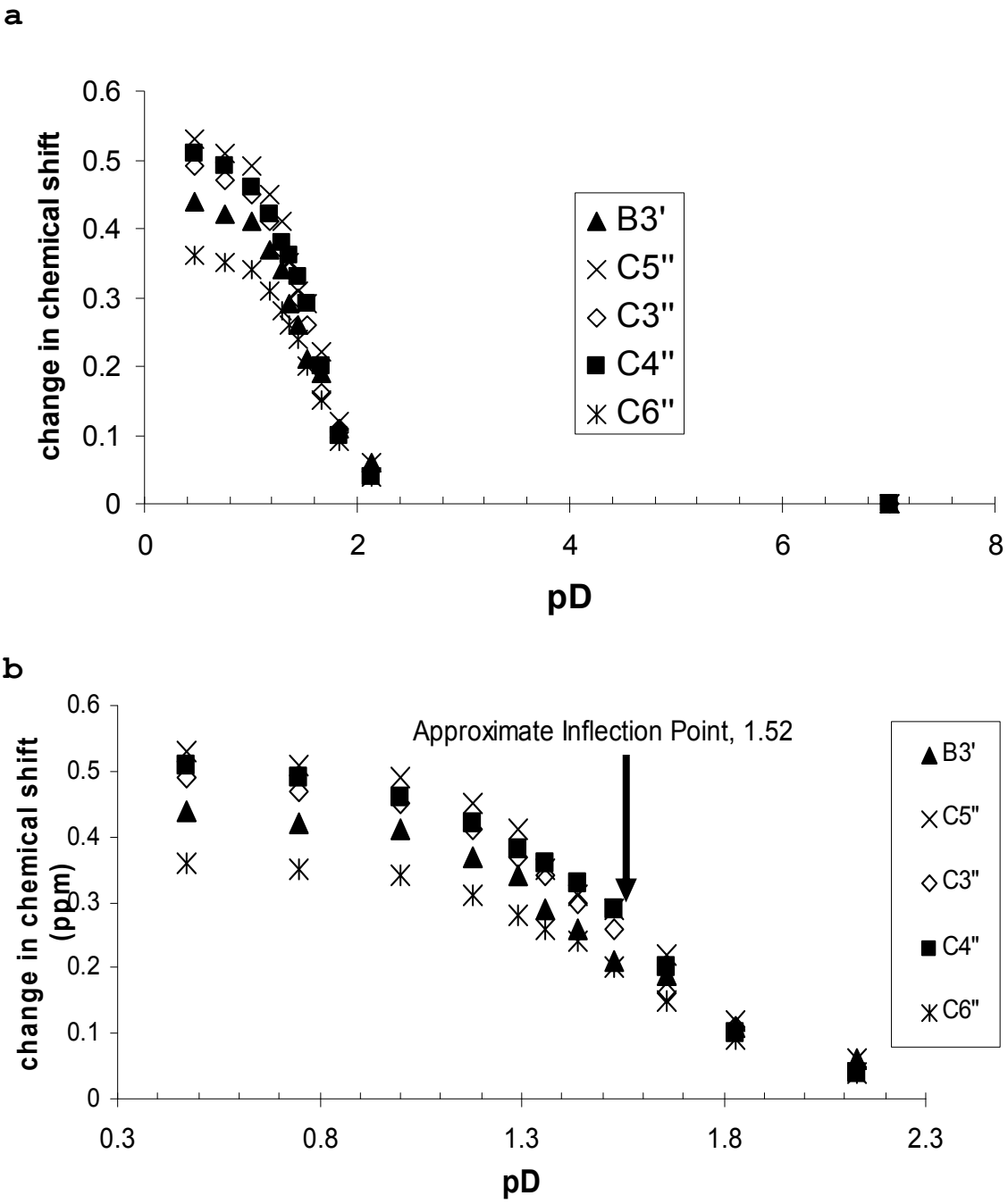

Figure 33. Sigmoidal plots of NMR pD titration of $[(bpy)_2Ru(dpp)]^{2+}$: (a) full range; (b) at inflection point.

at lower excitations wavelengths, such as 458 nm, the 620 nm is enhanced relative to the 735 nm. Going to longer wavelength, such as 514 nm, the 735 nm emission is enhanced relative to the 620 nm. This effect is demonstrated in Figure 34a. Standing out in all three emissions is the Raman scattering band due to water. The spectra are shown without subtracting the blank. The band is expected to be red-shifted 3382 cm^{-1} to the excitation,[148] and the energy difference, taken from the peak of the bands is in this vicinity (Table 9).[xxvi]

Table 9. Raman scattering band from excitation wavelengths of the Argon ion laser.

Excitation (nm)	Wavelength max of Raman band (nm)	Energy difference (cm^{-1})
458	544	3452
488	570	2948
514	626	3481

The intensity of the Raman band is not always matched between sample and blank, since it is expected to be attenuated in the sample. Therefore, subtracted the blank often leads to negative dips in the resulting spectrum at the wavelengths of the Raman band. One way to observe the

[xxvi]The Raman scattering band also appears in most time-resolved spectrum at about 645 nm to the red of the 532 nm excitation. However, since spectra are analyzed beginning at a time point when the pulse has passed, it does not interfere with analysis.

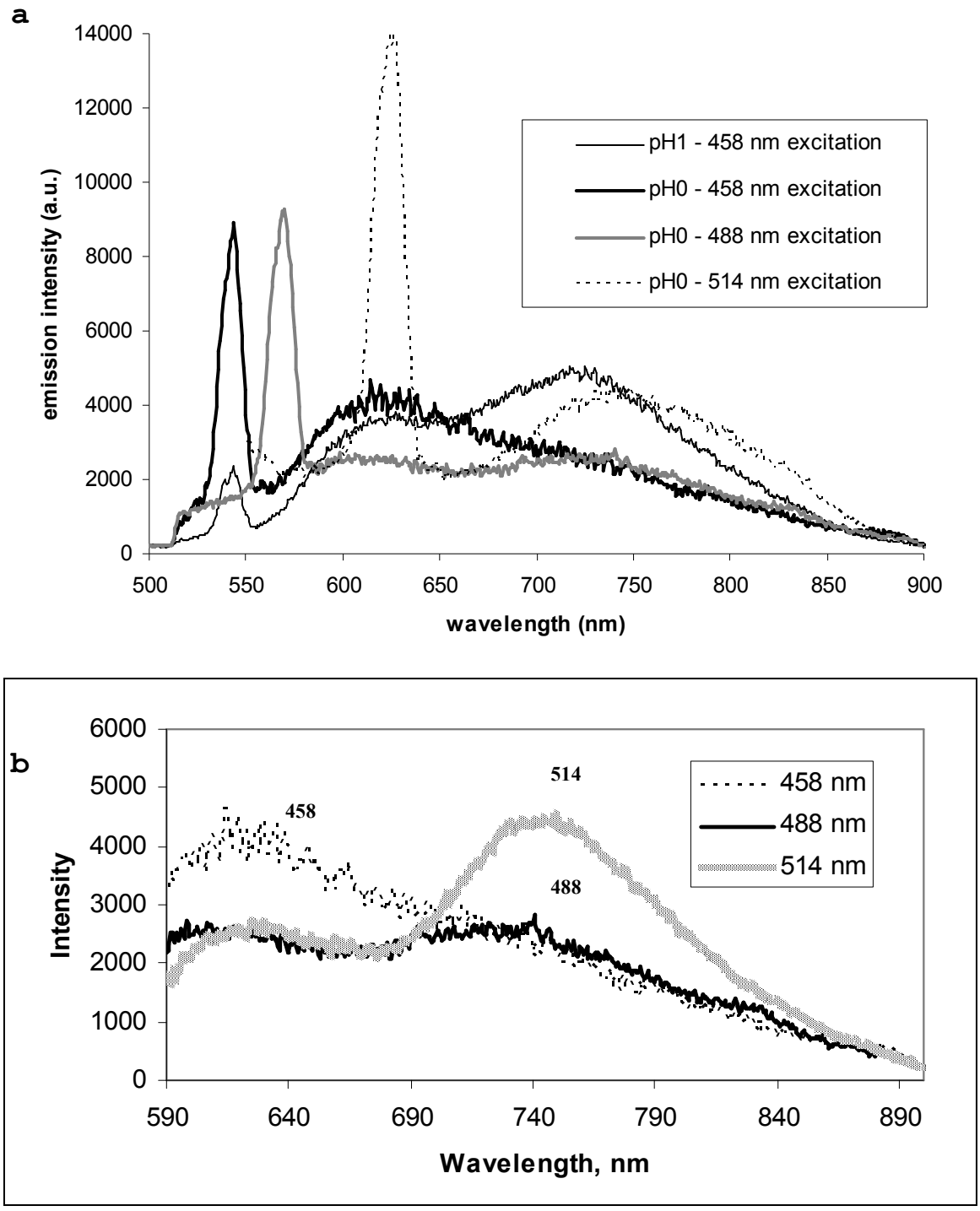

Figure 34. High acid concentration pH titration of $[(bpy)_2Ru(dpp)]^{2+}$: (a) with Raman water bands; (b) without Raman water bands.

two emissions unadulterated by the Raman band is to fit a "clean" template of an emission to the data. An emission from $[(bpy)_2Ru(dpp)]^{2+}$ works well and can be used to resolve the bands and remove the Raman band while maintaining the essential features of the spectrum. Examples are shown in Figure 35. The "cleaned-up" spectra are shown in Figure 34b.

3.E. Association $[(bpy)_2Ru(dpp)]^{2+}$ with Various Metal Cations

It can be quite informative to compare the fitting of the time-resolved data to a single exponential decay equation, of the form

$$y = y_o + Ae^{-t/\tau} , \tag{91}$$

and a double exponential decay equation, of the form

$$y = y_o + A_1e^{-t/\tau_1} + A_2e^{-t/\tau_2} , \tag{92}$$

where y_o is the y-intercept, or signal baseline, A, A_1, *and* A_2 are the pre-exponential factors at a given wavelength, and τ_1 and τ_2 are the accompanying lifetimes. It is critical to once again note that the pre-exponential factor weights the emission intensity at any given wavelength, and ideally, matches the corresponding absorption to that

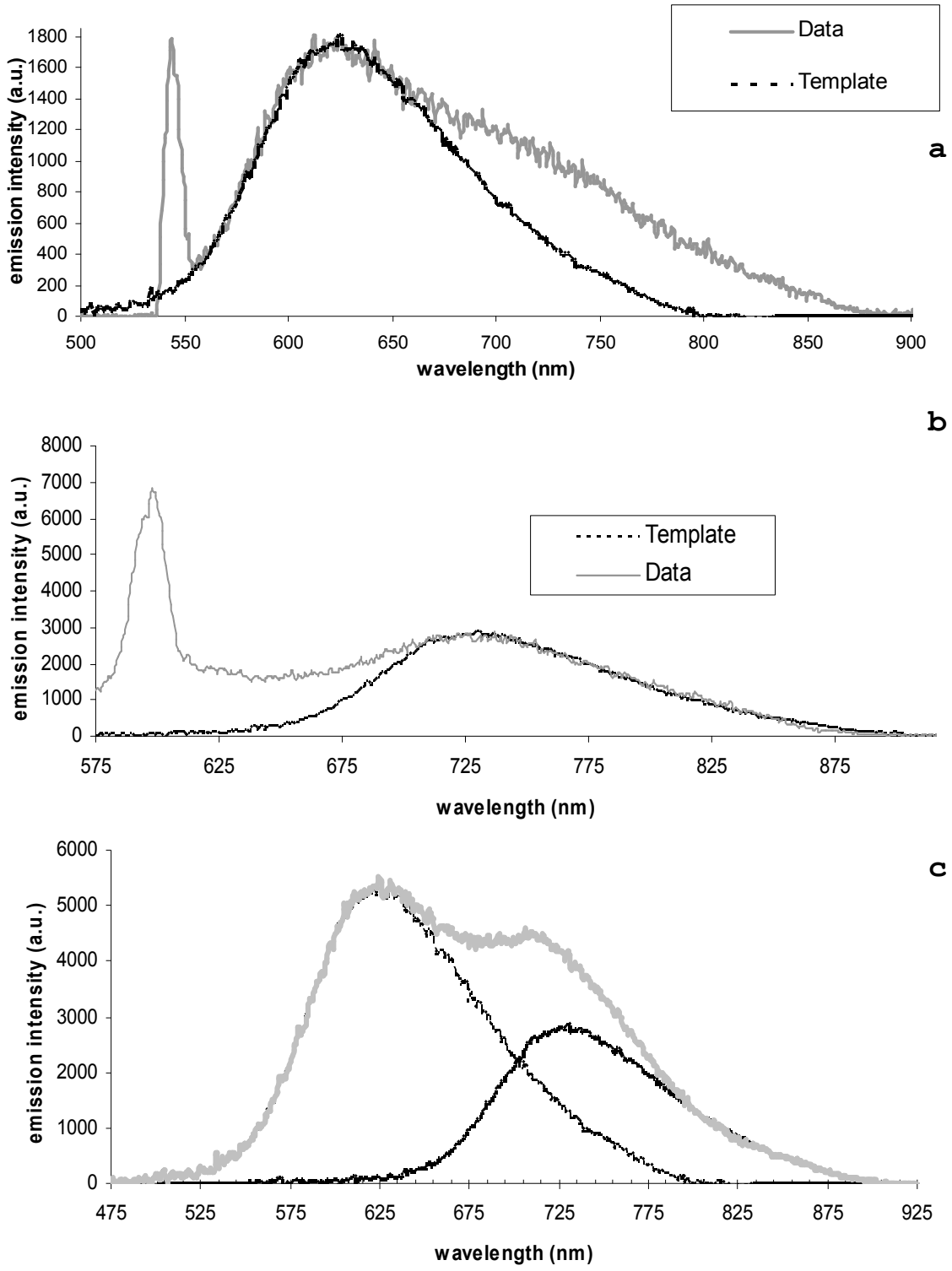

Figure 35. Use of templates to clear water Raman band in high acid concentration pH titration of $[(bpy)_2Ru(dpp)]^{2+}$: (a) high energy transition; (b) low energy transition; (c) fits.

particular emitting state. For an emissive species with one lifetime, plotting the set of *A* values *vs.* wavelength will give the emission profile of that emitting species, and will usually match that from the steady-state assuming no time-dependent interactions. In the case of two simultaneous emissions with distinctly different lifetimes, when the emitters have no time-dependent interactions, fitting to (92) at *every* wavelength should yield two different, *invariant* lifetimes, τ_1 and τ_2, and two *sets* of pre-exponential factors, A_1 and A_2 at every wavelength. A plot of the sets A_1 and A_2 *vs.* wavelength will give the "emission spectrum" of each emitting species. In essence, the analysis uses time-resolved data to "resolve" the spectrum that is a composite from more than one emitting species. If, however, those emitting species are interacting, τ_1 and τ_2 do not automatically correspond to the lifetimes of each species, but are designated m_1 and m_2 according to the differential equations (43)-(46) which describes the time-dependency of interacting emitting species. Instead, m_1 approaches τ_1 for higher concentrations of species 1, and m_2 approaches k_{de}, the rate constant for deactivation at higher concentrations of species 2. The ability of the analysis to distinguish emission profiles and lifetimes are close is highly

dependent on the signal to noise ratio. Hence, lifetime data, in cases of double exponential fits, are reported to one standard deviation as a method of judging whether the lifetimes are distinct.

The interactions of $[(bpy)_2Ru(dpp)]^{2+}$ with various metal cations in both the ground and excited state were examined. Starting with 6M $Ca(NO_3)_2$, very small changes are seen in the absorbance and emission spectra (Figure 36), both shifting every so slightly to the red. Fitting the time-resolved data to single and double exponential decays yielded similar results. The plot of *A vs.* wavelength from time-resolved fits is slightly red-shifted compared to the steady-state spectrum (Figure 36b). Even so, the presence of only one emission is implied. The lifetime of 125 ± 9 ns over the range from 650 nm – 850 nm is invariant and matches that of $[(bpy)_2Ru(dpp)]^{2+}$ in water.

The results for $[(bpy)_2Ru(dpp)]^{2+}$ in 3M $Fe(NO_3)_3$ and 3M $Al(NO_3)_3$ are shown in Figure 37. The absorption spectrum for the former is truncated at 410 nm due to absorption from the ferric ion at shorter wavelengths. The spectra for $[(bpy)_2Ru(dppH)]^{3+}$ are included for comparison. Both sets show shifts to the red in all spectra beyond that seen for Ca^{2+}. Also in both cases, the emission intensity is significantly reduced, by a factor of about 23 for

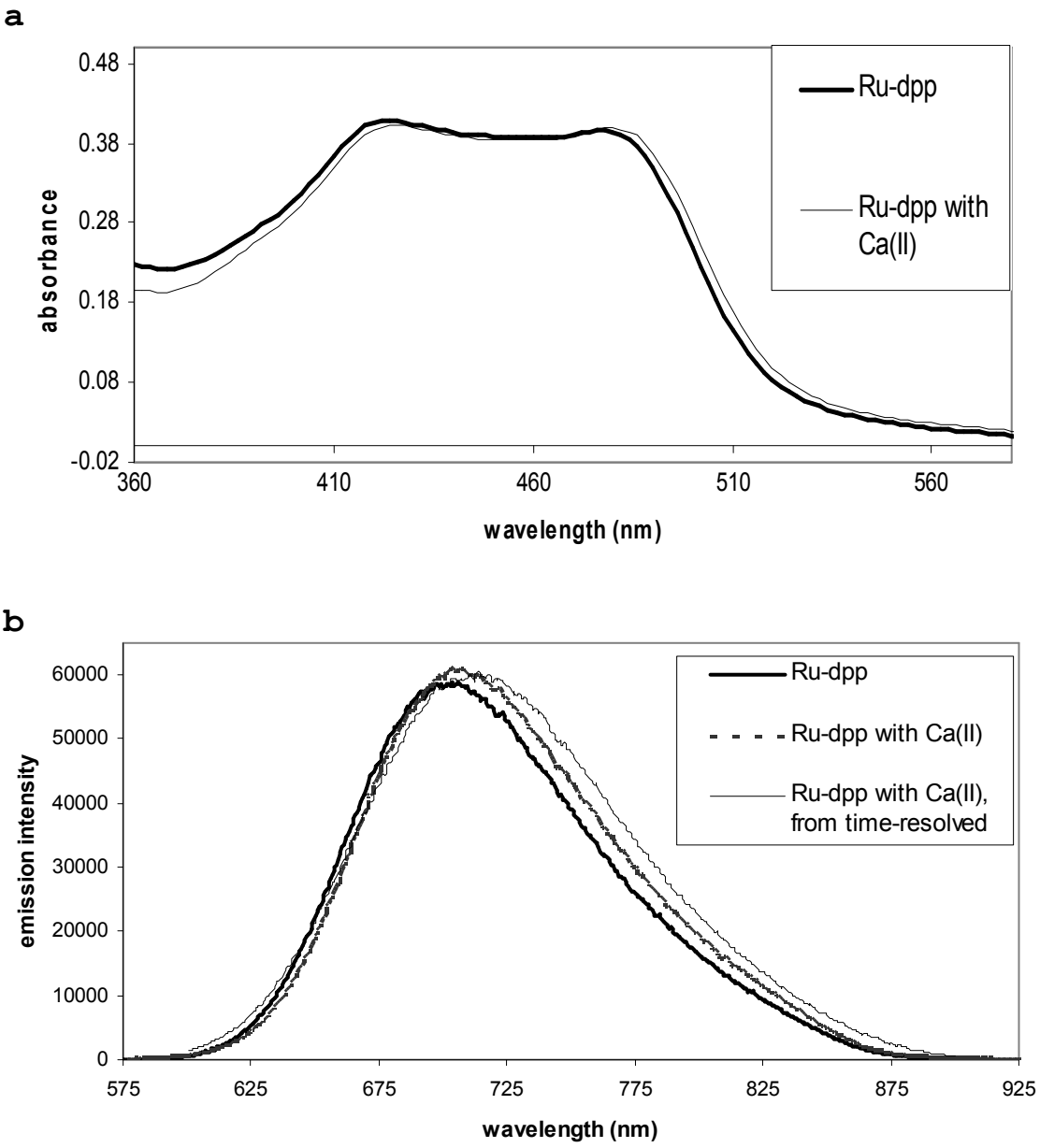

Figure 36. Electronic spectra of 2.5 x 10^{-5} M $[(bpy)_2Ru(dpp)]^{2+}$ with 3 M Ca^{2+}: (a) absorption spectrum; (b) emission spectra.

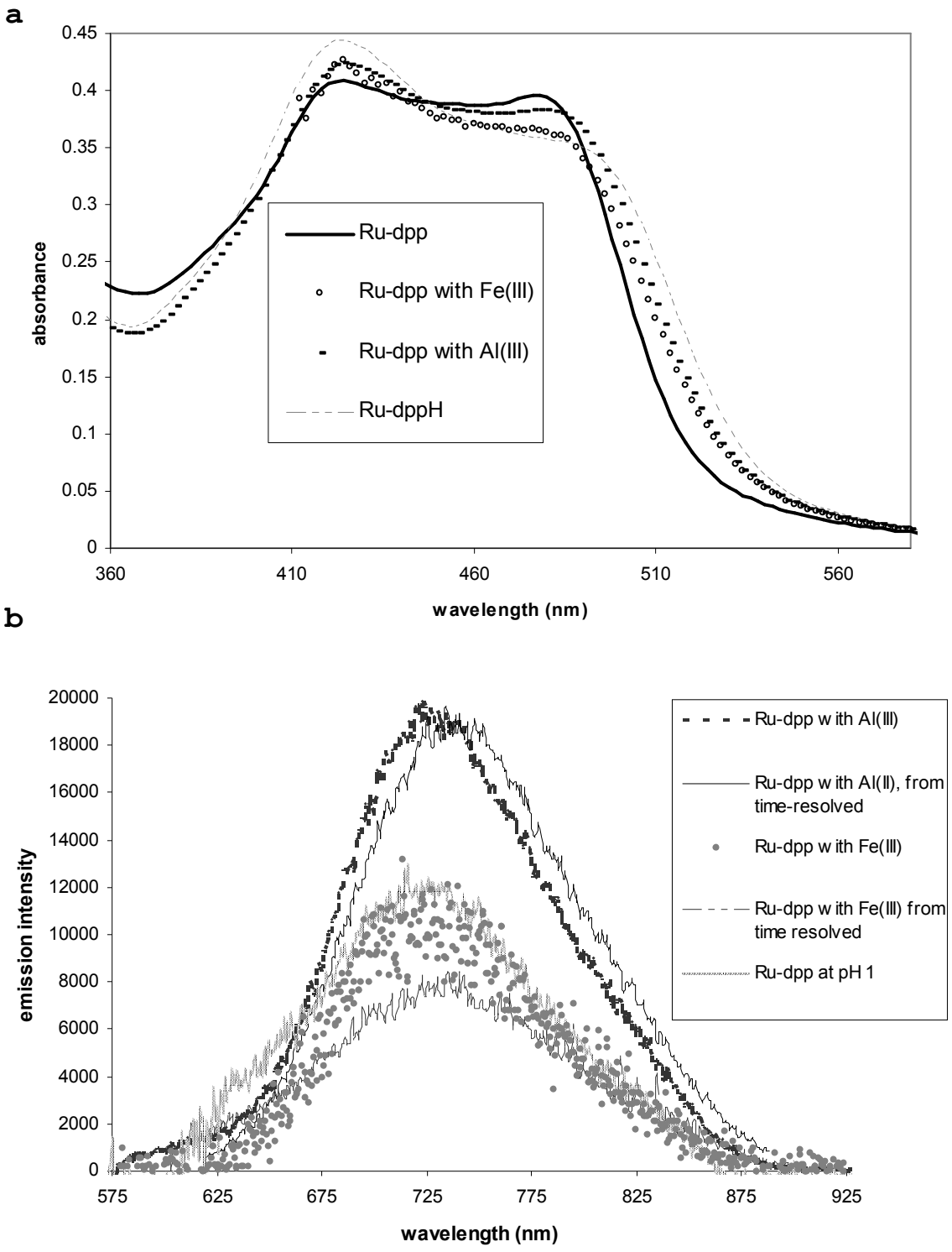

Figure 37. Electronic spectra of 2.5 x 10^{-5} M $[(bpy)_2Ru(dpp)]^{2+}$ with 3 M Fe^{3+} and 3 M Al^{3+}: (a) absorption spectra; (b) emission spectra, both from steady state and time resolved data.

interaction with Al^{3+} and 390 for Fe^{3+}. Single and double exponential fits for the time-resolved data yielded lifetimes within one standard deviation of each other, and plots of A_1 and A_2 *vs.* wavelength were indistinguishable. Single exponential fits to data at each wavelength yielded an invariant lifetime of 16.3 ± 2.0 ns with emission maxima at 726 nm (steady-state) and 735 nm (time-resolved) for $[(bpy)_2Ru(dpp)]^{2+}$ with Al^{3+}. Single exponential fits for $[(bpy)_2Ru(dpp)]^{2+}$ with Fe^{3+} yielded an invariant lifetime of 8.3 ± 3.4 ns with emission maxima at 726 nm (steady-state) and 731 nm (time-resolved).

The results of $[(bpy)_2Ru(dpp)]^{2+}$ with 0.03M $Cr(NO_3)_3$ are shown in Figure 38. Because $[Cr(OH_2)_6]^{3+}$ absorbs strongly in the 400-600 nm region (Figure 38b), the absorption spectrum of $[(bpy)_2Ru(dpp)]^{2+}$ is completely obscured. However, the emission spectrum is clear, though the intensity is reduced significantly, by a factor of about 7.5. Single exponential fits gave similar results to double exponential fits and thus were sufficient. Stunningly, at just 0.03M $[Cr^{3+}]$, the invariant lifetime over the range of emission wavelengths was 37.6 ± 1.5 ns. Compared to similar concentrations of $[(bpy)_2Ru(dpp)]^{2+}$ in water, the overall emission intensity was markedly reduced

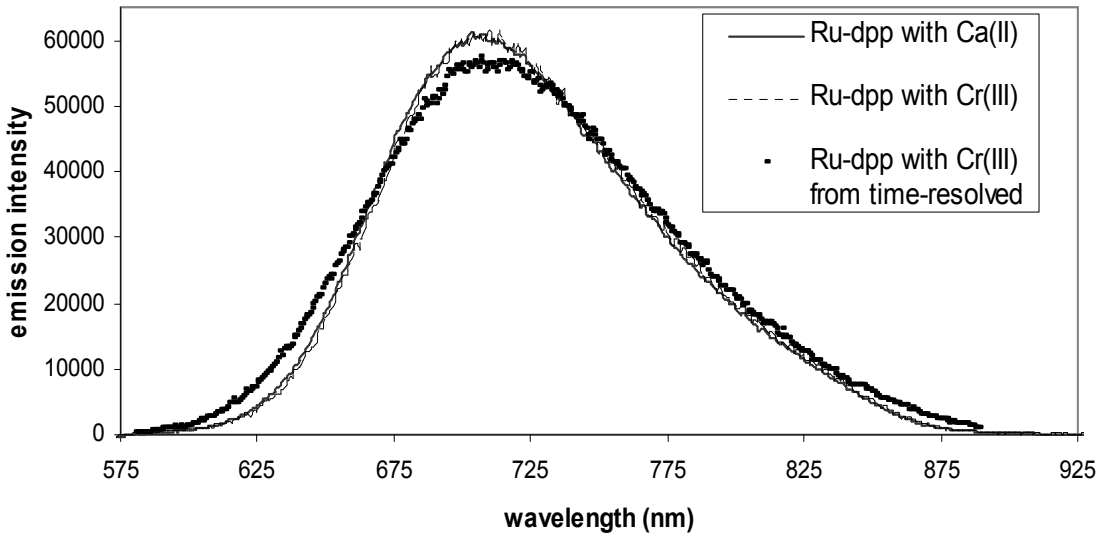

Figure 38. Emission spectrum of $[(bpy)_2Ru(dpp)]^{2+}$ with Cr^{3+}.

as well, but no significant shift in the emission spectrum is observed when compared to $[(bpy)_2Ru(dpp)]^{2+}$ with Ca^{2+}.

The absorption spectra results for $[(bpy)_2Ru(dpp)]^{2+}$ in 1.2 M $Pb(NO_3)_2$ and 3 M $SnCl_2$ are shown in Figure 39. The absorption spectra of $[(bpy)_2Ru(dpp)]^{2+}$ with Ca^{2+} and Pb^{2+} are remarkably similar, with the latter showing a very slight red-shift around 524 nm. Gaussian fits of the MLCT bands (Figure 40a) have two maxima at 424 nm and 484 nm. The absorption spectrum of $[(bpy)_2Ru(dpp)]^{2+}$ with Sn^{2+} is more similar to that of $[(bpy)_2Ru(dppH)]^{3+}$ as far as the higher energy MLCT goes, but red-shifted at the low energy MLCT. Gaussian fits of the MLCT bands (Figure 40b) also have two maxima at 418 nm and 486 nm.

The emission spectra for $[(bpy)_2Ru(dpp)]^{2+}$ with Pb^{2+} is shown in Figure 41. The steady-state emission intensity is reduced by a factor of 118 compared to $[(bpy)_2Ru(dpp)]^{2+}$ with Ca^{2+}. The time-resolved data necessitated fitting to double exponential fits. The plots of the pre-exponential values, A_1 and A_2 *vs.* wavelength reveal the presence of two emissions, with, respectively, maxima at 743 nm and 772 nm (obtained from the Gaussian fits), and averages lifetimes over the range 650nm – 850nm of 57 ± 13 ns and 20 ± 9 ns (one standard deviation). At two standard deviations the lifetimes would potentially converge. The lifetimes appear

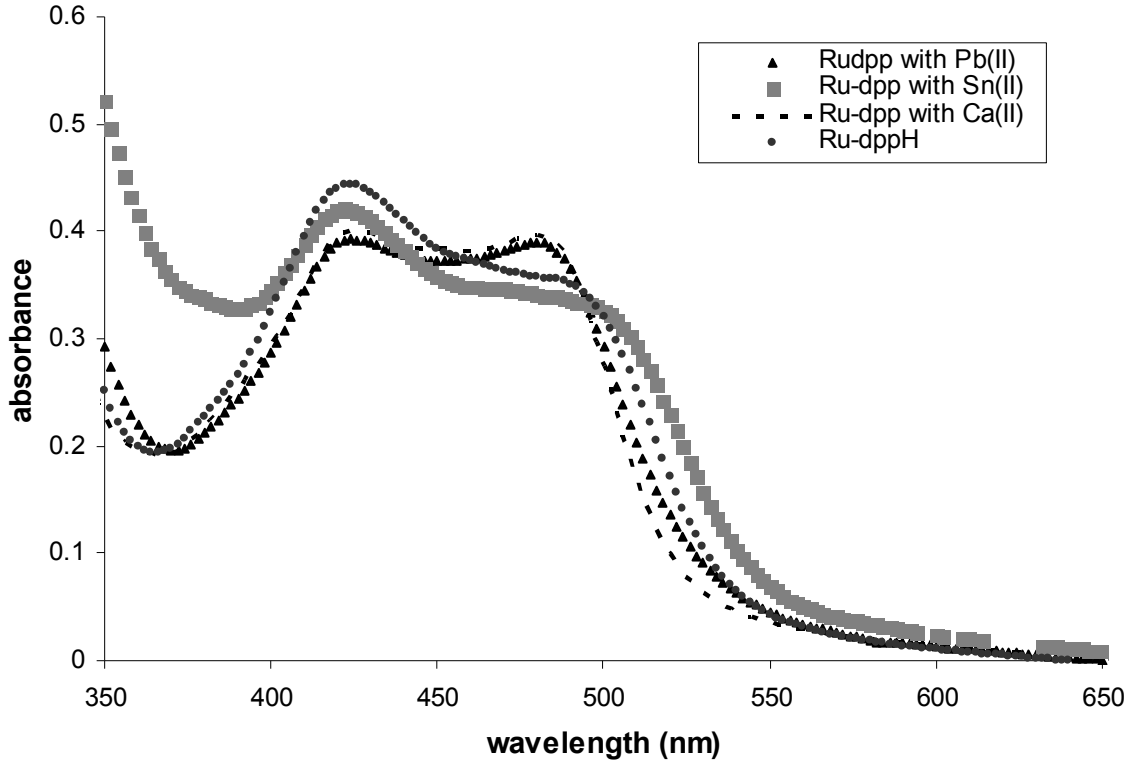

Figure 39. Absorption spectra of 2.5 x 10^{-5} M $[(bpy)_2Ru(dpp)]^{2+}$ with 1.2 M Pb^{2+} & 3 M Sn^{2+}.

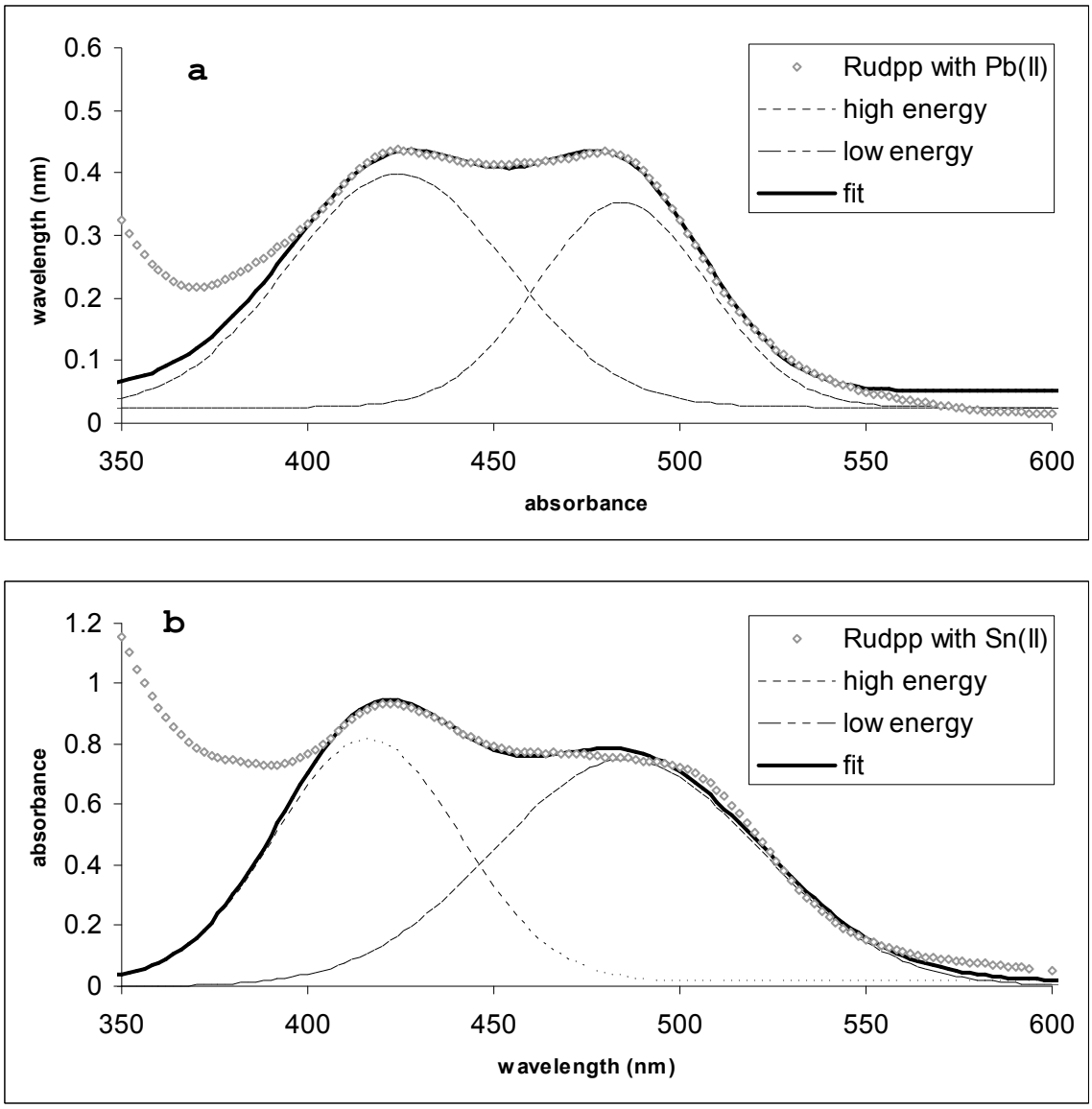

Figure 40. Fits of absorption spectra of $[(bpy)_2Ru(dpp)]^{2+}$ with Pb^{2+} & Sn^{2+}: (a) Pb^{2+}; (b) Sn^{2+}.

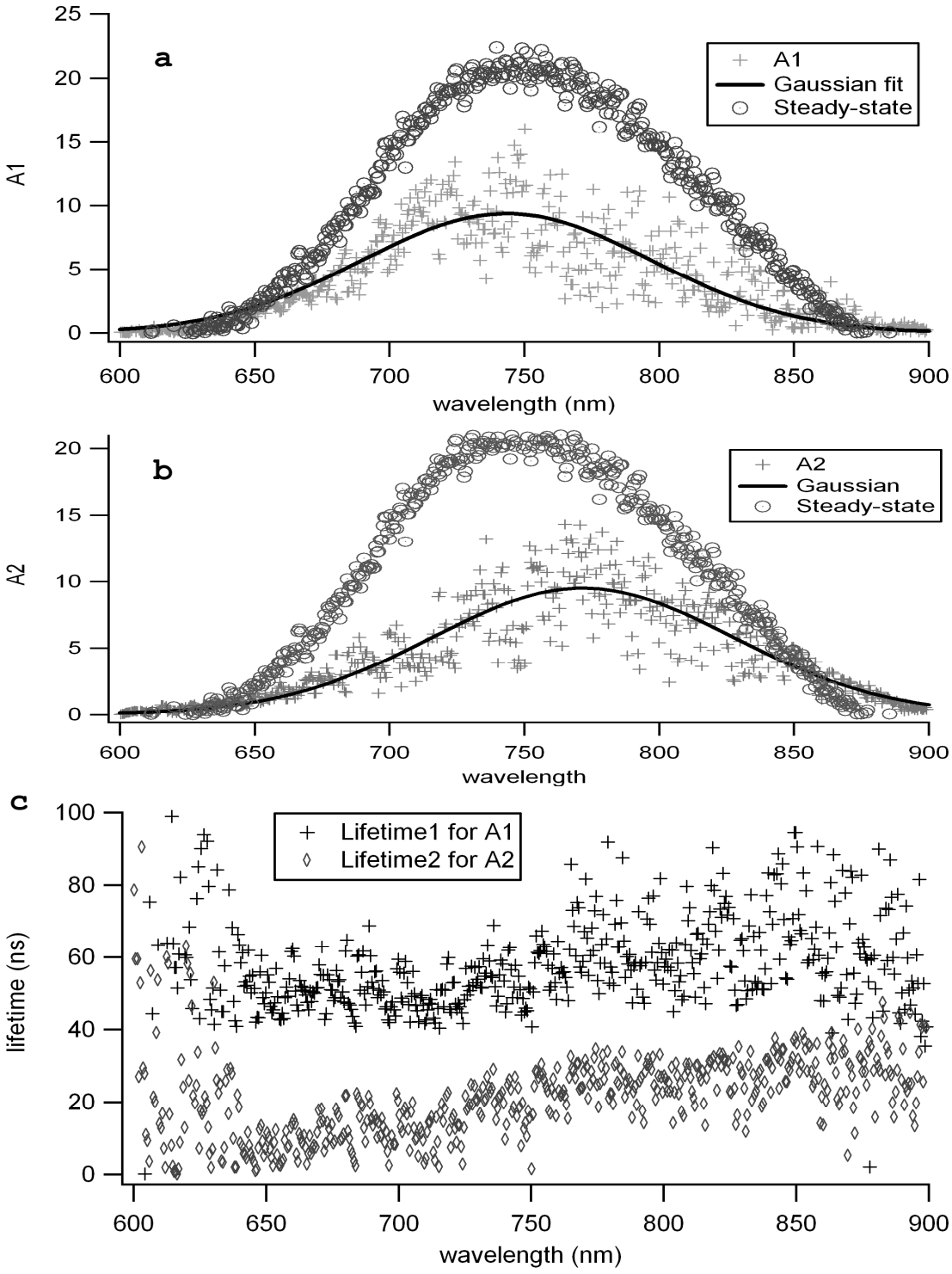

Figure 41. Emission spectra, fits, and lifetimes of 2.5 x 10^{-5} M $[(bpy)_2Ru(dpp)]^{2+}$ with 1.2 M Pb^{2+}: (a) Gaussian fit of A_1 data from double exponential fit; (b) Gaussian fit of A_2 data; (c) lifetimes.

to have minor wavelength dependencies, being shorter at shorter wavelengths (Figure 41c). This seems especially true of the shorter lifetime species (A2, τ_2). Interestingly though, when a double Gaussian fit is performed on the steady-state spectrum, (Figure 42a) which is broad and has both a maximum at 750 nm and what appears to be a shoulder at 810 nm, the fits under the curve have maxima instead at 740 nm and 814 nm. Figure 42b compares the steady-state emission curve to two snapshots of the time-resolved data: at maximum intensity, and 52 ns later, adjusting for the same height. The snapshots are nearly identical to the steady-state spectrum, and to each other, suggesting that if there is a separate emission with a wavelength maximum at 814 nm, its lifetime is so similar to the other emission that the double exponential fit cannot distinguish it. With data obtained at 2 ns resolution on the laser/ICCD camera system, the double exponential fit is successful in revealing two different simultaneous emissions if those emissions have different wavelength maxima and different lifetimes beyond one standard deviation. If either set of those parameters are close to each other, the fit will not distinguish the two because of inherent experimental error.

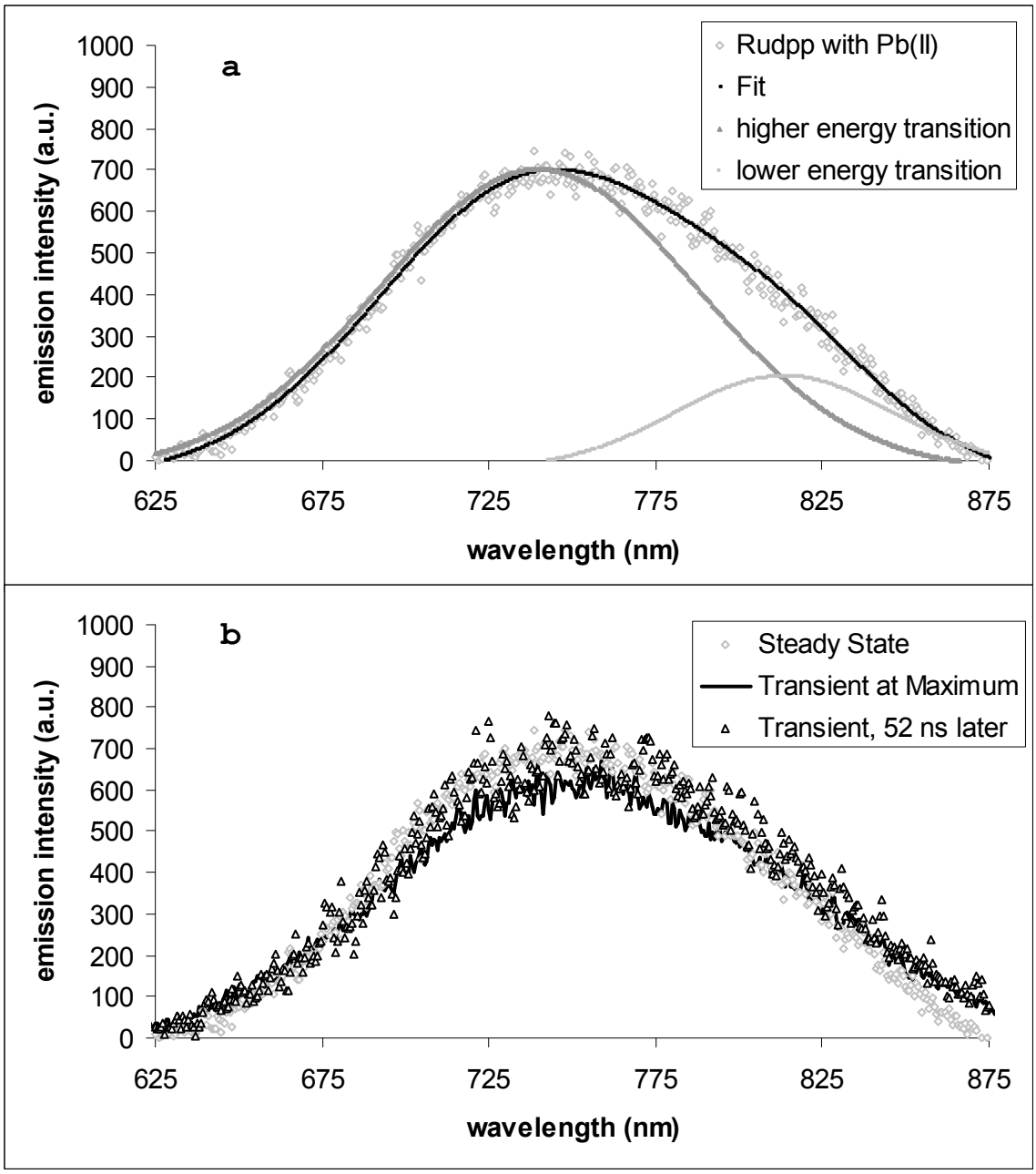

Figure 42. Gaussian fits of steady-state emission of 2.5 x 10^{-5} M $[(bpy)_2Ru(dpp)]^{2+}$ with 1.3 M Pb^{2+} and comparison to transient data: (a) steady-state emission; (b) comparison of emission data sets.

The steady-state emission is compared to that of $[(bpy)_2Ru(dpp)]^{2+}$ with Sn^{2+} in Figure 43. There is no detectable red-shift. Double exponential fits of the time-resolved data yielded only one invariant lifetime of 8.1 ± 0.5 ns, remarkably short. The steady-state emission spectrum is reduced in intensity at the wavelength maximum by a factor of about 9.

The absorption results for $[(bpy)_2Ru(dpp)]^{2+}$ in 3 M $Cd(NO_3)_2$ and 3 M $Zn(NO_3)_2$ are shown in Figure 44 along with that of the bimetallic $[(bpy)_2Ru(dpp)Ru(bpy)_2]^{4+}$. The absorption spectra are all together distinct from that of $[(bpy)_2Ru(dpp)]^{2+}$ with Ca^{2+}, and similar to each other, showing a pronounced widening and red-shifting of the lower energy MLCT transition, particularly with the bimetallic. The spectrum of $[(bpy)_2Ru(dppH)]^{3+}$ is included for comparison. Gaussian fits for Cd^{2+} (Figure 45a) have maxima at 422 nm and 491 nm, and for Zn^{2+} (Figure 45b), 421 nm and 495 nm. The steady-state emission spectra are reduced in intensity by a factor of 9.6 for $[(bpy)_2Ru(dpp)]^{2+}$ with Cd^{2+}, and 5.3 with Zn^{2+}.

The analysis of the time-resolved emission spectra of $[(bpy)_2Ru(dpp)]^{2+}$ with Cd^{2+} is shown in Figure 46. The double-exponential fit reveals two emissions with nearly the same wavelength dependency, but different average

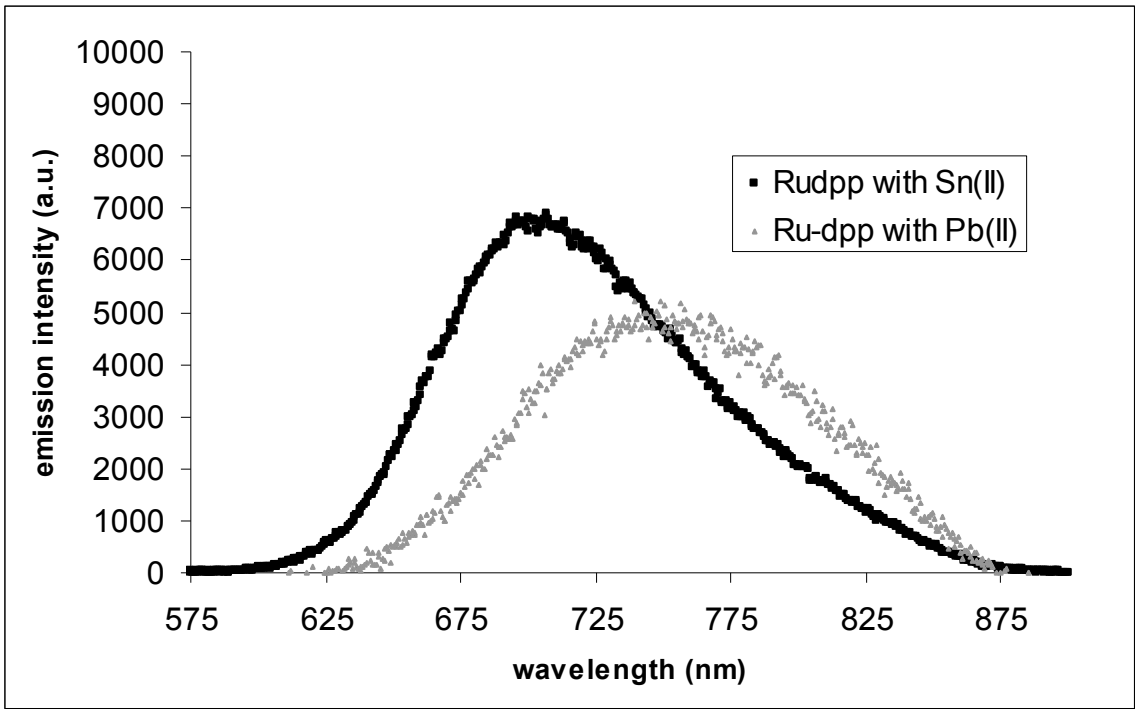

Figure 43. Steady-state emission of 2.5 x 10^{-5} M $[(bpy)_2Ru(dpp)]^{2+}$ with 1.3 M Pb^{2+} and 3 M Sn^{2+}.

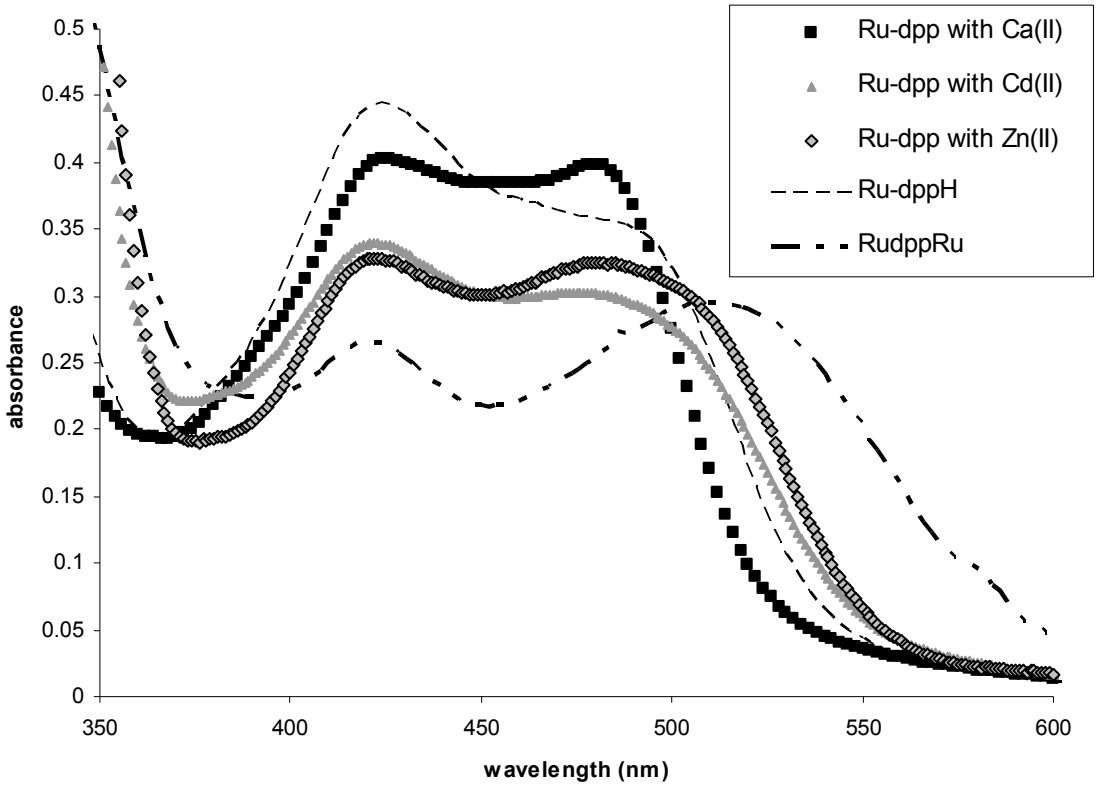

Figure 44. Absorption spectra of 2.5 x 10^{-5} M $[(bpy)_2Ru(dpp)]^{2+}$ with 3 M Cd^{2+} and 3M Zn^{2+}, and 2.5 x 10^{-5} M $[(bpy_2)Ru(dpp)Ru(bpy_2)]^{4+}$.

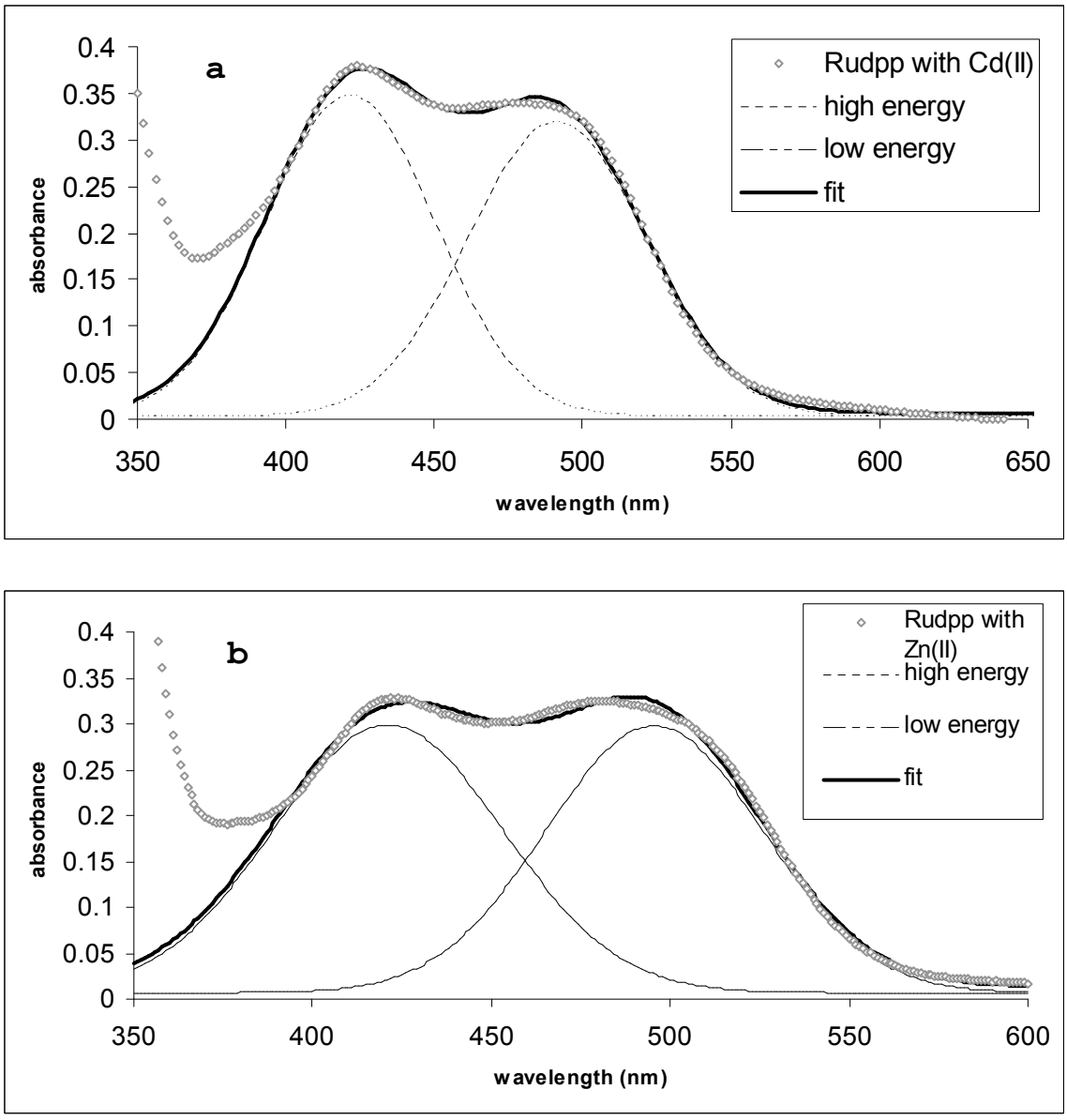

Figure 45. Gaussian fits to absorption spectra of 2.5×10^{-5} M $[(bpy)_2Ru(dpp)]^{2+}$ with 3 M Cd^{2+} and 3M Zn^{2+}: (a) Cd^{2+}; (b) Zn^{2+}.

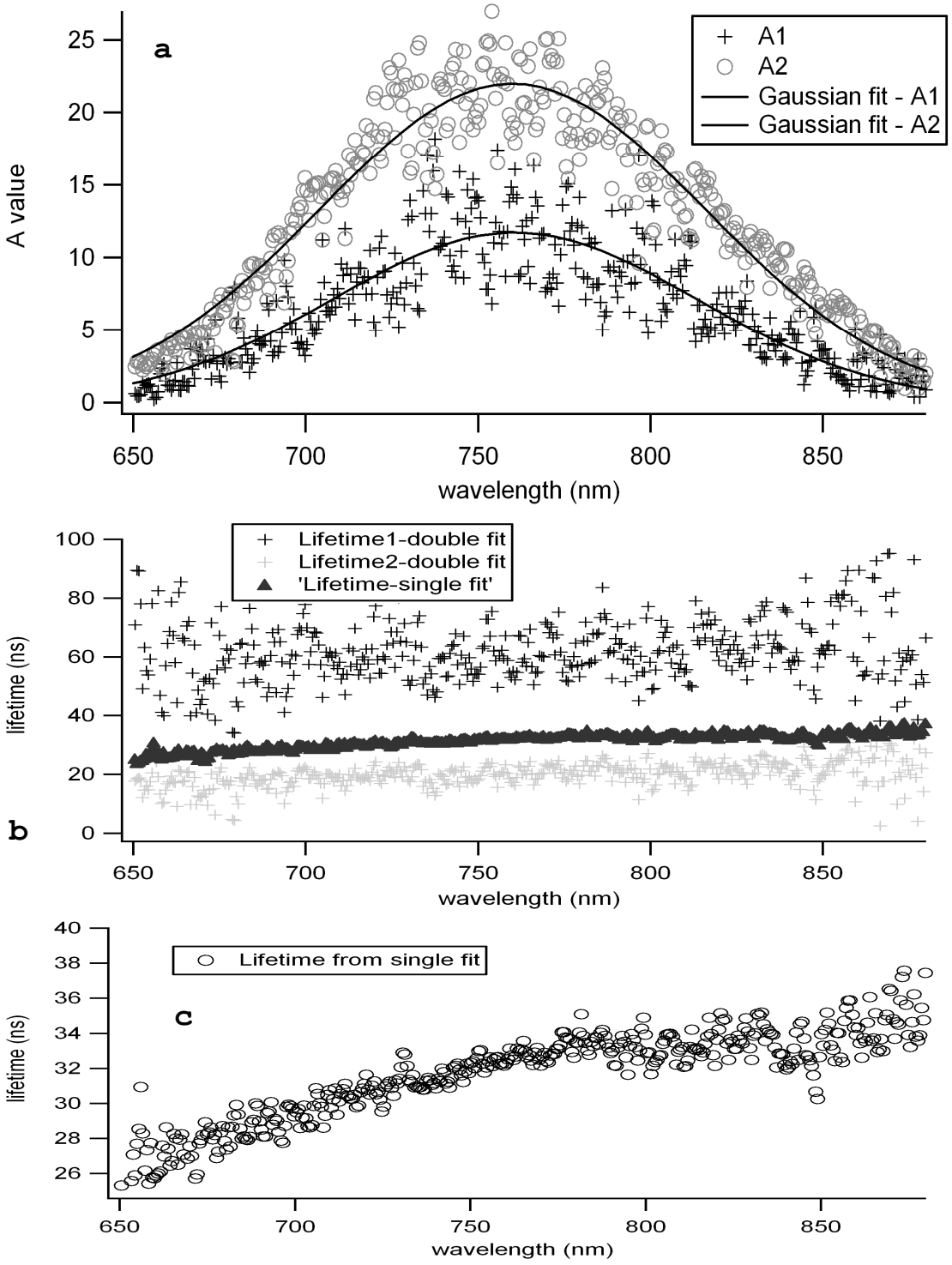

Figure 46. Gaussian fits and lifetimes of emission of 2.5 x 10^{-5} M $[(bpy)_2Ru(dpp)]^{2+}$ with 3 M Cd^{2+} from exponential fits: (a) A values from double exponential fits; (b) lifetimes from double & single exponential fits; (c) single exponential lifetimes.

lifetimes, at 63 ± 16 ns and 20 ± 4 ns (to one standard deviation). Gaussian fits to both profiles of the pre-exponential factors place the emission maximum at 760 nm for both. When the time-resolved data is fit to single exponentials (Figure 46b), there is an average lifetime of 32 ± 3 ns, but what appears to be a wavelength dependence (Figure 46c), with decreasing lifetimes towards shorter wavelengths. Similar to the results seen with Pb^{2+}, Gaussian fits of the steady-state spectrum (Figure 47a) show potentially two spectra with maxima at 745 nm and 816 nm. The steady-state emission and the emission snapshots of the time-resolved data at maximum intensity and 52 ns later are nearly identical (Figure 47b), though again suggesting that the fits are not able to distinguish a potential 816 nm emission if its lifetime is similar. The emission of $[(bpy)_2Ru(dpp)]^{2+}$ with Zn^{2+} parallels that with Cd^{2+}. Double exponential fits of the time-resolved data show nearly identical sets of pre-exponential values (Figure 48a), with Gaussian fits agreeing on a maximum at 773 nm. There are two sets of average lifetimes over the range 700 nm – 850 nm (Figure 48b), 54 ± 6 ns and 17 ± 4 ns (to one standard deviation). Different from Cd^{2+}, the lifetimes do not suggest wavelength dependencies. The average lifetime from single exponential fits is 33 ± 1 ns. The double Gaussian

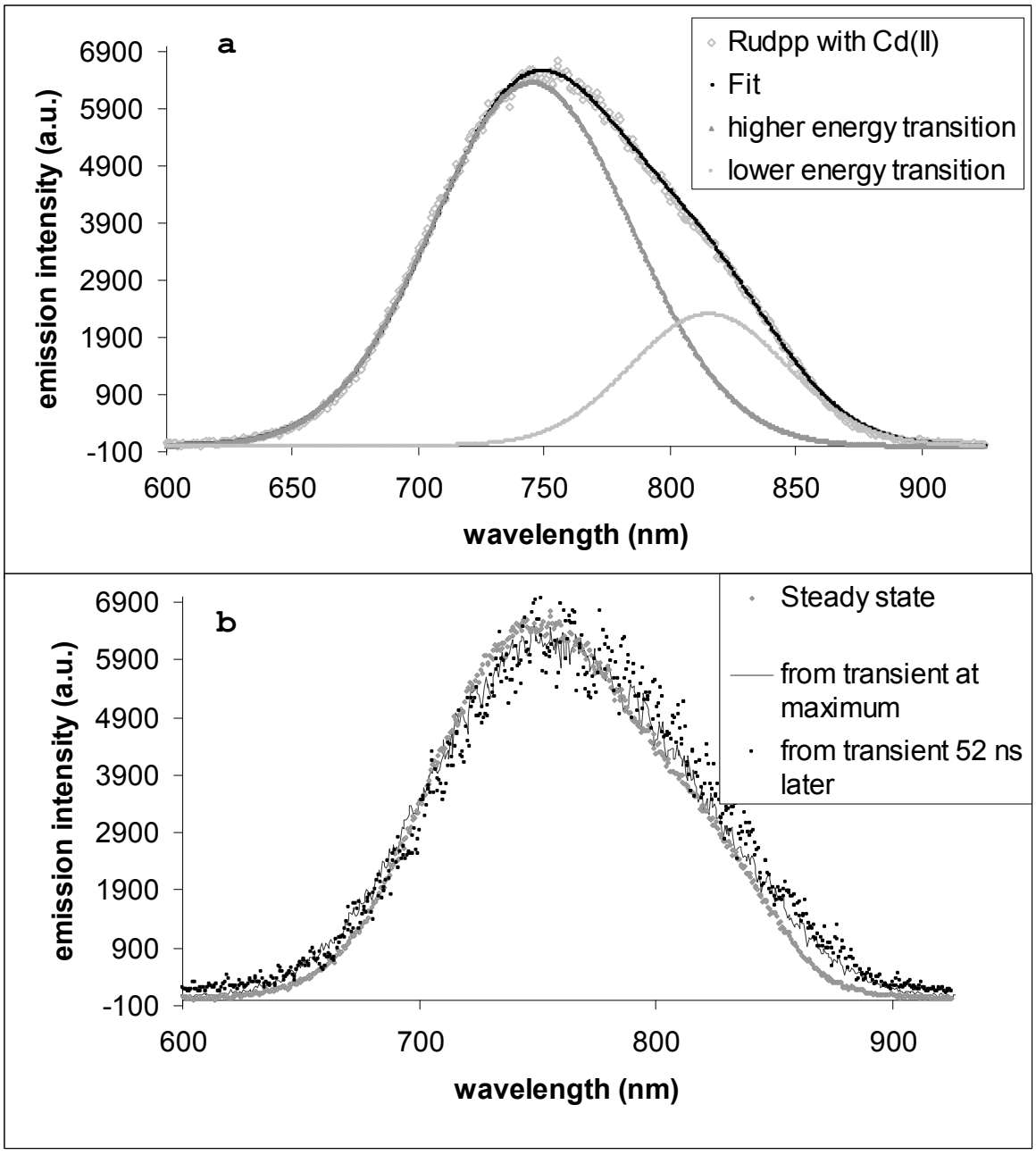

Figure 47. Gaussian fits of steady-state emission of 2.5 x 10^{-5} M $[(bpy)_2Ru(dpp)]^{2+}$ with 3 M Cd^{2+} and comparison to transient data: (a) steady state; (b) transient data.

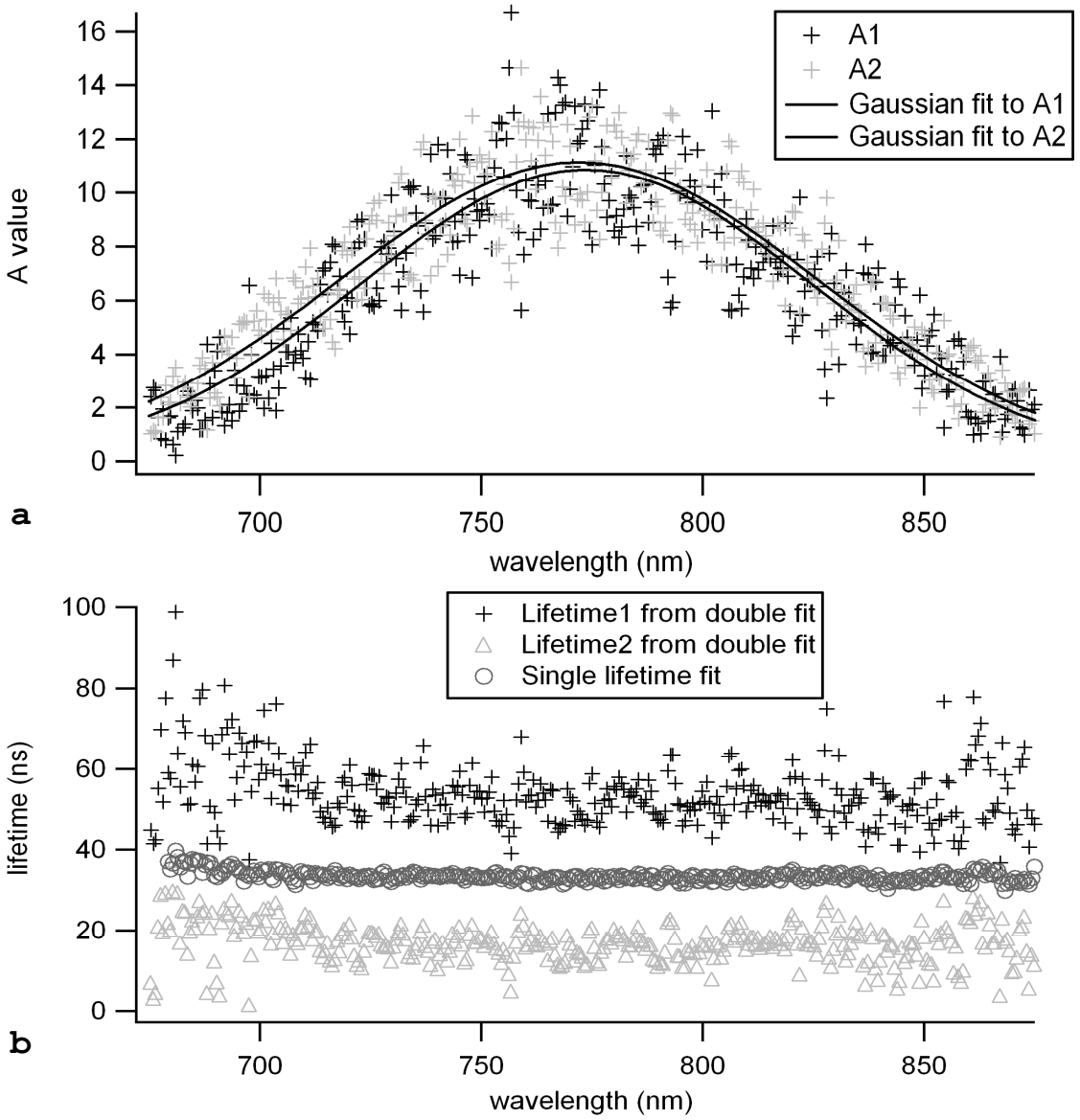

Figure 48. Gaussian fits and lifetimes from exponential fits of emission of 2.5 x 10^{-5} M $[(bpy)_2Ru(dpp)]^{2+}$ with 3 M Zn^{2+}: (a) fits; (b) lifetimes.

fit to the steady-state spectrum (Figure 49a) reveal two possible emissions, with maxima at 752 nm and 815 nm. The steady-state spectrum is quite similar to snapshots from the transient (Figure 49b), with the transients being nearly identical from the maximum intensity to 52 ns later.

For the bimetallic, $[(bpy)_2Ru(dpp)Ru(bpy)_2]^{4+}$ Gaussian fits of the absorption spectrum (Figure 50) have two maxima, at 413 nm and 510 nm. The bimetallic exhibits similar emission analysis to that reported for Cd^{2+} and Zn^{2+}. The double exponential fits (Figure 51a) yield sets of pre-exponential factors that have the same wavelength dependencies with maxima at 786 nm. In the same analysis there are two different sets of average lifetimes (Figure 51b) over the range from 700-900 nm, at 55 ± 35 ns and 13 ± 8 ns (to one standard deviation). The single exponential fit analysis (Figure 52b) has an average lifetime of 32 ± 3 ns, and fits a near perfect Gaussian with a maximum at 786 nm (Figure 52a). Two Gaussians fit the steady state spectrum with maxima at 772 nm and 820 nm (Figure 53a). Comparison of the transient snapshots reveals a persistent similarity (Figure 53b).

All in all it seems that in cases when the double-exponential fits yield sets of pre-exponential factors with the same wavelength dependence, and average lifetimes with

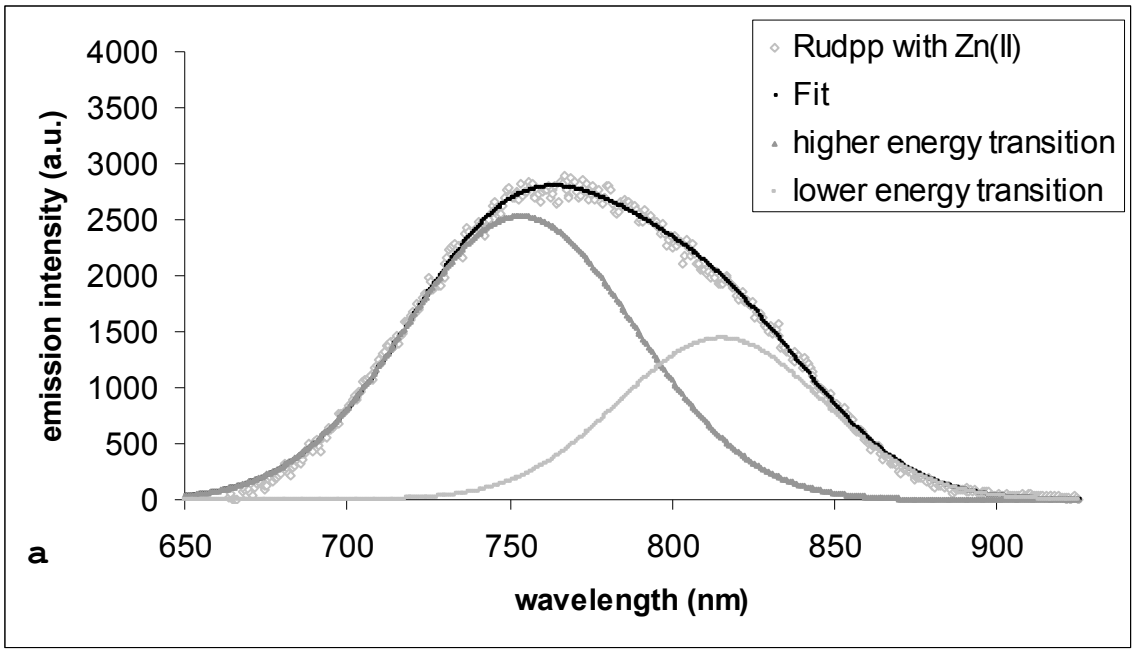

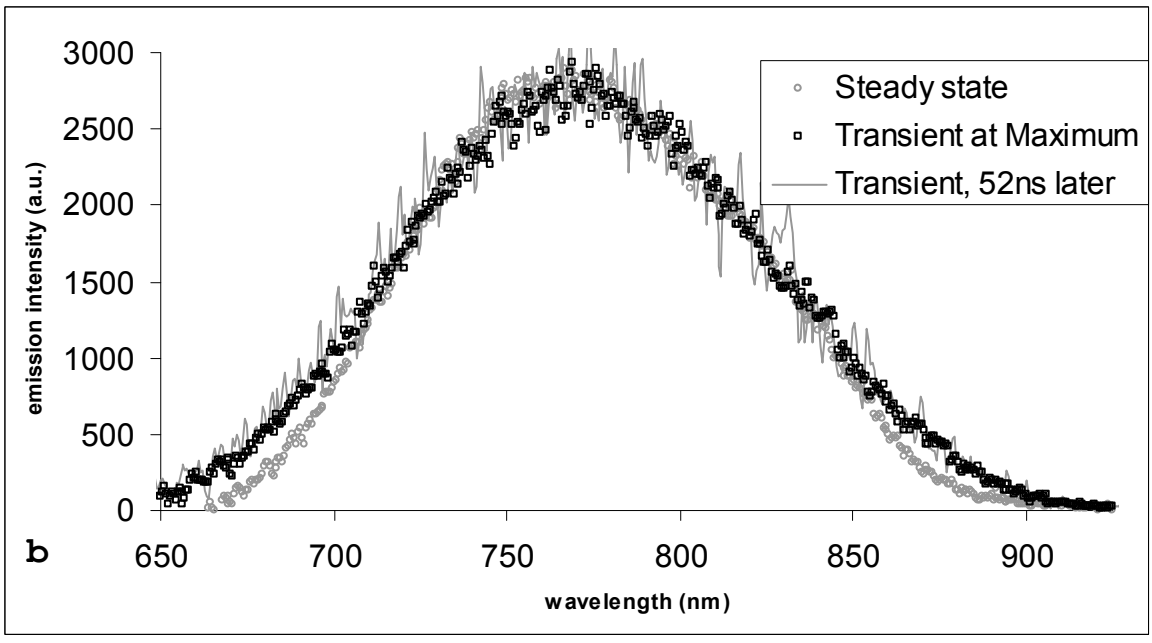

Figure 49. Gaussian fits of steady-state emission of 2.5 x 10^{-5} M $[(bpy)_2Ru(dpp)]^{2+}$ with 3 M Zn^{2+} and comparison to transient data: (a) fits; (b) transient data.

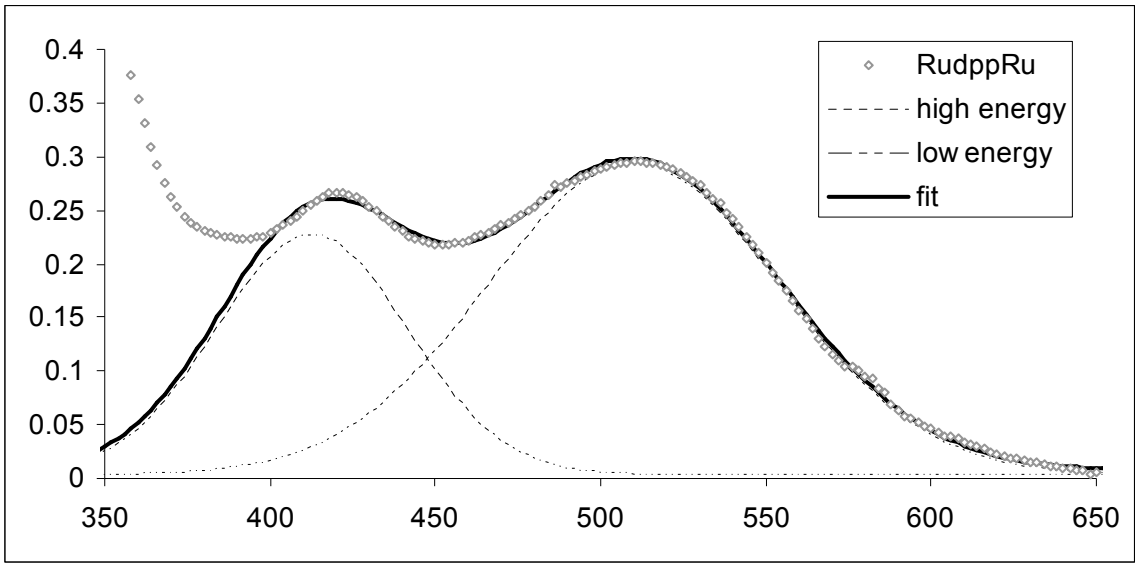

Figure 50. Gaussian fits of absorption spectrum of $[(bpy)_2Ru(dpp)Ru[(bpy)_2]^{4+}$.

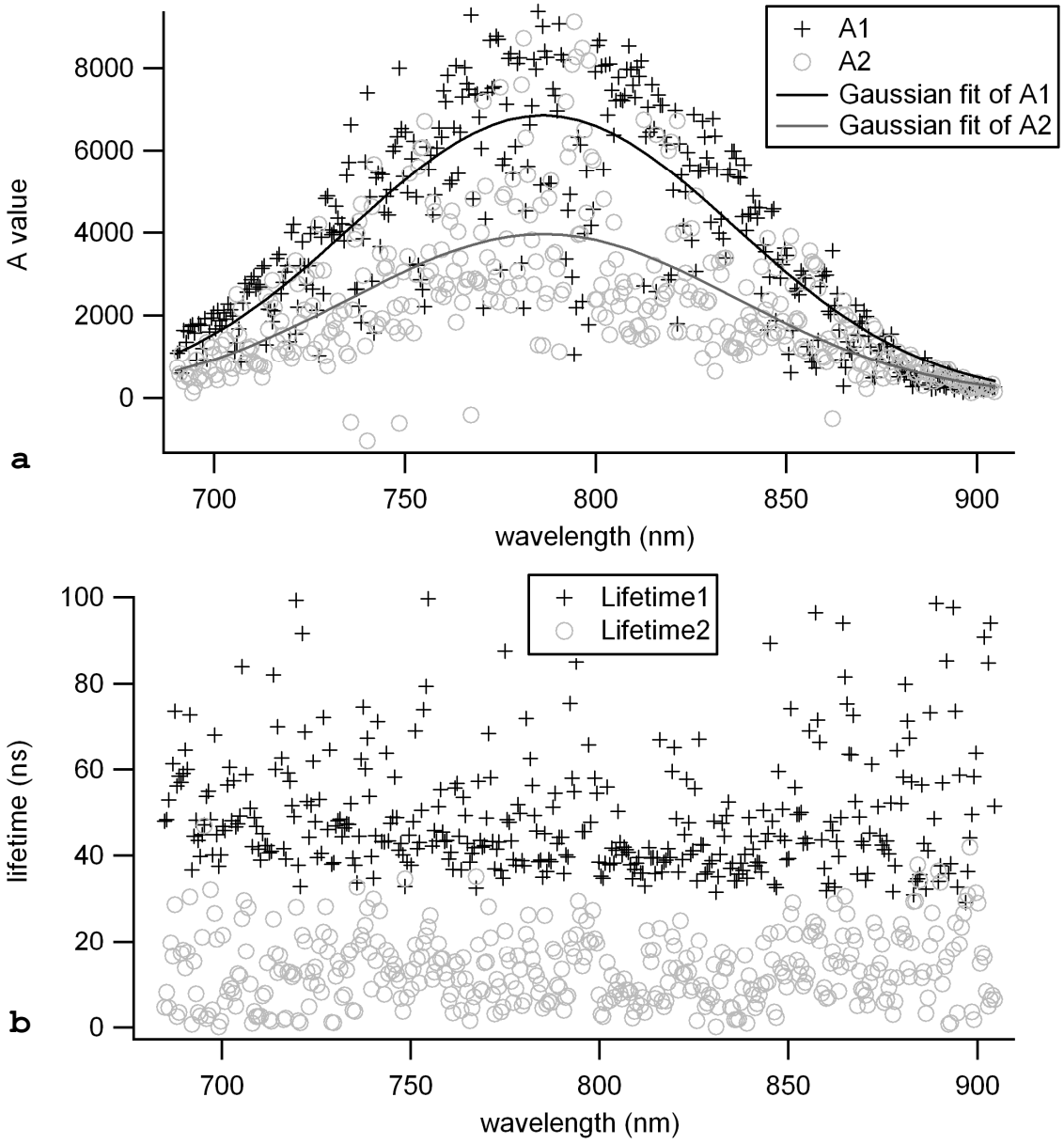

Figure 51. Gaussian fits and lifetimes of emission of $[(bpy)_2Ru(dpp)Ru(bpy)_2]^{2+}$ using double exponentials: (a) A values with Gaussian fits; (b) lifetimes.

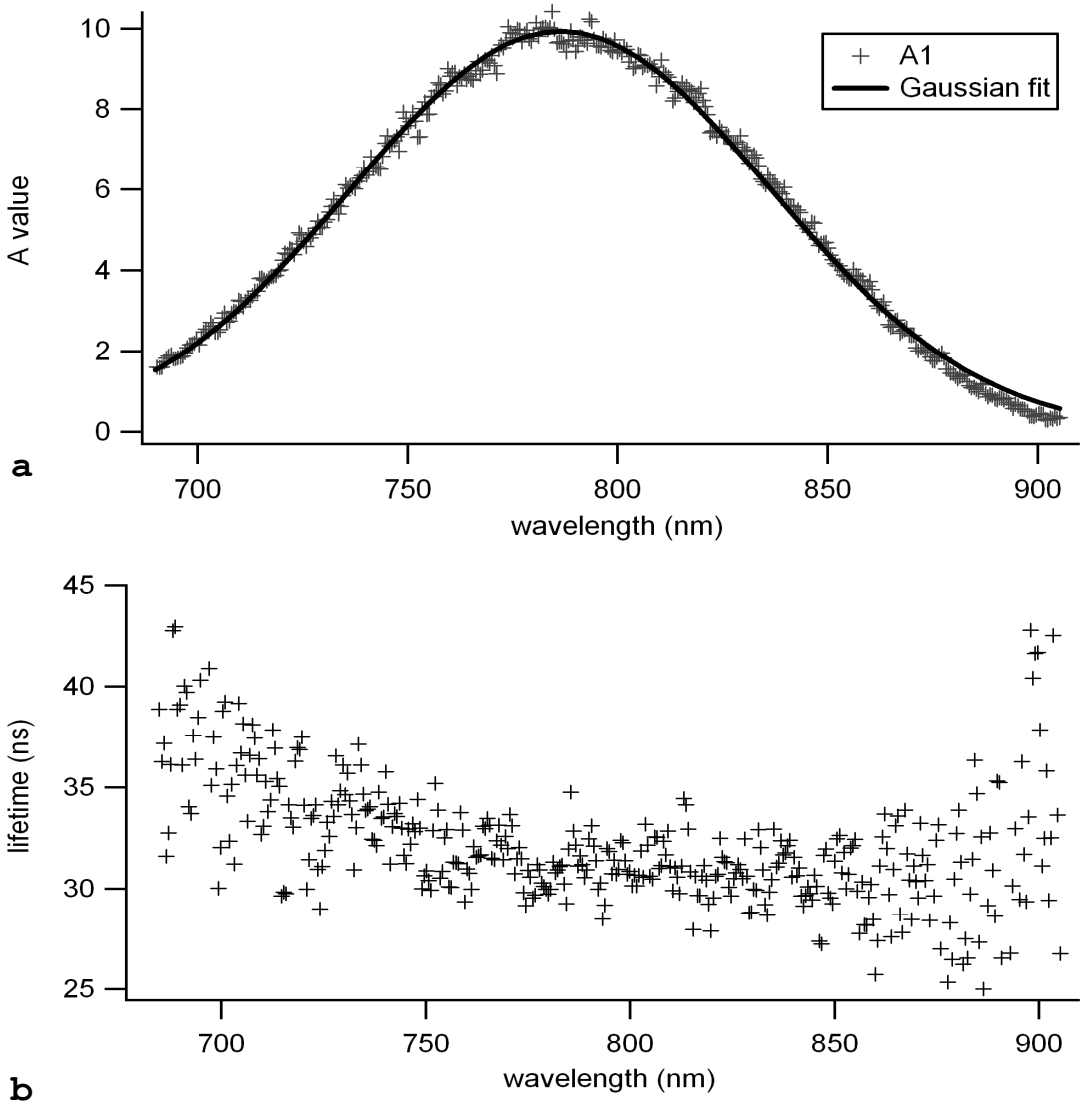

Figure 52. Gaussian fits and lifetimes of emission of $[(bpy)_2Ru(dpp)Ru(bpy)_2]^{4+}$ using single exponentials.

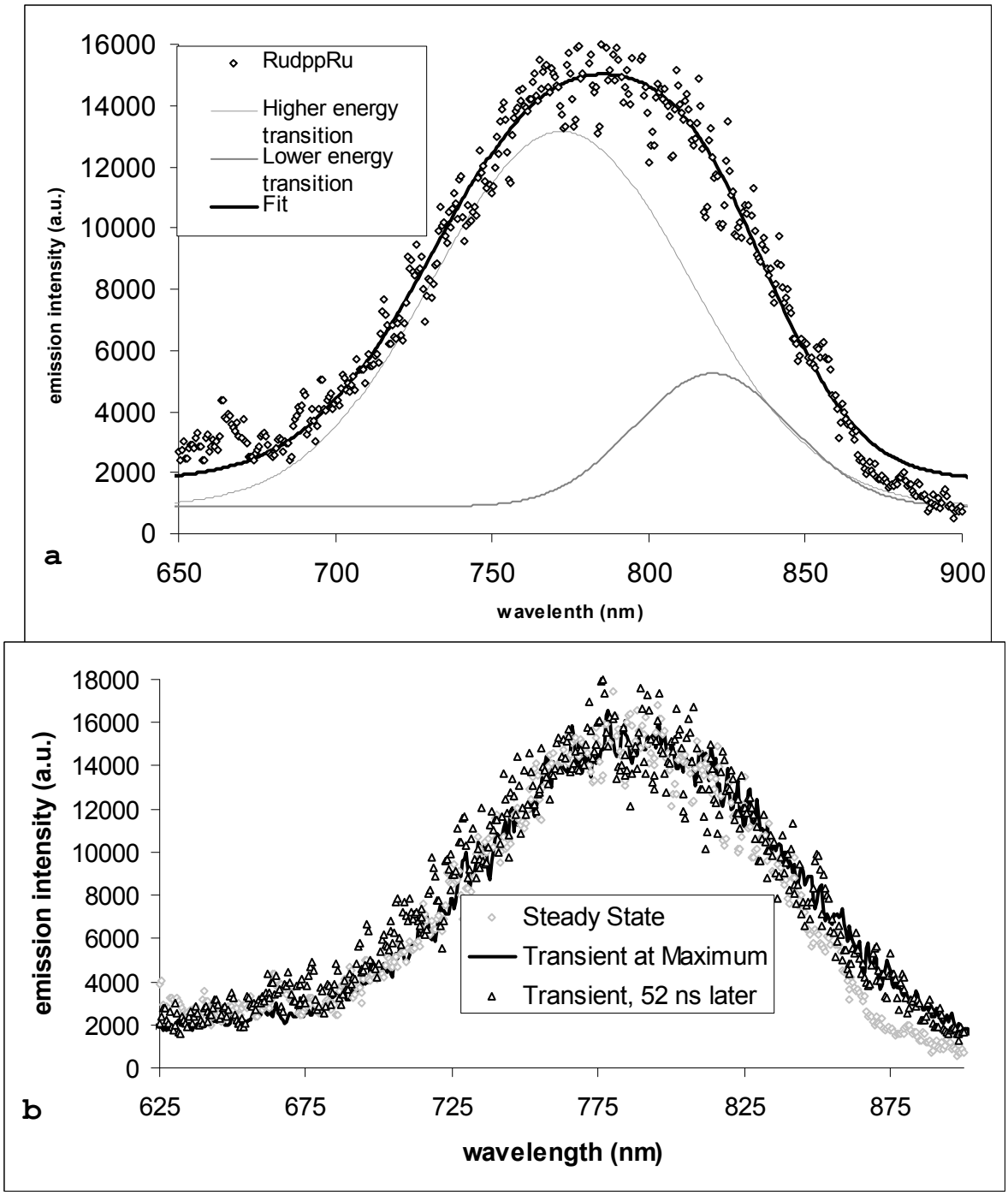

Figure 53. Gaussian fits of steady-state emission of $[(bpy)_2Ru(dpp)Ru(bpy)_2]^{4+}$ and comparison to transient data: (a) steady-state; (b) compare to transients.

large standard deviations, expectation of a single exponential fit is appropriate, with the proviso that the presence of another emission with a similar lifetime may be hidden. A complete summary table is provided below (Table 10).

3.F. Quantum Yield Determinations

3.F.1. Method

$[Ru(bpy)_3]^{2+}$ is more thoroughly characterized in the literature than $[Os(bpy)_3]^{2+}$, with several independent reports agreeing on its quantum yield of 0.0429.[149-152] For $[Os(bpy)_3]^{2+}$, the quantum yield in acetonitrile is reported to be Φ_{em} = 0.005.[133] Assuming better reliability of the reported quantum yield value of $[Ru(bpy)_3]^{2+}$, repeated attempts yielded Φ_{em} = 0.0015 for $[Os(bpy)_3]^{2+}$ in acetonitrile at room temperature, 22 ± 1°C, a value three times as large. Given that this called into question the reported Φ_{em} for $[Os(bpy)_3]^{2+}$, $[Ru(bpy)_3]^{2+}$ and $[Ru(phen)_3]^{2+}$ were first cross-standardized instead. $[Ru(phen)_3]^{2+}$ is another well-characterized complex in the literature with reported quantum yield values of 0.05810[150] and 0.07212[153] (average, 0.065) which are within experimental error of each other.

Table 10. Comparison of analysis of electronic spectra, $[(bpy)_2Ru(dpp)]^{2+}$ in Acid and with Various Metal Cations

	Ru-dpp	w/ H^+	w/ Ca^{2+}	w/ H_2^{2+}	w/ Fe^{3+}	w/ Al^{3+}	w/ Cr^{3+}	w/ Pb^{2+}	w/ Sn^{2+}	w/ Cd^{2+}	w/ Zn^{2+}	Ru-dpp-Ru
[]	n/a	1	6	15	3	3	.03	1.2	3	3	3	n/a
ab_1 (nm)	426	423	425	519	423	423	n/a	424	418	422	421	413
ab_2 (nm)	487	491	488	575	490	489	n/a	484	486	491	495	510
SS λ_{max} (nm)	704	735	706	n/a	726	726	704	750	704	750	760	780
SS λ_{max}-fit1 (nm)	n/a	n/a	n/a	n/a	n/a	n/a	n/a	740	n/a	745	752	772
SS λ_{max}-fit2 (nm)	n/a	n/a	n/a	n/a	n/a	n/a	n/a	814	n/a	815	815	820
I_o/I	n/a	137	1	∞	390	23	7.5	118	9	9.6	5.3	13.6
TR λ_{max} (nm)	705	735	708	n/a	731	735	705	n/a	705	760	773	786
τ_o (ns)	125 [9]	.01 6	125 [9]	n/a	8.3 [3.4]	16.3 [2]	37.6 [1.5]	n/a	8.1 [.5]	32 [3]	33 [1]	32 [3]
TR λ_{max}-fit1 (nm)	n/a	n/a	n/a	n/a	n/a	n/a	n/a	750	n/a	760	773	786
TR λ_{max}-fit2 (nm)	n/a	n/a	n/a	n/a	n/a	n/a	n/a	786	n/a	760	773	786
τ_1 (ns) [error]	n/a	n/a	n/a	n/a	n/a	n/a	n/a	57 [13]	n/a	63 [16]	54 [6]	55 [35]
τ_2 (ns) [error]	n/a	n/a	n/a	n/a	n/a	n/a	n/a	20 [9]	n/a	20 [4]	17 [4]	13 [8]

KEY: Concentrations are in M; n/a means not applicable; ab_1 and ab_2 are for two Gaussian fits of the absorption spectra; SS refers to steady-state data and TR to time-resolved; τ_o is from a single exponential fit; values designated "fit1" and "fit2" are for two Gaussian fits of the steady-state spectrum or double exponential fits of the time-resolved spectra.

It was useful and constructive to follow the *ratios* of the obtained quantum yields, both reported and obtained by experiment. The ratio of the (average) reported quantum yield values of $[Ru(phen)_3]^{2+}$ to $[Ru(bpy)_3]^{2+}$ is 1.55:1. Although plotted as area under the emission spectrum, which is proportional to Φ_{em}, both instrument systems yielded nearly the exact same quantum yield ratios, at 1.56:1 (Figure 54). This confirmed the reliability of the technique employed, as well as the success of using the ICCD camera system with excitation from the argon ion laser for quantum yield experiments, a preferred strategy given the ability of the ICCD camera to provide excellent signal gain and red sensitivity.[xxvii]

3.F.2. Quantum Yield of $[(bpy)_2Ru(dpp)]^{2+}$

Using $[Ru(bpy)_3]^{2+}$ as a standard, the Spex Fluorolog instrument gave a quantum yield of emission from $[(bpy)_2Ru(dpp)]^{2+}$, Φ_{em}, of 0.00175 ± .0002, and the argon/ ICCD system gave Φ_{em} = 0.00198 ± .0002, which are within experimental error of each other. The side-by-side comparison of absorbance *vs.* emission and the gradients are

[xxvii] Whereas normally the photomultiplier of the Fluorolog spectrometer would provide superior gain, its age at the time of the experiments made it unsuitable for determining quantum yield values of very weakly emissive species, such as the protonated form of $[(bpy)_2Ru(dpp)]^{2+}$.

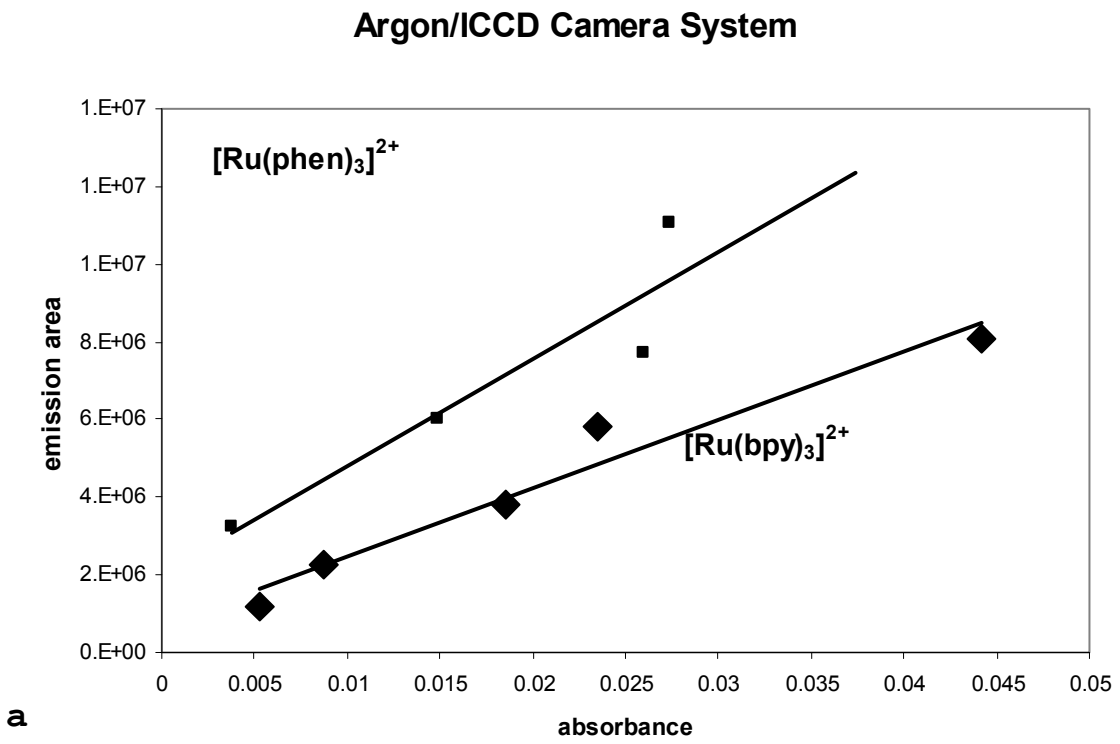

a

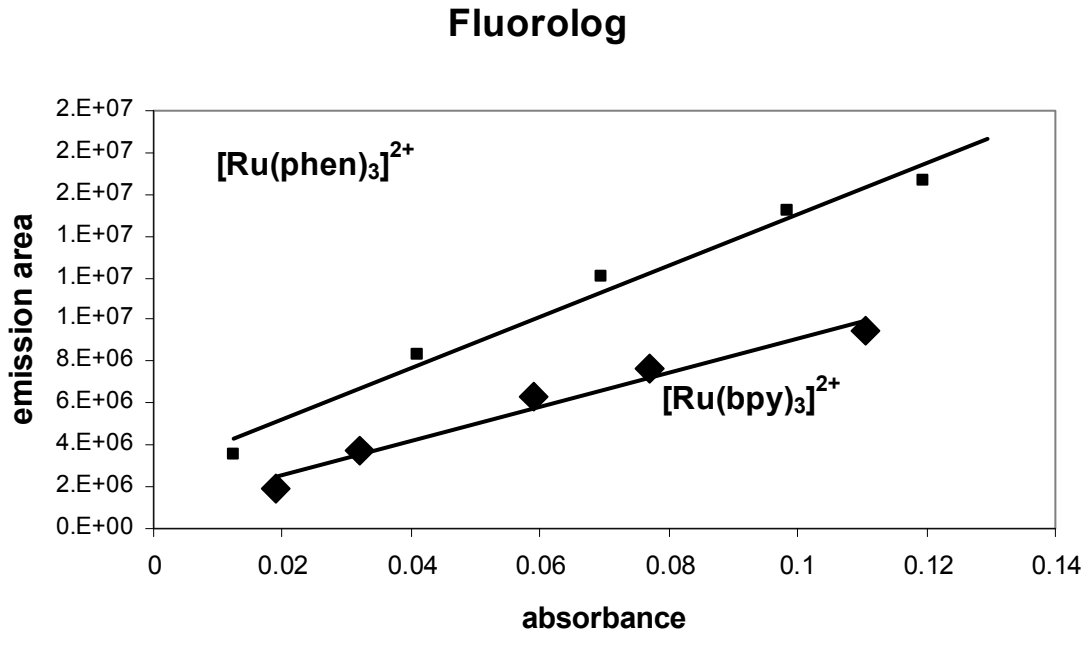

b

Figure 54. Cross-standardization of reference quantum yields using the gradient method: (a) results on ICCD camera system; (b) results on Fluorolog spectrometer.

shown in Figure 55. The higher value with the argon/ICCD system makes sense since the Fluorolog PMT sensitivity declines to the red of the $[Ru(bpy)_3]^{2+}$ emission standard having an emission maximum at 620 nm, whereas the $[(bpy)_2Ru(dpp)]^{2+}$ maximum is at 702nm. Also, the grating for the spectrometer for the ICCD is blazed at 800 nm, thereby providing more efficient transmission of longer wavelength emitted light. With the quantum yield available, the radiative and non-radiative rate constants, k_r and k_{nr}, are calculated from equations (26) and (27). For $[(bpy)_2Ru(dpp)]^{2+}$, k_r = 2.0 ± .3 x 10^4 s^{-1} and k_{nr} = 9.8 ± 1 x 10^6 s^{-1}.

3.F.3. Quantum Yield Determination of $[Os(bpy)_3]^{2+}$

The gradient for $[Os(bpy)_3]^{2+}$ in acetonitrile was compared directly to $[(bpy)_2Ru(dpp)]^{2+}$ in pH=7 buffer, and pH=5 buffer (Figure 56). Their gradients and thus quantum yields are quite similar. Based on the data and equation (84), for $[Os(bpy)_3]^{2+}$ in acetonitrile Φ_{em} is measured to be 0.00215 ± .0003. Relative to this value, the quantum yield of $[(bpy)_2Ru(dpp)]^{2+}$ in pH=5 buffer is determined to be 0.00173 ± .0002.

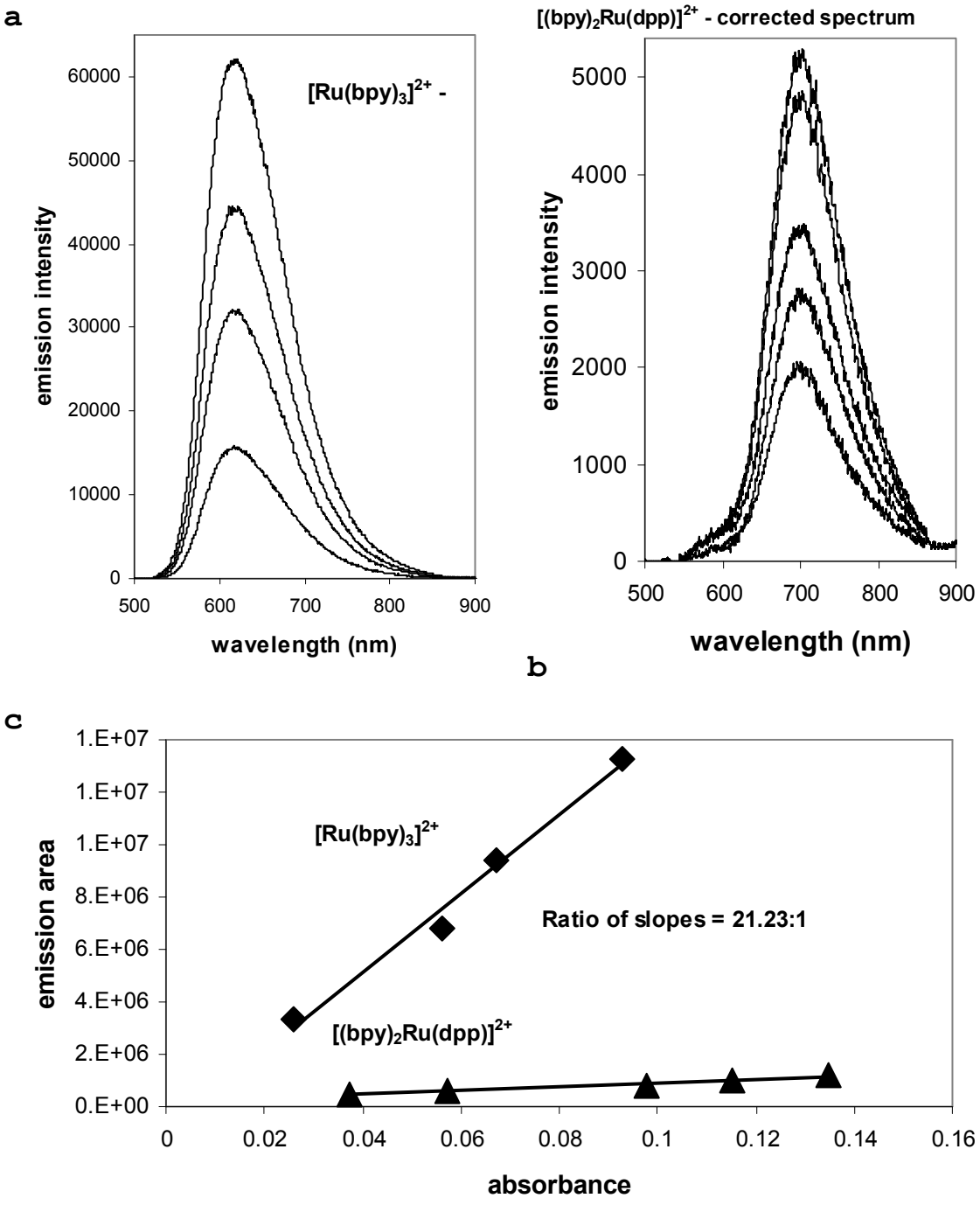

Figure 55. Quantum yield determination of $[(bpy)_2Ru(dpp)]^{2+}$: (a) $[Ru(bpy)_3]^{2+}$ emission spectra; (b) $[(bpy)_2Ru(dpp)]^{2+}$ emission spectra; (c) gradients.

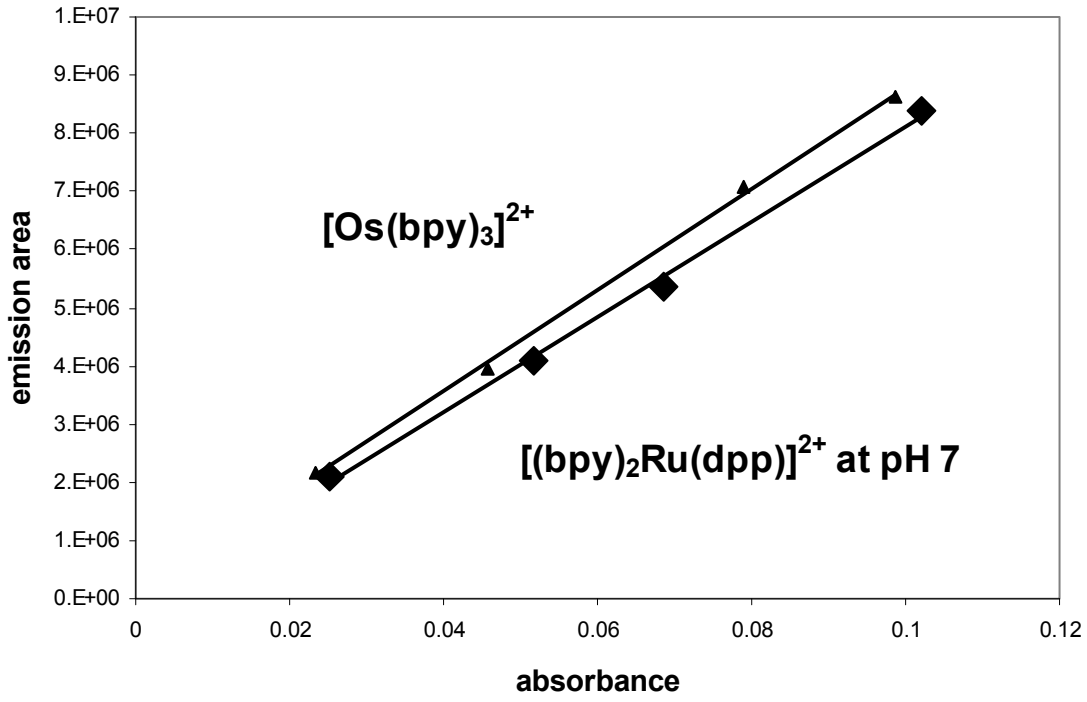

a

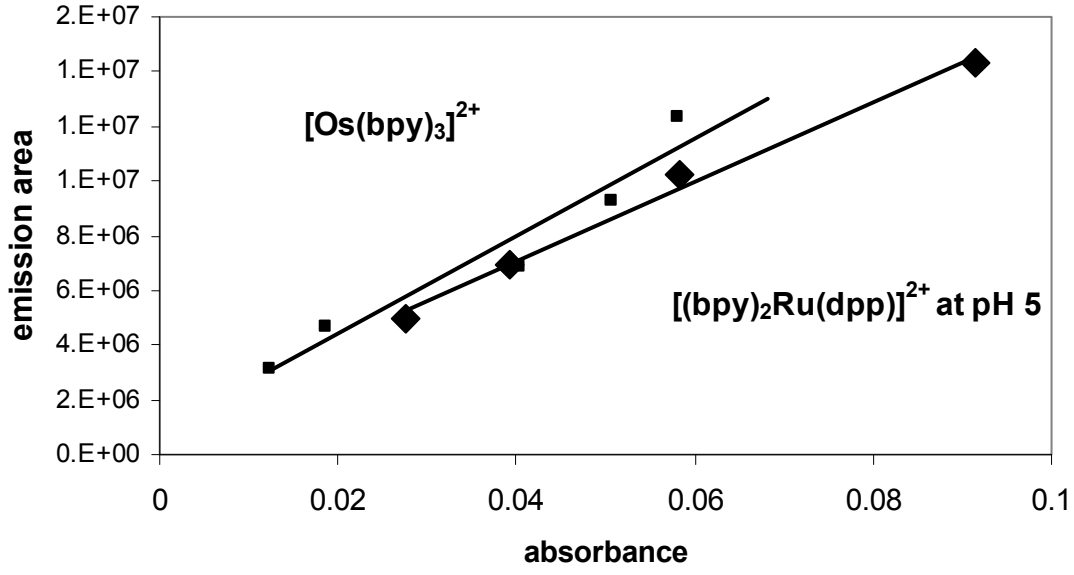

b

Figure 56. Quantum yield determination of $[Os(bpy)_3]^{2+}$: (a) *vs.* $[(bpy)_2Ru(dpp)]^{2+}$ at pH = 7; (b) *vs.* $[(bpy)_2Ru(dpp)]^{2+}$ at pH = 5.

3.F.4. Quantum Yield of $[(bpy)_2Ru(dppH)]^{3+}$

A number of challenges arose is attempting to determine the quantum yield of the monoprotonated species by comparison to the unprotonated. First, as mentioned, the camera gain had to be changed. Second, high concentrations and therefore high absorbances of the protonated species were needed. Third, the presence of multiple emissions was another complicating factor. Fourth, subtracting out the blank was not straightforward as the Raman water band was attenuated in the samples, thus causing negative dips in the subtracted spectra.

The plot of relative emission quantum yield of $[(bpy)_2Ru(dpp)]^{2+}$ *vs.* camera gain is shown in Figure 57a. An exponential fit (Figure 57b) gave the following relationship,

$$\Phi_{em} = 6.749\text{x}10^5 + (2.584\text{x}10^6)e^{(0.033844)(\text{gain})} \quad . \qquad (93)$$

Therefore, changing the camera gain from 73 to 200 in the experiment introduces a factor of 1:72 ± 12 when looking at the emission from species at different gain values. The multiple emissions can be accounted for by using templates to fit the data. This also helps with the problem of the

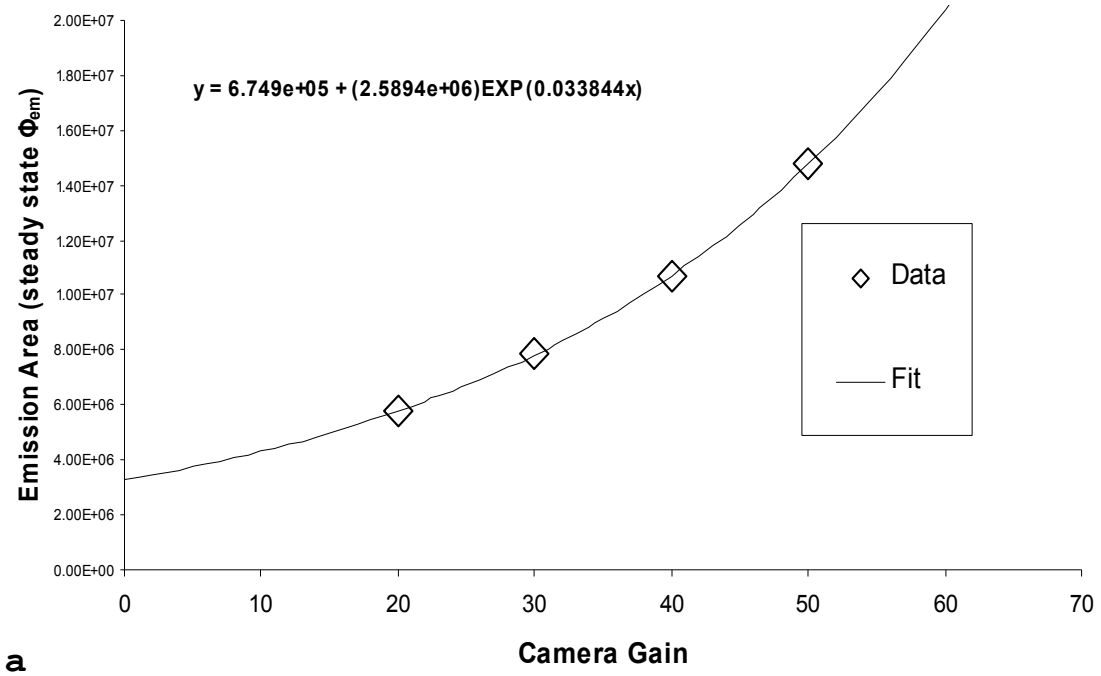

a

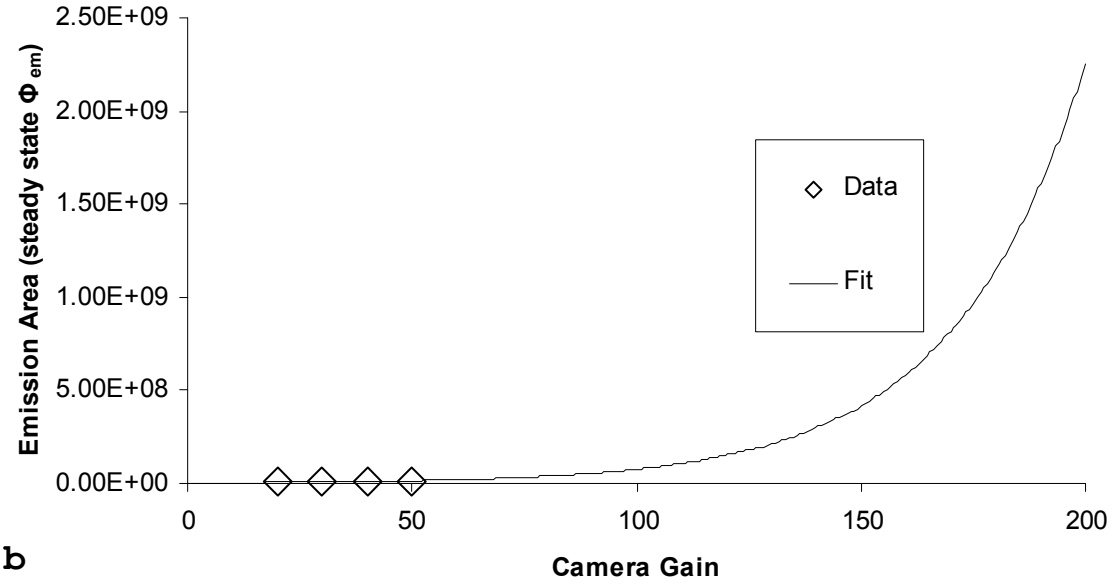

b

Figure 57. Calibration of ICCD camera gain *vs.* emission of $[(bpy)_2Ru(dpp)]^{2+}$: (a) data points; (b) extrapolation.

blank subtraction, by subtracting only a fraction of the blank sample to avoid negative dips at the Raman shift wavelength. The original unsubtracted data (Figure 58a), partially subtracted data (Figure 58b) and fitted data (Figure 58c) are derived from the template fits for each data set (Figure 59a-d). The areas under the resolved fits (Figure 59e) can then be used for the relative quantum yield determination. The two fitting templates are centered at 624 nm and 730 nm. The ratio of the gradients of the unprotonated to the lower energy transition of the protonated, which is presumably the one associated with an emissive MLCT at the dpp ligand, is 6700:1. The quantum yield is estimated to be $4 \pm 1 \times 10^{-9}$. The ratio of the gradients of the multiple emissions (Figure 60), the higher energy transition to the lower energy is 7.56:1. Thus the quantum yield of the higher energy transition, possibly associated with the bpy ligands, is estimated to be $3 \pm 1 \times 10^{-8}$.

3.G. Association of $[(bpy)_2Ru(dpp)]^{2+}$ with Ag^+

The absorption spectrum from the titration of $[(bpy)_2Ru(dpp)]^{2+}$ with Ag^+ is shown in Figure 61a. All spectra were normalized to an absorbance of 0 at 700 nm. With increasing $[Ag^+]$ there is a decrease in the extinction

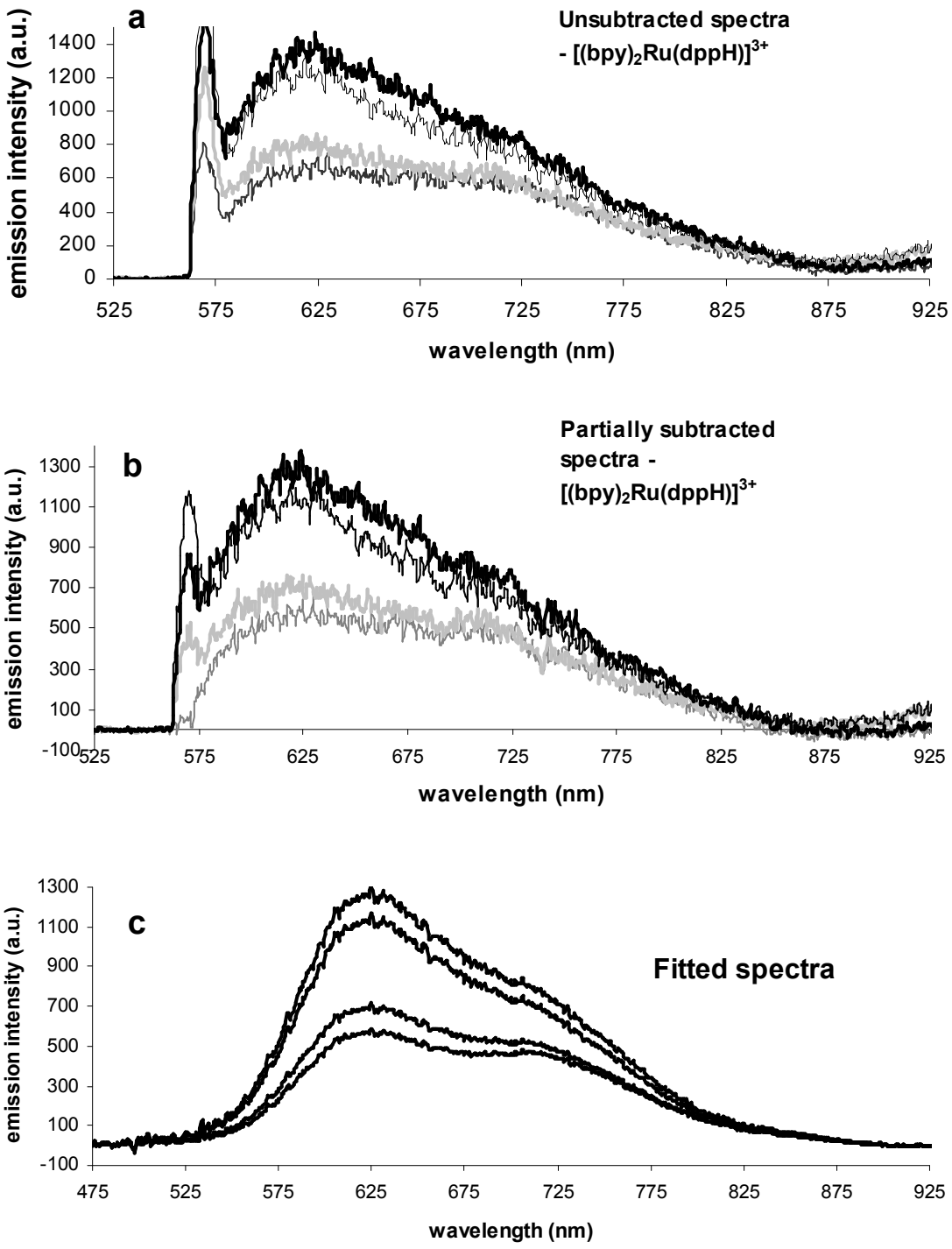

Figure 58. Emission data of $[(bpy)_2Ru(dppH)]^{3+}$ for quantum yield determination: (a) raw data; (b) partially subtracted spectra; (c) fitted spectra.

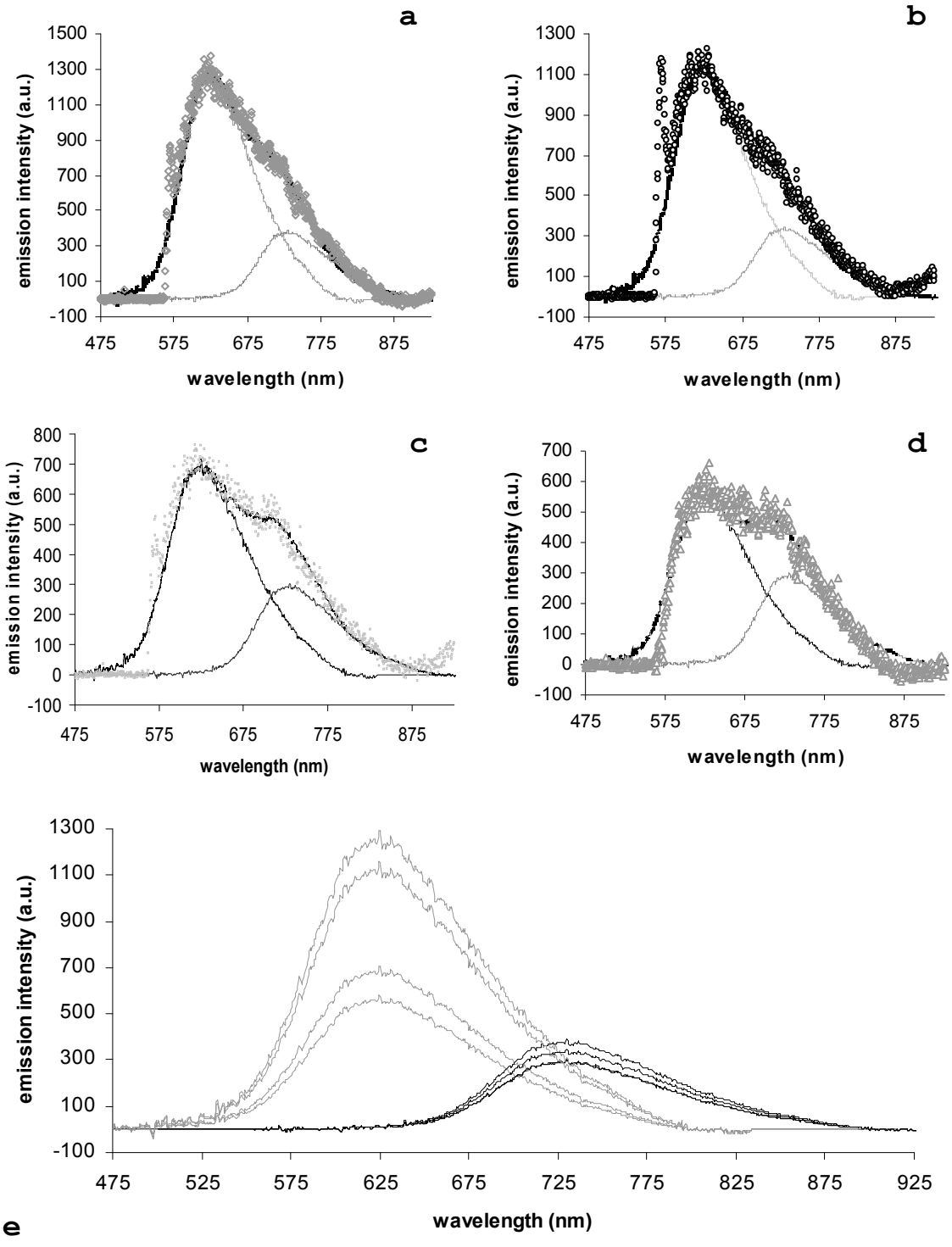

Figure 59. Fitting of emission data of $[(bpy)_2Ru(dppH)]^{3+}$ for quantum yield determination: (a)-(d) individual data sets; (e) combination of template fits.

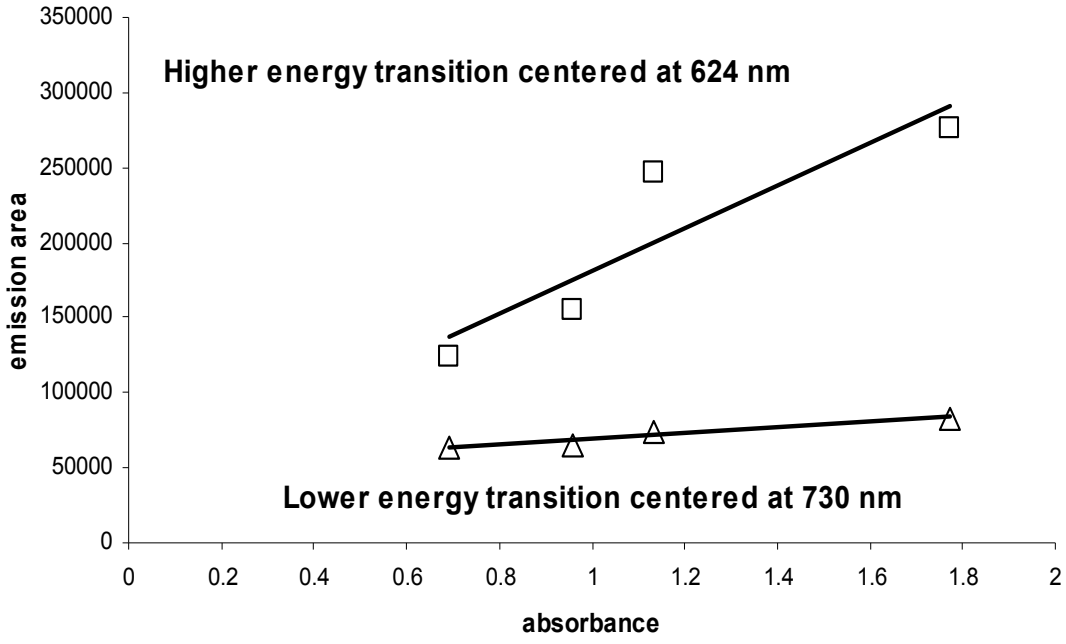

Figure 60. Ratio of quantum yield gradients of multiple emissions from $[(bpy)_2Ru(dppH)]^{3+}$.

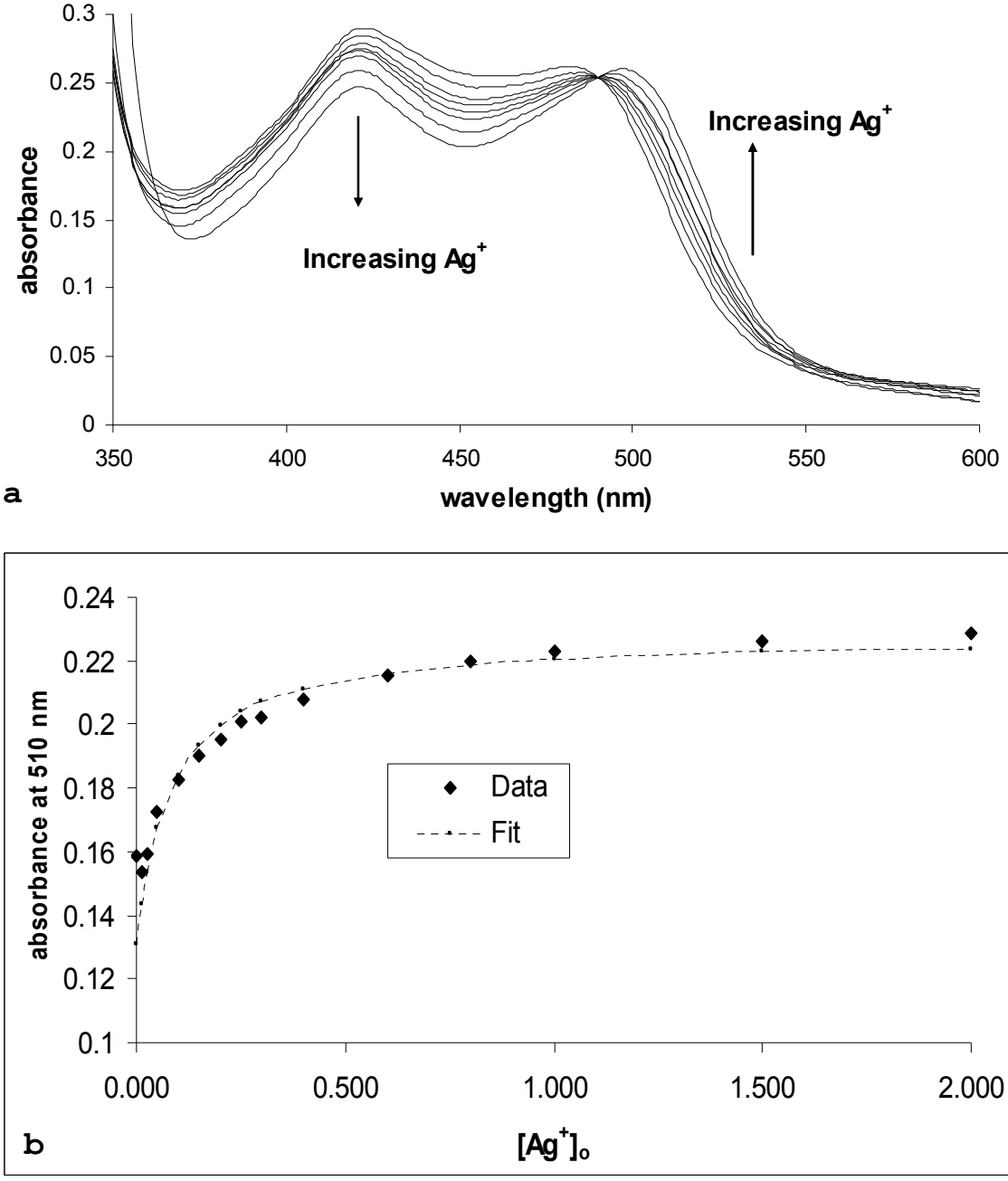

Figure 61. Absorption spectra from titration of $[(bpy)_2Ru(dpp)]^{2+}$ with Ag^+: (a) absorption spectra; (b) change in absorbance at 510 nm and accompanying fit.

coefficient of the bpy transition of about 15% at 420 nm, coupled with a red-shift of the dpp transition to about 495 nm. Assuming one-to-one ground-state association of Ag^{+} with $[(bpy)_2Ru(dpp)]^{2+}$ and that the absorption spectrum is a linear combination of the spectrum of the associated and free species, the following relationship between absorbance, A, at an analytical wavelength $l=\lambda$, and initial metal concentration, $[M]_o$, can be derived similar to that done for the NMR fits:

$$A_{l=\lambda} = (\varepsilon_{RuM} - \varepsilon_{Ru})\left(\frac{1}{2}([M]_o + [Ru]_o + \frac{1}{K_{eq}}) - \sqrt{\left(\frac{1}{2}([M]_o + [Ru]_o + \frac{1}{K_{eq}})\right)^2 - [M]_o[Ru]_o}\right) \quad (94)$$

where ε_{RuM} and ε_{Ru} are the extinction coefficients of the associated and free species at the analytical wavelength, $[Ru]_o$ is the initial concentration of the free ruthenium species, and K_{eq} is the equilibrium constant for association. Since ε_{Ru} is known, K_{eq} and ε_{RuM} are the two parameters for the non-linear regression. Following the absorbance at 510 nm the fit (Figure 61b) to (94) yields an association equilibrium constant of 12.3, and an extinction coefficient for the bimetallic, $[(bpy)_2Ru(dpp\text{-}Ag)]^{3+}$ of 7189 M^{-1} cm^{-1}.

Somewhat similar to the acid titration, increasing concentrations of Ag^+ cause several peaks to shift downfield in the ^1H NMR spectrum (Figure 62, with structural assignment of $[(bpy)_2Ru(dpp)]^{2+}$ included for convenience), specifically B3′, C3″, C5″, and C6″, but not to same extent as was seen with H^+. Also, slight downfield shifts are also seen with A6 which were not seen in the proton titration, and slight upfield shifts occur with C4″. The change in chemical shift at B3′, C3″, C5″, and C6″ can be plotted *vs.* initial silver ion concentration, $[Ag]_o$, and fits to equation (90) to yield the equilibrium constant for association and δ_{bound} (Figure 63). The parameters for the fits are tabulated below (Table 11).

Table 11. NMR parameter fits, titration with Ag^+.

Proton	δ_{free} (ppm)	δ_{bound} (ppm)	K_{eq}
B3′	7.05	7.40	32
C3″	7.82	7.92	16.5
C5″	7.66	9.16	0.30
C6″	8.61	8.81	19

The response of C5″ is markedly different from the others and its profile does not plateau, hence the disparate K_{eq} value. The average of the other three is 22.5 ± 8.3 M^{-1}, which is nearly within experimental error of that derived from the absorbance fit data.

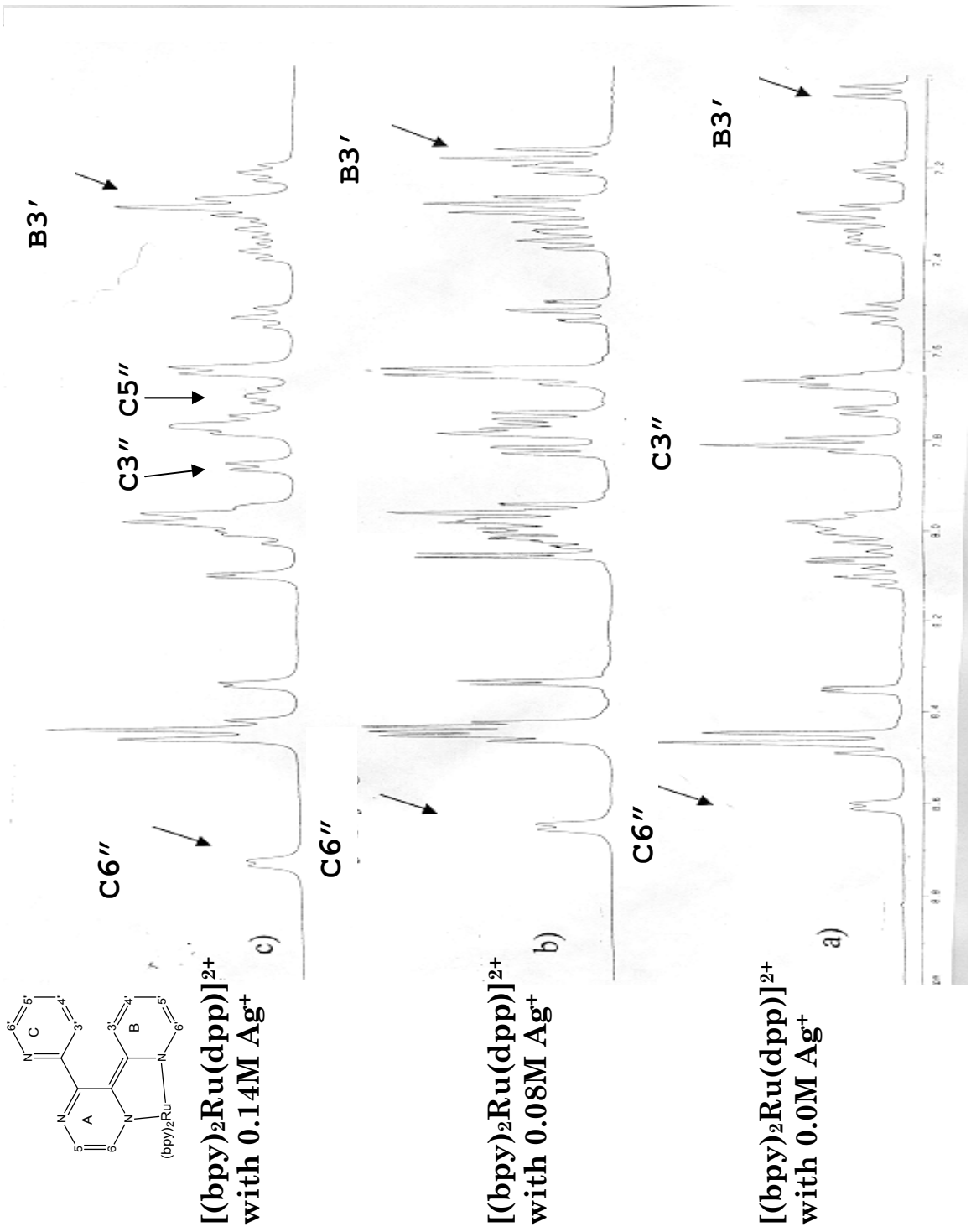

Figure 62. NMR spectra from titration of $[(bpy)_2Ru(dpp)]^{2+}$ with Ag^+: (a) no Ag^+; (b) 0.08M Ag^+; (c) 0.14M Ag^+.

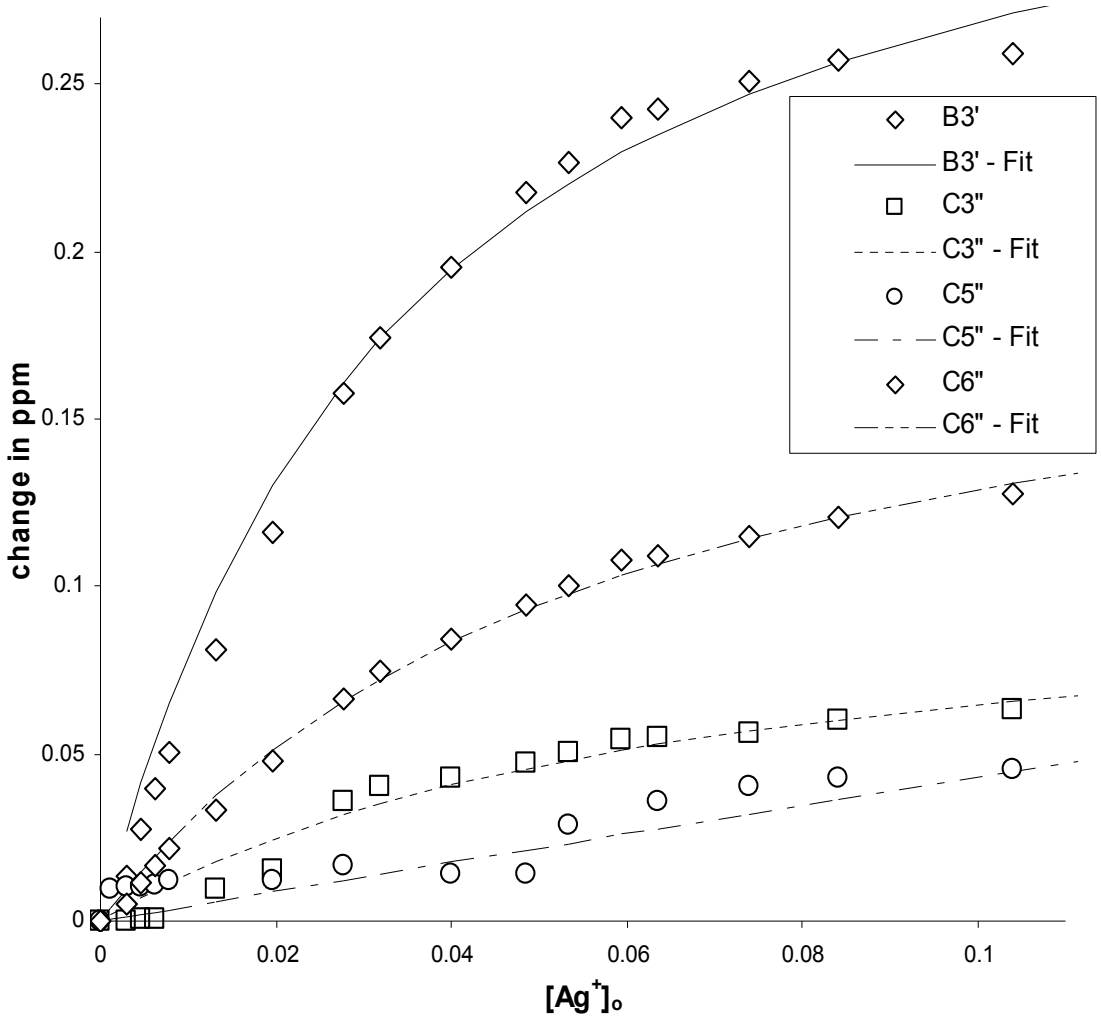

Figure 63. Change in chemical shift and fits from titration of 0.008M $[(bpy)_2Ru(dpp)]^{2+}$ with increasing $[Ag^+]$.

The emission of $[(bpy)_2Ru(dpp)]^{2+}$ in aqueous solution with increasing $[Ag^+]$ red-shifts to about 740 nm and reduces in intensity (Figure 64). All data sets were analyzed by both single and exponential decays. The double exponential fits do elicit differing lifetimes, though the plots of the *A* values do not suggested emissions with differing wavelength maxima. The presumed bimetallic, $[(bpy)_2Ru(dpp\text{-}Ag)]^{3+}$ has a single exponential decay lifetime of 57.5 ± 3 ns over the range of wavelengths from 700-900 nm, with an emission maximum at 750 nm (Figure 65). The steady-increase in lifetime towards higher energy may be related to Ag^+-complexes with the π systems of bpy (*vide infra*). Using the lifetimes obtained from both single and bi-exponential fits, a Stern-Volmer plot of $(\tau_o/\tau - 1)$ *vs.* $[Ag^+]$ has strong negative deviations (Figure 66). For $[(bpy)_2Ru(dpp)]^{2+}$ in 3 M $AgNO_3$ in methanol double exponential fits of the time-resolved spectra yielded two apparent emissions, centered at 721 nm and 745 nm, with average lifetimes of 178 ± 46 ns and 81 ± 11 ns (Figure 67). The comparative data in the two solvents are shown in Table 12.

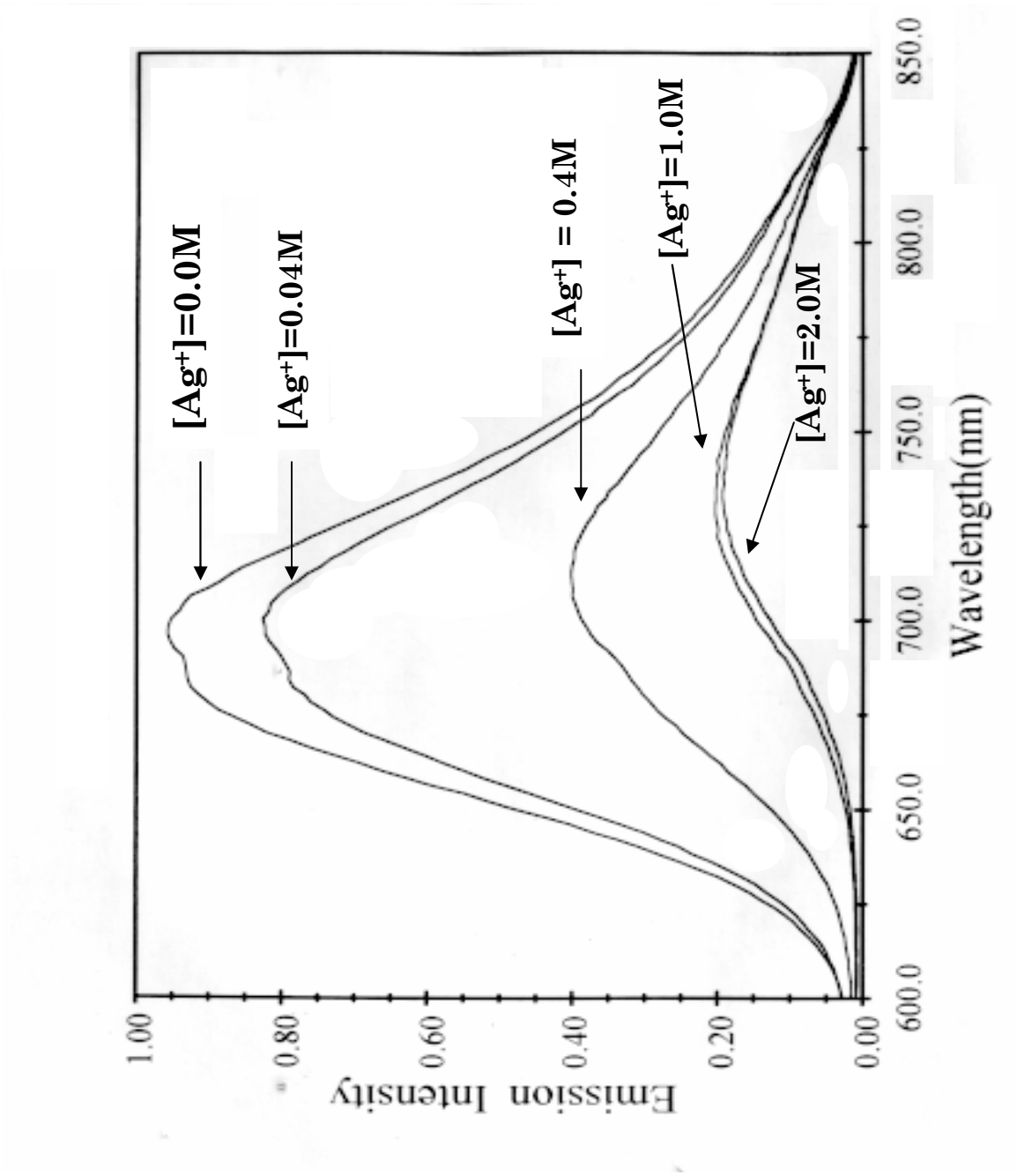

Figure 64. Steady-state emission spectra of 2.5×10^{-5} M $[(bpy)_2Ru(dpp)]^{2+}$ with increasing $[Ag^+]$.

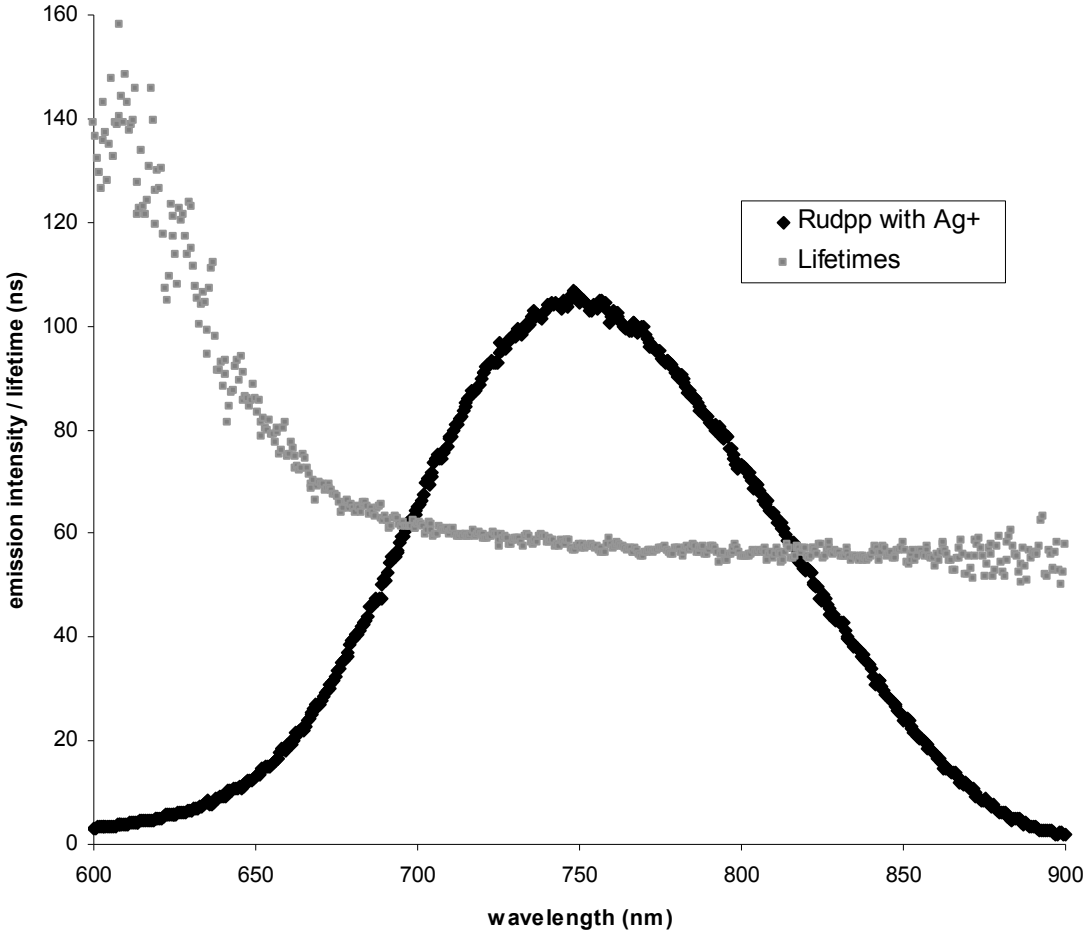

Figure 65. Emission spectrum and lifetimes of 3.17 x 10^{-5} M $[(bpy)_2Ru(dpp)]^{2+}$ with 3 M Ag^{+} in water.

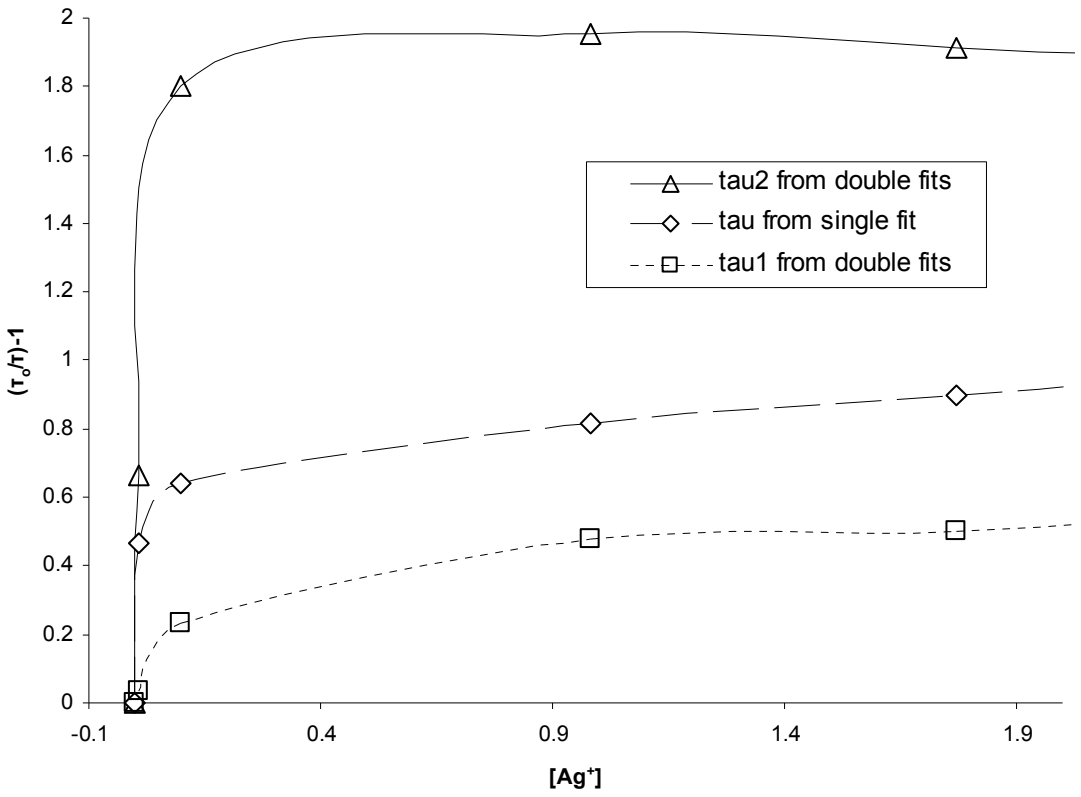

Figure 66. Stern Volmer plot of lifetimes from titration of 2.5 x 10^{-5} M $[(bpy)_2Ru(dpp)]^{2+}$ with increasing $[Ag^+]$.

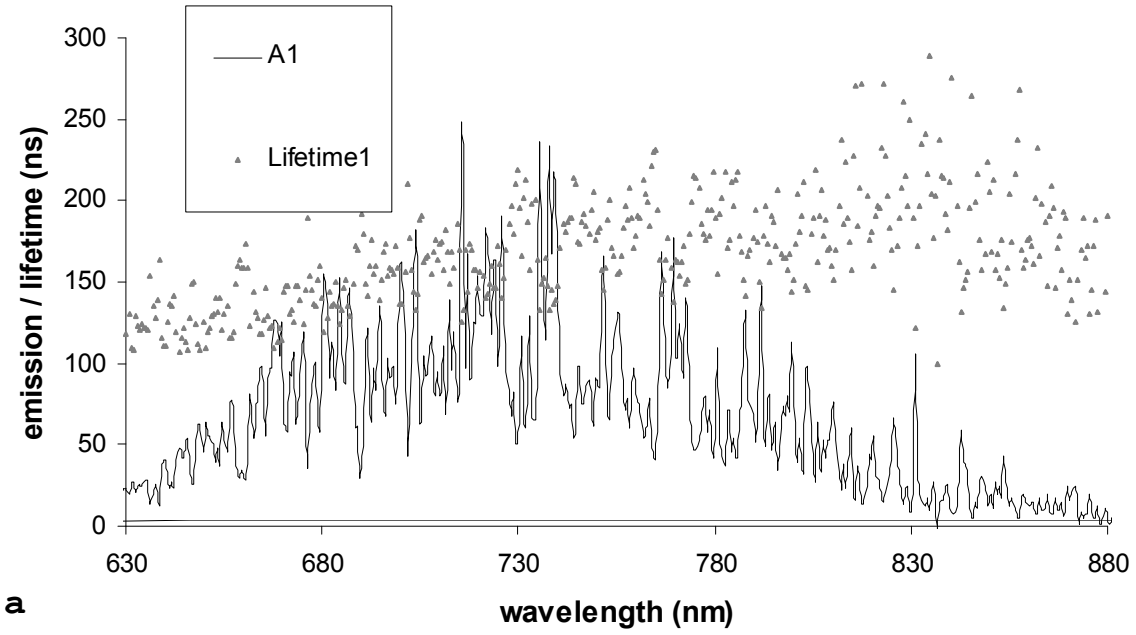

a

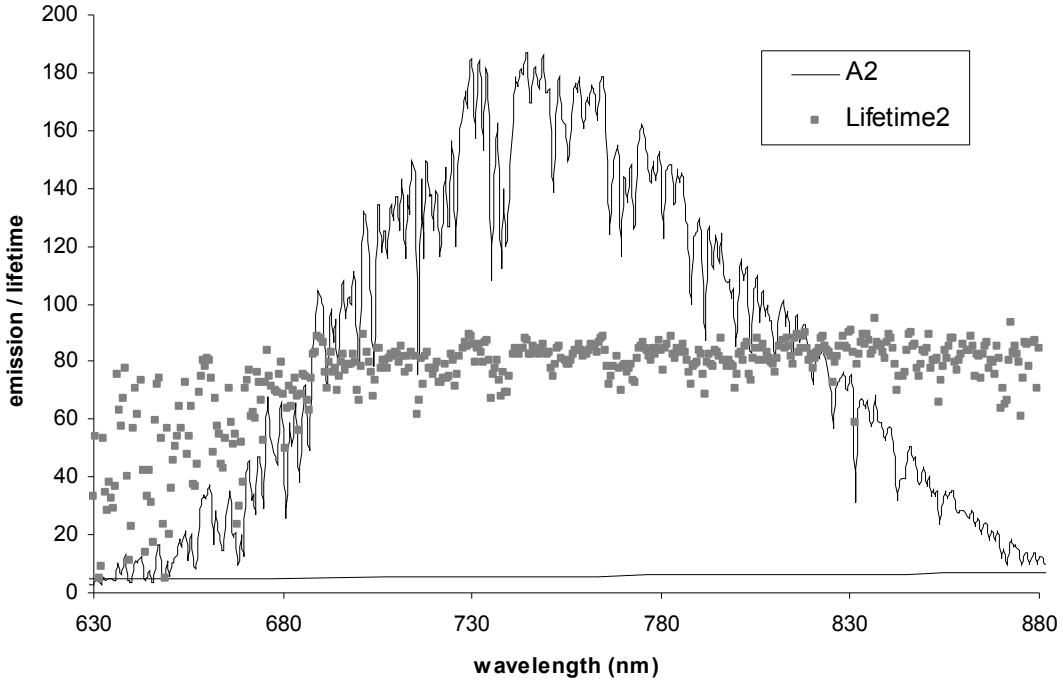

b

Figure 67. Time-resolved emission spectra of 3.17 x 10^{-5} M $[(bpy)_2Ru(dpp)]^{2+}$ with 3 M Ag^+ in methanol: (a) A_1 set; (b) A_2 set.

Table 12. Emission of $[(bpy)_2Ru(dpp)]^{2+}$ with Ag^+ in water and methanol.

	Ru-dpp (H_2O)	Ru-dpp-Ag (H_2O)	Ru-dpp (MeOH)	Ru-dpp-Ag (MeOH)
λ_{max1} (nm)	704	750	698	721
λ_{max2} (nm)	n/a	750	n/a	745
τ_1 (ns) [error]	125 [9]	90 [19]	150 [8]	178 [46]
τ_2 (ns) [error]	n/a	33 [7]	n/a	81 [11]

3.H. Association of $[(bpy)_2Ru(dpp)]^{2+}$ with Cd^{2+} and Zn^{2+}

A more thorough examination of the association of Cd^{2+} and Zn^{2+} with $[(bpy)_2Ru(dpp)]^{2+}$ was accomplished. The absorption spectra from the titration of $[(bpy)_2Ru(dpp)]^{2+}$ with increasing $[Cd^{2+}]$ is shown in Figure 68a. The bpy transition at 422 nm is reduced by 7% and the low energy dpp transition red-shifts. The absorbance at 520 nm can be plotted *vs.* $[Cd^{2+}]_o$ (Figure 68b) and the equilibrium constant for association from the data fit to equation (94) is 9 ± 2 M^{-1}. The extinction coefficient for the presumed bimetallic $[(bpy)_2Ru(dpp\text{-}Cd)]^{4+}$ at 520 nm is 5545 M^{-1} cm^{-1} compared to 2623 M^{-1} cm^{-1} for the free species. One isosbestic point at 491 nm is observed. A strikingly similar effect is seen with Zn^{2+} (Figure 69a) including the reduction in intensity at the 420 nm by 7% and red-shift of the low energy MLCT transition. For the fit of changing

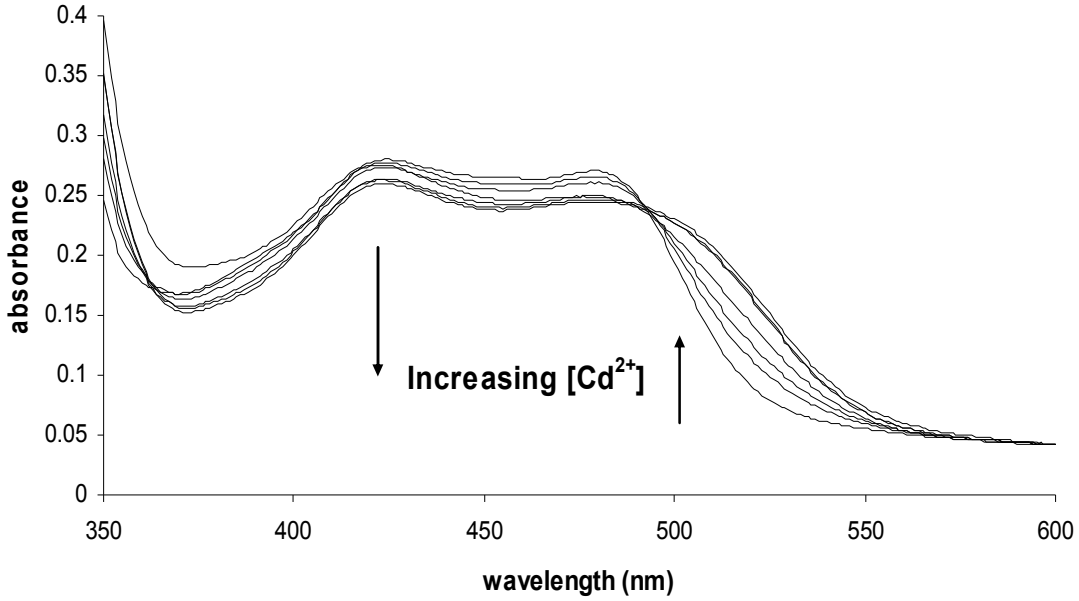

a

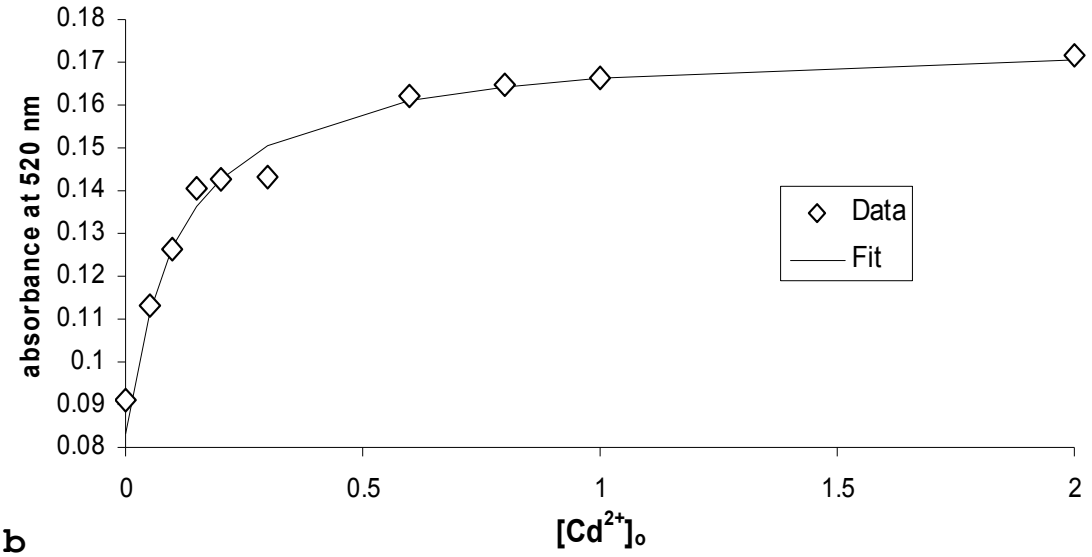

b

Figure 68. Absorption spectra of 3.17 x 10^{-5} M $[(bpy)_2Ru(dpp)]^{2+}$ with increasing $[Cd^{2+}]$: (a) spectra; (b) fit.

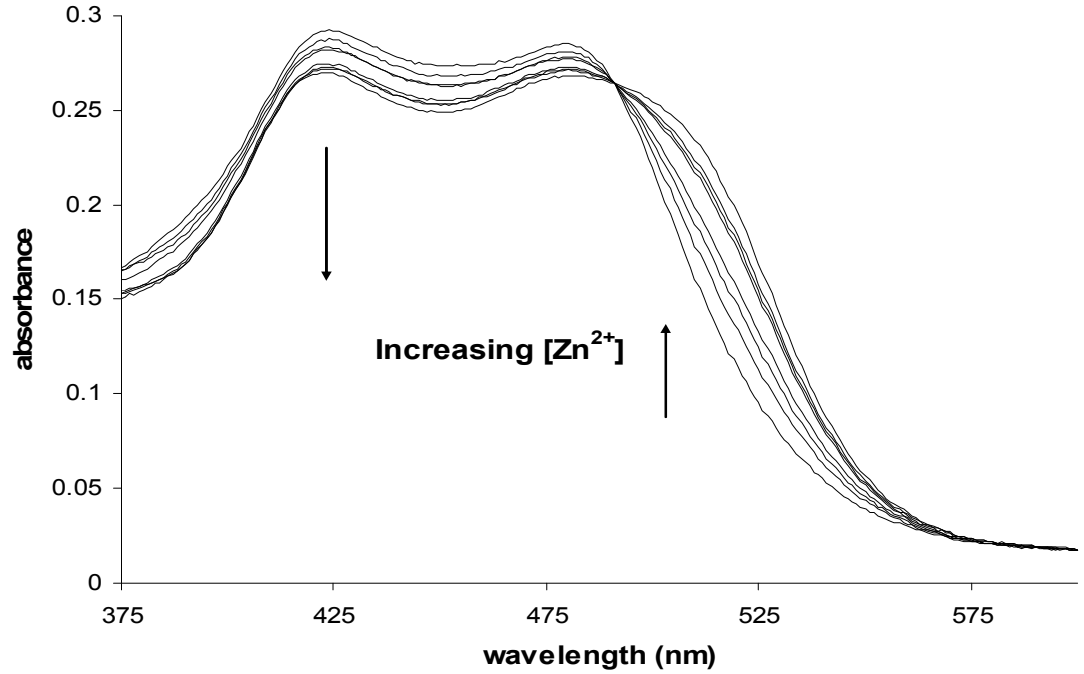

a

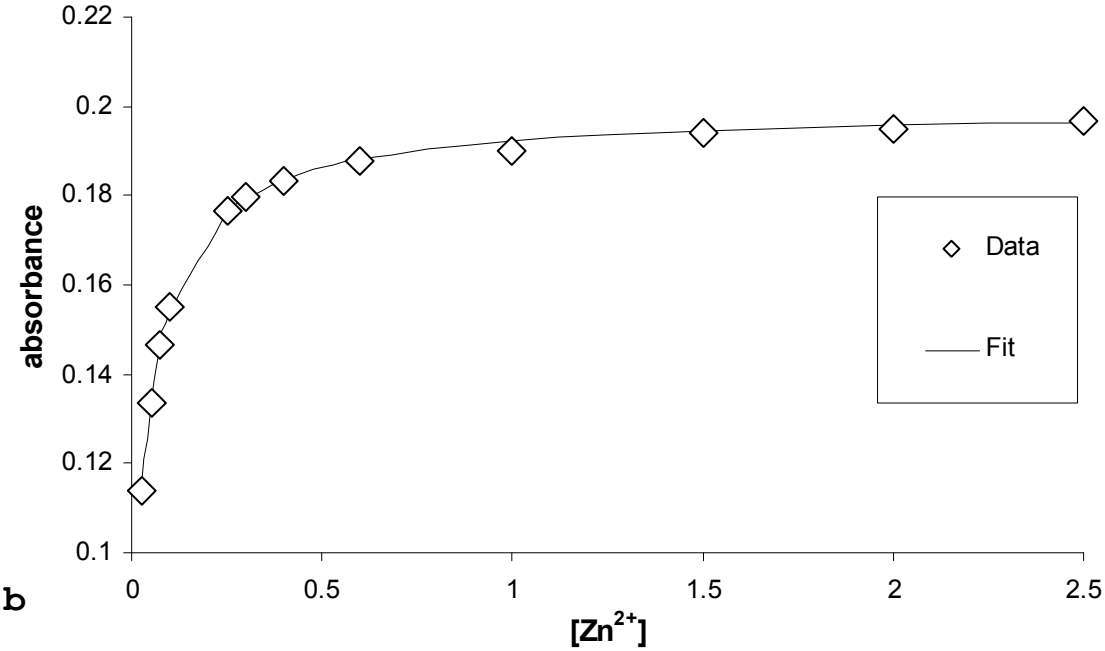

b

Figure 69. Absorption spectra of 3.17 x 10^{-5} M $[(bpy)_2Ru(dpp)]^{2+}$ with increasing $[Zn^{2+}]$: (a) spectra; (b) fit.

absorbance at 520 nm, the extracted extinction coefficient is 6294 M^{-1} cm^{-1}, and the equilibrium constant is 15 ± 3 M^{-1}.

The ^{1}H NMR spectra for titration with both Zn^{2+} and Cd^{2+} displayed the same shifts as that seen for titration with Ag^{+}. Representative samples of NMR spectra are shown in Figure 70 for titration with Zn^{2+} and Figure 71 for titration with Cd^{2+}. B3′ and C6″ shift downfield the most. Other downfield shifts are seen in C5″ and C3″. Interestingly, C4″, also on the free pyridyl ring, seems to shift upfield. Distinct from the results with protonation, the A5 proton, which is associated with the pyrazinyl ring, does shift downfield at high metal concentrations. For the Zn^{2+} titration, a plot of change in chemical shift for C6″ and B3″, chosen because their plots reached a limiting value and because they are easily identified in the complicated NMR, yielded sigmoidal curves (Figure 72a). The same is observed for the Cd^{2+} titration (Figure 73a). When the two data sets were normalized for % change, they are nearly coincident (Figures 72b and 73b). Fits to equation (90) did not match the data, and yielded equilibrium constants that average to about 1 M^{-1} for association with both Zn^{2+} and Cd^{2+}, much different from that obtained with the absorption spectra. Imagining the possibility of a chelate effect, meaning, that there could be an equilibrium

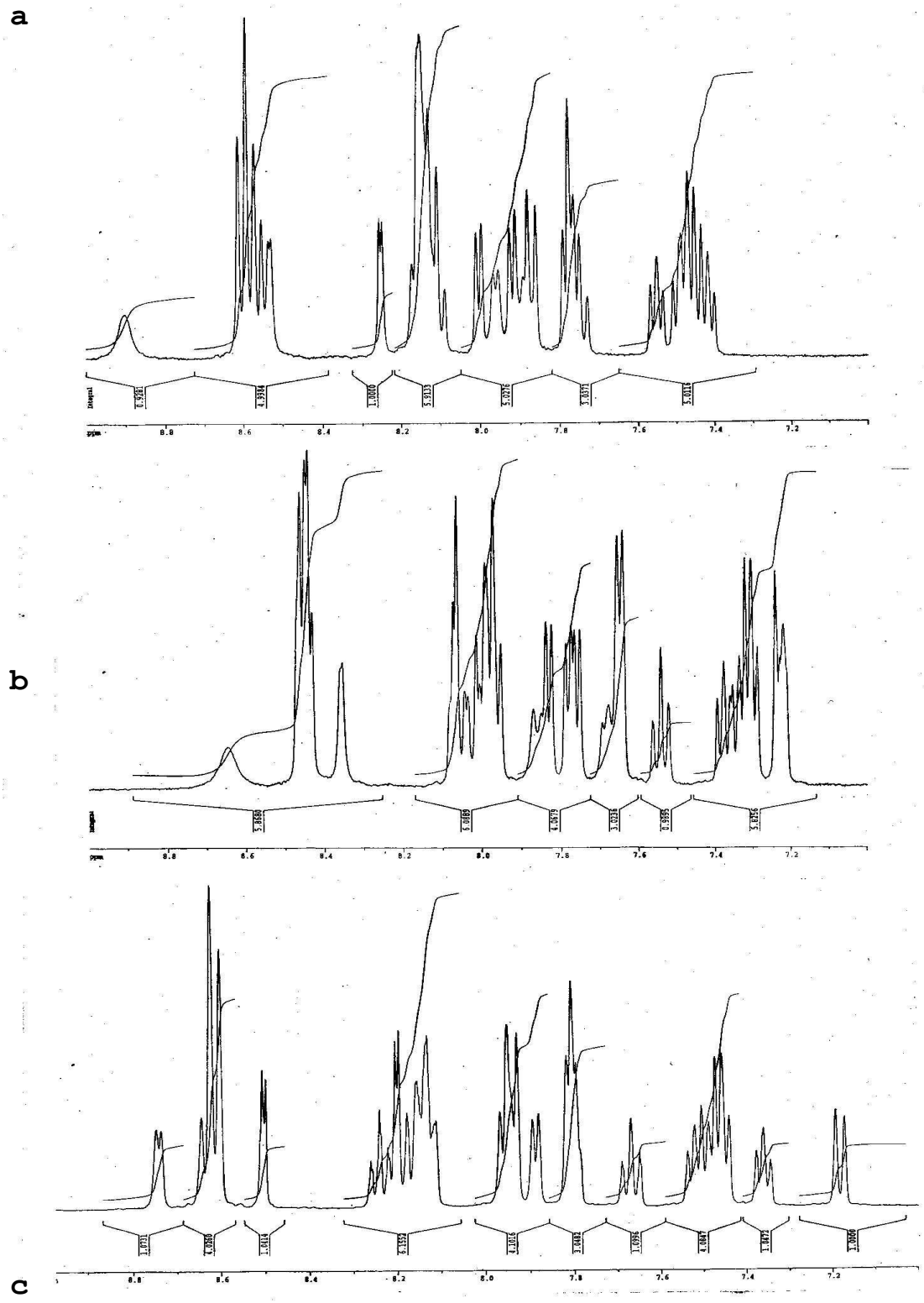

Figure 70. NMR spectra of 0.01 M $[(bpy)_2Ru(dpp)]^{2+}$ with increasing $[Zn^{2+}]$: (a) 0 M; (b) .51 M; (c) 1.33 M.

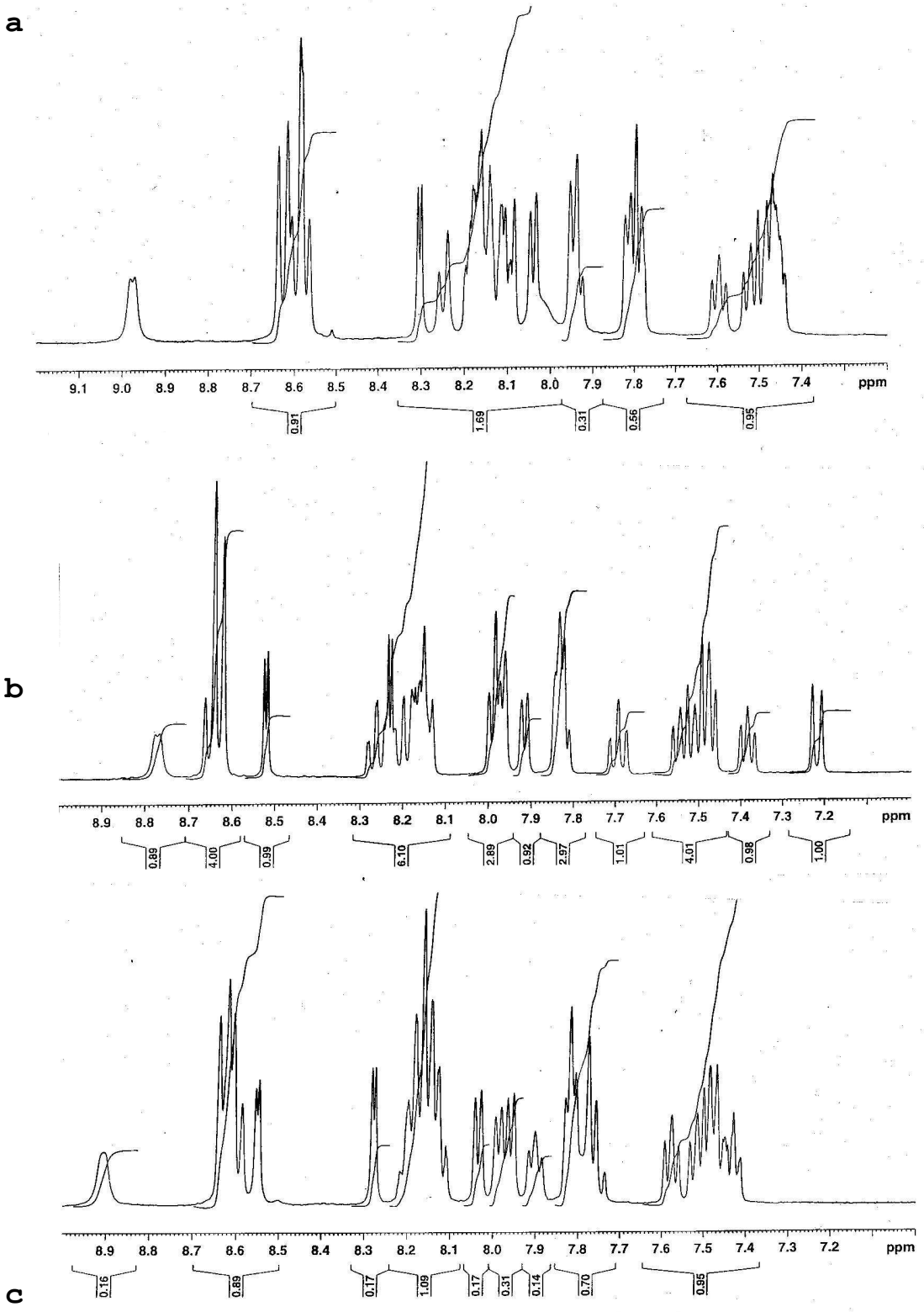

Figure 71. NMR spectra of 0.01 M $[(bpy)_2Ru(dpp)]^{2+}$ with increasing $[Cd^{2+}]$: (a) 0 M; (b) 0.68 M; (c) 2.0 M.

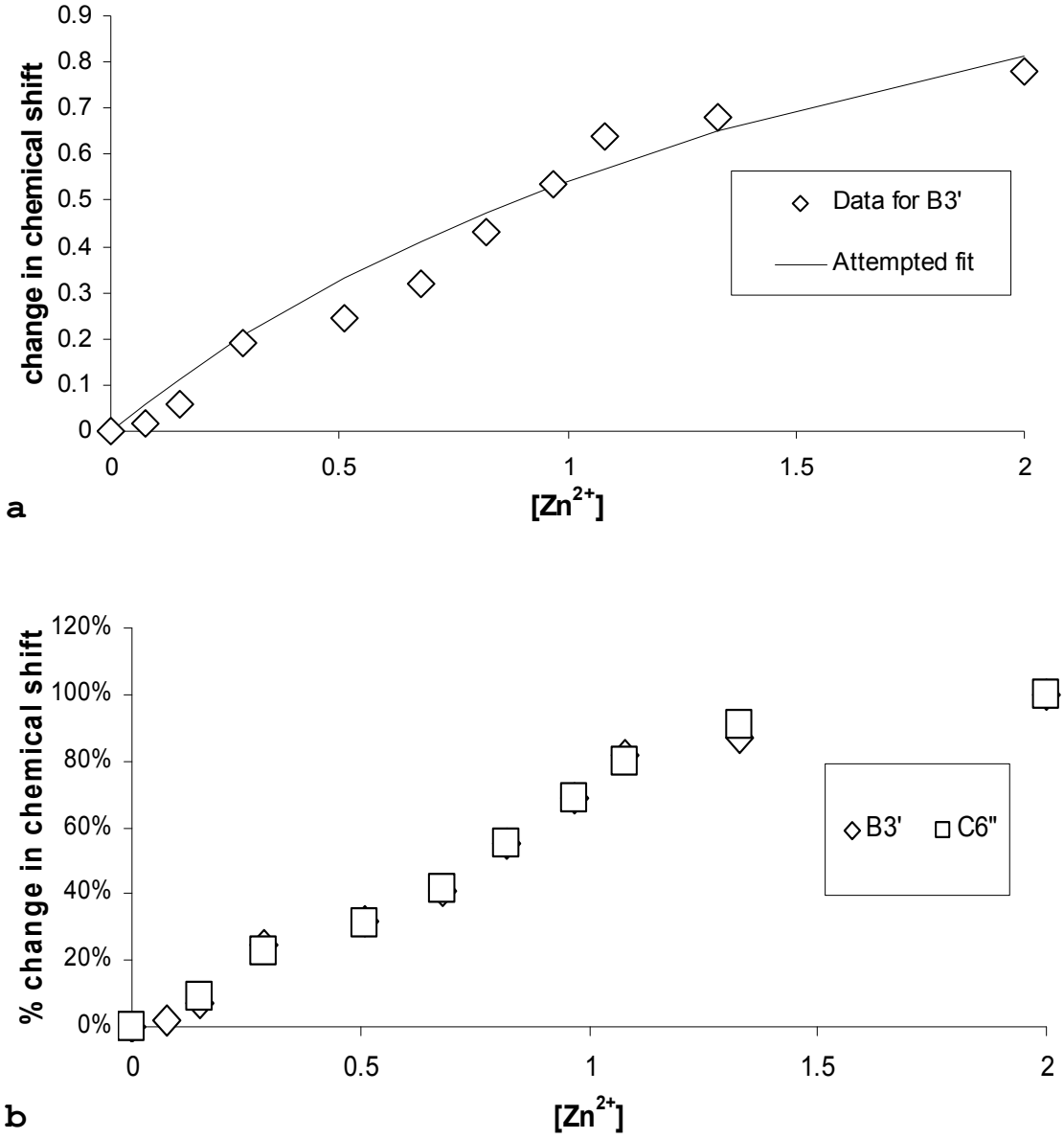

Figure 72. Change in chemical shifts for titration of 0.01M $[(bpy)_2Ru(dpp)]^{2+}$ with increasing $[Zn^{2+}]$: (a) for proton B3′; (b) normalized to % change.

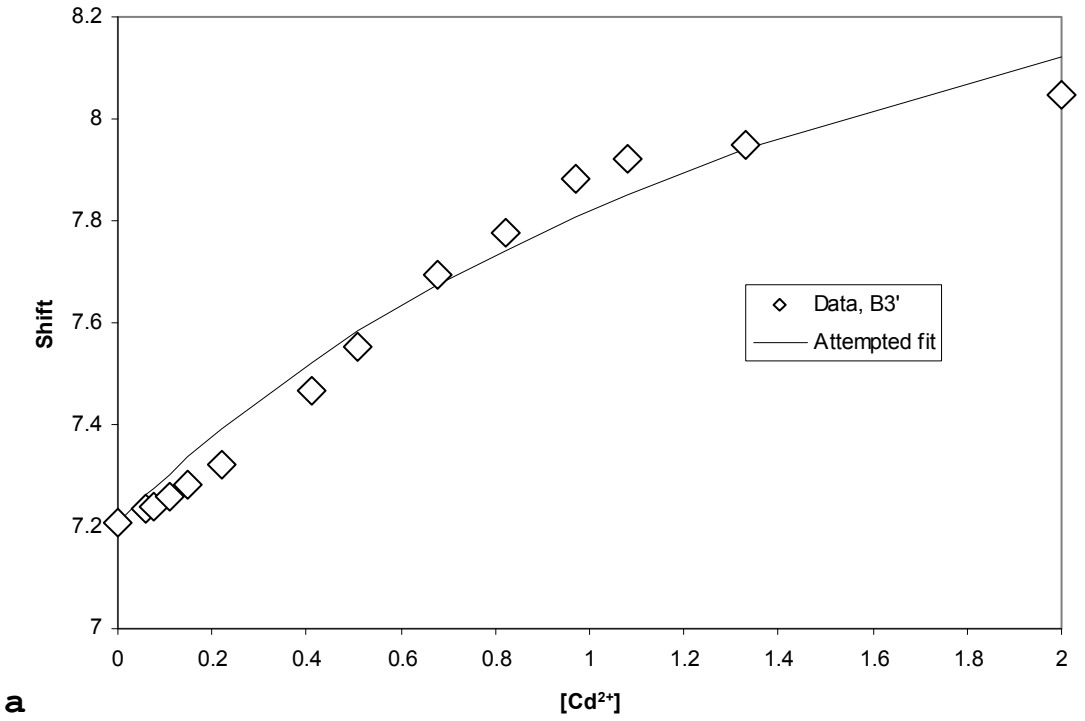

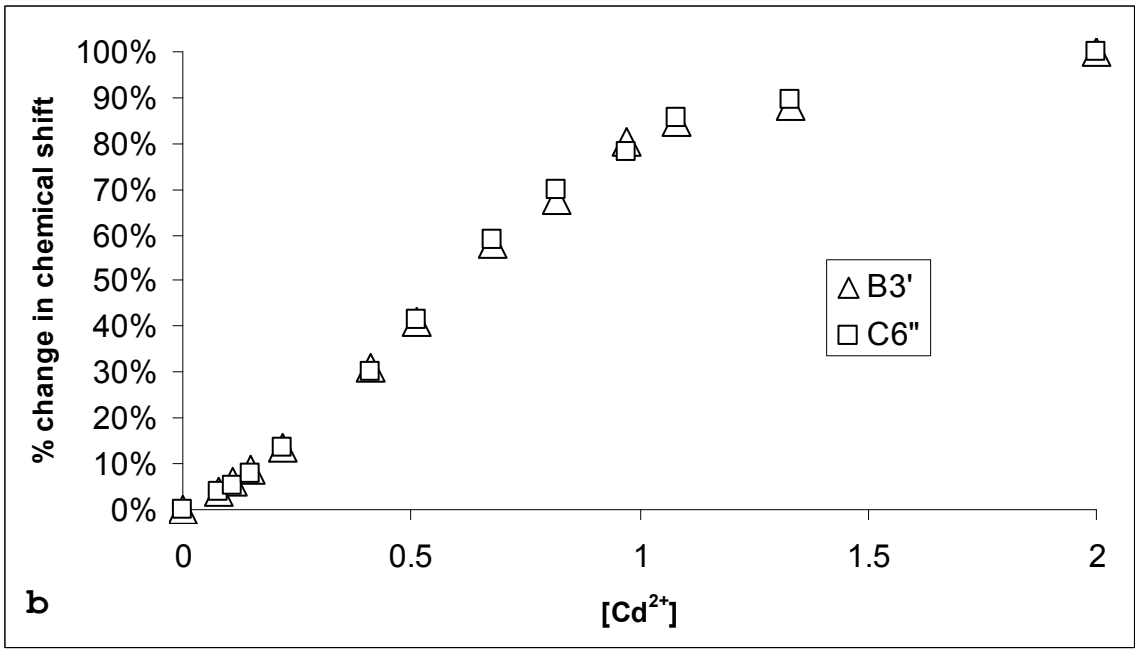

Figure 73. Change in chemical shifts for titration of 0.01 M $[(bpy)_2Ru(dpp)]^{2+}$ increasing $[Cd^{2+}]$: (a) for proton B3′; (b) normalized to % change.

constant for monodentate association followed by an equilibrium constant for bidentate coordination of the metal to the dpp ligand, the mathematical program *Mathematica* was employed to solve the cubic equation that describes the dependency of the chemical shift on *initial* metal cation concentration. Microsoft Excel's internal calculator proved insufficient to work at the needed precision, so the mathematical program *Maple* was integrated into *Excel* to allow use of its internal calculator algorithms joined with *Excel's* feature of non-linear regression fitting with constraints. Even with two equilibrium constants, the shape of the fitting curve was still an inverted exponential (c.f. Figure 62 for Ag^{+}) rather than a sigmoidal curve. It yielded two equilibrium constants whose product would be the observed, overall equilibrium constant, at about 1 M^{-1}. The sigmoidal curve may be due to competing deshielding and shielding effects as the metals coordinate. The sigmoidal fit may also imply consecutive rather than simultaneous equilibria involving more than one site, and is reminiscent of cooperative effects. Given the reliability of the equilibrium constants obtained from the absorbance fits, they will be used for further data analysis.

With increasing concentration of both Zn^{2+} and Cd^{2+} the emission of $[(bpy)_2Ru(dpp)]^{2+}$ decreases in intensity and shift to the red (Figures 74 & 75a respectively). $[(bpy)_2Ru(dpp)]^{2+}$ emission templates can be used to clear the spectra from deviations from Gaussian fits at high energy (Figures 74b and 75b). No further changes are observed on going from 1 M to 4 M $[M^{2+}]$, and the final emission maxima are 750 and 755 nm for Cd^{2+} and Zn^{2+}. The red shifts are accompanied by decreases in the emission lifetimes. Double exponential fits to all data sets, including the sample without any Cd^{2+} or Zn^{2+} reveal the presence of a red-shifted emission with an emission maximum at about 740nm (A_2 values). Following it in the Cd^{2+} titration, it does not significantly red shift (Figure 76) as compared with the A_1 values that red shift, similar to the steady state (Figure 77). For titration with Zn^{2+} no discernable pattern could be seen in terms of changing intensity, though both sets of A_1 and A_2 values red shift. For titration with Cd^{2+}, the lifetime, τ_2, is consistent throughout, at 28 ± 7 ns. However for the titration with Zn^{2+}, the lifetime reaches a limiting value. This second emission may in fact be the analysis resolving the spectra of the two emitting species at intermediate values. Or, given that it appears in samples without any titrant, its

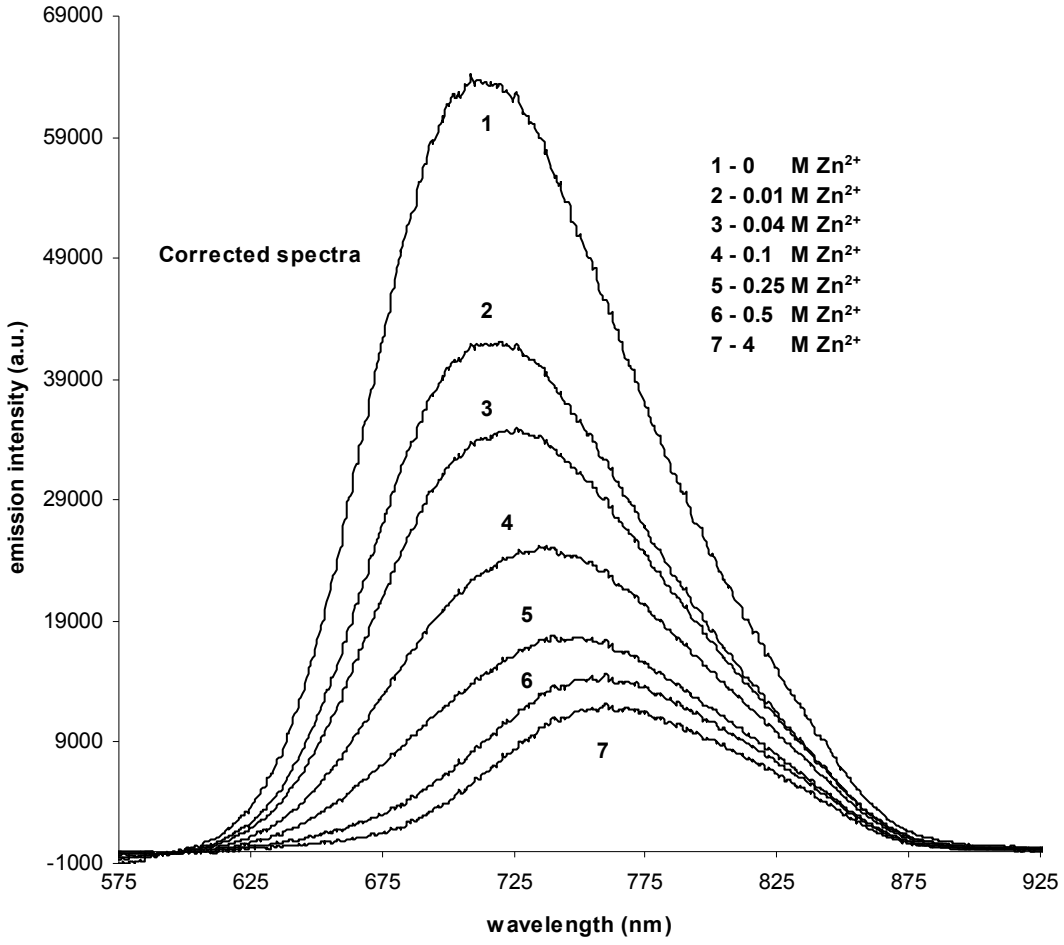

Figure 74. Corrected emission spectra of titration of 3.17 x 10^{-5} $[(bpy)_2Ru(dpp)]^{2+}$ with increasing $[Zn^{2+}]$.

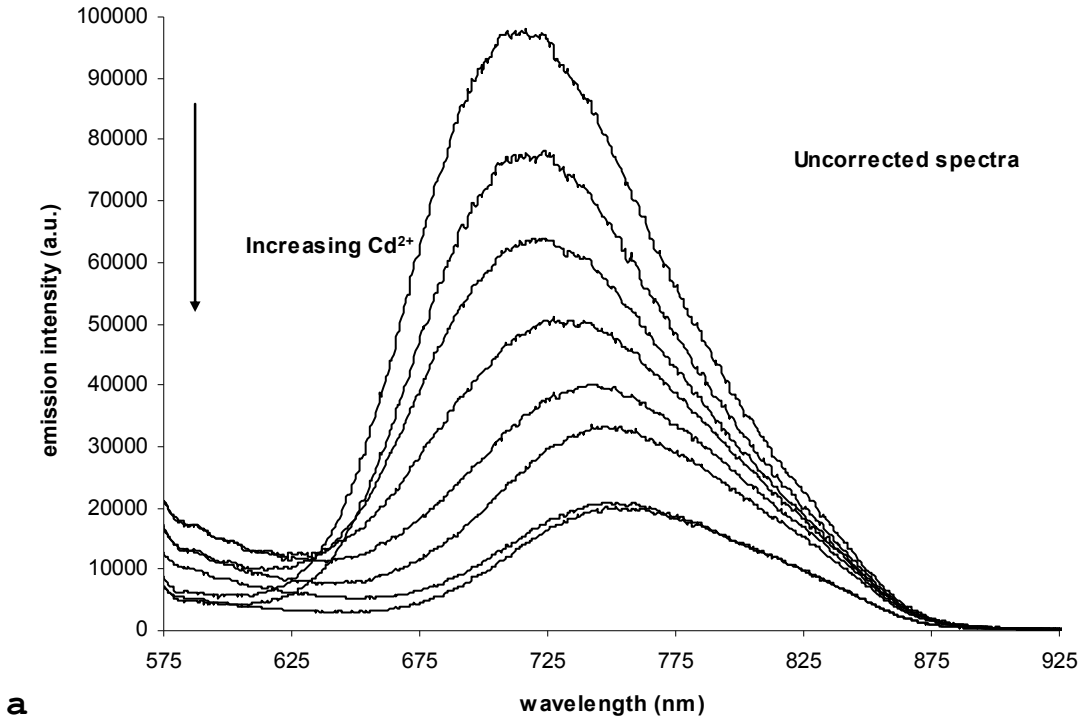

a

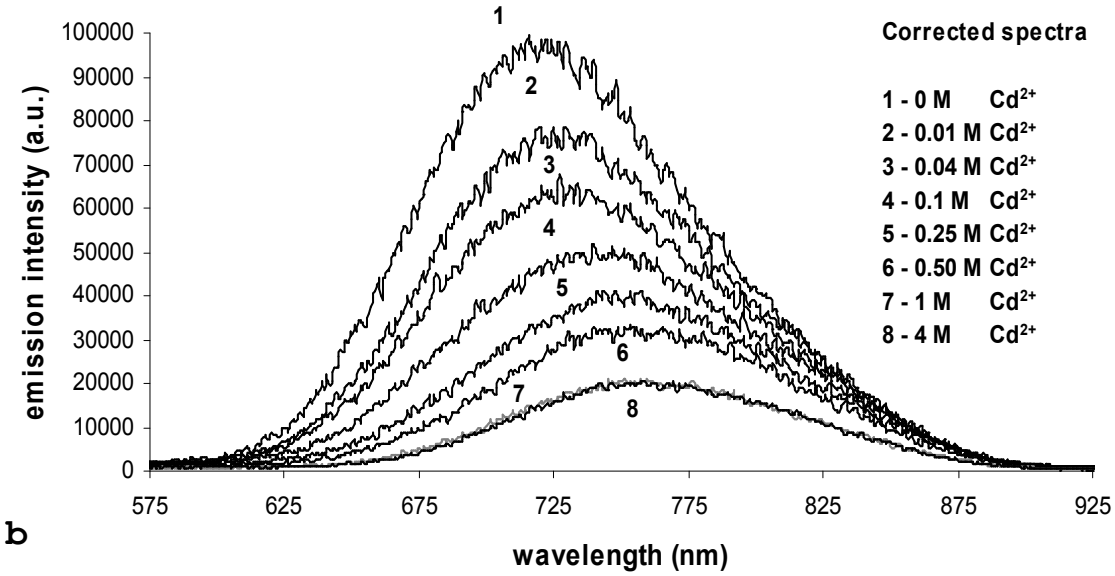

b

Figure 75. Emission spectra of titration of 3.17 x 10^{-5} M $[(bpy)_2Ru(dpp)]^{2+}$ with increasing $[Cd^{2+}]$: (a) uncorrected spectra; (b) corrected spectra.

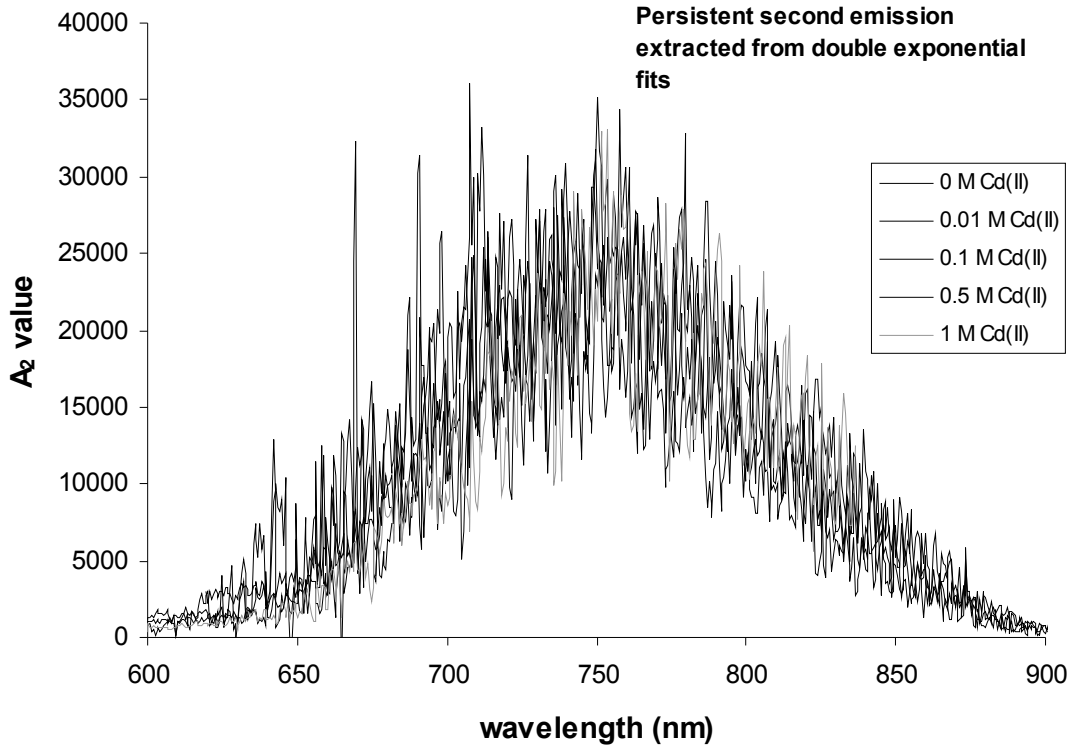

Figure 76. Persistent, separate, red-shifted emission in the titration of 3.17 x 10^{-5} M $[(bpy)_2Ru(dpp)]^{2+}$ with increasing $[Cd^{2+}]$.

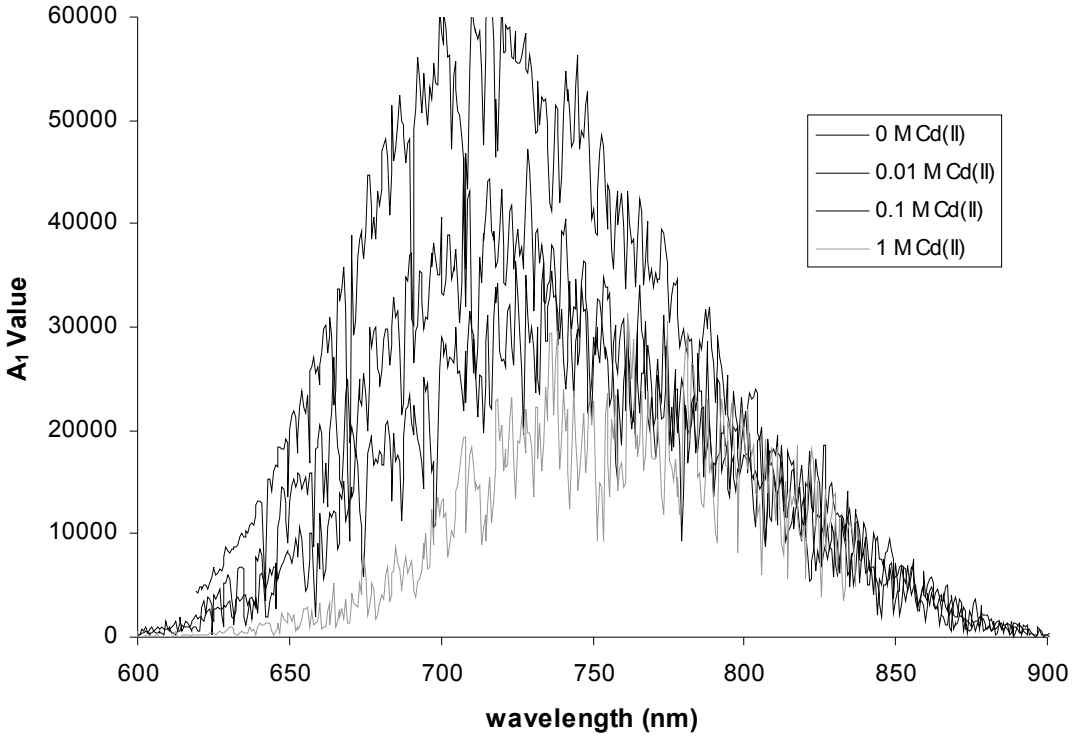

Figure 77. Red-shifting emission in titration of 3.17×10^{-5} M $[(bpy)_2Ru(dpp)]^{2+}$ with increasing $[Cd^{2+}]$.

presence may possibly have to do with the buffer solution, the presence of high concentration $Ca(NO_3)_2$ to fix the nitrate concentration and ionic strength, the reduced pH, or an anomaly of the mathematical analysis *(vide infra)*. For the A_1 values, the lifetimes are consistently reduced and levels off at 41 ± 15 ns for Cd^{2+} and 54 ± 15 ns for Zn^{2+}. As can be seen from the Stern-Volmer plot of these lifetime data, τ_1, a plot of $(\tau_o/\tau)-1$ *vs.* concentration shows negative deviations (Figure 78a-b). A full analysis of the steady-state and time-resolved spectra, in order to extract rate constants for quenching, and excited state equilibrium constants, will be presented in the discussion below (Section 4.G).

The quantum yields of the presumed bimetallic complexes, $[(bpy)_2Ru(dpp\text{-}Zn)]^{4+}$ (Figure 79) and $[(bpy)_2Ru(dpp\text{-}Cd)]^{4+}$ in pH=5 buffer solution (Figure 80) were determined to be 0.00063 ± .0001 and 0.00026 ± .00003, respectively, relative to $[(bpy)_2Ru(dpp)]^{2+}$. Templates (at pH=5) were used to obtain spectra suitable for integration under the steady-state curve (Figures 79b and 80b) from 565nm-915nm. From the quantum yield values, the radiative and non-radiative rate constants can be calculated. The lifetimes used are the limiting lifetimes from the double

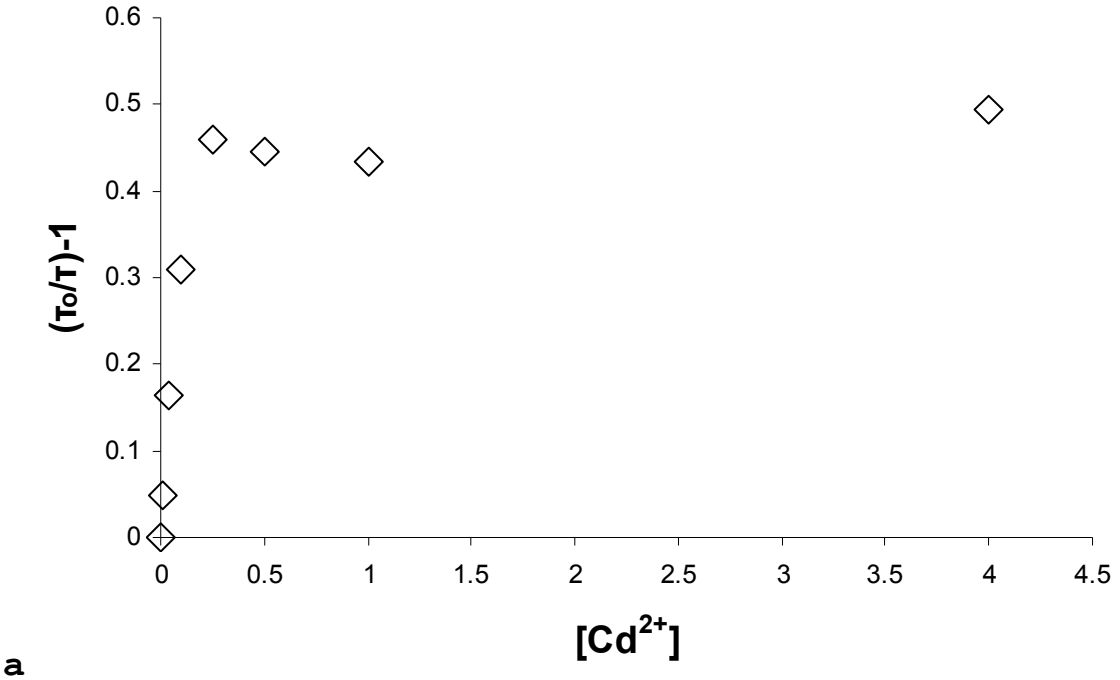

a

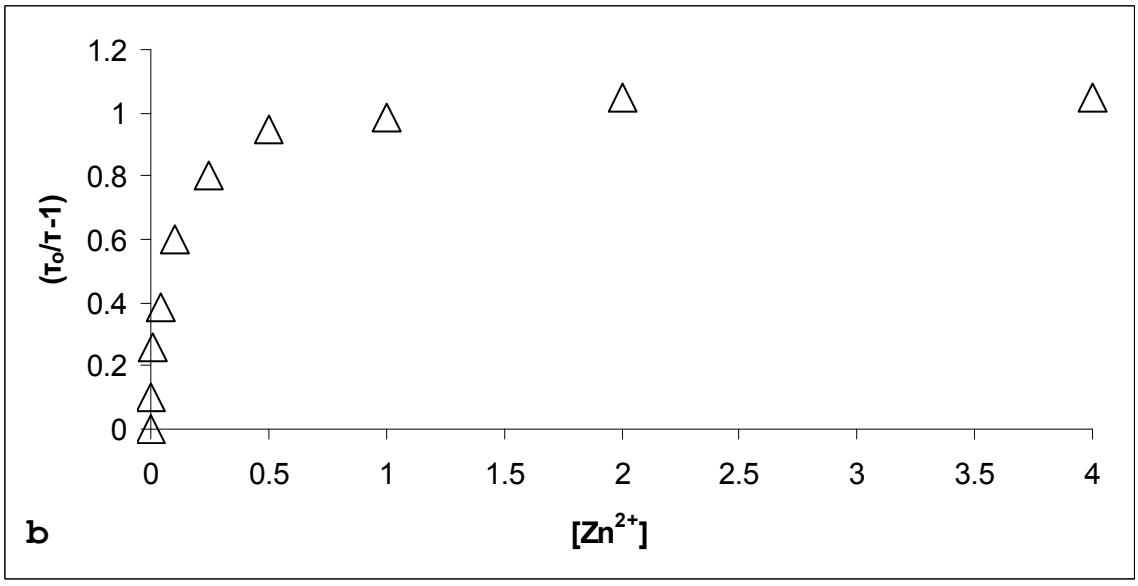

b

Figure 78. Stern Volmer plots of lifetime data for titration of 3.17 x 10^{-5} M $[(bpy)_2Ru(dpp)]^{2+}$ with increasing $[Cd^{2+}]$ & $[Zn^{2+}]$: (a) with Cd^{2+}; (b) with Zn^{2+}.

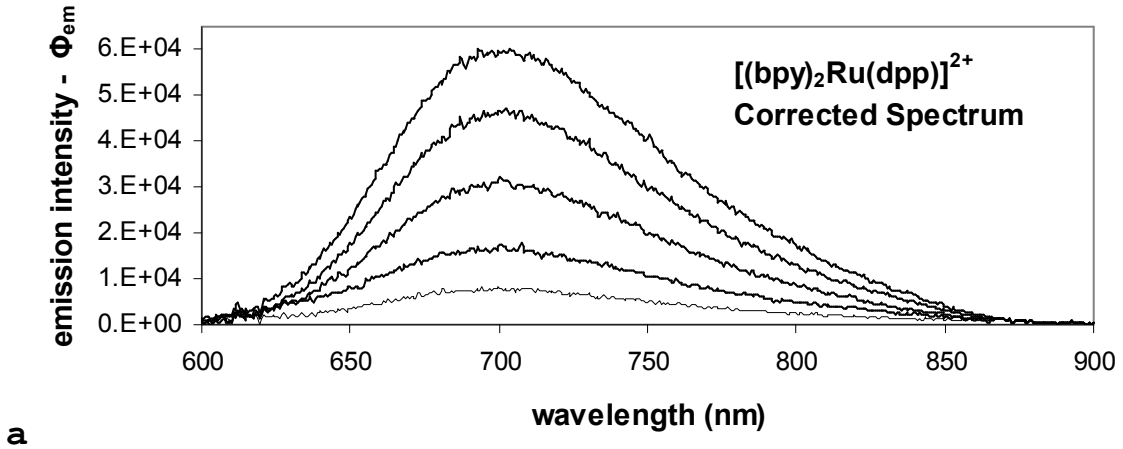

a

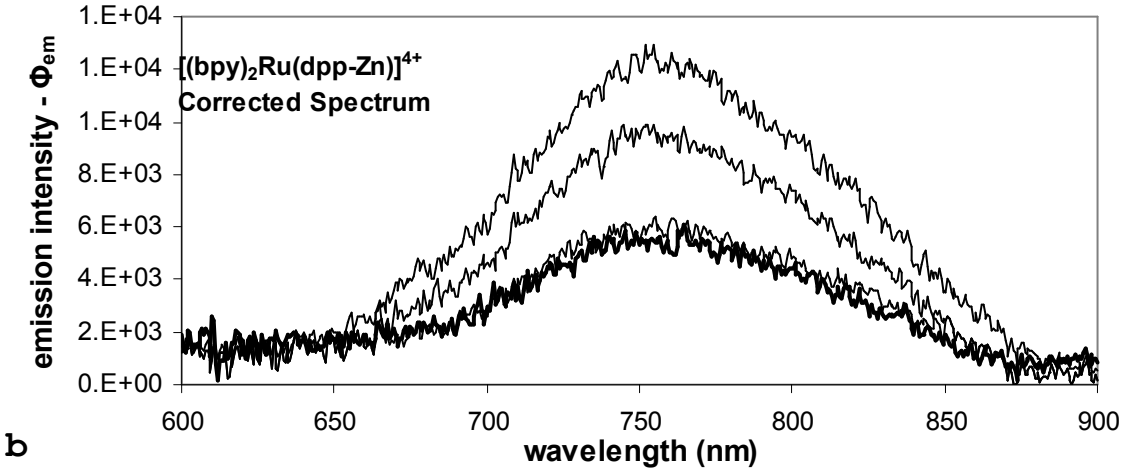

b

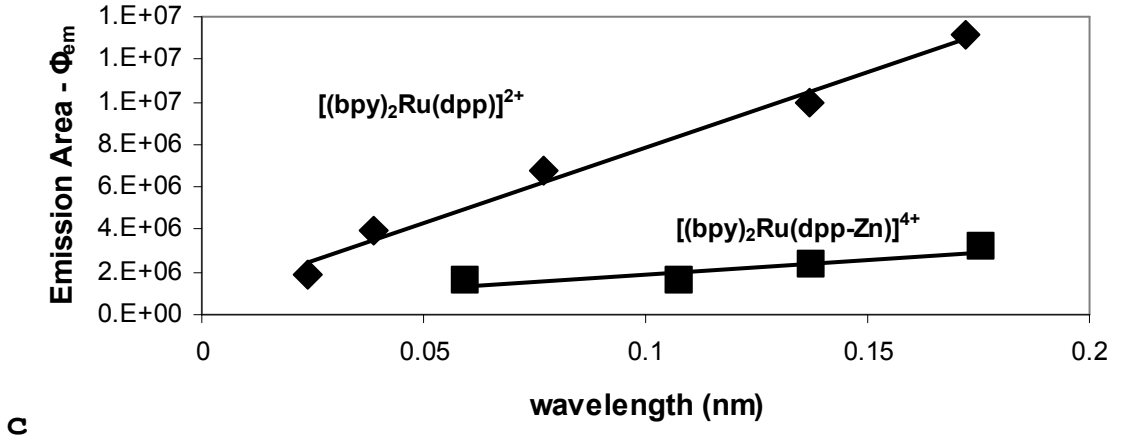

c

Figure 79. Quantum yield determination of $[(bpy)_2Ru(dpp\text{-}Zn)]^{4+}$: (a) uncorrected spectra; (b) corrected spectra; (c) gradients.

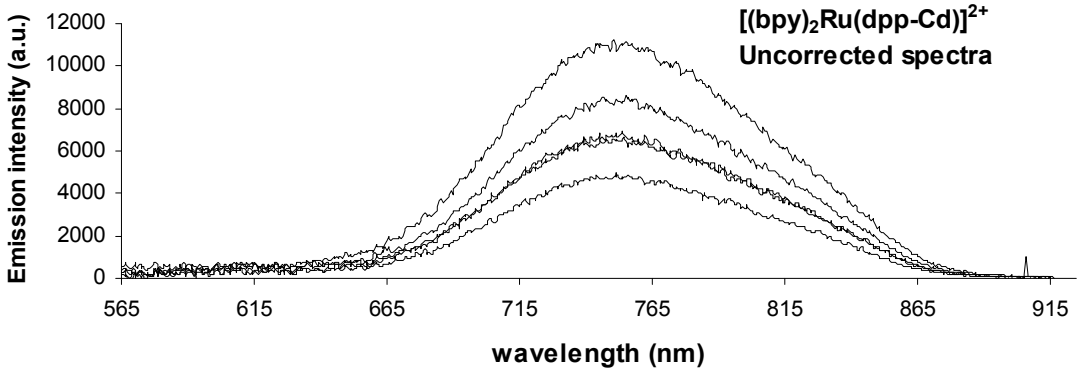

a

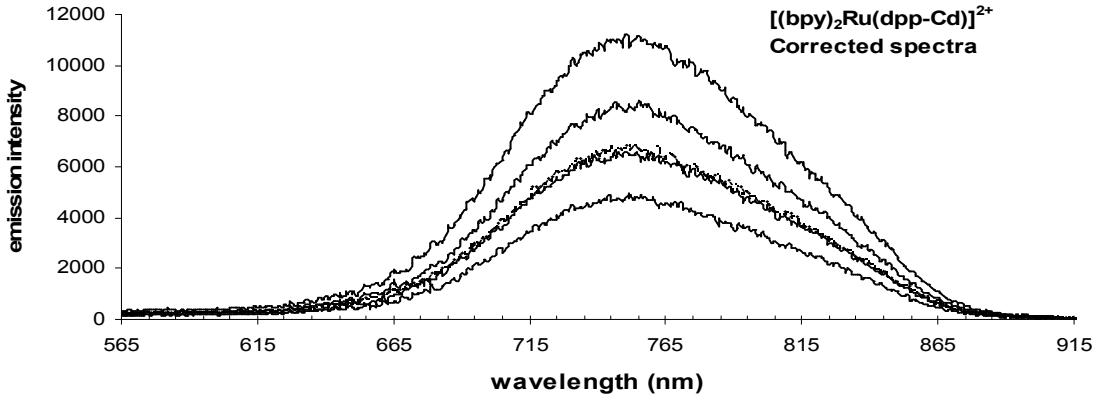

b

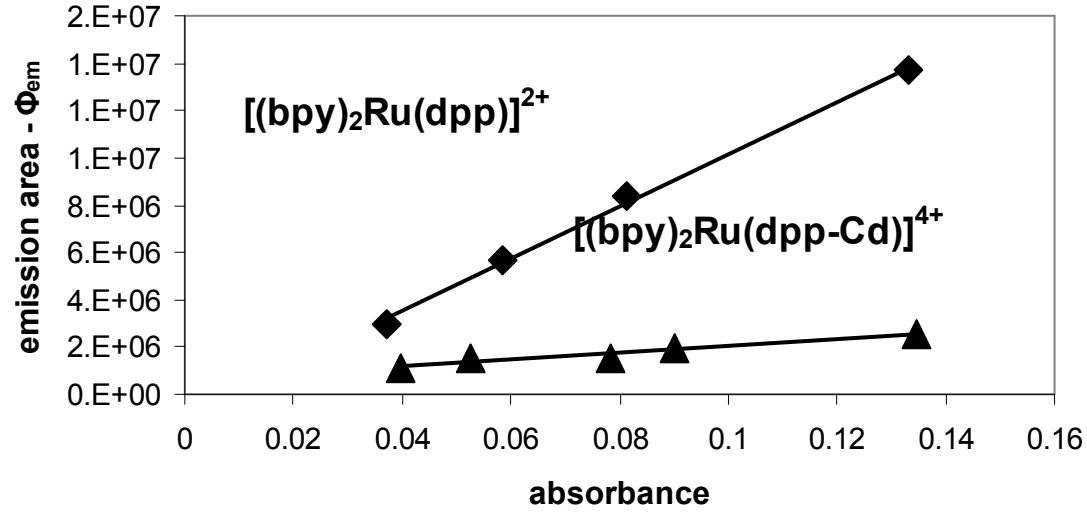

c

Figure 80. Quantum yield determination of $[(bpy)_2Ru(dpp\text{-}Cd)]^{4+}$: (a) uncorrected spectra; (b) corrected spectra; (c) gradients.

exponential fits *(vide infra)*. The photophysical properties are compiled in Table 13.

Table 13. Comparative photophysical properties of $[(bpy)_2Ru(dpp\text{-}Zn)]^{4+}$ and $[(bpy)_2Ru(dpp\text{-}Cd)]^{4+}$

	Ru-dpp (pH7)	Ru-dpp (pH5)	Ru-dpp-Zn^{2+} (pH5)	Ru-dpp-Cd^{2+} (pH5)
λ_{max} (nm)	704	704	762	745
τ_1 (ns)	101.5	78	54	63
Φ_{em}	0.00198	0.00173	0.00063	0.00026
k_r (s^{-1})	2.0×10^4	2.0×10^4	1.2×10^4	4.1×10^3
k_{nr} (s^{-1})	9.8×10^6	1.2×10^7	1.9×10^7	1.6×10^7

For comparison the emission of $[(bpy)_2Ru(dpp)]^{2+}$ in 0.5 M Hg^{2+} was examined in 1 M nitric acid to accomplish better solubility of the mercuric ion. Fits of the time-resolved emission of double exponentials yielded two red-shifted emissions with wavelength maxima at 757 nm and 775 nm determined from Gaussian fits (Figure 81a). The 757 nm plot of A_1 *vs.* wavelength has considerable scatter in the data points and is similar to the second emission seen under many of the analyzed time-resolved spectrum from titrations with Cd^{2+} and Zn^{2+}. Its average lifetimes is 26 ns ± 26 whilst that of the 775 nm emission is 8 ± 8 ns, and exhibits a wavelength dependence (Figure 81b). Analysis by single exponential fits (Figure 82) yields an emission with

a

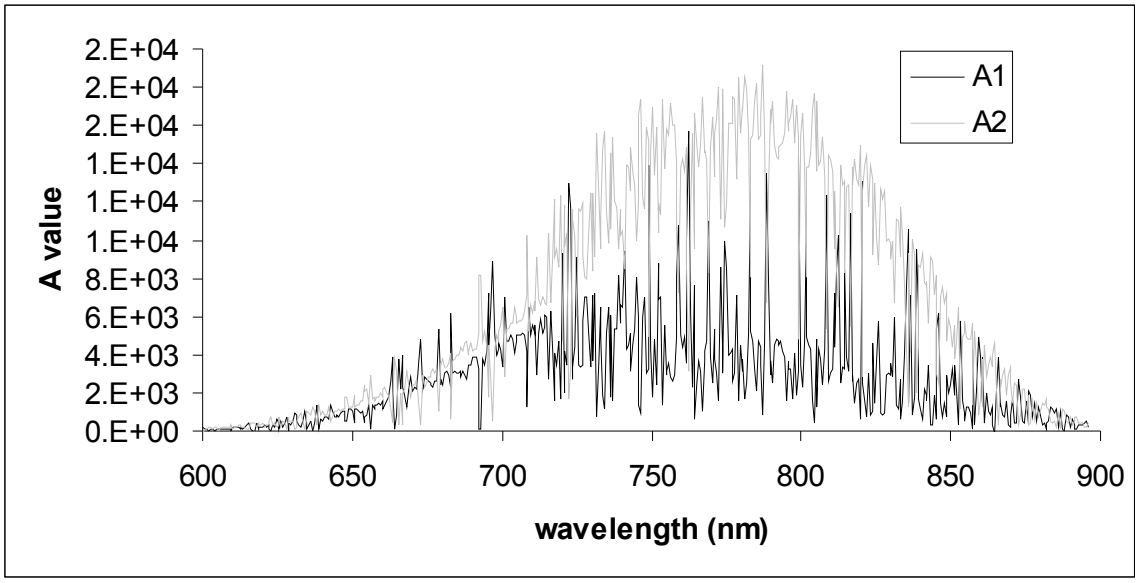

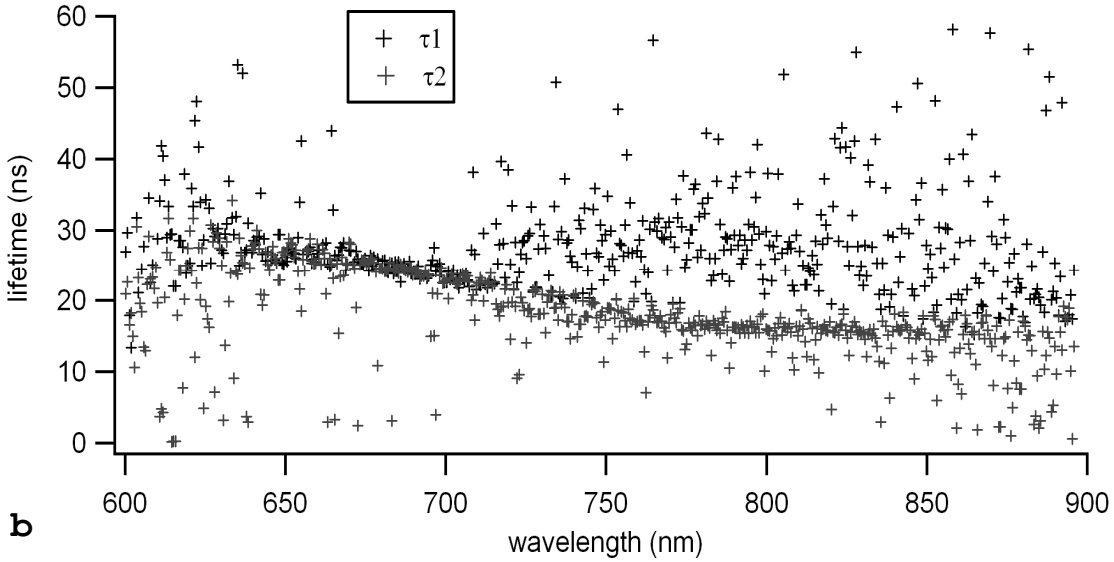

b

Figure 81. Emission spectra, double exponential fits, and lifetimes of 3.17 x 10^{-5} M $[(bpy)_2Ru(dpp)]^{2+}$ with 0.5 M Hg^{2+} in 1M HNO_3: (a) A_1/A_2; (b) lifetimes.

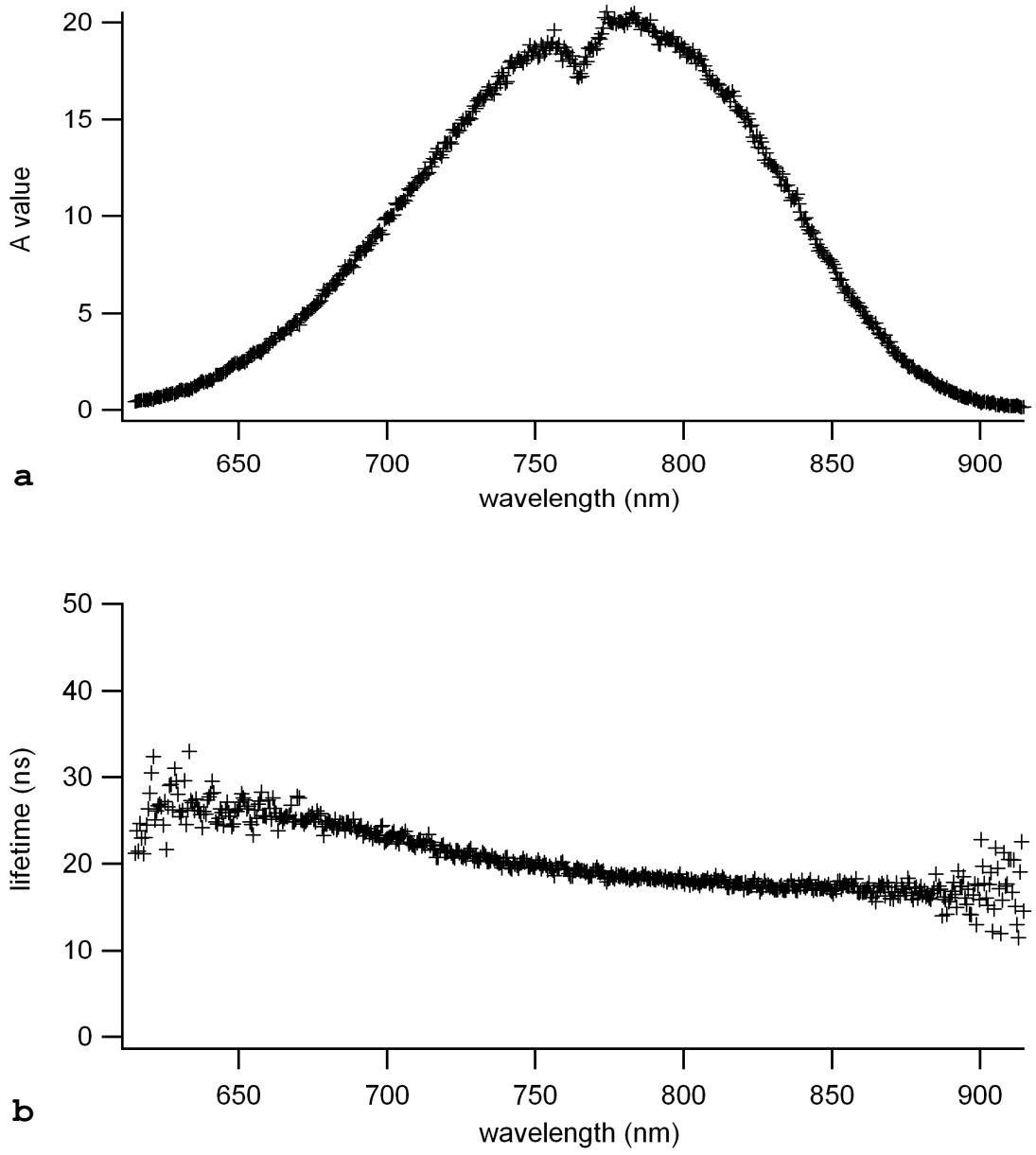

Figure 82. Emission spectra, single exponential fit, and lifetimes of 3.17 x 10^{-5} M $[(bpy)_2Ru(dpp)]^{2+}$ with 0.5 M Hg^{2+} in 1M HNO_3: (a) A_1; (b) lifetimes.

a wavelength maximum at 775 nm and an average lifetime over the wavelengths 650-850 nm of 9 ± 1 ns.[xxviii]

First, quite clearly, $[(bpy)_2Ru(dpp)]^{2+}$ forms emissive bimetallics with several metal cations, which are not thermodynamically isolatable, but are observed only spectroscopically. Second, the imine nitrogens of the dpp ligand are the "active site" for association. The mechanism of these interactions, particularly with Cd^{2+} and Zn^{2+} are explored more intensely in the discussion below.

_____

[xxviii] The deviation in the spectrum is due to damage of the ICCD camera being borrowed at the time. The reduction was always seen at the same pixels. The lab camera was being repaired at the time.

4. DISCUSSION

4.A. Characterization of $[(bpy)_2Ru(dpp)]^{2+}$

4.A.1. Absorption & Emission Analysis

Resonance Raman experiments identify the 420 nm and 470 nm MLCT transitions as terminating in different ligands, with the higher energy, 420-nm transition to one of the bpy ligands, and the lower energy, 470-nm transition to the dpp ligand.[93,154,155] The fact that the emission of $[(bpy)_2Ru(dpp)]^{2+}$ originates from the dpp ligand regardless of excitation immediately implies that excitation of the MLCT terminating on bpy must migrate to the dpp ligand before emission. This is unsurprising given that emission is expected from the lowest energy state (Kasha's rule). In Ru(II) diimines based on $[Ru(bpy)_3]^{2+}$, singlet excitation is followed by near unity intersystem crossing to the "triplet" manifold from which emission occurs, although spin-orbit coupling blurs to some degree the singlet/ triplet distinction.[156-158] Interestingly, recent experiments have revealed that upon excitation of $[Ru(bpy)_3]^{2+}$ the excited electron is initially delocalized on three ligands, and then charge transfer occurs to one specific ligand, from which localized emission occurs.[134,135] A similar explanation can appropriately be invoked for $[(bpy)_2Ru(dpp)]^{2+}$ although further investigation has

revealed alternative, unconventional relaxation pathways (*vide infra*). Even so, based on the Gaussians fits in Figure 18b to equation (85), the full-width at half-maximum can be determined, in energy units (cm^{-1}), for the two absorption transitions to bpy and dpp, which are 5532 cm^{-1} and 2552 cm^{-1} respectively. The ratio of the energy width of the bpy to dpp transitions is 2.17:1. It might be approximated that an electron has equal opportunity to populate either of the three ligands. Given that there are two bpy ligands, it would seem that the probability of populating the bpy ligand would be twice that of populating the dpp ligand. In such cases, the molar absorptivities would sum and the absorption transition would be twice as intense as that of dpp. Instead though, the bpy transition is broadened, suggesting some differentiation between the ligands. Since the dpp ligand is asymmetric when coordinated, this would differentiate the bpy ligands, making them non-equivalent moieties. Hence, their MLCT absorption transitions would not necessarily coincide. Similar evidence is seen in the NMR spectrum with the chemical shifts of the bipyridine protons non-coincident, as they are in the symmetrical complex $[Ru(bpy)_3]^{2+}$.

Curiously though, the excitation spectrum for emission does not mirror the absorption spectrum (Figure 18a). The

excitation shows the outline of the dpp transition, but the bpy transition is a weak shoulder, and does not match its higher extinction coefficient in the absorption spectrum of 9703 M^{-1} cm^{-1} relative to 9214 M^{-1} cm^{-1} for dpp. This suggests the quantum yield of emission, when populating the MLCT *via* the bpy ligand, is slightly less than when populating *via* the dpp ligand, and thus a measurable amount of energy is lost during intersystem crossing.

Nevertheless, no wavelength dependence of the lifetime means there is only one emitting species and/or structure. Previous reports have indicated that MLCT population in similar Ru(II) diimines occurs on the order of 100 fs,[134,135] thus any risetime observed is solely due to the pulse itself. The lifetimes obtained are similar to those of published reports.[93] The lifetime of 125 ± 12 ns, coupled with a quantum yield of 0.00198,[xxix] corresponds to a radiative rate constant, k_r of 1.7 x 10^4 s^{-1}. Though $[(bpy)_2Ru(dpp)]^{2+}$ is 21 times less emissive than $[Ru(bpy)_3]^{2+}$, its radiative rate constant is only about 4 time less. From numerous studies of similar Ru(II) diimines, it is commonly accepted that the MLCT emissive state has mostly

[xxix] The quantum yield obtained differs from the published value of .046,[93] where the estimate was referenced to the quantum yield of $[Os(bpy)_3](PF_6)_2$ at 77 K. Since the work here specifically uses a reference standard with a known quantum yield at room temperature, it is considered to be more accurate.

triplet character,[33] part of the evidence being the ease with which it is quenched by oxygen.[71] Indeed, $[(bpy)_2Ru(dpp)]^{2+}$ is quenched to form singlet O_2 with a quenching rate constant of 10^9 L mol^{-1} s^{-1}.[159] The charge-transfer nature of the ^{3}MLCT is also confirmed by the slight red-shift on going to more polar solvents, from ethanol to methanol to water (Table 5), since more polar solvents are known to stabilize charge transfer states.[160]

4.A.2. NMR Analysis

It is interesting to note some effects on the proton shifts of metal chelated bipyridines. Figure 83 shows the "evolution" of the chemical shifts on going from pyridine, to bipyridine, to ruthenium tris-bipyridine, to $[(bpy)_2Ru(dpp)]^{2+}$. Upon chelation, proton 6, shown in bold, undergoes a dramatic upfield shift from 8.64 to 7.77 ppm, opposite of the expected downfield shift that results from the metal inductive effect, as seen in protons 4 & 5. Each proton 6 on the bpy ligands is affected by adjacent ring currents in the three-dimensional structure, particularly D6 which sits above the ring current of the dpp ligand. Such ring current effects on protons 6 and 6′ have been studied, particularly in the simpler $Ru(bpy)_2Cl_2$ system (Figure 84).[161] Proton 3, on the other hand, undergoes a

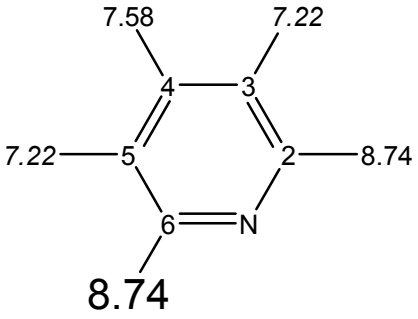

pyridine

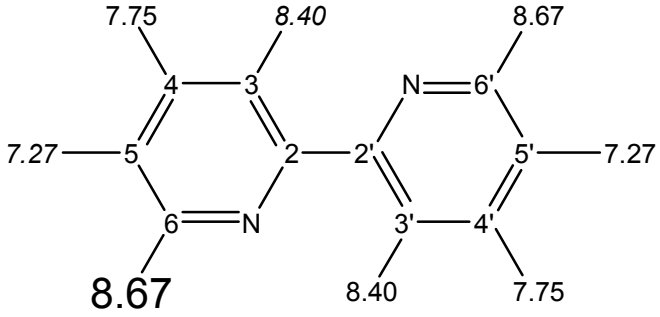

bipyridine

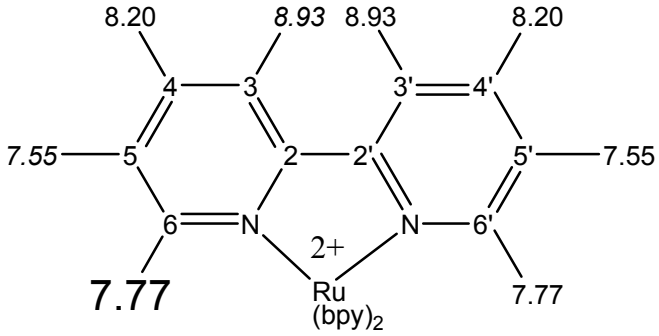

$[Ru(bpy)_3]^{2+}$

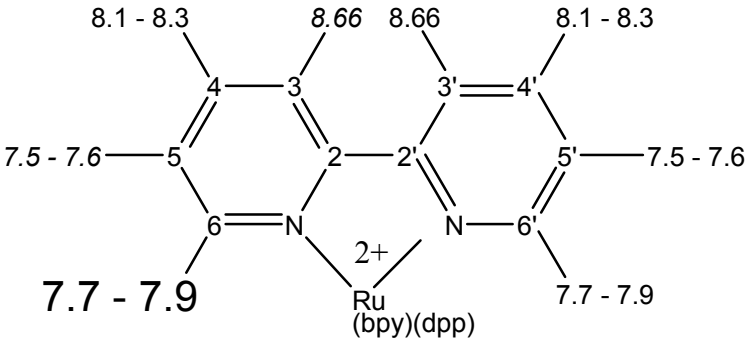

$[bpy_2Rudpp]^{2+}$

Figure 83: Evolution of bpy chemical shifts.

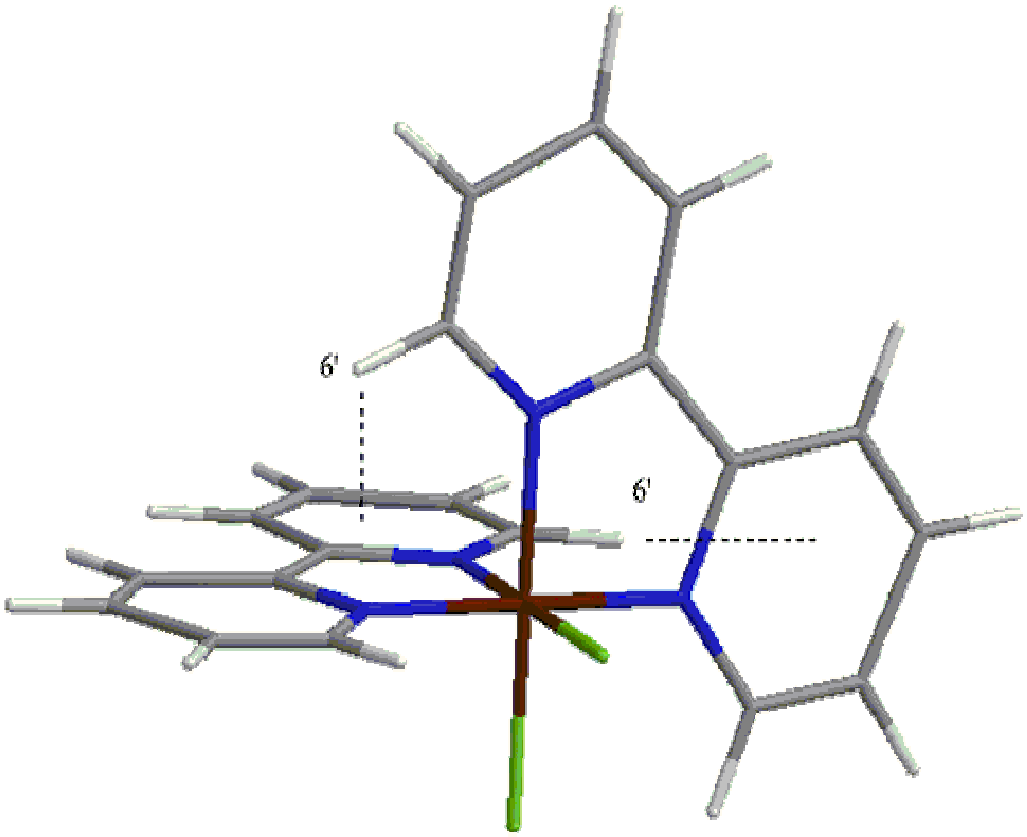

Figure 84: Adjacent ring current effects.

dramatic downfield shift, particularly on the change from pyridine to bipyridine. Besides the additional ring, one other possible explanation is the preferred "trans" conformation of free bipyridine, which would afford a deshielding hydrogen bonding interaction between proton 3 and the adjacent, basic imine nitrogen. A number of studies have looked at the conformation of bipyridine, analyzing its dipole moment,[162-165] polarizability,[166] crystal structure,[167,168] and NMR[137,169] with a general consensus that the near trans conformation is preferred, allowing for the deshielding of proton 3. When coordinated in a bidentate fashion, bipyridine must adopt a cis conformation.[15] While the metal cation will deshield protons 3 and 3′ as expected, their steric interaction will further deshield each other, making them somewhat acidic (reactive to deuteration).[170]

By contrast, the protons of the asymmetrically coordinated dpp ligand are scattered throughout the spectrum. The evolution of the dpp proton shifts is shown in Figure 85, on going from pyrazine and pyridine, to dpp, to $[(bpy)_2Ru(dpp)]^{2+}$. The published assignments for $[Ru(dpp)_3]^{2+}$ are included for comparison.[171] A5 and A6 in $[(bpy)_2Ru(dpp)]^{2+}$ are recognizable as a distinct ring system with co-coupling constants, with A6 in a position to be

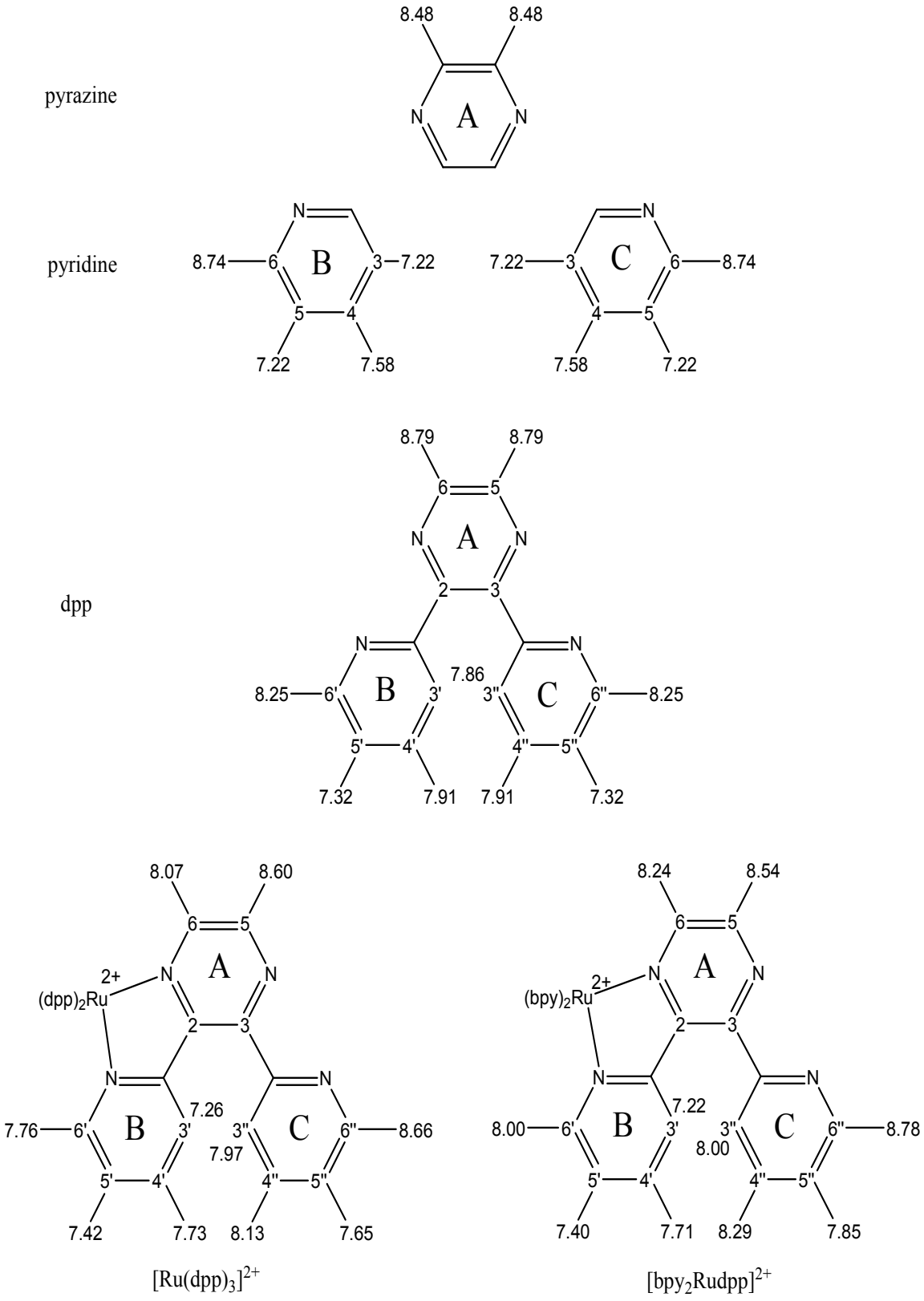

Figure 85: Evolution of dpp chemical shifts.

shielded by the ring current of an adjacent bpy ring. Compared to its counterparts on bpy (c.f. 8.66 ppm), B3′ oddly appears the farthest upfield, at 7.22 ppm. The exceptional shielding is due to the ring current of C in close proximity, implying that it is somewhat perpendicular to the plane of coordination (rings A & B). Crystallographic studies of the free dpp ligand reveal a symmetrical structure with a C2 rotational axis, and a dihedral angle between the pyrazine and pyridine moieties of 42.2°.[172] The X-ray crystal structure of $[Re(dpp)(CO)_3Cl]$ shows a similar dihedral angle of 45.2°,[112] but the crystallographic analysis of the chloride form of $[(bpy)_2Ru(dpp)]^{2+}$, a larger structure with more steric interactions, exhibits a dihedral angle of 106.8°, thus accounting for the tremendous ring current shielding of B3′. Conversely, C6″ is the most deshielded proton at 8.78 ppm, which is not surprising given that it is normally one of the most downfield protons in its evolutionary descent in Figure 85. By following the coupling relationships elucidated in the COSY spectrum, the remaining protons of the dpp ligand can be assigned and are similar to the corresponding assignments in $[Ru(dpp)_3]^{2+}$.

4.B. Protonation of $[(bpy)_2Ru(dpp)]^{2+}$

4.B.1. NMR Analysis

Figure 24 is shown again for reference. First and foremost, the change in the NMR spectra with increasing acidity down to pD = 0 indicates a fundamental structural change in $[(bpy)_2Ru(dpp)]^{2+}$. Given the imine basic nitrogens, protonation of one of them is the obvious choice. Second, the fact that the protonation occurs in the pH region between 5 and 1 suggests that it takes place at the free pyridyl nitrogen. The free dpp ligand (Figure 9) has four protonable sites, 2 "pyridyl" and 2 "pyrazinyl", with both pyridyl sites being the most easily protonated if one considers the pK_a values for pyridine (5.25) and 2,2'-bipyridine (4.45, 1.80) versus pyrazine (0.65, -6.25) and 2,2'-bipyrazine (0.45, -1.35 for first two). Hosek *et. al*.[118] estimates the first two p*K*a's (at the pyridyl nitrogens) to be 1.7 and 2.3, and Nazeeruddin and Kalyanasundaram[139] calculated them to be 2.90 and 0.80, also at the pyridyl N-centers. The critical point is that the pyrazinyl nitrogens are much more difficult to protonate, having very negative pK_a values (estimated at -6.9 for $[(bpy)_2Ru(dpp)]^{2+}$)[118] than the pyridyl nitrogens in the free ligand (calculated pK_a values ranging from 0.8 to 2.90). What effect then does chelation to $[(bpy)_2Ru]^{2+}$ have on the

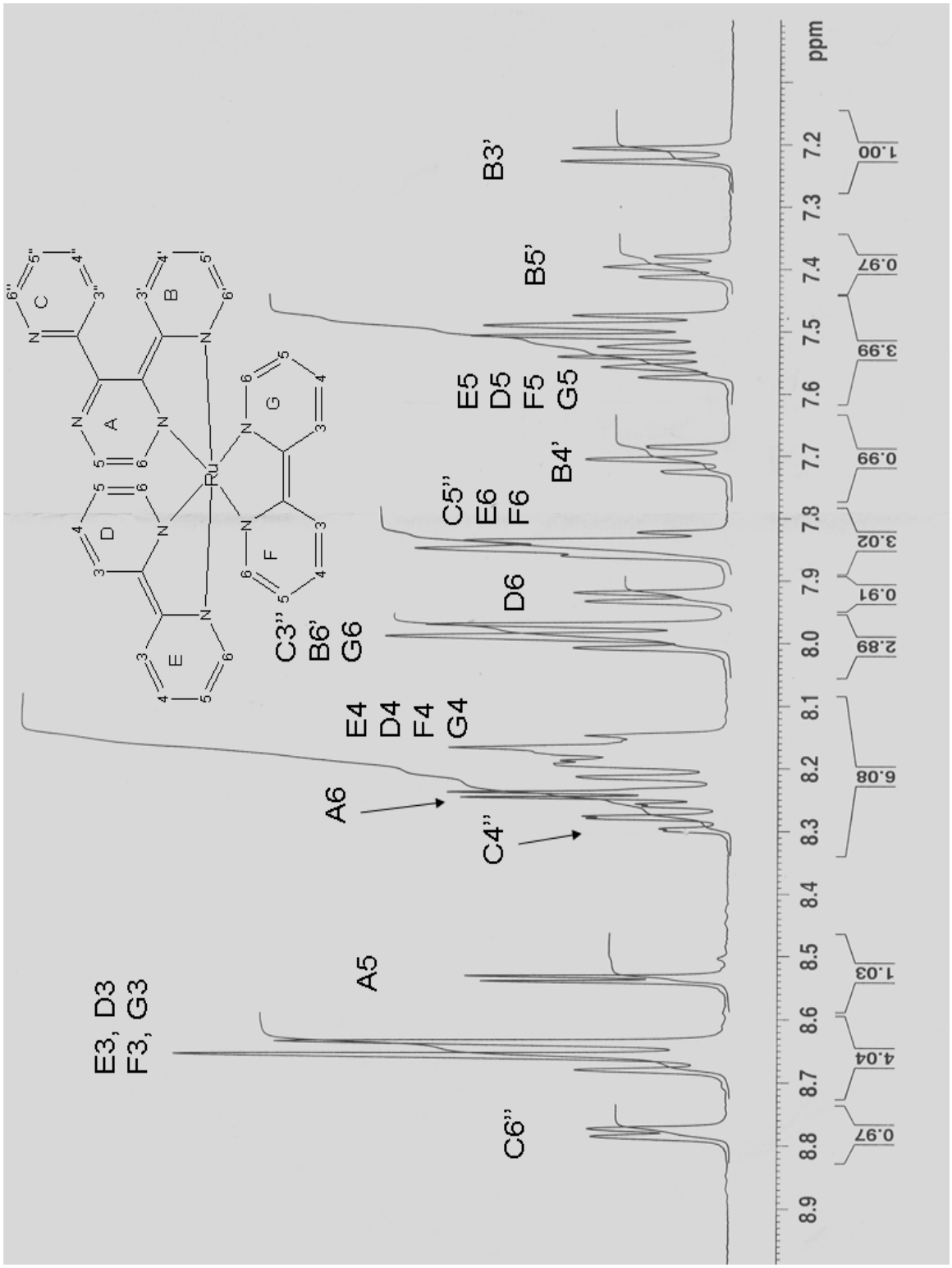

Figure 24. ^{1}H NMR spectrum of 0.01 M $[(bpy)_2Ru(dpp)]^{2+}$ in D_2O.

basicities of the nitrogens? It has been reasoned[118] that due to backbonding from ruthenium, chelation enhances the basicity of the ligand, but less so at the more remote, free pyridyl ring. Complexation to ruthenium leaves only two protonable sites—one pyridyl and the other pyrazinyl. A pK_a value for the free pyridyl ring would be predicted to be around 2.[118] Third, a majority of the shifting protons are structurally on the free pyridyl ring of the dpp ligand. Protonation of this ring will withdraw electron density throughout the ring, leading to deshielding of all the ring protons, which is observed (Table 8). Fourth, protonation of the free pyridyl ring would correlate with the minimal changes observed in the absorption spectrum, as aforementioned.

The chemical shift changes of protons on other rings of the dpp ligand need to be accounted for. As discussed, the chemical shift of B3′ on the coordinated pyridyl ring is highly influenced by the relative geometry of the adjacent free pyridyl ring. Because of the twist angle, B3′ becomes shielded by the ring current of the free pyridyl ring (Figure 86b). If protonation disrupts the geometry, causing the free pyridyl ring to become more planar with the rest of the ligand, the shielding effect will be lost and B3′ will move downfield to its more likely position

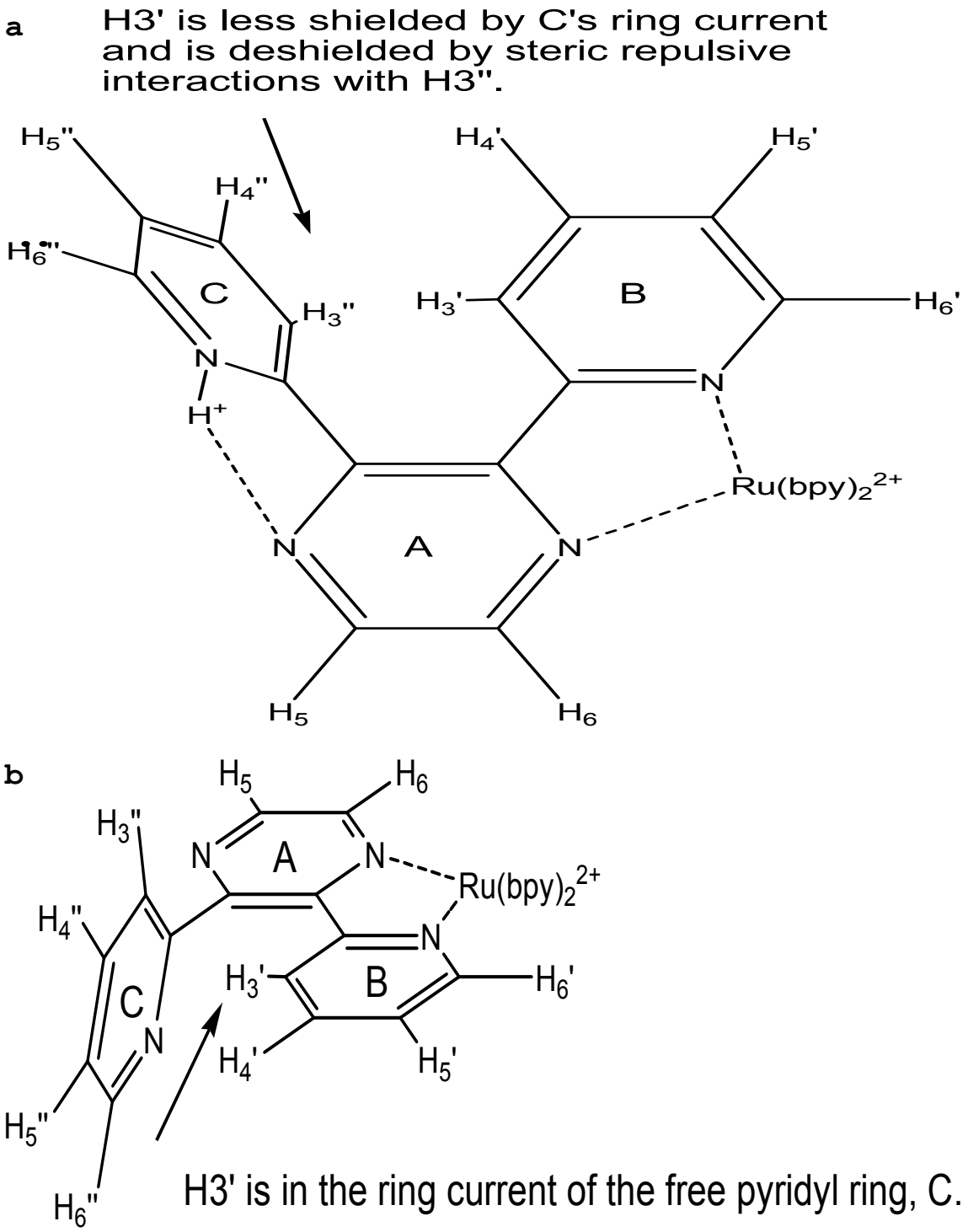

Figure 86. Ring current effect on B3′ proton chemical shift in $[(bpy)_2Ru(dpp)]^{2+}$:(a) monoprotonated structure; (b) unprotonated structure.

absent the adjacent ring. Concurrently, a more planar, free pyridyl ring will bring C3″ into proximity with B3′ (Figure 83a). The steric proximity of these two protons will deshield them both because of van der Waals interactions,[138] enhancing the overall deshielding of both protons. Is there a reason for this change in geometry? Indeed, protonation at the free pyridyl ring would allow for a hydrogen-bonding interaction with the basic pyrazinyl nitrogen (Figure 86a). Such an interaction will favor a more planar structure, and can be possible even without causing any significant energy-raising steric hindrance between C3″ and B3′. Hydrogen-bonding interactions with the coordinated pyrazinyl will perturb it slightly. A slight chemical shift change is seen in A5, but not in A6 which is closer to the interaction.

The coordinated pyrazinyl and free pyridyl rings, together, form a moiety similar to bpy. A number of studies have confirmed that free bpy adopts a *trans*-configuration with the imine nitrogens opposite each other.[163,167,168] Additionally, two published reports, one examining the structure of monoprotonated bypyridines crystallographically[173] and the other a theoretical treatise on the species in the gas phase,[166] confirm the chelation of a proton by both imine nitrogens. The crystal structure of

2,2′-pyridyl-pyridinium perchlorate has a twist angle of about 15° between the rings, allowing the "internal salvation" of the proton. Also, protonation causes a "puckering" of the free pyridyl ring, whose structure then deviates from planarity.[173] However, energies calculated for internal solvation in the gas phase yield pK_a values greater than that observed in solution. Thus, it is reasoned that hydration precludes the possibility for hydrogen bonding in the monoprotonated structure. Others, using absorption spectroscopy, have confirmed that the mono-protonated bpy prefers a *cis* structure, but that a hydrogen bonding interaction in protic solvents is not significant.[174,175] However, an actual NMR study of the monoprotonated bpy details the complex responses of the protons of a pyridyl ring to protonation, and proffers a hydrogen-bonding interaction to explain the data.[137] The hydrogen-bonding interaction is estimated to exist at a dihdedral angle of even 80°. The dpp ligand is of course only analogous to bpy, the free pyridyl nitrogens in dpp may be able to better accommodate a hydrogen-bonding interaction when protonated then it would in bpy.

The dramatic shift in the resonance of B3′ must be accounted for: it may results from an energetic preference for minimal hydrogen bonding interaction in the

monoprotonated structure that twists the free pyridyl ring enough to reduce its ring current effect on B3′; and/or, protonation itself, in causing puckering of the free pyridyl ring, may reduce the ring current itself. Since the ring current deshields protons on the ring, a reduction in current would cause less deshielding, so the chemical shifts should move upfield. The opposite is observed, perhaps completely counterbalanced by the presence of a positive charge. In any case, some sort of hydrogen-bonding interaction seems preferable as an explanation, and supported by the data.

From the fits of the NMR shifts, an average pK_a of 1.52 ± .03 was obtained. This is the first definitive evidence for assigning the first protonation of $[(bpy)_2Ru(dpp)]^{2+}$ at the free pyridyl ring, and evaluating its pK_a to be 1.52. The value is close to a predicted value of 2.0, corresponding closely to the protonation of uncoordinated dpp at the pyridyl ring. More importantly, knowledge of this first protonation has incredible implications on the discussion of the excited-state protonation properties of $[(bpy)_2Ru(dpp)]^{2+}$.

4.B.2. Absorption Analysis

The slight changes in the absorption spectrum (Figure 26) while titrating with [H^+] down to pH 0 are similar to those previously reported, where ionic strength effects and/or ion-pairing effects were invoked.[85,93] Close examination indicates a slight red-shift of the lower transition absorption to dpp of several nm, and a slight enhancement of the bpy transition at 428 nm of about 7% relative to the intensity of the dpp MLCT. Considering the discussion above, these slight changes most likely signal single protonation of the pyridyl moiety at the dpp ligand. Since the MLCT "sends" charge out to the dpp ligand, an extra positive charge will favor this transition, thus reducing its energy and exhibiting a red-shift. However, the free pyridyl ring, being relatively "uncoupled" from the remainder of the dpp, would have a small effect on the MLCT transitions observed. The slight increase at the bpy transitions may be related to the multiple emissions observed *(vide infra).* Protonation at the free pyridyl ring explains the differing responses of the absorption and NMR spectra: since the free pyridyl ring is fairly uncoupled to the MLCT system, there are few changes in the absorption, whereas the NMR will be quite sensitive to protonation. The fact that protonation of the dpp ligand at the pyridyl ring

takes place between pH 4 and 1 means that previous interpretations of the proton quenching of $[(bpy)_2Ru(dpp)]^{2+}$ and its excited state pK_a must be reexamined.

The marked change in the absorption spectrum of the diprotonated species, $[(bpy)_2Ru(dppH_2)]^{4+}$ parallels the significant structural changes that accompany protonation. Protons have a high charge-to-mass ratio, thus placing two positive charges at the imine nitrogens is expected to significantly lower the energy gap of the MLCT by lowering the π* orbital. In essence, since charge is transferred to the dpp ligand, the presence of positive charge there favors the charge transfer. Since the charge transfer is primarily coupled to the pyrazine ligand, protonation of the pyrazinyl nitrogen expectedly leads to a bathochromic shift in the absorption spectrum. The pK_a is easily extracted from the change in the absorption spectrum, and the value obtained, -4.50 ± 0.07, matches well with published values (-4.9[118] and -3.7[139]). Whereas pyrazinyl protonation is precluded in the free ligand by its very low pK_a (estimated at about -6.9), backbonding from chelation to ruthenium increases the basicity enough to be observed using sulfuric acid.

4.B.3. Emission Analysis

The single inflection point in the log plot of changes in the emission spectra *vs.* [H^+] (Figure 32) is indicative of one protonation step with a characteristic pK^*_a at the inflection point. The "gentle" inflection change, as opposed to a sharp, steep change, may be indicative of a weak acid–weak base titration in buffer solutions or may reflect the kinetics of protonation. The inflection points derived from the sigmoidal fits are quite the same, within experimental error, and average to 4.5 ± 0.3.

Initially, the data are interpreted as indicative of a single protonation in the excited state. An inflection point at 4.5 means that the excited state is a stronger base than the ground state. Since the MLCT absorption transfers charge to the dpp ligand, increased electron density would understandably translate to increased basicity. However, two major questions arise. First, the two possible protonation sites beg the question as to which is being protonated in the excited state. Second, the differing lifetimes between the protonated and unprotonated forms means the system cannot attain equilibrium in the excited state. The shorter lifetime species will "disappear" more quickly than the longer and the system will shift its equilibrium towards replenishment of the

shorter lived species. If the unprotonated species is longer lived, this effect makes it appear to be a stronger base, *i.e.* its apparent pK^*_a will be greater than the actual pK^*_a assuming the system could reach equilibrium. In such a case the lifetime correction (67) should be applied.

4.B.4. General Discussion

It is useful to confront the issue of the excited-state protonated structure first. In the simplest models at higher pH values (>4), the excited state unprotonated structure, while still excited, either protonates at the pyrazinyl nitrogen to form $^*[(bpy)_2Ru(dppH_{pz})]^{3+}$, or at the free pyridyl nitrogen to form $^*[(bpy)_2Ru(dppH_{py})]^{3+}$. The protonated structure would then relax, and the system in the ground state would re-attain equilibrium. At high pH, this would mean deprotonation. The only available data that may shed light on this question is Resonance Raman data. The excited state can be thought of as a Ru^{3+} metal center with an electron out on the dpp ligand, or formally, $^*[(bpy)_2Ru(III)(dpp\cdot^-)]^{2+}$. Experiments on one-electron reduced Ru(II) diimines confirm this designation and also indicate that the pK_a of the one-electron reduced species is a startling 10.5![176] Previous experiments have also shown that excitation into the dpp MLCT transition leads to

enhancement in vibrations associated with the dpp ligand, and specifically, that the electron density is polarized towards the pyrazinyl portion of the ligand.[155] This would be expected since the pyrazinyl portion is coordinated to the metal directly, leaving the pendant, uncoordinated pyridyl ring relatively uncoupled to the MLCT system. Similar polarization is seen in the related compound $[(bpy)_2Ru(pypz)]^{2+}$, where pypz is the pyridylpyrazine ligand, simlar to dpp without the pendant pyridyl ring.[177]

Given as such, enhancement of the basicity of the dpp ligand is expected to occur primarily at the pyrazinyl nitrogen due to this polarization of electron density, and thus excited state protonation. Given this likelihood, does the entire pH titration curve always concern, specifically, the formation of $^{*}[(bpy)_2Ru(dppH_{pz})]^{3+}$? If so, then the discussion of the size of the enhanced basicity must compare the pK_a and *pK_a where only protonation of the pyrazinyl ring is concerned. While this may be possible in the excited state, it is certainly not entirely possible in the ground state, given the evidence of ground state protonation at the pendant pyridyl, first, with increasing $[H^+]$. However, the pK_a (H_o) for ground state protonation of the pyrazinyl nitrogen, -4.5, which is the second protonation of the complex, would not be expected to be

vastly different with or without the pendant pyridyl ring which can easily "rotate away" from a protonated pyrazinyl ring. Thus one can consider the second pK_a of the dpp ligand in $[(bpy)_2Ru(dpp)]^{2+}$ an excellent approximation of the pK_a for the pyrazinyl nitrogen alone. Obtaining, or estimating, the *pK_a of the pyrazinyl nitrogen alone rests on the accuracy and reliability of the *pK_a from the inflection point of the emission titration curve, which itself depends upon issues related to the differing lifetimes of the protonated and unprotonated forms.

Now concerning the differing lifetimes, when the emissions at pH 0 of $[(bpy)_2Ru(dpp)]^{2+}$ were examined with the streak camera system, all detected emissions in the 400-750 nm range decayed within the lifetime of the exciting pulse, 16 ps. If one assumes that the lifetime of the protonated species is 16 ps, then using equation (67) and the ratios of the lifetimes garnered from the titration experiment, 125 ns for the unprotonated and 16 ps for the protonated, a true pK^*_a value of 0.6 is obtained. If this value were reliable, it would mean that the excited state of the pyrazinyl nitrogen, assuming that is where protonation takes place in the excited state, is *less* basic than the ground state of the pyridyl. Similarly, if excited state protonation is actually at the pyridyl, again, the

true $^{*}pK_a$ value would mean the excited state of the pyridyl nitrogen is less basic than the ground state. Although the redistribution of electron density from the metal to the dpp ligand is polarized towards the pyrazinyl nitrogen, a portion of the electron density is at the pyridyl as well. This slight enhancement of electron density at the pyridyl would certainly enhance its basicity and the $^{*}pK_a$ value for the pendant pyridyl should be greater than 1.52.

Since we cannot definitely assign the protonation structure of the excited state, the only handle on the $^{*}pK_a$ value for protonation of either imine nitrogen is the value obtained of 4.5 from the emission titration. The lifetime correction factor wipes out the apparent increase in basicity, reducing it to 0.6, thereby implying that the excited state is more acidic, but only appears more basic because of the shift in equilibrium caused by the very small lifetime exhibited by the protonated form. Frankly, this defies common sense, the known effect of increased basicity with increasing electron density, and it contradicts corroborating evidence from similar structures with single sites, known to have MCLT-induced increases in basicity.[139,178,179] To resolve the discrepancy, the lifetime correction must be inadequate to explain these phenomena, particularly in $[(bpy)_2Ru(dpp)]^{2+}$ where disparate

protonation sites are in question. Indeed, some have also called into question the wisdom of reporting pK^*_a values from the emission titration of just one species, the other protonated species being non-emissive.[180] In such a case, the inflection point more aptly represents the rate of the back reaction,

$$^*AH \leftrightarrows {}^*A^- + H^+ \quad (95)$$

However, a weakly emissive protonated complex is evident here. Additionally, other models of excited-state enhanced basicity should be invoked to offer an explanation that satisfies chemical understandings of protonation, and the data.

Another useful approximation of the excited-state pK_a (pK^*), the Förster cycle, is invoked when either the protonated form or unprotonated form does not emit.[38] Restating equation (63),

$$pK^* = pK_a + 0.00209(\nu_B - \nu_{BH+})/cm^{-1}, \quad (63)$$

where ν_B-ν_{BH+} is the difference between difference in energies between the protonated and unprotonated forms. This difference can be calculated from the differing maxima in the corresponding absorption and emission spectra. From the emission spectra, if the maximal values 705 nm

(unprotonated) and 735 nm (protonated) are used, the ΔpKa is 1.21. If the excited state is protonated at the pyridyl ring, the $^{*}pK_a$ value obtained is 2.73. Alternately, if the excited state is protonated at the pyrazinyl ring, the $^{*}pK_a$ is -2.3. The small enhancement of 1.21 pK units however would match more with protonation at the pyridyl ring where there is a slight increase in electron density from population of the MLCT. A *pKa of -2.6 for protonation at the pyrazinyl is not supported by the emission data.

Looking at the absorption spectra, monoprotonation causes only a slight red shift in the dpp transition. This can either represent that "portion" of the MLCT onto dpp that goes specifically to the pyridyl ring, or a hydrogen bonding interaction with the pyrazinyl nitrogen. Based on the Förster cycle, a 6 nm red shift (the approximate red shift calculated from Gaussian fits) translates to a ΔpK_a of 0.52. In either case, this small change corresponds with the small ΔpK_a calculated from the emission titration, and highly suggests that the 735-nm emission corresponds to $[(bpy)_2Ru(dppH_{py})]^{3+}$. To judge the ΔpK_a at the pyrazinyl nitrogen with the Förster cycle, one must look at the absorption changes that correspond with protonation at that site, which means the second protonation of $[(bpy)_2Ru(dpp)]^{2+}$. Gaussian fits to the diprotonated

absorption spectra (Figure 30) reveal two transitions at 520 nm and 580 nm. Interestingly, the ratio of the widths (in cm^{-1}) of the higher energy to lower energy is 2.17:1, nearly exactly that of the unprotonated where the two absorptions are assigned as MLCT to bpy and dpp. The 580-nm, lower energy transition would still be to dpp, again, because of coupling considerations, primarily to the pyrazinyl nitrogen. Therefore 580 nm is compared to 486 nm in the unprotonated, and the ΔpK_a is 6.97, an extraordinary increase. The excited state pK_a would be 3.0. The expectation that the excited state pK_a is fairly high is bolstered by reports that the pK_a of the one-electron reduced species, $[(bpy)_2Ru^{3+}(dpp^{\cdot -})]$ is 10.5.[176]

The implications are critical and is assisted graphically, but plotting all three titration plots, emission, mono-protonated from the NMR data, and double protonation from the absorption data, on the same scale (Figure 87). It suggests that when $[(bpy)_2Ru(dpp)]^{2+}$ is excited in a protic solvent, the extraordinary change in basicity, primarily at the pyrazinyl nitrogen, will lead to protonation at that site and thus transient formation of $[(bpy)_2Ru(dppH_{pz})]^{3+}$. Since the pyrazinyl nitrogen is more strongly coupled to the MLCT system, vibronic coupling of the N-H bond will efficiently dissipate the excitation

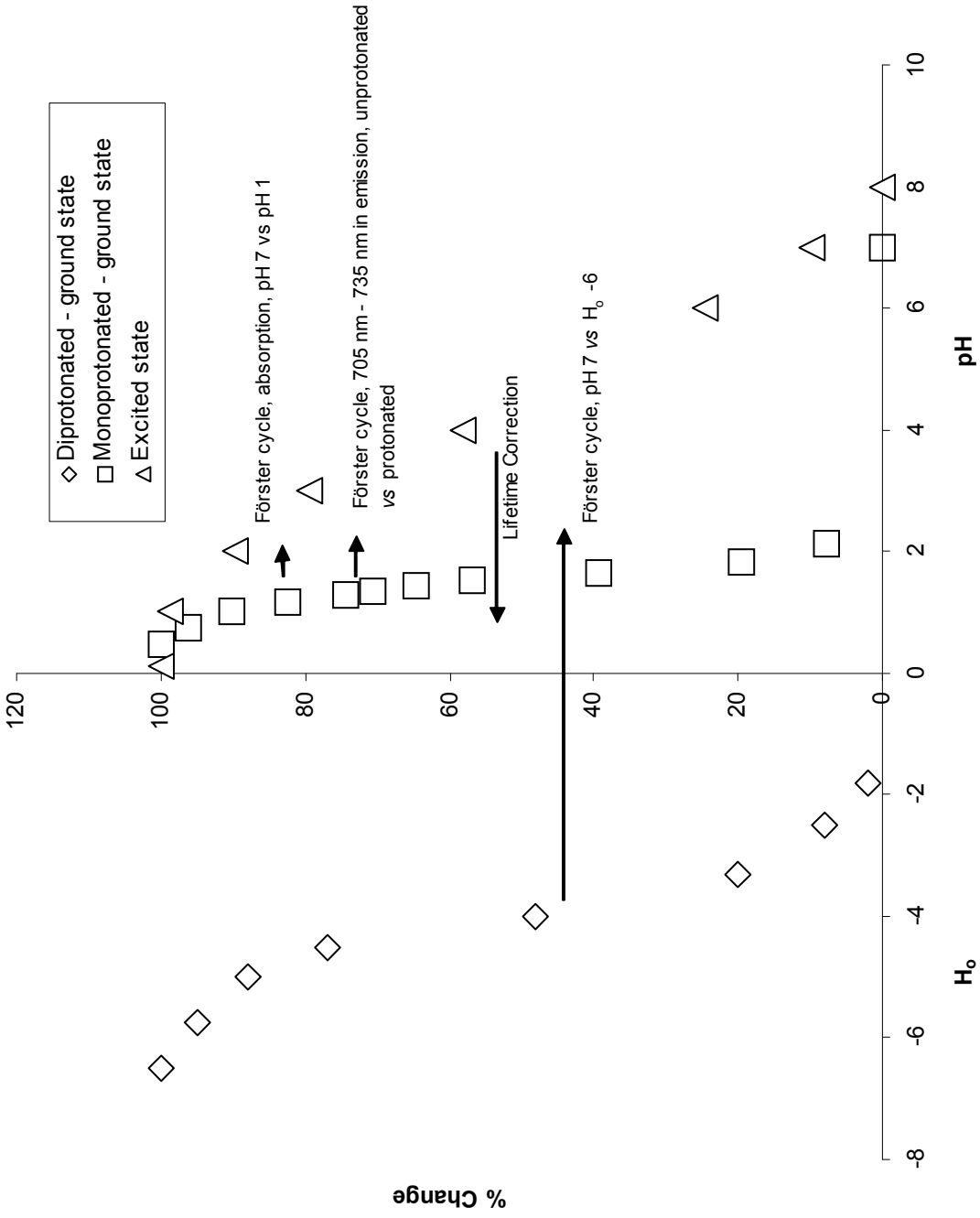

Figure 87. Plots of ground- and excited-state titration curves for $[(bpy)_2Ru(dpp)]^{2+}$ with implied changes in basicity due to lifetime corrections and Förster cycle calculations.

energy leading to a non-emissive species. This is why simple quenching is observed at most pH values above 3.

However, at low pH, a large percentage of the species are protonated as $[(bpy)_2Ru(dppH_{py})]^{3+}$. Using the p$K_a$ value of 1.52, 78% of the ruthenium complexes are protonated at pH 1. With similar absorption coefficients (c.f. little change in absorption spectra), the protonated form absorbs light with near equal efficiency, and being less emissive, would also reduce the emission intensity giving the impression of quenching. Alternatively, upon population of the MLCT of $[(bpy)_2Ru(dppH_{py})]^{3+}$ several subsequent deactivation pathways are available which are detailed in Figures 88 & 89. First, the MLCT onto dpp does place additional electron density onto the pyridyl nitrogen. This would enhance its basicity and therefore its "hold" on the proton. Bonds to protons are still efficient energy dumps: protonation at the pyridyl ring is sufficient to reduce the quantum yield of emission significantly. However, with the degree of uncoupling, the molecule is still left slightly emissive, with the energy gap smaller (red shifted) as expected (Figure 88, Model 1). Secondly, if the ground state protonation does involve a degree of H-bonding with the pyrazinyl ring, the MLCT onto dpp would facilitate sharing between the proton and *both* nitrogens (Figure 88,

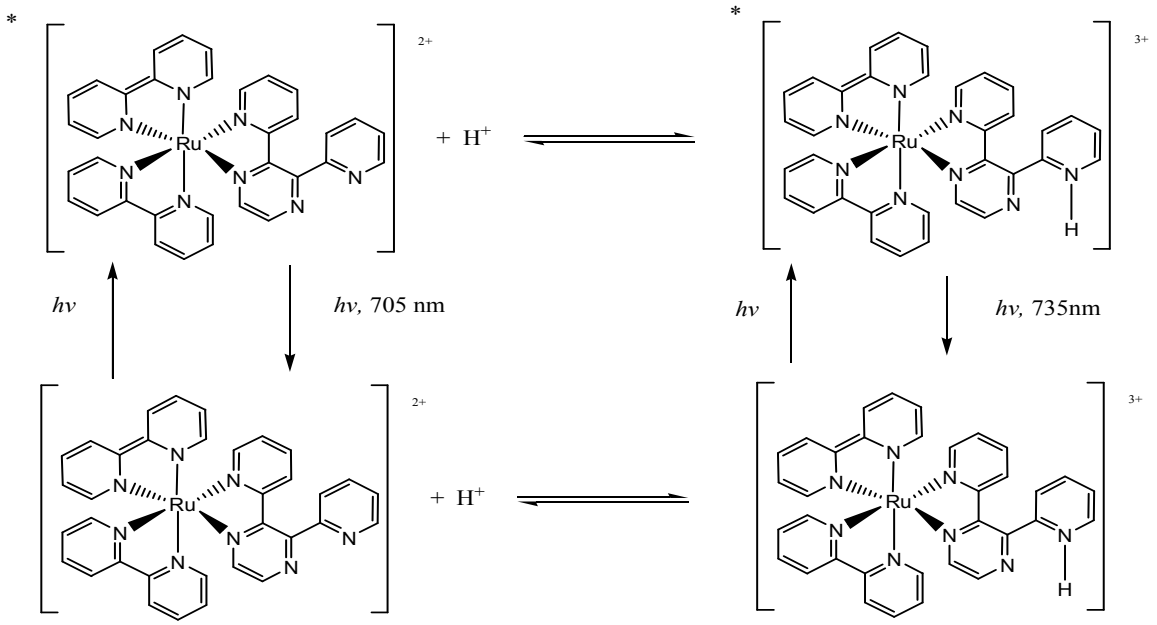

MODEL 1

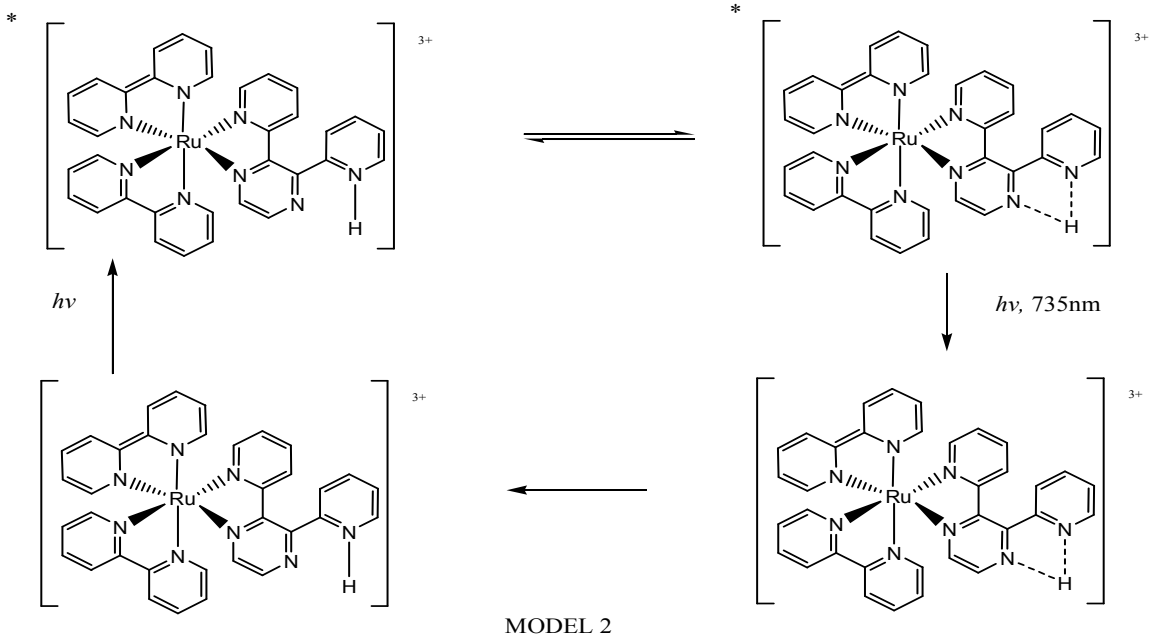

MODEL 2

Figure 88. Models 1 & 2 for excited-state protonation of $[(bpy)_2Ru(dpp)]^{2+}$.

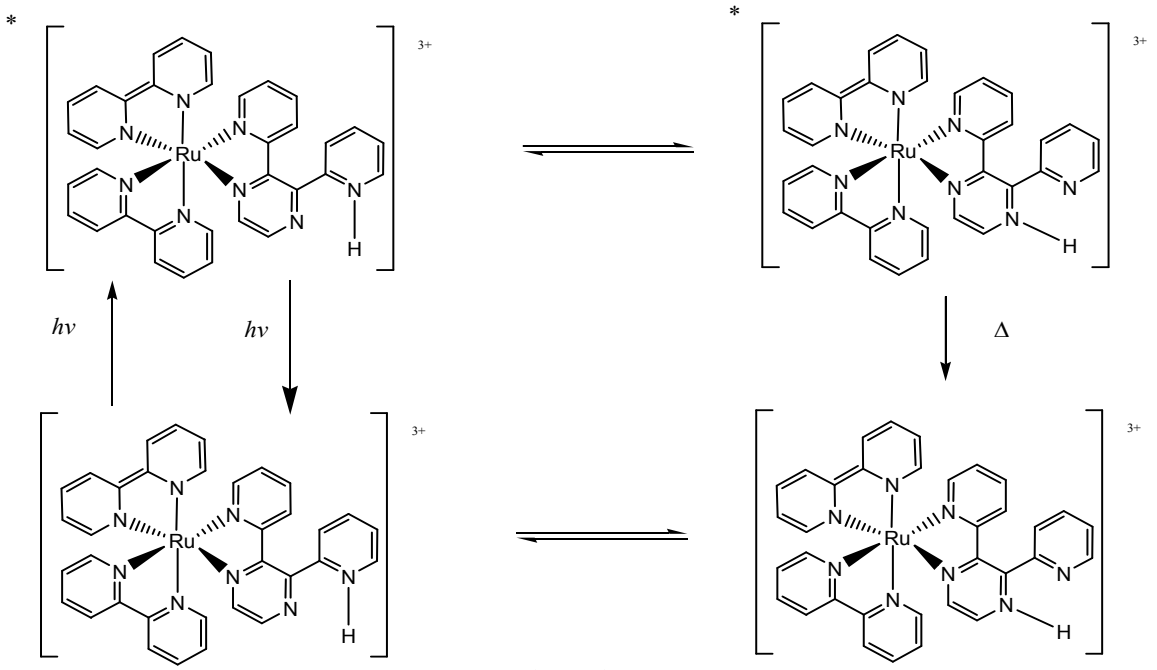

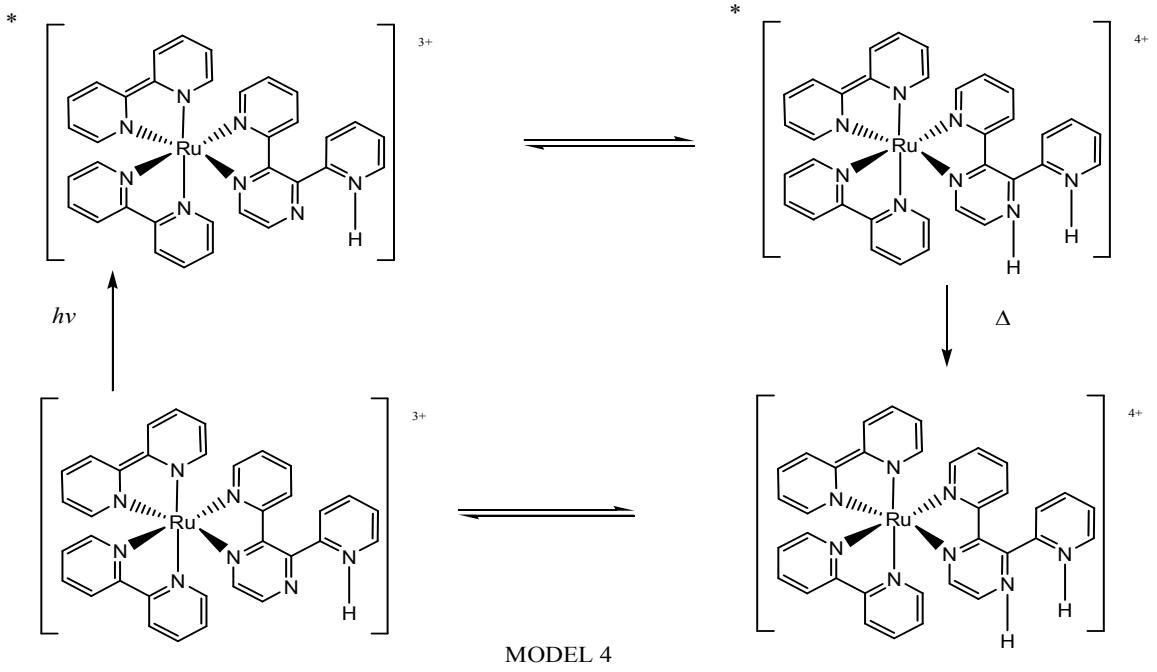

Figure 89. Models 3 & 4 for excited-state protonation of $[(bpy)_2Ru(dpp)]^{2+}$.

Model 2). The deactivation considerations would be the same. Thirdly, if the MLCT actually makes the pyrazinyl nitrogen a stronger base in the excited state than the pyridyl nitrogen, the proton may actually be transferred, transiently, to the pyrazinyl nitrogen in the excited state, creating a "phototautomer" (Figure 89, Model 3). In this case the excited state molecule would be completely non-emissive like at high pH. Lastly, the MLCT may facilitate the second protonation, at the pyrazinyl, in the excited state (Figure 89, Model 4). As no emission above 650 nm is evident from the diprotonated species (as would be expected with two N-H vibronic relaxations pathways at work), this model would create a non-emissive species. Beyond model 4, which seems unlikely since the monoprotonated species is emissive, no one model stands out as the only pathway. Since emission at 735 nm is seen at pH=0, Model 1 cannot be ruled out entirely. It is expected that all models contribute to some degree, with different fractions of a set of excited molecules taking different pathways. Even with decay rate constants as high as 6 x 10^{10} s^{-1} (assuming a 16 ps lifetime), protonation from the solvent is still possible, meaning phototautomerization is not necessary for facile deactivation.

Rather than justifying one model over another, it is constructive to note, that in the context of metallation, enhanced basicity is at work at both sites, and not equally. Interestingly, the asymmetric MLCT onto the dpp seemingly inverts the basicity of the sites, making both *pK_a value of the pyrazinyl above that of the pyridyl nitrogen. The leveling effect of water is well-known, where acids and bases stronger than water cannot persist in water, with H_3O^+ and OH^- forming instead. Ireland and Wyatt[38] detail that, because of this, immense changes in basicity and acidity due to excited states are often "leveled" to an apparent $^*pK_a$ of 2.0. Lastly, the alternate quenching possibilities in $[(bpy)_2Ru(dpp)]^{2+}$ explain a few trends in the data, including why a full Stern-Volmer plot of the proton quenching has strong negative deviations and plots of Φ_o/Φ and τ_o/τ are not coincident (Figure 90). Since in this scenario, the proton remains in the ground state, excited state protonation of $[(bpy)_2Ru(dpp)]^{2+}$ can be treated like an exciplex, and the data can be fit to equation (76). Parameters that can be varied include k_o and k''_o, the rate constants for deactivation for the base and acid forms, k_q, the quenching constant, and γ (from equation (74)) which represents the differential ratios of intensity and lifetime between the two forms. The ratio of

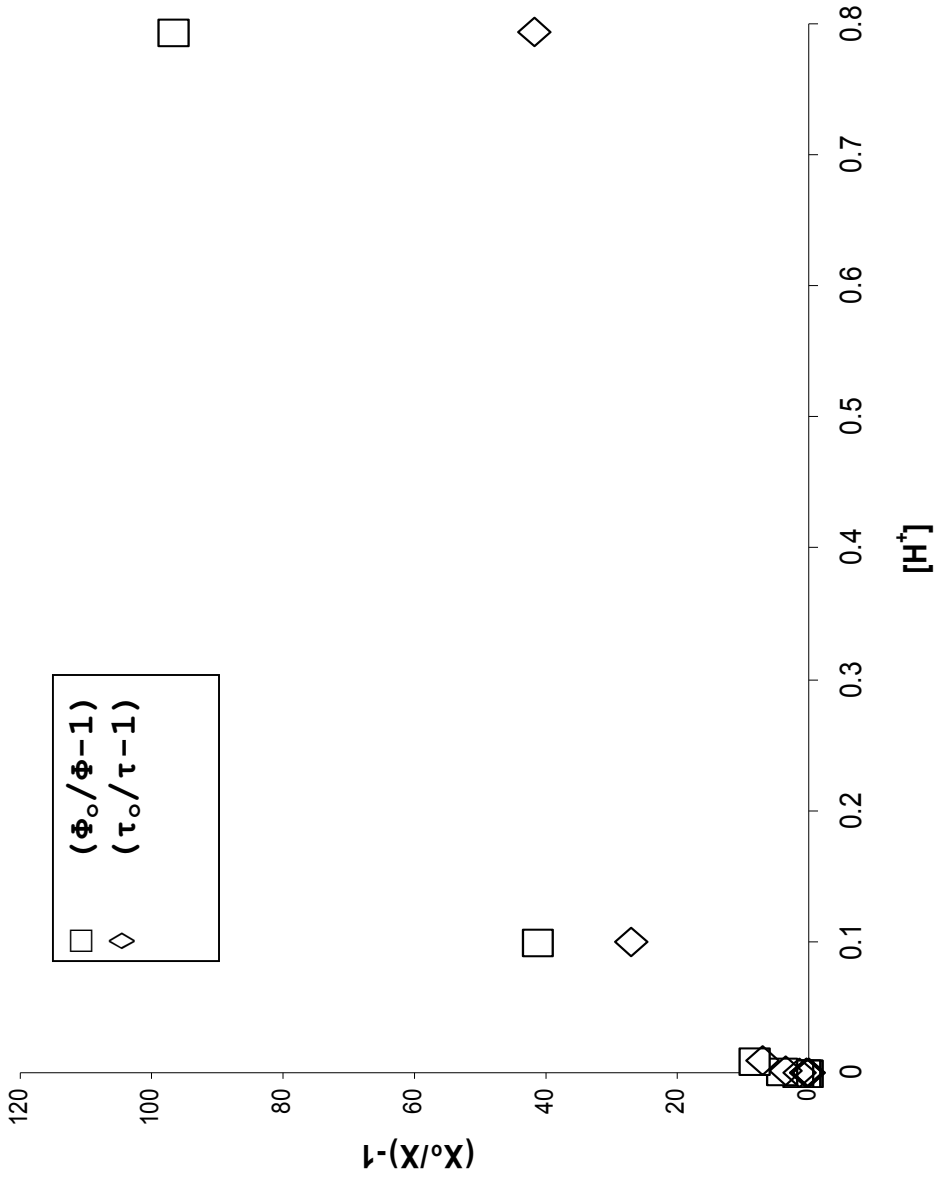

Figure 90: Stern-Volmer plots of pH titration of $[(bpy)_2Ru(dpp)]^{2+}$ comparing Φ_o/Φ and τ_o/τ.

k_q to k_o is the classic Stern-Volmer quenching constant, K_{SV}. When the fitting is attempted, it is found that one equation does not adequately fit all the points. In fact, it is possible to fit either the beginning of the curve, or the end, meaning, the high pH or low pH side (Figure 91). The differing values obtained are tabulated below for a side to side comparison.

Table 14. Photophysical properties for the protonation of $[(bpy)_2Ru(dpp)]^{2+}$ from the fit of emission data

	k_o (s^{-1})	k''_o (s^{-1})	K_{SV} (M^{-1})	γ	k_q (s^{-1} M^{-1})
high pH	8.0×10^5	3.9×10^9	3.4×10^6	2500	2.7×10^{12}
low pH	8.53×10^6	5.9×10^{10}	1174	44	1.0×10^{10}

At low pH, the values obtained for the lifetimes of the protonated and unprotonated forms fit the data and agree with the model that the 735-nm emission arises from $[(bpy)_2Ru(dppH_{py})]^{3+}$. Also, the calculated K_{SV}, 1174 M^{-1} s^{-1}, is in the vicinity of that previously reported (737 M^{-1} s^{-1}).[118] However, at high pH where protonation only at the pyrazinyl nitrogen is postulated, extremely high K_{SV} and k_q values are obtained—as if an entirely different system were at play. Indeed, as explained, quenching by protonation at the pyrazinyl would be quite facile and

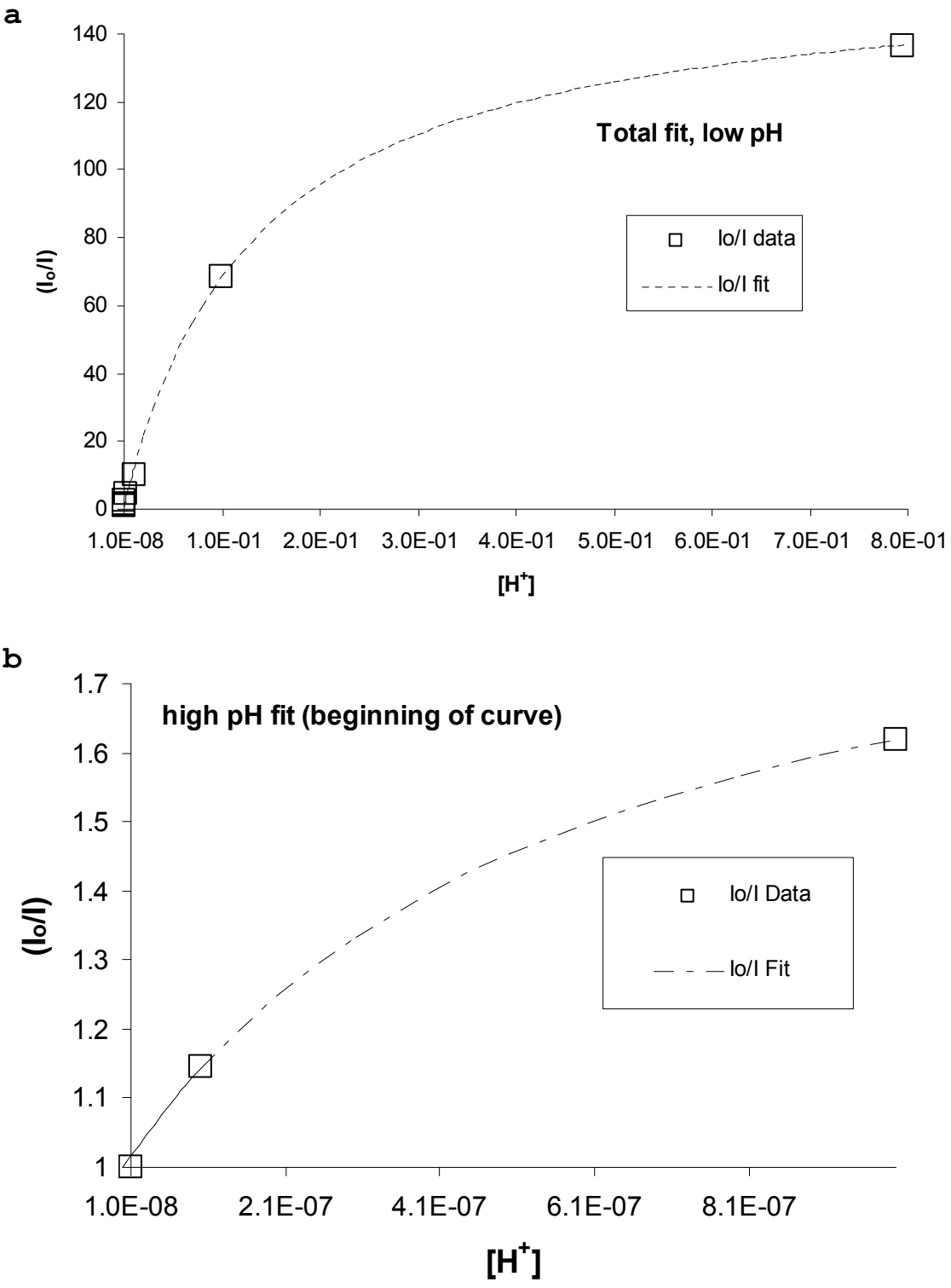

Figure 91. Fit of emission data for protonation of $[(bpy)_2Ru(dpp)]^{2+}$: (a) best fit for low pH region (includes all data points); (b) best fit for first few data points at high pH.

effective. As for protonation at the pyridyl, the very low quantum yield of emission, $\Phi_{em}=4 \times 10^{-9}$, confirms that even with protonation to a site that is weakly coupled to the MLCT, the non-radiative rate constant is drastically increased as the species dissipates most of its energy through vibrations coupled to the protic solvent.

Excited-state proton transfer involving Ru(II) diimines was first observed in $[(bpy)_2Ru(HOOC\text{-}bpy\text{-}COOH)]^{2+}$,[181] and then confirmed by others.[182],[183] The complex has carboxylic acid groups located at the 4/4′ positions on one bpy ligand. Excited-state proton transfer is claimed with a difference of excited-state pK_a between that sites calculated to be 0.9.[182] Given the structure of the monoprotonated complex $[(bpy)_2Ru(HOOC\text{-}bpy\text{-}COO)]^{+}$ compared to the monoprotonated Ru-dpp (Figure 92), facile proton transfer is expected to be much easier in the latter if differences in the excited state pK_a are present.

Section 4.C. Multiple Emissions from $[(bpy)_2Ru(dpp)]^{2+}$

Recent studies have highlighted the possibility of room temperature multiple emissions from Ru(II) diimines,[184,185] challenging the old adage that intersystem crossing to the lowest triplet manifold is unity.[186-188]

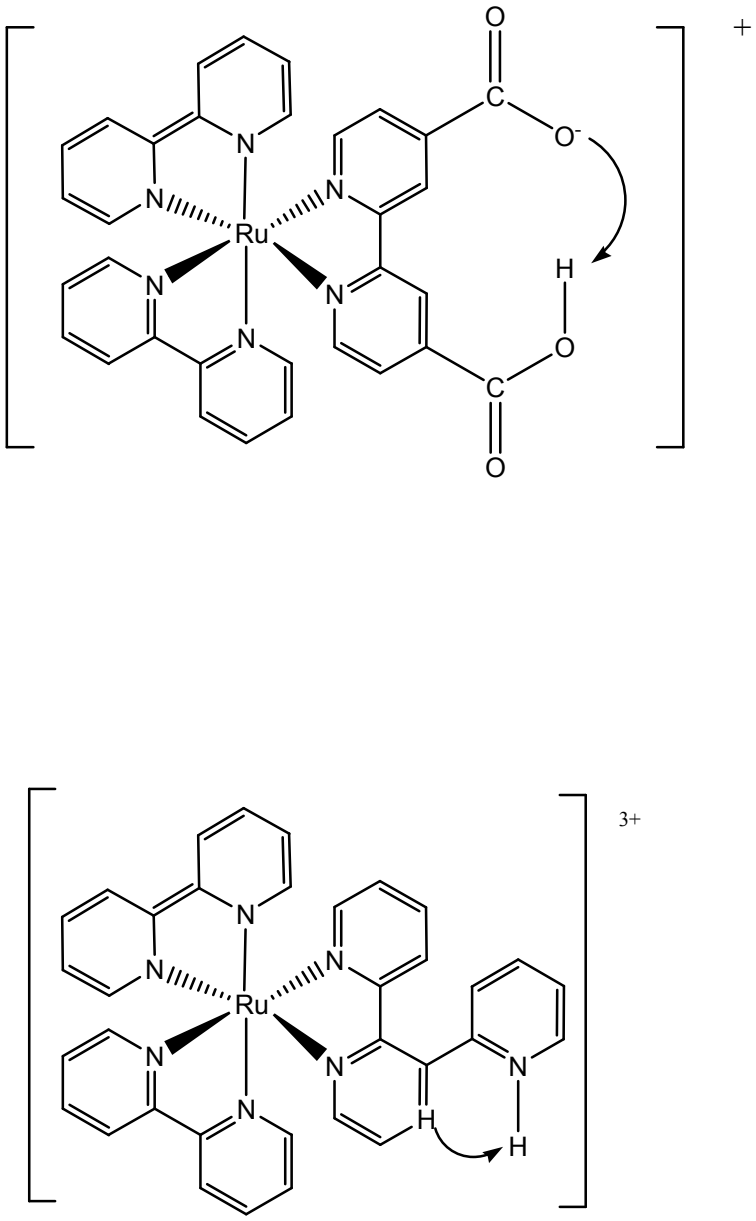

Figure 92. Proton transfer possibilities in $[(bpy)_2Ru(dppH)]^{3+}$ *vs.* $[(bpy)_2Ru(HOOC\text{-}bpy\text{-}COO^-)]^+$.

Several systems involve spatially separated emissions that can be switched on or off.[189,190] Perhaps one of the more fascinating reports is the seemingly "simple" observation of the singlet charge transfer, ^{1}MLCT, from $[Ru(bpy)_3]^{2+}$. The weak emitting state is centered at about 500 nm, red-shifted about 3800 cm^{-1} from the absorption at 420 nm and 2222 cm^{-1} from the 450 nm absorption. The additional emission seen from $[(bpy)_2Ru(dpp)]^{2+}$ is centered about 620 nm. Using these shifts, one can calculate backwards to the presumed absorption, which would be at 502 nm and 545 nm. 502 nm is within the main transition envelope to dpp and 545 nm is at the low energy tail of the MLCT to dpp. Rather, excitation at higher energy, towards the MLCT to bpy transition envelope enhances the 620 nm emission (c.f. Figure 34). Thus it is unlikely that the 620 nm arise from ^{1}MLCT onto the dpp ligand. Rather, the 620 nm emission is reminiscent of emission from the parent complex $[Ru(bpy)_3]^{2+}$, which emits in aqueous solution with a wavelength maximum at 620 nm. One obvious possibility is contamination from $[Ru(bpy)_3]^{2+}$. Given the stability of $[(bpy)_2RuCl_2]$, it is unlikely that synthesis of $[(bpy)_2Ru(dpp)]^{2+}$ results in tris-bpy byproduct. Also, an emission from $[Ru(bpy)_3]^{2+}$, even if it were a low concentration contaminant, should have an emission lifetime

on the order of 600 ns. The 620 nm emission has a lifetime within that of the pulse from the Ti:sapphire excitation, ≤ 16 ps, thereby precluding a $[Ru(bpy)_3]^{2+}$ emission.

One possibility is that when the MLCT onto the bpy ligand is populated, a fraction of the energy is quickly emitted competitive with intersystem crossing to the dpp ligand manifold. This possibility may either exist unseen in the unprotonated species due to the overwhelming emission from the ^{3}MLCT located on the dpp ligand, or result from a perturbation of energy levels due to protonation that allows for this additional radiative pathway. The relaxation pathway is shown in a Jablonski diagram in Figure 93. Deviations from Gaussians at the higher energy tail of emissions from the bimetallics $[(bpy)_2Ru(dpp\text{-}M)]^{4+}$ (M=Cd,Zn) suggest the presence of the 620 nm in these species. The short lifetime of the 620 nm emission suggests it is more singlet in character, and the presence of other metal cations might be thought to enable intersystem crossing to the triplet manifold because of spin-orbit coupling. However, the dpp ligand site is spatially distinct from the bpy ligands and thus this effect may be minimal. The slight difference between the excitation and absorption spectrum of $[(bpy)_2Ru(dpp)]^{2+}$ may point to this additional radiative pathway when the MLCT

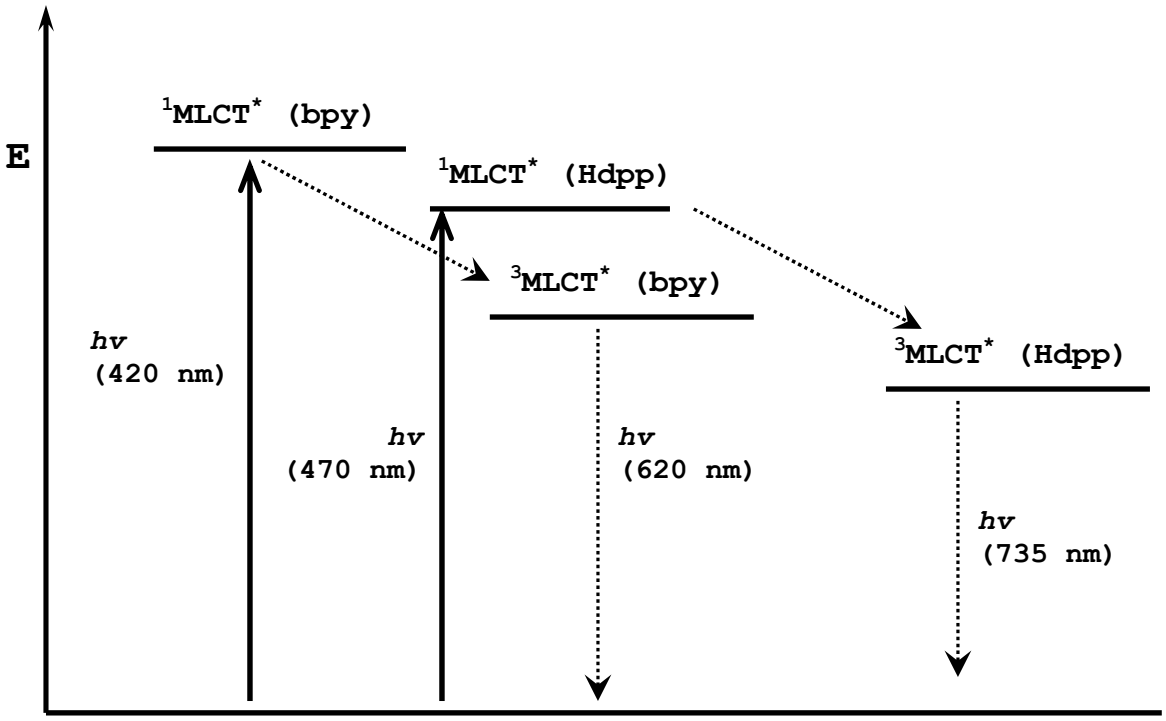

Figure 93. Jablonski diagram of multiple emissions from $[(bpy)_2Ru(dppH)]^{3+}$.

onto the bpy ligand is populated. In this model, protonation does not "turn on" the 620 nm, but simply allows it to be observed with a very sensitive camera, once the quantum yield of emission from the dpp ligand is reduced. In resolving the two emissions during the quantum yield determination of $[(bpy)_2Ru(dppH)]^{3+}$, it is estimated that the quantum yield for emission at the 620 nm is $3 \pm 1 \times 10^{-8}$. Given these data, it is proffered that this emission originates from the bpy ligand and is spatially separated from the dpp ligand transitions. Additional investigation is needed to further understand this unexpected phenomena, which has critical implications for re-thinking the full range of relaxation pathways available to Ru(II) diimines.

Section 4.D. Association of $[(bpy)_2Ru(dpp)]^{2+}$ with Various Metal Cations

The small changes in the absorbance and emission data of $[(bpy)_2Ru(dpp)]^{2+}$ in 6M $Ca(NO_3)_2$ are rationalized as being due to ionic strength effects. With increasing ionic strength, the increase in dielectric constant of the solution will stabilize the ^{3}MLCT since it is fundamentally a charge separation.[160] This slight lowering of the energy is observed, and serves as an important baseline for

comparison with other metal cations. It also means calcium nitrate is suitable to fix the ionic strength of solutions during titrations with other metal cations of interest.

The red-shifted results with ferric and aluminum ion surpasses the effects of ionic strength seen with calcium ion. In fact, they are reminiscent of the protonated species $[(bpy)_2Ru(dppH)]^{3+}$. Since the pK_a for the reaction

$$[Al(H_2O)_6]^{3+} \leftrightarrows [Al(H_2O)_5(OH^-)]^{2+} + H^+ \quad (96)$$

is 4.85, and that for the reaction

$$[Fe(H_2O)_6]^{3+} \leftrightarrows [Fe(H_2O)_5(OH^-)]^{2+} + H^+ \quad (97)$$

is 2.20, the pH values of 3M aluminum nitrate and 3M ferric nitrate solutions are 2.14 and 0.87 respectively! This means that for the iron solutions, 82% of the ruthenium complexes are protonated. The data observed for the iron solution coincides with the same data for $[(bpy)_2Ru(dppH)]^{3+}$. On the contrary, there is only 19% protonation for the aluminum solutions, and the red-shifts are not completely accounted for either by protonation or ionic strength effects. The lifetime does coincide with $[(bpy)_2Ru(dpp)]^{2+}$ at pH 2 (c.f. Figure 28). In the work presented here, this may be the initial example of an

interaction between $[(bpy)_2Ru(dpp)]^{2+}$ and metal ion in the excited state.

Electron transfer must be energetically favorable for it to occur successfully.[36] An excited state species can undergo electron transfer if the overall driving force is favorable, *i.e.* $\Delta G < 0$. The excited state redox potential is calculated from the energy of the excited state (normally taken from the wavelength maximum of the emission) minus the ground state redox potential. The electron transfer quenching of $[Ru(bpy)_3]^{2+}$ and other Ru(II) diimines by both oxidants and reductants is well known.[33,84] The oxidation potential for redox pair $^*[Ru(bpy)_3]^{2+}$/ $[Ru(bpy)_3]^{3+}$ is 0.84 V. For $*[(bpy)_2Ru(dpp)]^{2+}$, the oxidation potential is 0.53 V and the reduction potential is 0.76 V (Figure 93).[191] One of the few reported examples of quenching of $[(bpy)_2Ru(dpp)]^{2+}$ by electron transfer is the quenching by singlet oxygen. Moreover, the quenching of $^*[(Ru(bpy)_3]^{2+}$ by Fe^{3+} by reductive electron transfer to form $[(Ru(bpy)_3]^{3+}$ and Fe^{2+} is known to occur with a quenching constant, k_q, of 1.9×10^9 M^{-1} s^{-1}.[192] Given the similarity of the oxidation potentials of $^*[(Ru(bpy)_3]^{2+}$ and $^*[(bpy)_2Ru(dpp)]^{2+}$, and the standard reduction potential for the reaction

$$Fe^{3+} + e^- \leftrightarrows Fe^{2+}, \qquad (98)$$

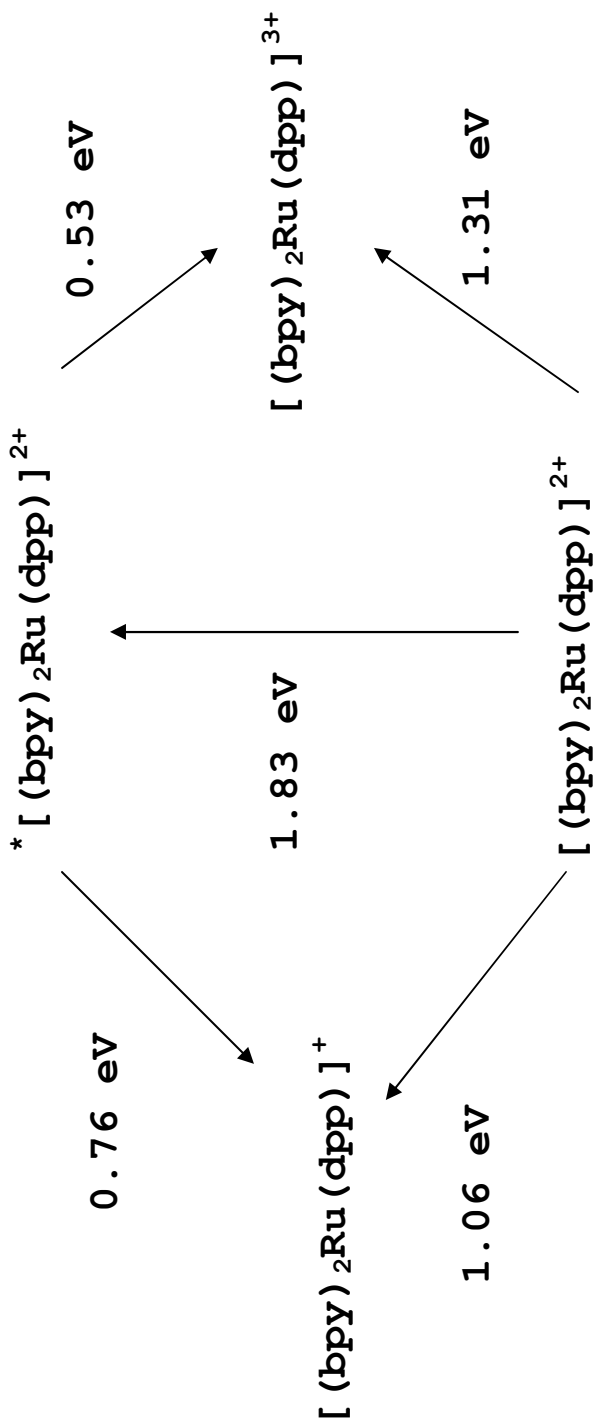

Figure 93. Schematic of excited-state redox potentials of $[(bpy)_2Ru(dpp)]^{2+}$.

which is 0.77 V, it would be reasonable to assume that the latter is also reductively quenched by Fe^{3+} since the overall driving force will be 1.30 V. The low intensity emission of $[(bpy)_2Ru(dpp)]^{2+}$ in 3M $Fe(NO_3)_3$ can partially be explained by the acidity of the solution, and thus the emission of the protonated species, $[(bpy)_2Ru(dppH)]^{3+}$ is being observed. However, at such high ferric ion concentrations, quenching by electron transfer is almost certainly expected to extinguish all emission. Thus, there are four possible explanations: 1) protonation of $[(bpy)_2Ru(dpp)]^{2+}$ prevents interactions with Fe^{3+} that would lead to quenching; 2) protonation of $[(bpy)_2Ru(dpp)]^{2+}$ reduces the excited-state oxidation potential enough to make electron transfer unfavorable; 3) back electron transfer occurs to repopulate the excited species before emitting, or; 4) some other mechanism of quenching besides protonation is at play. The reductive quenching of $[Ru(bpy)_3]^{2+}$ by Fe^{3+}, which does not necessitate base sites for an interaction, may seem to rule out the first option. However, protonation may reduced the rate for electron transfer, k_{ret} enough to make it non-competitive with other relaxation processes. The redox potentials of the monoprotonated species $[(bpy)_2Ru(dppH)]^{3+}$, were not examined here, but the small perturbation of pyridyl protonation

suggest the π^* orbital is not significantly changed in energy, thus precluding option 2 and probably option 1 as well. Option 4 is possible and is explored below with other metal cations. Option 3 (c.f. Figure 6) also seems highly unlikely: since ΔG is positive, there would not be sufficient energy to re-populate the MLCT state. At pH 0.87 for 3 M $Fe(NO_3)_3$ solution, the reduction in intensity due to formation of the protonated species is about 130:1, the same as that observed. This means the emission is solely explained by the protonation of species, and that the ferric iron seemingly has no visible effect on the emission. Where Al^{3+} is concerned, the exact same argument is plausible, with the reduction in emission intensity explained entirely by protonation. Since the standard reduction potential for the reaction

$$Al^{3+} + 3\ e^- \leftrightarrows Al(s) \qquad (99)$$

is -1.66 V, and three electrons are required, quenching of $[(bpy)_2Ru(dpp)]^{2+}$ by Al^{3+} is endergonic and unlikely.

The results with Cr^{3+} clearly indicate a dynamic quenching mechanism, since the lifetime is significantly reduced by a factor of about 200. An obvious explanation can be seen by the absorption spectrum of $[Cr(OH_2)_6]^{3+}$

(Figure 94) where a portion overlaps the typical emission spectrum of $[(bpy)_2Ru(dpp)]^{2+}$. For this reason, energy transfer will occur to $[Cr(OH_2)_6]^{3+}$, *i.e.* it will absorb the emitted light from $[(bpy)_2Ru(dpp)]^{2+}$ to itself become excited. Furthermore, the quenching involves some sort of interaction with $[(bpy)_2Ru(dpp)]^{2+}$: if Cr^{3+} simply absorbed the emitted light, the emission of $[(bpy)_2Ru(dpp)]^{2+}$ would be decreased by this "inner filter" but the lifetime would remain the same. The reduction in lifetime indicates the formation of an encounter complex, followed by deactivation. An estimate of the Stern-Volmer quenching from two data points is 216 M^{-1}, which translates to a quenching constant, k_q, of 2 x 10^9 M^{-1} s^{-1}. Cr^{3+} has been shown to quench $[Ru(bpy)_3]^{2+}$ by energy transfer.[193,194]

The emission of $[(bpy)_2Ru(dpp)]^{2+}$ in $SnCl_2$ solution also suggests a quenching mechanism since both the emission intensity and lifetime are reduced. The quenching may be static since there are changes in the absorption spectrum indicative of association at the dpp ligand (Figure 43). Sn^{2+} forms complex hydrolyzed species in weakly basic solutions such as $[Sn_2O(OH)_4]^{2-}$.[195] Such a species, with an overall negative charge will prefer to pair with $[(bpy)_2Ru(dpp)]^{2+}$. One possible quenching mechanism is oxidative electron transfer whereby $[(bpy)_2Ru(dpp)]^{2+}$ is

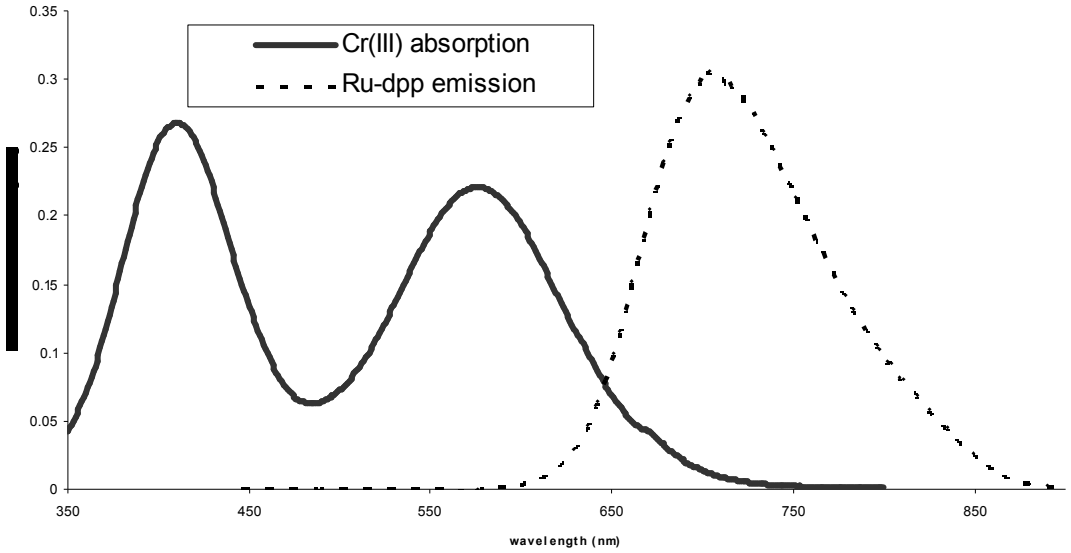

Figure 94. Absorbance of Cr(III) and emission from $[(bpy)_2Ru(dpp)]^{2+}$.

reduced and Sn^{2+} is oxidized. The oxidation potential for $Sn^{2+} \leftrightarrows Sn^{4+} + 2e^-$ is -0.15, well within range of that possible by $*[(bpy)_2Ru(dpp)]^{2+}$. However, one possible issue with oxidative electron transfer is the need for two electrons in the transfer. Any possible adduct with Sn^{2+} may form a non-emissive complex, leading to static associational quenching. The estimated Stern-Volmer constant is 8 M^{-1} with a calculated quenching constant, k_q, of 7 x 10^7 M^{-1} s^{-1}.

The similarity of the absorption spectrum of $[(bpy)_2Ru(dpp)]^{2+}$ in 3 M $Ca(NO_3)_2$ and 1.2 M $Pb(NO_3)_2$ suggests little if any ground-state association of Pb^{2+} with the dpp ligand. The red-shift of the emission though, along with the seeming presence of two emissive species in the time-resolved spectrum suggests a dynamic interaction between $[(bpy)_2Ru(dpp)]^{2+}$ and Pb^{2+}. It is possible that more than one mechanistic interaction is involved, perhaps with two Pb^{2+} ions associating with $[(bpy)_2Ru(dpp)]^{2+}$ in the excited state. Regardless, there is a strong likelihood of exciplex formation in the excited state. The standard reduction potential for the reaction

$$Pb^{2+} + 2e^- \leftrightarrows Pb(s) \qquad (100)$$

is -0.126V. The red-shifted emission is distinct from that of the parent complex. The possible 815 nm emission, which also appears in spectra in the presence of Cd^{2+} and Zn^{2+} is discussed below. The estimated Stern-Volmer constant is 97 M^{-1}, and quenching constant, k_q, is 8.4 x 10^8 M^{-1} s^{-1}. Clearly, further work will need to be done to vet the particular quenching mechanisms involved between $[(bpy)_2Ru(dpp)]^{2+}$ and both Pb^{2+} and Sn^{2+}.

The emission of $[(bpy)_2Ru(dpp)]^{2+}$ in the presence of Zn^{2+} and Cd^{2+}, a particular focus of the work presented here, is discussed in detail below. Additionally, the results of experiments with the bimetallic $[(bpy)_2Ru(dpp)Ru(bpy)_2]^{4+}$ and the association of $[(bpy)_2Ru(dpp)]^{2+}$ with Hg^{2+} will be discussed in that context.

Section 4.E. Association of $[(bpy)_2Ru(dpp)]^{2+}$ with Ag^+

Ag^+ has been shown to form emissive exciplexes with several Ru(II) diimines, including with $[Ru(bpy)_3]^{2+}$,[56,57,196] $[Ru(bpz)_3]^{2+}$,[59] and $[(bpy)_2Ru(bpz)]^{2+}$.[179] Initial debate surrounded the quenching of $[Ru(bpy)_3]^{2+}$ by Ag^+, questioning whether the interaction was electron transfer to form Ag_o and Ag_2^+, or purely exciplex in nature. Even so, the interaction was understood to involve association of the

Ag^+ with the aromatic π system of the bpy ligands. In the work by Shinozaki *et.al.*,[179] two excited-state species with Ag^+, $[(bpy)_2Ru(bpzAg)]^{3+}$, and $[(bpy)_2Ru(bpzAg_2)]^{4+}$ were described as mechanistic possibilities to explain the quenching data, with Ag^+ associating at the pyrazinyl imine nitrogens. The excited-state equilibrium for association, K^*, was calculated to be 130 M^{-1} —an enhancement over the observed ground state association constant of 30 M^{-1}. The increase in basicity upon population of the excited state was invoked as an explanation, and for this reason, the quenching of $[(bpy)_2Ru(dpp)]^{2+}$ by Ag^+ was initially explored in this work.

The change in the absorption spectrum (Figure 61) clearly suggests association of Ag^+. The red-shift of the dpp transition would correspond to placing a positive charge out on the dpp ligand. Since the MLCT transfers electron density to the ligand, the presence of a positive charge in the vicinity would stabilize the transition. In other words, association of Ag^+ would reduce the energy of the π* orbital by formation of a lower energy LUMO. The changes in the absorption spectrum are more significant than protonation in terms of the red-shift of the dpp transition, although the bond length between Ag^+ and either of the imine nitrogens is expected to be much longer than

an N-H bond given the much larger size of Ag^+ compared to H^+. One possible reason is that Ag^+ coordinates to *both* imine nitrogens. Although linear structures of Ag(I) are most commonly known, such as $[Ag(NH_3)_2]^+$, tetrahedral silver is also possible. Given as such, monodentate coordination of Ag^+ to the dpp ligand is expected to be linear, with a water molecule opposite the Ag-N bond, and bidentate coordination would most likely be tetrahedral, with two water molecules (Figure 95).[xxx] Though monodentate coordination of Ag^+ to the dpp ligand at the more basic pyridyl nitrogen, cannot be ruled out, two pieces of evidence support the idea of some degree of bidentate coordination: the observable shift in the absorption band where the MLCT is primarily coupled to the pyrazine nitrogen; and, the upfield shift of the B3' proton (Figure 62) in the NMR spectrum which most likely results from a twisting of the free pyridyl ring. It is certain that coordination occurs at the free pyridyl ring given the downfield shift in the resonances associated with it. The average equilibrium constant obtained from analysis of the NMR shift changes, 22.5 ± 8.3 M^{-1}, is within experimental error of that obtained from the absorption titration, 12 ±

[xxx] Six coordinate Ag(I) complexes are known but rare.[187]

a

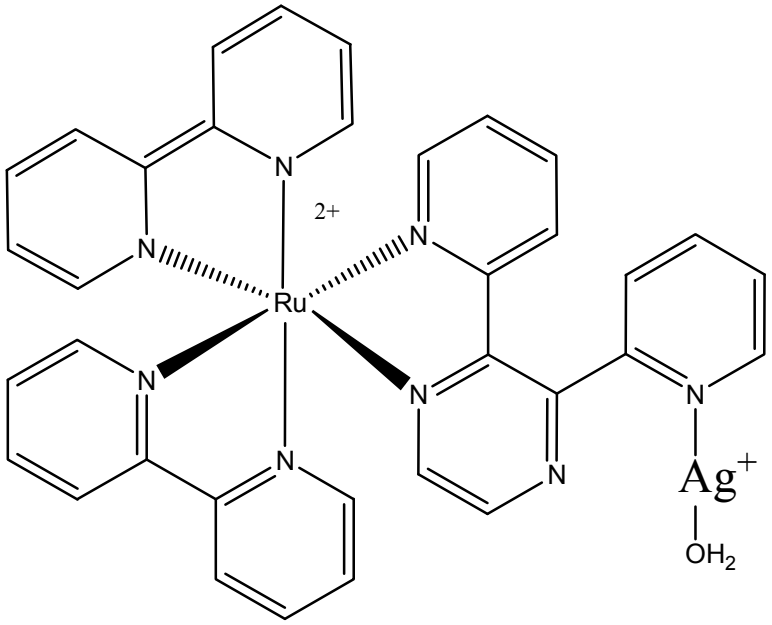

b

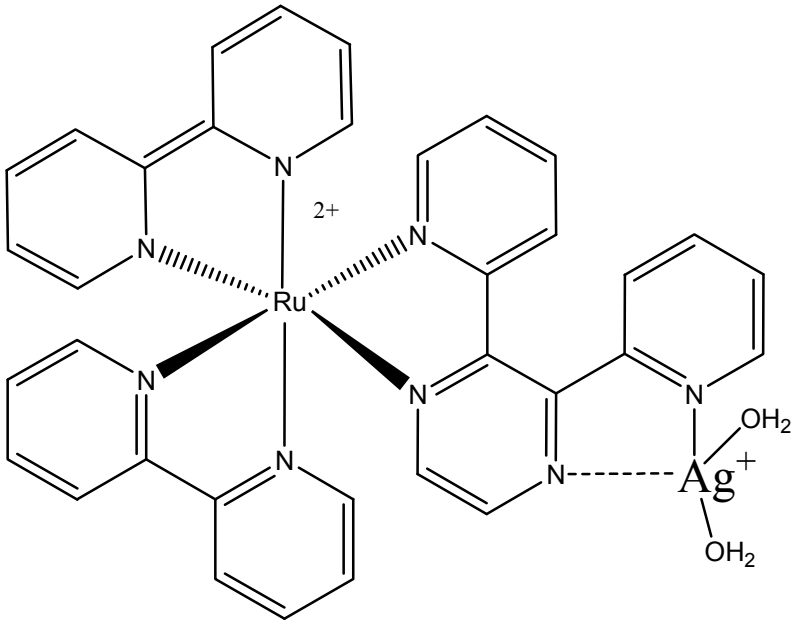

Figure 95. Association structure of $[(bpy)_2Ru(dpp)]^{2+}$ with Ag^+: (a) monodentate; (b) bidentate.

2 M^{-1}. The association is understandably weak given that it involves positively charged species.

Given the red-shift in the emission spectrum which is due to a different emitting species, a simple plot of the reduction in emission intensity, I_o/I *vs.* [Ag^+] is inappropriate. Instead, it is necessary to account for the overlap of the emission spectra. Ireland and Wyatt[38] provide a simplified approach. The overlap ratios for the free and associated species, p_{Ru} and p'_{RuM} are defined:

$$p_{Ru} = I_{\lambda\text{-max-RuM}} \; / \; I_{\lambda\text{-max-Ru}} \tag{101}$$

$$p'_{RuM} = I_{\lambda\text{-max-Ru}} \; / \; I_{\lambda\text{-max-RuM}} \tag{102}$$

where $I_{\lambda\text{-max-Ru}}$ is the emission intensity at the wavelength maximum for the free species, and $I_{\lambda\text{-max-RuM}}$ is the emission intensity at the wavelength maximum for the bimetallic. Using the measured intensities, I_λ and I'_λ of the free and associated species at some analytical wavelength λ, the corresponding corrected intensities, φ and φ' are calculated as follows:

$$\phi = \frac{I_\lambda - pI'_\lambda}{1 - pp'} \text{, and} \tag{103}$$

$$\phi' = \frac{I'_\lambda - p'I_\lambda}{1 - pp'} \text{.} \tag{104}$$

The inflection point of the plots *vs.* the –log [M^+] is the apparent pK^*. For the titration of [$(bpy)_2Ru(dpp)]^{2+}$, the inflection point from the plot (Figure 96) translates to an apparent K^* of 54 M^{-1}. If the lifetime correction is applied (63) accounting for the lower emission lifetime of the bimetallic [$(bpy)_2Ru(dpp\text{-}Ag)]^{3+}$, the K^* is 25 M^{-1}, a slight enhancement over of the ground state equilibrium constant of 12 M^{-1} (from the absorption titration). Combined with the Stern-Volmer plot of lifetimes (Figure 66) which exhibits negative deviations from linearity, Ag^+ appears to interact with $^*[(bpy)_2Ru(dpp)]^{2+}$ by associational quenching. A dynamic element is also possible. A similar red-shift in seen in methanol as well. Different though, the lifetimes of the [$(bpy)_2Ru(dpp\text{-}Ag)]^{3+}$ bimetallic in methanol appears to be *greater* than the free species in methanol (Table 12). Further studies are necessary to investigate this particular phenomenon. Methanol may in fact facilitate exciplex formation at the Π aromatic system instead which may enhanced the radiative rates in decouping the MLCT from the solvent system.

The exact structural mechanism of the excited-state complex between [$(bpy)_2Ru(dpp)]^{2+}$ and Ag^+ in water is difficult to surmise. Although there is definitive bonding at the dpp ligand in the ground state, and the

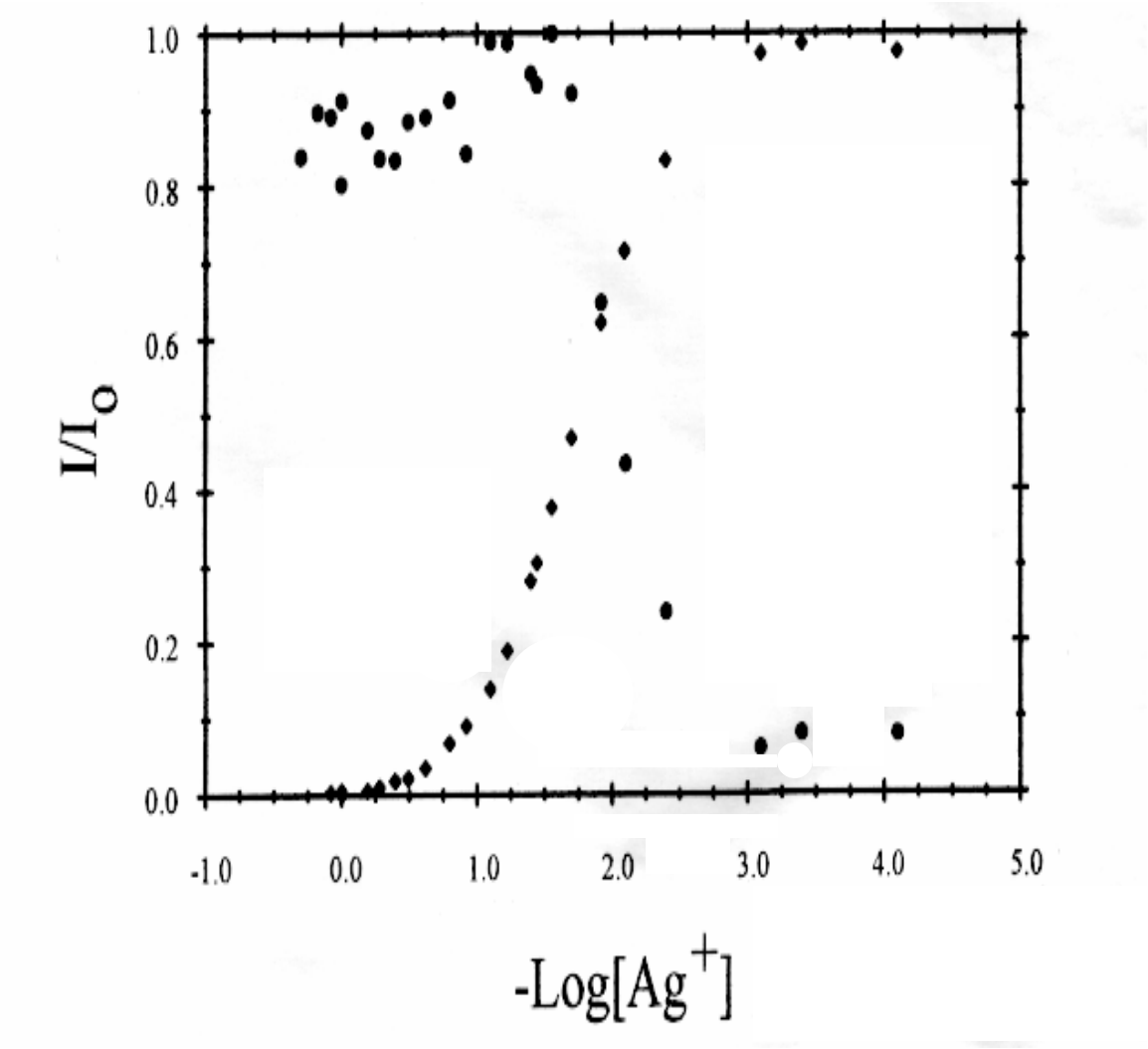

Figure 96. Sigmoidal plot of emission titration of $[(bpy)_2Ru(dpp)]^{2+}$ with Ag^+.

presupposition is that a similar structure exists in the excited-state, it cannot be ruled out that the Ag^+ associates with the Π aromatic system of the dpp ligand, since the analogous situation is invoked for exciplex formation between Ag^+ and $[Ru(bpy)_3]^{2+}$.[55] Additionally, Demas *et. al.*[57] rule out electron transfer to Ag^+ in its interaction with $[Ru(bpy)_3]^{2+}$ despite the energetic drive of its reduction:

$$Ag^+ + e^- \rightarrow Ag^0, \qquad E^0 = 0.80 \text{ V.} \qquad (101)$$

Given that an emissive species is observed in $[(bpy)_2Ru(dpp\text{-}Ag]^+$, it is unlikely that electron transfer to produce non-emissive Ru(III) is a viable quenching mechanism. Demas *et. al.*[57] also claim higher order interactions involving more than one silver ion in its interaction with $[Ru(bpy)_3]^{2+}$. Given the two base sites available on the dpp ligand, the inversion of basicity observed in the excited state, and the ability of Ag^+ to form monodentate linear complexes with imine nitrogens, it is quite possible at higher $[Ag^+]$ to get di-argentation. To better understand the mechanism of metal cation association using a more direct system, the metal cations Cd^{2+} and Zn^{2+} were extensively explored given that their reduction potentials disfavor electron transfer, and they are not

observed to have any Π aromatic interactions with diimine ligands in excited Ru(II) diimines.

Section 4.F. Association of $[(bpy)_2Ru(dpp)]^{2+}$ with Cd^{2+} and Zn^{2+}

There are no reported quenching interactions between Cd^{2+}/Zn^{2+} and Ru(II) diimines. On the contrary, mercuric complexes are known quenchers of transition metal complexes.[78] For example $HgCl_2$ has been shown to interact associationally with $[Ir(phen)_3]^{3+}$ and $[Ir(terp)_2]^{3+}$ to enhance their emission lifetimes and quantum yields.[66] Also, $[Ru(bpy)_3]^{2+}$ is quenched by Hg^{2+} by electron transfer, with a quenching constant of k_q, of 2.09 x 10^8 M^{-1} s^{-1}.[197]

Similar to results seen with Ag^+, changes in the absorption spectrum (Figure 44) suggest association of Cd^{2+}/Zn^{2+} with the dpp ligand in $[(bpy)_2Ru(dpp)]^{2+}$. The absorption spectra of the bimetallics $[(bpy)_2Ru(dpp\text{-}Zn)]^{4+}$ and $[(bpy)_2Ru(dpp\text{-}Cd)]^{4+}$ appear intermediate between the absorption spectra of the free species and the bimetallic $[(bpy)_2Ru(dpp)Ru(bpy)_2]^{4+}$. For the Ru-Ru bimetallic, the additional bpy ligands would be expected to stabilize the MLCT, and thus the more red-shifted absorption transition is understandable.

Both NMR sets of data of titrations with increasing [Cd^{2+}] and [Zn^{2+}] show similar results. Obtaining ground-state equilibrium constants for formation of the bimetallics proved difficult because the changes in chemical shifts of the protons are not consistent with equation (90). However, the sigmoidal shapes of the curves are not uncommon: in fact, even in cases of 1-to-1 association, sigmoidal curves of $\Delta\delta$ have been observed.[198] This is because the chemical shifts of the protons are responsive to several factors. These include the magnetic anisotropy of the ring current, van der Waals interactions, the vicinity of charged species, changes in dihedral angles, and interactions with other moieties in the molecule. These effects may vary in size and in which way they ultimately shield or deshield a proton as an association interaction occurs. Whilst the NMR spectra show coordination, definitely involving the free pyridyl ligand, and possibly involving the pyrazinyl nitrogen, given the NMR shift of A3, equilibrium constants obtained from fits of the absorption data will be employed.

In solution the dications Zn^{2+} and Cd^{2+} are aquated to form $[Zn(OH_2)_6]^{2+}$ and $[Cd(OH_2)_6]^{2+}$. Both aquated species are very acidic, according to the following equilibria:

$$[Zn(OH_2)_6]^{2+} \leftrightarrows [Zn(OH_2)_5(OH)]^{+} + H^{+} \quad (105)$$

$$[Cd(OH_2)_6]^{2+} \leftrightarrows [Cd(OH_2)_5(OH)]^{+} + H^{+} \quad (106)$$

and, have associated pK_a values of 8.96 and 9.00 respectively.[199] At 3 M concentrations, the solution pH values are 4.2 with Zn^{2+} and 4.3 with Cd^{2+}. Experiments done in both aqueous solution and pH=5 buffer solution yielded similar results: those presented here are for the buffered solutions at pH=5.[xxxi] With bidentate coordination, it is assumed that the coordination number of 6 is maintained in accordance with the 18-electron rule, which means each metal dication would retain 4 coordinated water molecules (Figure 97). The question of whether or not the aquated dications becomes more or less acidic upon coordination was not investigated, but most species are expected to be fully aquated because of the equilibria in (105) and (106) are strongly biased towards the left.

Efforts to isolate the bimetallic complexes, $[(bpy)_2Ru(dpp\text{-}Zn)](NO_3)_4$ and $[(bpy)_2Ru(dpp\text{-}Cd)](NO_3)_4$ were unsuccessful. Evaporation of solvent would leave behind a solid, inseparable mixture of $[(bpy)_2Ru(dpp)](NO_3)_2$ and metal nitrate salt. Addition of NH_4PF_6 would precipitate only the ruthenium complex. Attempts to soak porous Vycor

[xxxi] In higher pH buffer solutions, the metal hydroxides precipitate.

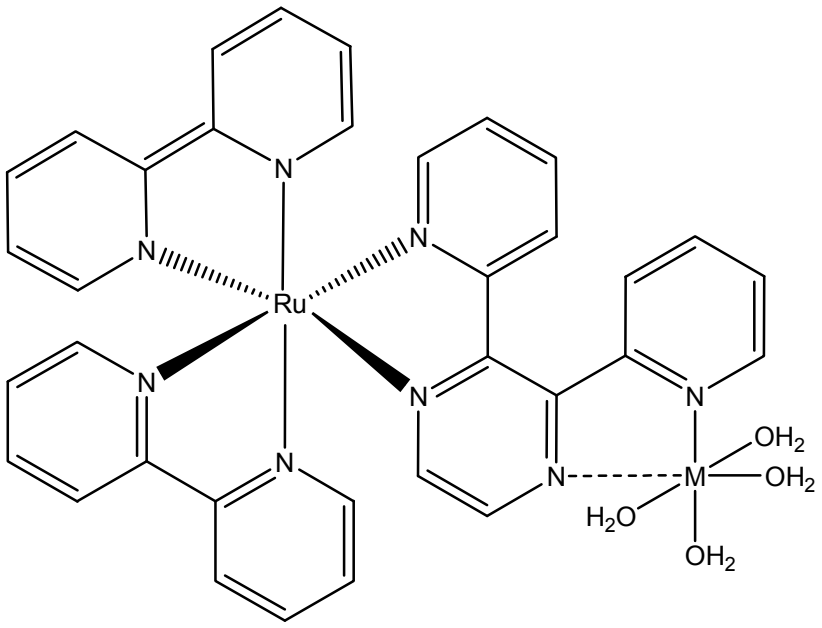

Figure 97. Structure of $[(bpy)_2Ru(dpp\text{-}M(OH_2)_4)]^{4+}$.

glass with metal nitrate solutions followed by solutions of $[(bpy)_2Ru(dpp)](NO_3)_2$ were inconclusive. Lastly, attempts to add bpy ligand to form $[(bpy)_2Ru(dpp)Zn(bpy)_2]^{4+}$ and $[(bpy)_2Ru(dpp)Cd(bpy)_2]^{4+}$ only led to the formation of the metal-bpy complexes alone. The stepwise formation constants for Zn^{2+} and Cd^{2+} with 2,2′-bipyridine have been reported and are given in table (Table 15). Clearly, the equilibrium constants for formation of the metal-bpy-complexes far exceeds the association constant with $[(bpy)_2Ru(dpp)]^{2+}$ by 4-5 orders of magnitude, thus precluding formation of the bimetallics with Ru. Interestingly, the formation for the first bpy complex, $[Zn(bpy)]^{2+}$ exceeds that of $[Cd(bpy)]^{2+}$ by a ratio of 1.2:1. Similarly, the association constant for formation of $[(bpy)_2Ru(dpp\text{-}Zn)]^{4+}$, at 15 ± 3 M^{-1} exceeds that for formation of $[(bpy)_2Ru(dpp\text{-}Cd)]^{4+}$, at 9 ± 2 M^{-1} by a ratio of 1.7:1. The absorption spectra of the association bimetallics in solution are therefore considered “absorption complexes”. By their definition, the association is too weak to form an isolatable compound, but absorption spectra are indicative of an associated complex as different from either of the parent complexes’ spectra.[14]

Table 15. Stepwise formation constants of Zn^{2+}-bpy and Cd^{2+}-bpy complexes.

Complex	$[M(bpy)]^{2+}$	$[M(bpy)_2]^{2+}$	$[M(bpy)_3]^{2+}$
	log K_1	log K_2	log K_3
Cd^{2+}	4.5	3.5	2.5
Zn^{2+}	5.4	4.4	13.3

At the very least, the emission titrations of $[(bpy)_2Ru(dpp)]^{2+}$ with Cd^{2+} and Zn^{2+} parallel changes in the absorption spectra: with increasing concentration of metal dication and further red-shift of the MLCT band to dpp, concomitant red-shifts are seen in the emission, as well as reductions in the intensity and lifetime of emission. At intermediate concentrations of metal dication, $0M<[M^{2+}]<1M$, exponential decays are biexponential, suggestive of two emitting species. Clearly there is associational quenching, but the critical question is whether or not there is a dynamic component to the quenching, meaning, does the data suggest that association between the diimine and metal dication are favored in the excited state?

In approaching the time-resolved data, the issue of the additional emission of $[(bpy)_2Ru(dpp)]^{2+}$ in pH=5 buffer solution and 5 M $Ca(NO_3)_2$ must be addressed. When preliminary experiments were carried out in just aqueous solution, single exponential decays were evident for the free $[(bpy)_2Ru(dpp)]^{2+}$ and associated species at high $[M^{2+}]$.

One possibility is that the data analysis itself yields spurious emissions. When comparing the double-exponential fit to the steady state, the steady-state emission matches that of the longer lifetime, higher energy species, which would presumably be the free species. If the longer wavelength species were real, the steady-state spectrum should be an average of the two resolved emission. Since it is not, it is discounted as spurious. However, is the greater lifetime obtained in the double exponential fit dependable? The full set of issues surrounding this new analysis has yet to be fully understood. When the spurious emission in the titration with Cd^{2+} is extracted from the double exponential fits and plotted (see Figure 76), its presence and average lifetime remain the same, although steady-state data continue to match the other A_1 set. This places a limitation on the ability of the IGOR analysis to successfully time-resolve spectra. Even so, the time-dependent equations (43)-(52) are sufficiently complicated, that preference is given to using the steady-state data for analysis.

In order to resolve simultaneous emissions in steady-state spectrum, instead of correcting the intensities for the overlap ratios as suggested by Wyatt and Ireland,[38] (c.f. Figure 96) a novel approach is to take the limiting

emission spectra of free and associated $[(bpy)_2Ru(dpp)]^{2+}$ species, and use linear regression to "fit" the in-between spectra. The steady-state spectra of partially associated metal cation are composites of the free and complexed emission spectra according to the following:

$$\text{Observed spectrum} = f_o\ (\text{free spectrum}) + f_1\ (\text{associated spectrum}) \quad (107)$$

where f_o and f_1 are the fractions of free and associated species, and are the fitting parameters. In essence, the fits provide the relative "proportions" of each emitting species, f_o and f_1, and thus resolves the steady-state spectra into its component parts.

The limiting emission spectra from the free and associated $[(bpy)_2Ru(dpp)]^{2+}$ with Zn^{2+} and Cd^{2+} can be used to fit the emission spectra in between. The results for association with Cd^{2+} are shown in Figure 98, and for Zn^{2+}, Figure 99. By resolving the spectra in this way, the contribution of each fit is proportional to the fraction of excited states of that emitting species. A feel for the excited state equilibrium constant for association, K^* can be obtained from the simple equation

$$K^* = \frac{^*[RuM]}{^*[Ru][M]_o} \quad (108)$$

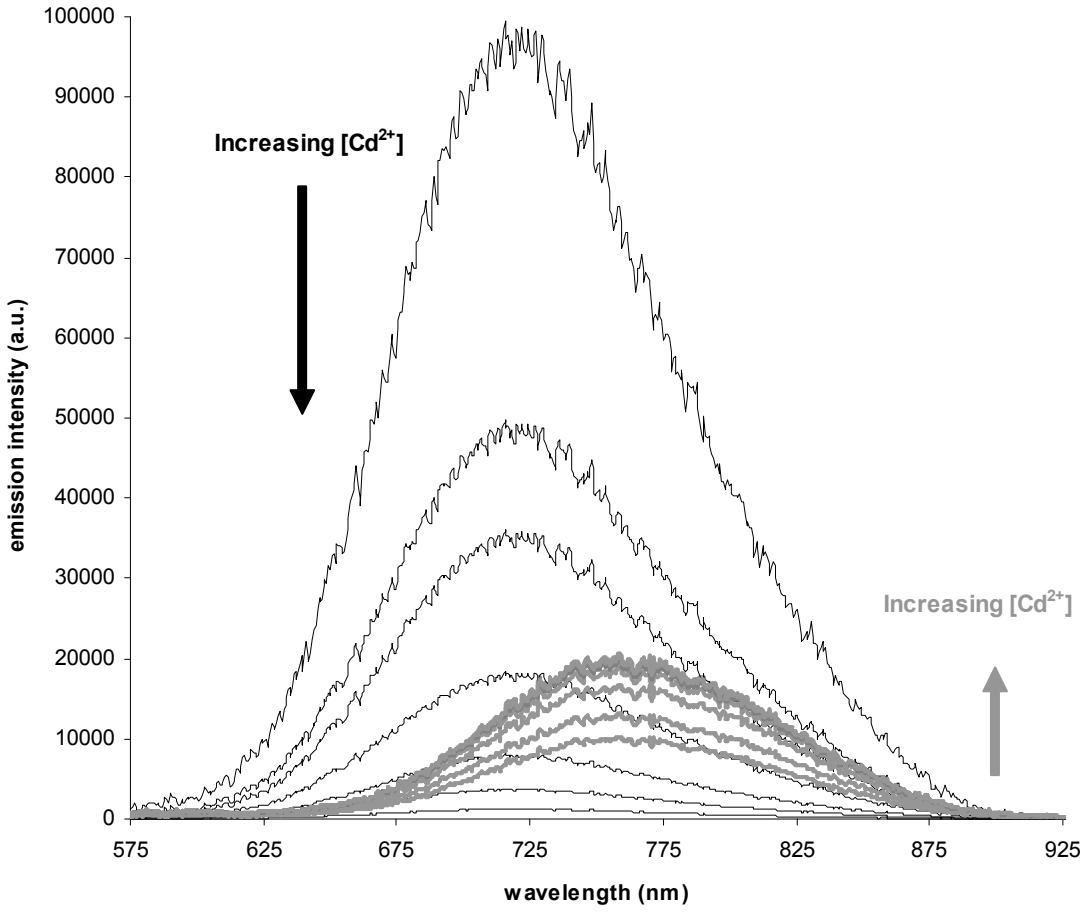

Figure 98. Resolved spectra from steady-state emission titration of $[(bpy)_2Ru(dpp)]^{2+}$ with Cd^{2+}.

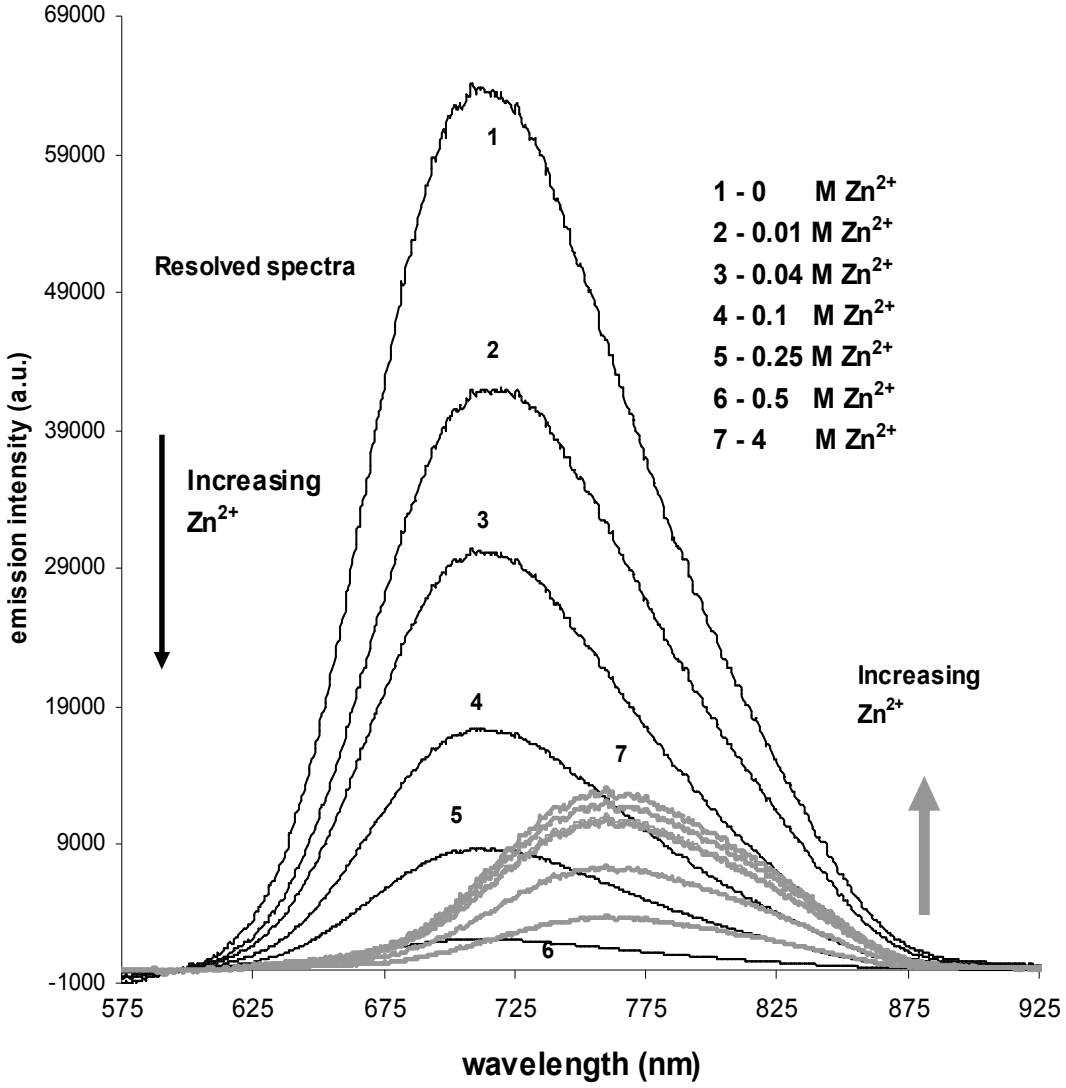

Figure 99. Resolved spectra from steady-state emission titration of $[(bpy)_2Ru(dpp)]^{2+}$ with Zn^{2+}.

if the initial $[M^{2+}]_o$ far exceeds the concentration of excited state bimetallic, $^*[RuM]$. The apparent K^* *vs.* $[M^{2+}]_o$ is shown in table 16.

Table 16. Apparent K^* from emission titration of $[(bpy)_2Ru(dpp)]^{2+}$ with Cd^{2+} and Zn^{2+}.

$[M^{2+}]_o$	apparent K^* M^{-1} (Cd^{2+})	apparent K^* M^{-1} (Zn^{2+})
0.01	100	50
0.04	44	33
0.1	44	33
0.25	45	27
0.5	50	63
1	78	98

At intermediate $[M^{2+}]_o$, the apparent K^* values are in fairly good agreement, averaging to 60 ± 23 M^{-1} for Cd^{2+} and 51 ± 27 M^{-1} for Zn^{2+}. All are greater than the corresponding ground-state association constant. The second approach is to plot the fractions of each species *vs.* $-\log [M^{2+}]_o$, or pM_o to yield similar results to the Wyatt and Ireland analysis. The shared inflection point represents the pK^* assuming the species have similar lifetimes. The plots for association with Cd^{2+} and Zn^{2+} are shown in Figure 100. Using sigmoidal fits, the shared inflection point is 1.85 for association with Cd^{2+} and 1.54 for association Zn^{2+}. This translate into excited state equilibrium constants for association, K^*, of 71 ± 7 M^{-1} for Cd^{2+} and 35 ± 4 M^{-1} for

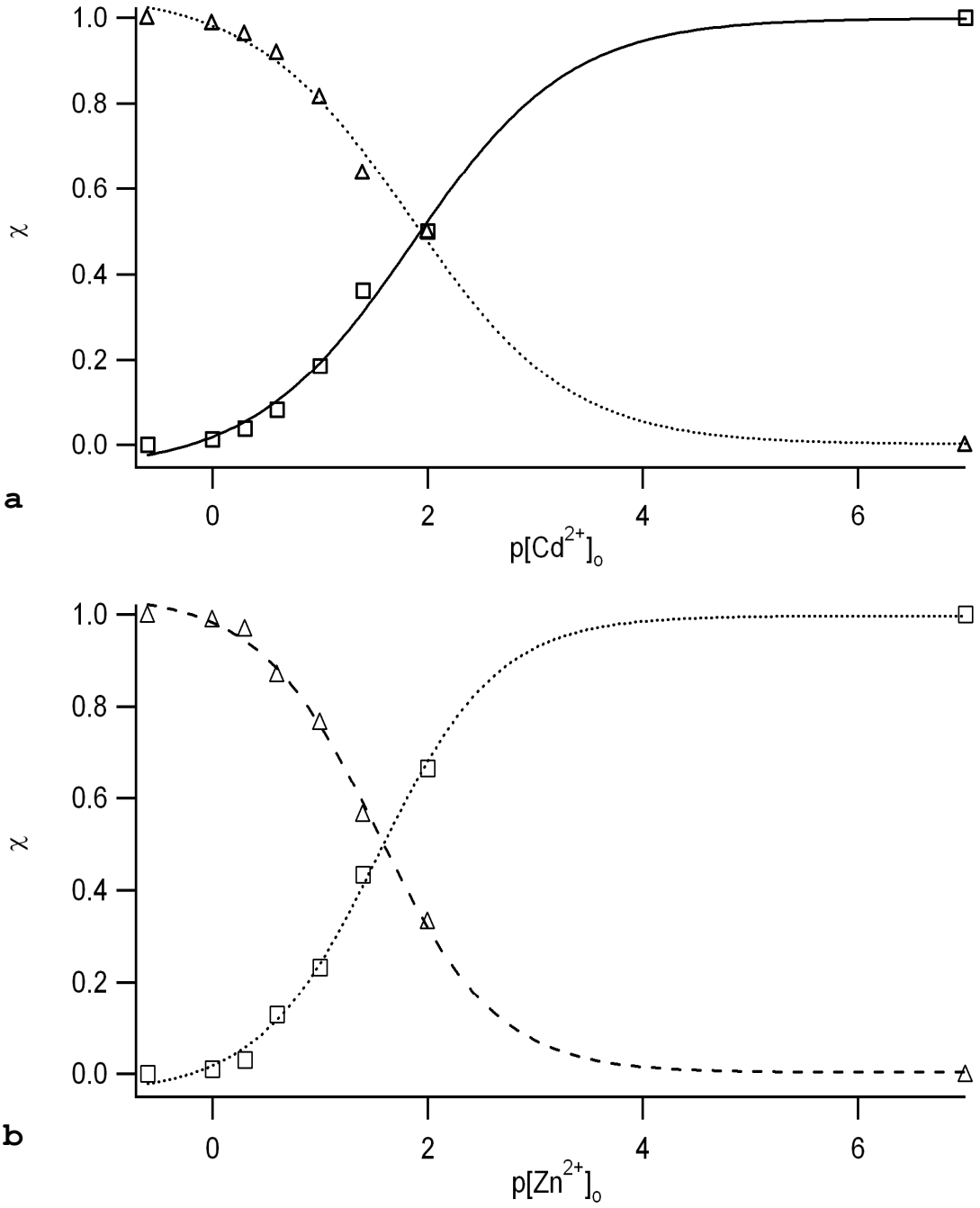

Figure 100. Sigmoidal plots of emission titration of $[(bpy)_2Ru(dpp)]^{2+}$ with Cd^{2+} and Zn^{2+}: (a) with Cd^{2+}; (b) with Zn^{2+}.

Zn^{2+}. When the lifetime correction (63) is applied because of the lower lifetimes of metallated species, the K^* is now 20 ± 2 M^{-1} for Cd^{2+} and 9.6 ± 1 M^{-1} for Zn^{2+}. The corrected values are in the vicinity of the ground-state equilibrium constants, strongly indicated that association in the ground-state determines to a large degree the kinetics of interaction in the excited. These are summarized in Table 17.

Table 17. Ground- and excited-state association equilibrium constants from sigmoidal plots of the emission intensities of association of $[(bpy)_2Ru(dpp)]^{2+}$ with Zn^{2+} and Cd^{2+}.

	Apparent K^* M^{-1}	Corrected K^* M^{-1}	K M^{-1}
Cd^{2+}	71	20	9
Zn^{2+}	35	9.6	15

If 1:1 association is assumed and just pure exciplex formation, meaning, no ground-state association, the following equations can be fit to yield K^* where χ_{Ru} and χ_{RuM} are the respective fractions of excited state species present:

$$\chi_{Ru} = 1/(1 + K^*[M]) \quad (109)$$

and,

$$\chi_{RuM} = K^*[M]/(1+K^*[M]). \quad (110)$$

Fits of the plots (Figure 101) agree on an uncorrected

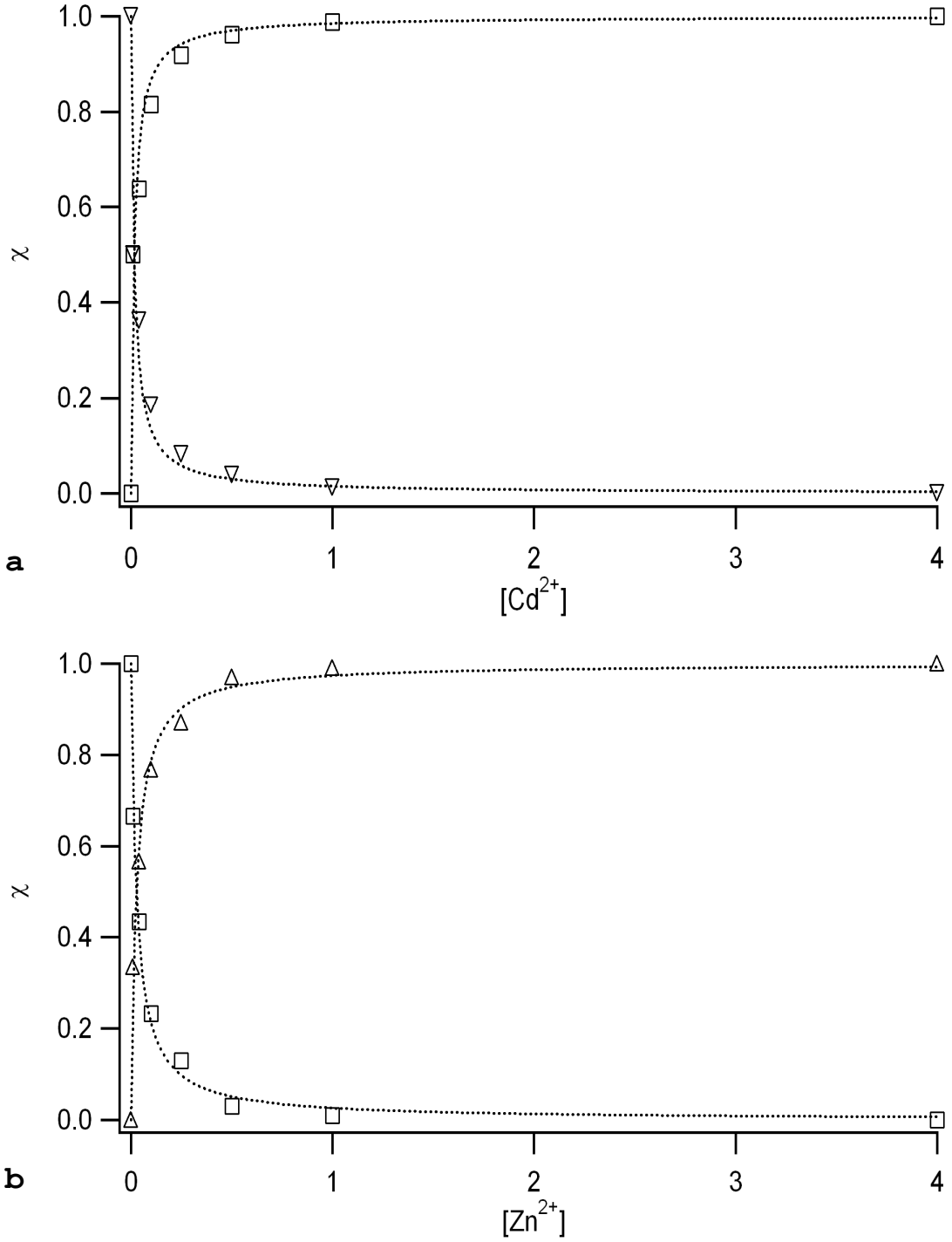

Figure 101. Simple exciplex model fits of association of Cd^{2+} and Zn^{2+} with $[(bpy)_2Ru(dpp)]^{2+}$: (a) with Cd^{2+}; (b) with Zn^{2+}.

excited-state equilibrium constants, 66 ± 7 M^{-1}, for association with Cd^{2+}, and 37 ± 4 M^{-1} for Zn^{2+}.

Stern-Volmer plots of the decrease in intensity of the steady-state emission from the free species, steady-state quantum yield, and lifetime for the resolved spectrum of the free species all exhibit negative deviations from linearity (Figure 102). Lifetimes were taken from the double exponential fits, always using the larger value.[xxxii] The non-coincidence of the plots suggests dynamic interactions as well, and negative deviations suggest associational quenching. In essence, the limiting lifetime appears to be reached prior to the limiting steady-state equilibrium. Clearly then, the Stern-Volmer equation for associational quenching[31] (78) must be employed to fit the data for change in intensity. Using (42) to substitute for k_q, and replacing K_{SV} with $k_q\tau_o$, the following equation for fitting is obtained:

$$\frac{I_o}{I} = \frac{1 + (k_q\tau_o + K_{eq})[M]_o + k_q\tau_o K_{eq}[M]_o^2}{1 + (1+\gamma)\left[\frac{k_q[M]_o}{k_{de}}\right] + \gamma\left[\frac{k_q(k_o + k_d[M]_o)K_{eq}[M]_o}{k_d k_{de}}\right]} \qquad (111)$$

[xxxii] The smaller value is invariant.

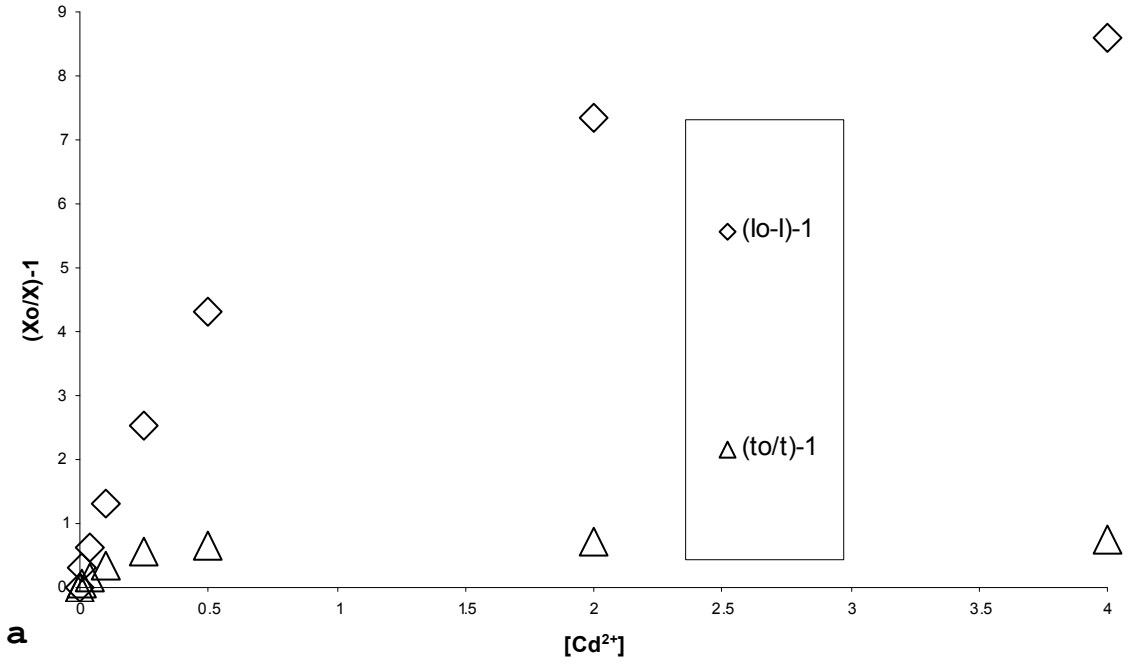

a

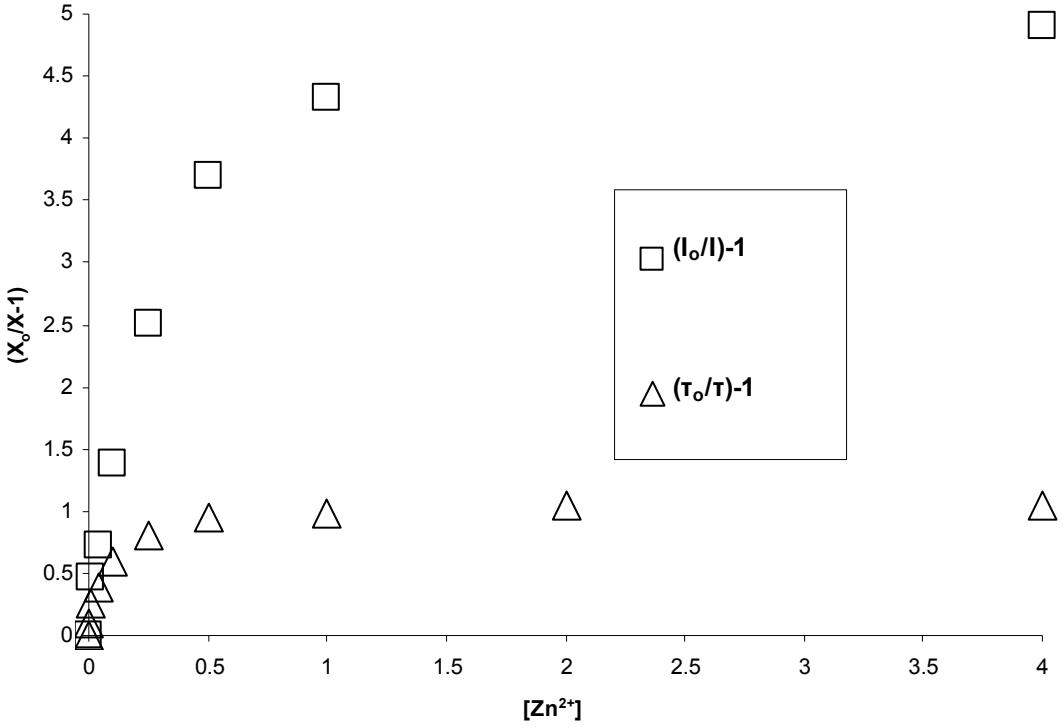

b

Figure 102. Stern-Volmer plots of association of $[(bpy)_2Ru(dpp)]^{2+}$ with Cd^{2+} and Zn^{2+}: (a) with Cd^{2+}; (b) with Zn^{2+}.

where k_q and k_{de} are the fitting parameters, τ_o is the lifetime of the free species, γ is calculated from the differential intensities of the two emissive species and their quantum yields by equations (71)-(73), and $[M]_o$ is the initial concentration of metal dication. For a sufficiently sophisticated software program, k_d, the diffusion constant, can also varied in a three-parameter fit. Alternatively k_d can be estimated and set constant for a two-parameter fit. A value of 10^9 s^{-1} has been reported for the diffusion of Hg^{2+} and $[Ru(bpy)_3]^{2+}$ in 0.002 ionic strength aqueous solution and is used in the two-parameter fits.[189] To fit equation (111), the relative emissivities, or Φ_{em} of the free and metallated ruthenium(II) complex are needed. The quantum yield of emission for the bimetallics $[(bpy)_2Ru(dpp\text{-}Zn)]^{4+}$ and $[(bpy)_2Ru(dpp\text{-}Cd)]^{4+}$ in aqueous solution at room temperature, 22 ± 1 °C, were determined to be 0.0006 ± .0001 and 0.00025 ± .0003.

The Zn^{2+} bimetallic is more emissive than the Cd^{2+} bimetallic. This may parallel its slightly higher association constant with $[(bpy)_2Ru(dpp)]^{2+}$ then with Cd^{2+}, indicative of a more stable species and/or its smaller size. Indeed the wavelength maximum for the Zn^{2+} bimetallic alone, at 775 nm, is reduced in energy than that with Cd^{2+} which has wavelength maximum at 755 nm.

The software program IGOR was used for both the two and three parameter fits. Clearly, with three parameter-fitting, there are often many solutions will give local minimizations. Interestingly though, when k_d was also a fitting parameter, the best minimizations yielded unexpected results that led to negative K^* values and rate constants for quenching exceeding rate constants for diffusion, meaning $k_q > k_d$.

It is useful to restate equation (42):

$$k_q = \frac{k_d k_{de}}{k_{de} + k_{-d}} \quad . \tag{42}$$

For diffusion-controlled deactivation, quenching will occur nearly immediately upon diffusion, meaning the rate constant for dissociation of the encounter complex, k_{-d},is small compared to the deactivation rate constant, k_{de} and $k_q \sim k_d$. In the pre-equilibrium limit rather, $k_{-d} >> k_{de}$, and $k_q/k_{de} = K^*$. Lastly, at high $[M]_o$, equation (111) will approach a value of $k_{de}/k_o\gamma$. Two fits each for Cd^{2+} and Zn^{2+} (Figure 103) with k_d estimated at 10^9 s^{-1} and fitted are provided in Table 18.

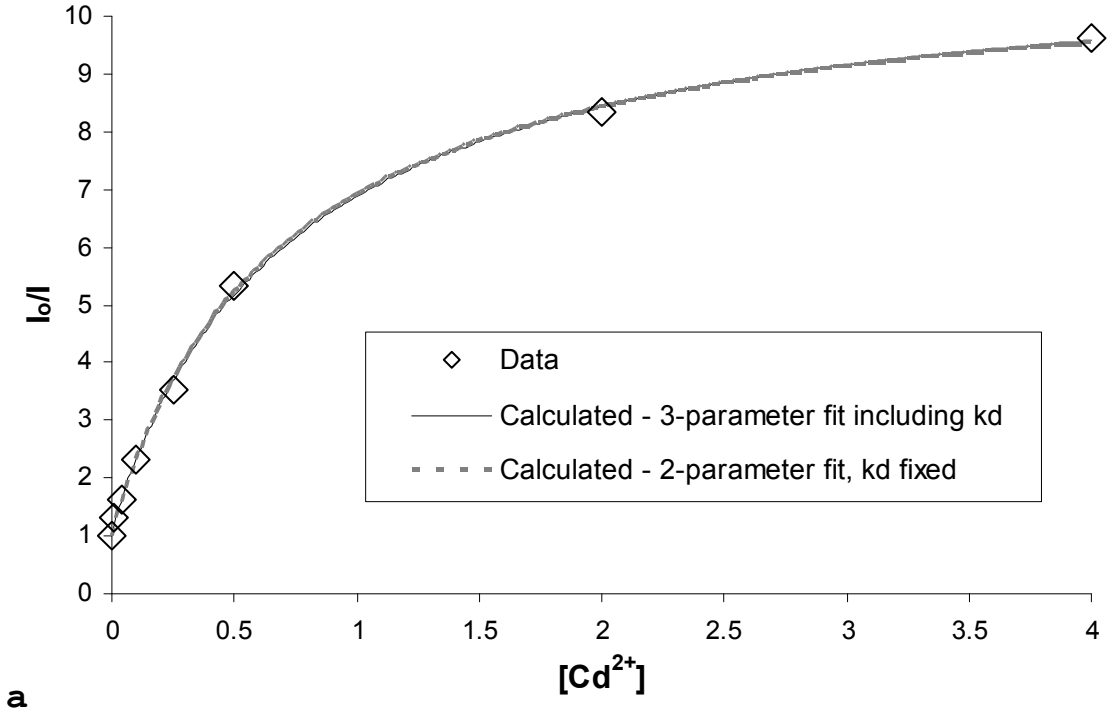

a

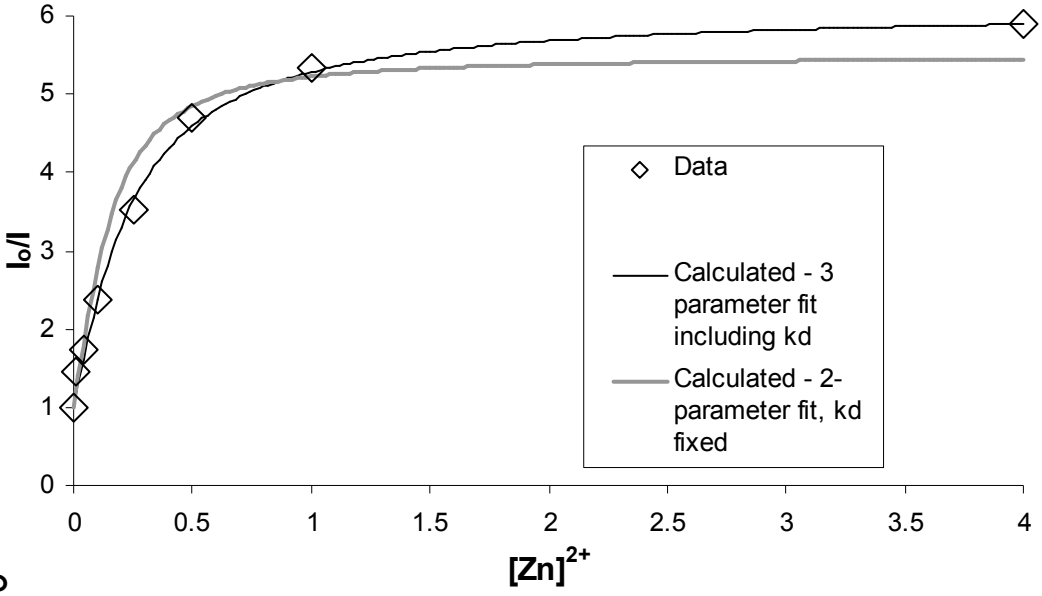

b

Figure 103. Fits of Stern-Volmer plots for associational quenching of $[(bpy)_2Ru(dpp)]^{2+}$ by Cd^{2+} and Zn^{2+}: (a) by Cd^{2+}; (b) by Zn^{2+}.

Table 18. Fit parameters for Stern-Volmer quenching of $[(bpy)_2Ru(dpp)]^{2+}$ by Cd^{2+} and Zn^{2+}

	$[Cd^{2+}]$ k_d held	$[Cd^{2+}]$ k_d fit	$[Zn^{2+}]$ k_d held	$[Zn^{2+}]$ k_d fit
K_{SV} M^{-1}	21	25.6	10.7	6.2
k_q M^{-1} s^{-1}	2.07×10^8	2.53×10^8	1.05×10^8	6.52×10^7
k_{de} M^{-1} s^{-1}	1.77×10^7	1.79×10^7	3.09×10^7	3.43×10^7
k_d s^{-1}	1×10^9	3.16×10^8	1×10^9	5.65×10^7
k_{-d} s^{-1}	6.79×10^7	4.46×10^6	2.63×10^8	1.07×10^8
K^* M^{-1}	14.7	70	3.80	- 12.3

The two-parameter fits with k_d held suggest a pre-equilibrium since $k_{-d} > k_{de}$ by a factor of 8.5 for Zn^{2+} and 3.8 for Cd^{2+}. In these cases, the K^* values are on the order of the ground state equilibrium constants. Given the fact that the metal dications associate with $[(bpy)_2Ru(dpp)]^{2+}$ in the ground-state, one would surmise that the bimetallic complex is "pre-formed". However, since the association is weak and forms a new emitting species, the Stern-Volmer plot does not exhibit positive deviations as would be seen for pure static associational quenching. However, if one follows the reduction of the $[(bpy)_2Ru(dpp)]^{2+}$ emission only from the resolved spectrum, then the Stern-Volmer plot does exhibit positive deviations according to equation (77).

A dynamic portion though of the associational quenching should not be ruled out. The three-parameter fit yields better minimizations, but rate constants and a

negative K^* that on first examination make little sense. The diffusions constants are lower than that estimated by a factor of 3.2 for association with Cd^{2+} and 18 for Zn^{2+}. Additionally, the quenching constant is greater than the diffusion constant: in other words, how is it possible for the diimine to be quenched faster than it forms an encounter complex with the quencher? Though it might be tempting to simply discard the fit because of these discrepancies, in fact they can be quite revealing that the diffusional model is completely inadequate to fit the data. As can be seen from the fits in Figure 103, disparate values of k_q and k_d can give quite satisfactory fits. The rate constant for total deactivation, k_{de}, in both fits is quite similar at 2×10^7 s^{-1}. This though makes sense as the equation reaches the same limit, $k_{de}/k_o\gamma$ at high $[M^{2+}]$.

If the rate of quenching can exceed the rate of diffusion, then quenching has nothing to do with diffusion. Consider the previous extensive discussion on the significant increase in basicity at the pyrazinyl ring concomitant with population of the MLCT state on the dpp ligand: it is quite possible that once a metal has associated with $[(bpy)_2Ru(dpp)]^{2+}$ primarily at the pyridyl ring, formation of an emissive, *bidentate* complex quickly occurs in the excited state. At low concentrations of metal

cation, there would be a diffusional, dynamic portion of the quenching as metal cations would associate with the excited dpp ligand to form an emissive species. This corresponds to the first part of the quenching curve in Figure 103. As further metallation takes place at higher $[M^{2+}]$, the complex is pre-formed, with association primarily at the free pyridyl ligand. Upon excitation, formation of the emissive bimetallic, with an association interaction primarily at the pyrazinyl nitrogen is fast, and faster than diffusion. In such a case K^*, which equals k_d/k_{-d} is meaningless since neither diffusion nor separation is at play. This model is summed up in Figure 104. It explains why, in the overall picture, there is an apparent increase in the excited-state equilibrium constant for association, but when examining mechanistic rate constants, the presence of pre-equilibrated associational quenching is evident.

The preliminary results of association of $[(bpy)_2Ru(dpp)]^{2+}$ with Hg^{2+} are also suggestive of associational quenching. It is startling that where oxidative quenching of Hg^{2+} is favorable since for the redox equation,

$$2\ Hg^{2+} + {}^{2e-} \leftrightarrows Hg_2^{2+} \qquad (112)$$

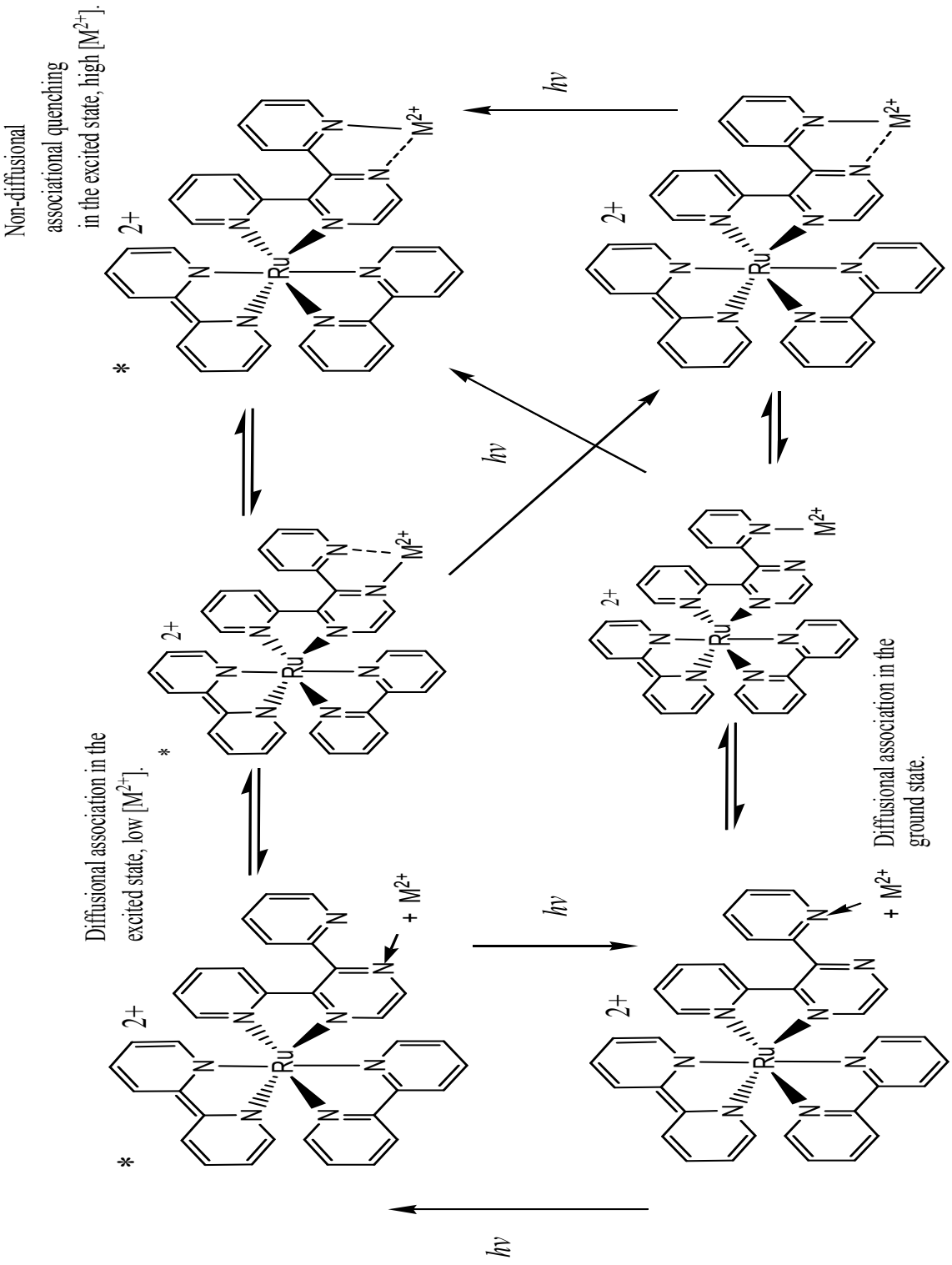

Figure 104. Model of associational quenching of $[(bpy)_2Ru(bpp)]^{2+}$ by Cd^{2+} and Zn^{2+}.

the overall driving potential is 1.4V. If reductive electron transfer by $[(bpy)_2Ru(dpp)]^{2+}$ was a competitive process, the ensuing $[(bpy)_2Ru(dpp)]^{3+}$ would be non-emissive since excited state Ru(III) diimines relax by non-radiative means. Similar to Ag^+, Hg^{2+} is thought to interact with the π system of the aromatic ligands in cases of interactions with Ru(II) diimines.[65] However, the base sites on the dpp ligand would be expected to specify the structure of the interaction on the periphery of the dpp ligand. Clearly, Hg^{2+} is an excellent candidate for further investigations into these associational mechanisms.

A last word should be offered about the seeming 815 nm emission seen in the steady-state emission spectra of fully metallated species such as $[(bpy)_2Ru(dpp\text{-}Cd)]^{4+}$, $[(bpy)_2Ru(dpp\text{-}Zn)]^{4+}$, and $[(bpy)_2Ru(dpp\text{-}Pb)]^{4+}$: it is possibly that higher order species also form and emit at such high metal ion concentrations. In previous studies where interactions between Ru(II) diimines and metal cations were observed, all cases involved the idea of higher order species at high metal ion concentration to explain deviations in the data from a 1:1 association model.[55,57] Several possibilities that will need to be further vetted can be imagined here and are shown in Figure 105. These involve the possibility of multi-metal bonding

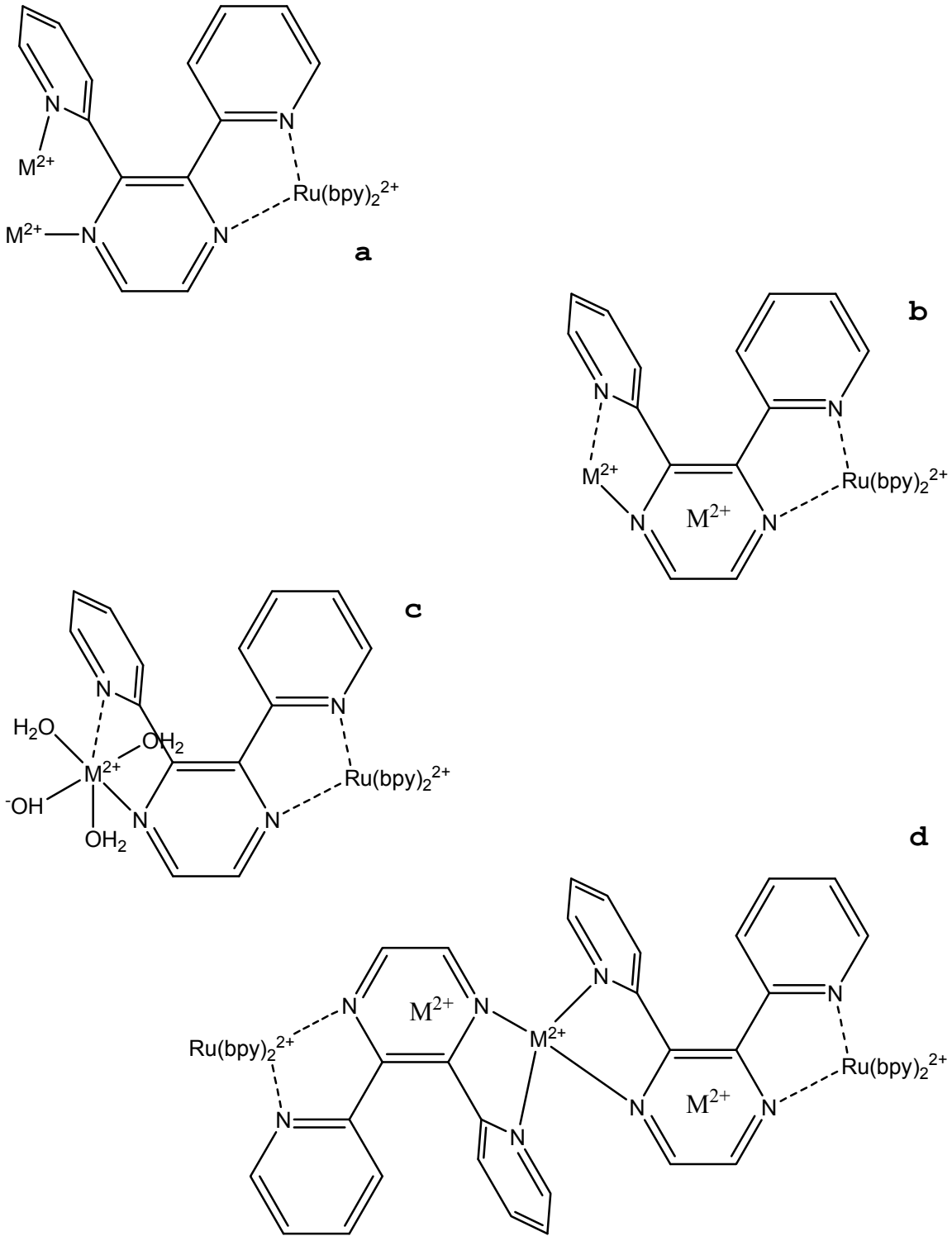

Figure 105. Other possible emissive structures at lower energy: (a) di-metallation; (b) metal cation-Π aromatic interactions; (c) deprotonated bimetallic; (d) trimetallic.

at the dpp ligand made possible by the ability of the pendant pyridyl ring to rotate at a 90° angle; transient association of additional metal cations with the aromatic portions of the ligands; emission from a deprotonated bimetallic of the type $[(bpy)_2Ru(II)(dpp)-(M(II))(OH_2)_3(OH^{-1})]^{3+}$; and finally, trimetallic formation of the type $[(bpy)_2Ru\text{-}dpp\text{-}M\text{-}dpp\text{-}Ru(bpy)_2]^{6+}$. Preliminary experiments have shown that the emission of $[Ru(bpy)_3]^{2+}$ in the presence of Zn^{2+} or Cd^{2+} is unchanged, so the idea of association with the aromatic π systems of the ligands is discounted. Of the possibilities, the deprotonated bimetallic is favored for two reasons. First, its emission lifetime should be similar to that of the protonated compound since the deprotonated water is remote and associated with the solvent cage. As discussed, the 815 nm emission seemingly had a lifetime invariant from the main bimetallic emitting species. Second, deprotonation would be favored thermodynamically as a stabilizing force on the dipositive metal cation, and thus a lower energy emitting state would be expected.

5. Conclusions

5.A. Analysis of Ground-state and Excited- state spectra

Proton NMR has been used to observe the initial protonation of $[(bpy)_2Ru(dpp)]^{2+}$, heretofore unseen and its pKa value unassigned. NMR has also been useful in estimating the ground state association constant for $[(bpy)_2Ru(dpp)]^{2+}$ with Ag^+. UV-VIS titrations have been more useful in determining ground state association constant for metallation.

Two novel approaches of analyzing emission titration spectra are presented based on data obtained from the successful integration of the ICCD camera system with both pulse and continuous wave laser coupled with a spectrograph with gratings blazed for maximal reflectivity at longer wavelengths. The first necessitates a case in which a free and associated species are both emissive in overlapping regions. The spectra of the free and associated complexes can be used to "fit" the in-between steady spectra, which are a weighted averages of the two, to extract the excited state fractional concentrations. From this, proper Stern-Volmer analyses can be accomplished. Second, curve fitting routines in the math program Igor have been used to resolve the wavelength dependence of time-resolved emission data

obtained from an ICCD camera system and plot the wavelength dependence of lifetimes. There will need to be further investigations of the information garnered from these kinds of analyses.

5.B. Excited-state Enhanced Coordination

Studies have shown that for a series of homologous binding interactions between diimines and a particular metal cation, the strength of association is directly related to the basicity of the ligand. More specifically, the equilibrium constant can be defined as such:

$$\log K_1 = A(pK_a) + B \quad (113)$$

where constants A and B are characteristic of the metal and ligand.[200] This has been observed for the combination of Fe^{2+} and various substituted phenanthrolines. For the case of phenanthroline itself,

$$Fe^{2+} + phen \rightarrow Fe(phen)^{2+}, \text{ and} \quad (114)$$

$$\log K_1 = 0.596 \times pK_a + 2.93.[200] \quad (115)$$

Here, the same idea is translated to the interaction of an excited Ru(II) diimine, known to have increases in basicity associated with peripheral immine sites, and other metal

cations. This effect is certainly expected for coordination of imines to Zn^{2+} and Cd^{2+}.[96] The asymmetry of the coordinated dpp ligand, both structurally and *kinetically* in terms of the differential change in basicities at the imine nitrogens in the excited state leads to a more complex view of this interaction. The ground-state interaction, especially at the more basic pendant pyridyl ring, sets up a pre-equilibrium that defines the excited state interaction. That excited-state interaction is thought to have a small degree of dynamism as different changes in the basicity alter the essential bimetallic structure, transiently.

It is remarkable that coordination to a metal cation leads to the formation of new emissive species and not primarily to non-radiative deactivation. The stark negative deviations from Stern-Volmer quenching are more an exception. The increase in non-radiative rates do not wipe out the emission. As different from protonation, bonding to a large metal cation does not serve as an extremely efficient energy dump. This was somewhat predictable given the emissive properties of $[(bpy)_2Ru(dpp)Ru(bpy)_2]^{4+}$. Indeed one of the triumphs of the dpp ligand was its ability to form emissive multi-metal species. The pendant pyridyl ring allows for bidentate coordination that can twist and

accommodate differently bonded metal cations.[101,108,120] Since the free pyridyl ring is not strongly coupled to the MLCT system, its rotation about several twist angles and bonding to metal cations does not lead to significant enhancements in non-radiative decay. The associational quenching of $[(bpy)_2Ru(dpp)]^{2+}$ by Cd^{2+} and Zn^{2+} is primarily static, but dynamic interactions associated with inversion of the relative basicities of the imine nitrogen sites accounts for a degree of dynamism. This dynamic quenching will be most evident at low concentrations of metal cation, as it is for low $[H^+]$ at the pyrazinyl site, and will involve some sort of transferred interaction at high proton and metal concentrations. The work presented here does provide valuable information on how differing interactions and energetic considerations mitigate the possibility of an excited-state enhanced basicity facilitating coordination to another metal.

5.C. Metallation *vs.* Protonation

Difference between metallation and protonation are initially seen in the absorption and NMR spectra of the ground state. It might be surprising that compared to protonation, metal chelation would have less effect on the NMR spectrum. However, H^+ has an extremely high charge to

mass ratio. It is effectively bringing a "full" positive charge in close proximity to the pyridyl ring. This incredible perturbation is sure to have significant effects, which are seen. On the other hand, a metal cation is much larger than a proton and the nitrogen-metal bond length is much greater than that of an N-H bond. Even with a +2 cation like Zn^{2+} or Cd^{2+}, the lower charge to mass ratio and the longer bond distances will perturb the pyridyl ring less, although the deshielding effects are still evident. Given this difference, again, one would expect parallel results in the absorption spectrum—that protonation would have a strong effect and metal chelation a small one. Yet, the opposite it observed. This disparity points to the essential structural differences between them. The MLCT transition is nearly exclusively out to the pyrazine of the dpp ligand. Strong interactions at the pyrazine nitrogen would be evident in the absorption spectrum whilst interactions at the (electronically uncoupled) pyridyl ring would only be evident in the NMR. This confirms that protonation is primarily at the pyridyl ring, with small hydrogen-bonding interactions with the pyrazyl, while metal chelation has an effect on BOTH spectra, indicative of some degree of bidentate chelation.

Protonation demonstrates the asymmetry of the imine nitrogen base sites both in the ground and excited states of $[(bpy)_2Ru(dpp)]^{2+}$. Inversion of the relative basicities is observed on population of the excited state. This effect is invoked for the results with metallation where one model allows for the quenching rate to be determined by the pre-equilibrium of association and not from diffusion. Therefore transient electronic reorganization may facilitate transient bond formation at the ligand of a coordination complex, particularly when the ground-state structure of an interaction facilitates this mechanism.

5.D. Exciplex Formation and Definition

This work implies slightly different interactions between $[(bpy)_2Ru(dpp)]^{2+}$ and metal cations in the ground and excited states. Weak ground state association is observed that serves as a model for the excited state interaction. The bimetallics $[(bpy)_2Ru(dpp\text{-}Zn)]^{4+}$ and $[(bpy)_2Ru(dpp\text{-}Cd)]^{4+}$ could not be isolated. Since the equilibrium constant for association cannot be “pushed” far enough to create an isolatable species, the absorption changes seen are indicative of an absorption complex. It is reasonable to imagine that the dynamism of the ground-state equilibrium constant is paralleled to some lesser or

greater degree in the excited state, given the extraordinary redistribution of electron density that occurs. The metal cation serves both as a buffer between the Ru(II) diimine and the solvent and a connection to it. The immense changes in electron distribution associated with population of the MLCT state almost certainly means extraordinary changes in the solvent cage around it in the excited state. Whereas protonation serves as an energy dump, metallation serves as a buffer of sorts. The metal, with associated waters of coordination has its own solvent cage. Thus upon excitation, the additional metal cation may be better able to respond to both the charge transfer to it, and to the solvent reorganization required to accommodate it.

There is a fundamental question as to whether an interaction will be electron transfer, or some sort of acid-base interaction. These possibilities are, to a certain extent, quite similar and only distinguish whether or not electron density is “between” species, or transferred from one to the other. An exciplex can be thought of as mixing these limiting ideas, according to equation (68). An absorption complex due to association represents a slight minimization of HOMO/LUMO energies. Correspondingly, exciplex formation requires that the new

emitting state be lower in energy than the parent states. Weak ground-state association may therefore imply a greater possibility of exciplex formation by virtue of the overlap and combination of orbitals. The bimetallic species presented here, only observable spectroscopically, are "previews" of isolatable bimetallic complexes where the MLCT states would be lower in energy.

Thus, an exciplex-like interaction is favored over other quenching mechanisms like energy transfer and electron transfer when the former is not possible, and the latter is endergonic. For the d^{10} cations Zn^{2+} and Cd^{2+}, there are no d-d transitions available to it, thus, energy transfer from $[(bpy)_2Ru(dpp)]^{2+}$ is precluded. Secondly, the reduction potentials for Zn^{2+} and Cd^{2+} are unfavorable,

$$Zn^{2+} + 2e^- \; D \; Zn^0 \; E^0 = -0.76 \text{ V} \qquad (116)$$

$$Cd^{2+} + 2e^- \; D \; Cd^0 \; E^0 = -0.40 \text{ V}, \qquad (117)$$

and represent an initial energy change needed to start the electron transfer process in the case of multi-electron reduction. Oxidation of $^*[(bpy)_2Ru(dpp)]^{2+}$ and reduction of the metal dications is endergonic in the case of Zn^{2+}, and slightly allowed in the case of Cd^{2+}, yet neither is observed since it would lead to an non-emissive Ru(III)

center. However, there is a definitive reduction in the emission intensity and lifetime of $^{*}[(bpy)_2Ru(dpp)]^{2+}$. Therefore, the "quenching" mechanism invoked is associational quenching, with a suspected degree of dynamic quenching akin to exciplex formation.

An alternative quenching mechanism was needed to explain the photoinduced combination of $^{*}[(bpy)_2Ru(dpp)]^{2+}$ and $PtCl_6^{2-}$ to form $[(bpy)_2Ru(dpp\text{-}PtCl_4)]^{2+}$. Studies precluded the likelihood of energy and electron transfer as quenching mechanisms.[121-123] In systems like these and those discussed in this work, the $^{*}[(bpy)_2Ru(dpp)]^{2+}$ species can be thought of as acting like a complexing ligand.[96] The asymmetry of the excited-state interactions of $^{*}[(bpy)_2Ru(dpp)]^{2+}$ mean that the excited state interaction with metal cations such as Zn^{2+} and Cd^{2+} is essentially <u>different</u> from the ground state interactions. The equilibrium constants, K and K^{*} speak to overall thermodynamic states. Given the speed of interactions in the excited state, perhaps idea of "K^{*}" provides the wrong impression: it is really the ratios of k_d to k_{-d} in the ground state, versus the same excited-state ratio of k''_d to k''_{-d} that speak to the changing interaction. In this sense, "excited-state complexes" or "exciplexes" may better be thought of as involving some essential change in an

associative or dissociative interaction in the excited state. In a true exciplex there is a dissociative ground-state and an associative excited state. However, in other kinds of dynamic systems, some have suggested that it may be better to conceive of "associative"[51,201] and "dissociative"[202] exciplexes where interactions are enhanced or lessened in the excited state (Figure 106).

The latter mechanism has been invoked for the bimetallic complex $[(bpy)_2Ru(CN)(\mu\text{-}CN)Rh(NH_3)_4Br]^{4+}$. In this circumstance, the parent compound, $(bpy)_2Ru(CN)_2$ is known to transfer electron density away from the basic nitrogens of the cyano groups and into bpy ligands.[203] One of the first examples of changes in the acidity and basicity of transition metal complexes was observed with the protonated species $[(bpy)_2Ru(CNH)_2]^{2+}$.[204] The *reduction* in basicity at the cyano groups lead to deprotonation and emission of the parent, unprotonated complex. Similarly, $[(bpy)_2Ru(CN)(\mu\text{-}CN)Rh(NH_3)_4Br]^{4+}$ is thought to transiently dissociate in the excited state at the bridging cyano group on account of the reduction in basicity there.[202] The parent compound emits, and upon relaxation, the bimetallic is reformed. This possibility is revealed by the ability of protons from the acidic medium to trap the separated species *only* after excitation and relaxation. Whereas a

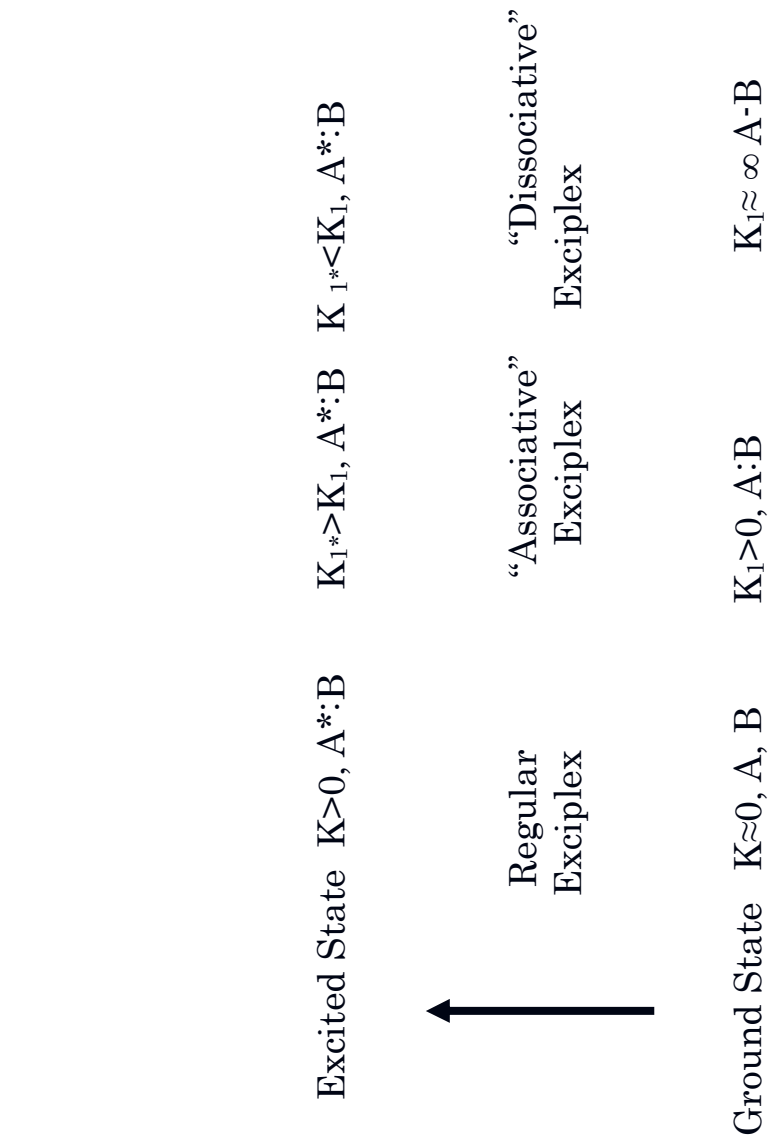

Figure 106. Schematic of exciplex types.

number of ions are known to quench the emission of $(bpy)_2Ru(CN)_2$,[205] including rhodium bromo-amines,[193] the bimetallic complex $[(bpy)_2Ru(CN)(\mu\text{-}CN)Rh(NH_3)_4Br]^{4+}$ which involves bonding between the "quencher" and emitter is observed to have an "unquenched" emission quite similar to that of the dicyano complex alone. This work supports the idea of re-envisioning terminologies related to excited-state complexes in order to acknowledge excited-state effects markedly different from ground-state ones between associating species.

5.E. Multiple Emissions

Finally, the protonation of $[(bpy)_2Ru(dpp)]^{2+}$ reduces its emission intensity enough to observe another higher energy emission at room temperature. With a wavelength maximum at 600 nm, this emission is similar to that of $[Ru(bpy)_3]^{2+}$, except that its lifetime is extremely short, $\leq$ 16 ps, and it quantum yield very low, 4×10^{-9}. At pH=1, both the emission from the protonated species, $[(bpy)_2Ru(dppH)]^{3+}$ at 735 nm and the 620 nm are observed on the sensitive ICCD camera system. Differential excitation into the absorption transitions, MLCT to bpy *vs.* MLCT to dpp leads to enhancement of the 620 nm relative to the 735 nm, and vice versa. With knowledge that intersystem

crossing to the triplet manifold in Ru(II) diimines is not unity, the 620 nm emission is assigned to a spatially distinct emission originating from the bpy ligands, concomitant with the regularly observed ^{3}MLCT originating from the dpp ligand.

5.F. Future Work

The work presented here can be furthered into a number of interesting experiments. First, much of the associations between $[(bpy)_2Ru(dpp)]^{2+}$ and other metal cations presented here such as Hg^{2+}, Pb^{2+}, Sn^{2+}, Fe^{3+}, Al^{3+}, and Cr^{3+} can be further explored to vet quenching and associations mechanisms. Second, the multiple emission from $[(bpy)_2Ru(dpp)]^{2+}$ can be further explored by making use of dueterated solvent and/or the partially deuterated analogue $[(bpy\text{-}d^{8})_2Ru(dpp)]^{2+}$. Lastly, a newly synthesized complex, $[(bpy)_2Ru(pypz)]^{2+}$ (Figure 107),[177] analogous to $[(bpy)_2Ru(dpp)]^{2+}$ but lacking the pendant pyridyl ring is an excellent candidate to explore interactions with metal cations. The expectation is that without the pendant pyridyl ring, metal cations will not associate with $[(bpy)_2Ru(pypz)]^{2+}$ in the ground state, but may in fact do so in the excited state.

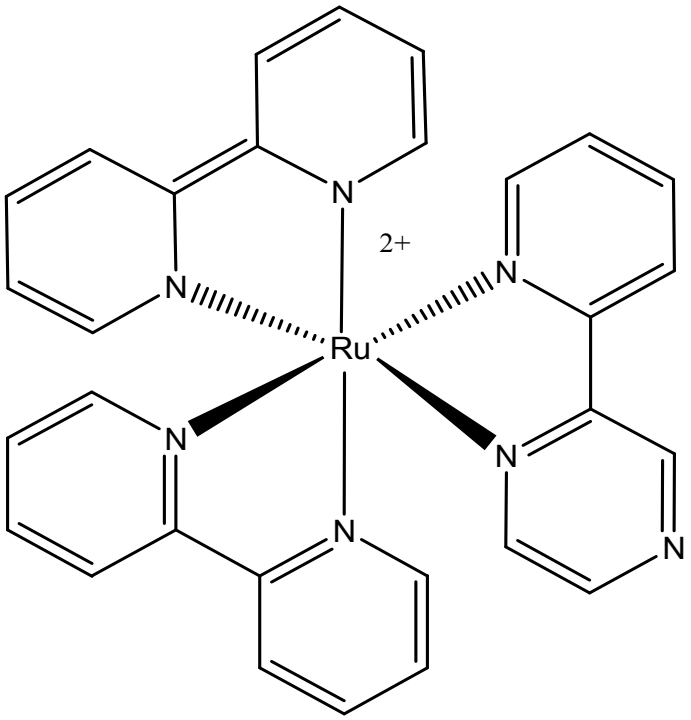

Figure 107. Structure of $[(bpy)_2Ru(pypz)]^{2+}$.

Although $[(bpy)_2Ru(dpp)]^{2+}$ has been around for sometime, it is exciting to see new "twists" concerning its excited state behavior. Monomeric systems like $[(bpy)_2Ru(dpp)]^{2+}$ are still important to further understanding the vast landscape of excited-state behaviors. It is hoped that this work will inspire further investigation into smaller systems like these. Despite the recent vogue of synthesizing larger and larger multi-metal centered systems, the understanding of them is predicated upon having a full understanding of the pieces of the whole and how their many possible interactions determine the ultimate chemistry of any system. For example, if two reagents come together and both electron transfer and an acid-base interaction are exergonic, our understanding is not currently sufficient to decide which event will occur. Yet it is these two interactions which underlie all of chemistry, that are accessible through the excited state chemistry of these molecules.

Appendices

Appendix 1. Programming of Igor Pro 5.00 to Fit Double Exponential Curves to Each Wavelength in a Time-Dependent Emission

Igor Pro 5.00 is a powerful program developed and distributed by WaveMetrics, Inc. Its inherent programmability and exceptional fitting routines made it an excellent candidate for quickly fitting exponentials to a large data set. The ICCD camera puts out time data for 1024 pixels. Since the intensifier does not cover the entire portion of the CCD chip data, not all 1024 data sets are used, but certainly about 600 data sets cover the normal range of any emission. To fit exponentials to 600 data sets manually, or even with Microsoft's Excel would be laborious and unnecessarily time consuming. Igor Pro 5.00 allowed these data sets to be fit to double exponential functions (and single when appropriate) in less than 5 minutes, and plot lifetime vs. wavelength. Although not customarily done, plots of lifetime *vs.* wavelength often shed light on processes that both effect lifetime decay and also show significant wavelength dependence. By plotting the pre-exponential factors, A_1 and A_2 from the biexponential fit equation (92) *vs.* wavelength, one is also able to directly compare the time-invariant "spectrum" extracted from the three-dimensional time-resolved data. This can be compared

to the steady-state spectrum to examine difference between time-dependent and independent processes.

It is theoretically possible to program a user procedure that prompts for all the critical information, including the data set. The procedure outlined here, however, involves manual steps before and after the programmed fitting procedure.

1) Preparation steps.

a. The 3D time resolved data set, in one ASCII (text) file, must be exported from the software used to obtain the data (WinSpec 32). The file contains the list of pixels, 1-1024, the corresponding wavelengths, and then the intensity listing for each pixel for the first exported frame (usually the maximal emission point after the rise time), the second, and so forth. Igor will ignore the pixels and wavelengths. It is possible to load the wavelengths separately, or, preferably, use the calibration curve (equation ??) to have Igor calculate the wavelengths needed for plotting.

b. It is necessary then to obtain the coefficients of the calibration curve (A, B, C), and decide the range of pixels to perform the fits on. It is useful to be mindful that because of the low intensities at the extrema of an emission curve, the fits produce large errors at those wavelengths. For emissions related to $[(bpy)_2Ru(dpp)]^{2+}$, usually fits were limited to the 600-900 nm wavelength range.

c. Lastly, it is necessary to know the time-resolution of the decay profile, *i.e.,* the gate width. Igor works more efficiently by setting the "scaling" of the ordinate of the data sets, rather than fit both x and y data explicitly. Since the gate width is linear (nearly always 2 ns), this works nicely.

2) Upon starting Igor Pro, the following commands are entered:

```
Make/N=1024/D   Wavelength,   A1,   Lifetime1,
Lifetime1_Error,   A2,   A2_Error,   Lifetime2,
Lifetime2_Error

AppendToTable   Wavelength,   A1,   Lifetime1,
Lifetime1_Error,   A2,   A2_Error,   Lifetime2,
Lifetime2_Error
```

This creates “waves”, or data sets for the wavelength, the parameters to be fit, and their errors.

3) The data is loaded by choosing “Data:Load Waves:Load General Text”. The data file is selected. The first two columns under “wave name” which are called “wave0” and “wave1” need to be skipped, since they represent the frame number and the strip number (always 1 with the ICCD camera). The data is loaded as a number format using double precision by clicking “Load”.

4) The x scaling of the waves are changed by choosing “Data:Change Wave Scaling”. The waves list, wave2 through wave1025 must be highlighted (using shift-click). The delta is set to 2, if the time-resolution is 2 ns. The last step is the click “Do it”.

5) The user procedure file is loaded simply by opening the appropriate file. In this case, the file created is named “FitEmissionDouble.ipf”.

6) The programming is loaded into the procedure window. It is important to manually adjust several parameters in the programming such as the range of pixels and wavelength calibration function. For the example below, the pixels range from 249-800, and for the wavelength calibration curve, A = -0.00000501584, B = 0.558247, and C = 445.216.

The code is given below.

```
#pragma rtGlobals=1           //Use modern global access method.
Function FitEmissionDouble(list)
      String list // A semicolon-separated list.
      String theWave
      Variable index=249
      Variable pixel=index+1
      WAVE Wavelength
      WAVE A1
      WAVE Lifetime1
      WAVE Lifetime1_Error
      WAVE A2
      WAVE A2_Error
      WAVE Lifetime2
      WAVE Lifetime2_Error
      WAVE W_sigma

do
      // Get the next wave name
      theWave = StringFromList(index, list)
            if (index==800)
            break // Ran out of waves
            endif
      if (index ==249) // Is this the first wave?
      CurveFit dblexp $theWave
      Wavelength[index]
                  =(-0.00000501584*pixel*pixel+.558247*pixel+445.216)
      A1[index]=K1
      Lifetime1[index]=(1/K2)
      Lifetime1_Error[index]
                  =((1/(K2+W_sigma[2]))-(1/(K2-W_sigma[2])))/2
      A2[index]=K3
      Lifetime2[index]=(1/K4)
      Lifetime2_Error[index]
                  =((1/(K4+W_sigma[4]))-(1/(K4-W_sigma[4])))/2
      else
CurveFit dblexp $theWave
      Wavelength[index]
                  =(-0.00000501584*pixel*pixel+.558247*pixel+445.216)
      A1[index]=K1
      Lifetime1[index]=(1/K2)
      Lifetime1_Error[index]
                  =((1/(K2+W_sigma[2]))-(1/(K2-W_sigma[2])))/2
      A2[index]=K3
      Lifetime2[index]=(1/K4)
      Lifetime2_Error[index]
                  =((1/(K4+W_sigma[4]))-(1/(K4-W_sigma[4])))/2
      endif
      index += 1
      pixel += 1
      while (index<800) // Loop until break above
```

7) The code is compiled by clicking “compile” in the user procedure window.

8) The command to perform the fits is entered:

```
FitEmissionDouble(WaveList("*",";",""))
```

9) The fitting procedures quickly. After completion, the graphs can be plotted and the mean lifetimes returned, using the following list of commands:

```
Display A1 vs Wavelength
AppendToGraph A2 vs Wavelength
SetAxis bottom 600,925
Display Lifetime1 vs Wavelength
AppendToGraph Lifetime2 vs Wavelength
SetAxis bottom 600,925
SetAxis left -10,150
Print mean(Lifetime1,249,800)
Print mean(Lifetime2,249,800)
```

10) Because of the complexity of how Igor maintains data and data holders in memory, it is expedient to save the results, then restart the program for a new data set.

Appendix 2: Derivation of the NMR Fit Equation for Binary Association

Assume a single equilibrium between $[(bpy)_2Ru(dpp)]^{2+}$, represented as *"Ru"*, and the metal cation, represented by *"M"*.

$$Ru + M \leftrightarrows RuM \quad (1)$$

The equilibrium constant for association, *K*, is defined as:

$$K = \frac{[RuM]}{[Ru][M]} \quad (2)$$

The equation is re-written to reflect amount of bimetallic formed, x, upon mixing of initial concentrations of the Ru (II) diimine, $[Ru]_o$, and metal cation, $[M]_o$. The mass balance is noted.

$$K = \frac{x}{([Ru]_o - x)([M]_o - x)} \quad (3)$$

where the mass balance is

$$[Ru] = [Ru]_o - [RuM] \quad (4)$$

If the time scale of the equilibrium is faster than the time scale of the NMR, the observed chemical shift will be a weighted contribution from the bound (bimetallic) and free forms:

$$\delta_{observed} = \alpha_{free}\,\delta_{free} + \alpha_{bound}\,\delta_{bound} \quad (5)$$

where

$$\alpha_{free} = \frac{[Ru]}{[Ru]_o} \quad \text{and,} \quad (6)$$

$$\alpha_{bound} = \frac{[RuM]}{[Ru]_o} \quad . \quad (7)$$

The change in chemical shift can be defined as:

$$\Delta\delta = \delta_{bound} - \delta_{free} \quad (8)$$

and will be positive for downfield shifts.

Combining (3)-(8),

$$\Delta\delta = \left[\left(\delta_{\text{bound}} - \delta_{\text{free}}\right)\right] * \frac{1}{2[Ru]_o} \left[\left(\frac{[M]_o}{} + \frac{[Ru]_o}{} + \frac{1}{K}\right) - \sqrt{\left(\frac{[M]_o}{} + \frac{[Ru]_o}{} + \frac{1}{K}\right)^2 - 4[Ru]_o[M]_o}\right] \quad (9)$$

$\Delta\delta$ is the dependent variable, whilst $[M]_o$ is the independent variable. The fitting parameters are thus K, and δ_{bound}.

The same procedure can be used for the pH titration, except that instead, the acid dissociation constant is defined as:

$$K_a = \frac{[\mathrm{Ru}][\mathrm{H}^+]}{[\mathrm{RuH}]} \quad (10)$$

The resulting equation is similar:

$$\Delta\delta = \left[\left(\delta_{\text{bound}} - \delta_{\text{free}}\right)\right] * \frac{1}{2[Ru]_o} \left[\left([H]_o + [Ru]_o + K_a\right) - \sqrt{\left([H]_o + [Ru]_o + K_a\right)^2 - 4[Ru]_o[H]_o}\right] \quad (11)$$

although in this case, δ_{bound} refers to the protonated complex while δ_{free} refers to the unprotonated complex. $[\mathrm{H}^+]_o$ is the independent variable, and the fitting parameters are K_a and δ_{bound}.

REFERENCES

(1) Ciamician, G. *Science (Washington, D. C., 1883-)* **1912**, *36*, 385.

(2) Ware, M.: http://www.mikeware.co.uk/mikeware/John_Herschel.html, accessed May 2006.

(3) Schrödinger, E. *Phys. Rev.* **1926**, *28*, 1049.

(4) Heisenberg, W. *Z. Physik* **1927**, *43*, 172.

(5) Born, M. O., R. J. *Annalen der Physik* **1927**, *389*, 4572.

(6) Pauli, W. *Z. Physik* **1925**, *31*, 765.

(7) Pauli, W. *Z. Physik* **1927**, *43*, 601.

(8) Bohr, N. *Z. Physik* **1922**, *9*, 1.

(9) Shriver, D. F.; Atkins, P.; Langford, C. H. *Inorganic Chemistry*; 2nd Edition ed.; W.H. Freeman and Company: New York, 1994.

(10) Hund, F. *Z. Physik* **1925**, *33*, 345.

(11) Hund, F. *Z. Physik* **1925**, *33*, 855.

(12) Laporte, O.; Meggers, W. F. *J. Opt. Soc. Am. B: Opt. Phys.* **1925**, *11*, 459.

(13) Orgel, L. E. *J. Chem. Soc.* **1952**, 4756.

(14) Turro, N. J. *Modern Molecular Chemistry*; University Science Books: Sausalito, California, 1991.

(15) Woodward, R. B.; Hoffmann, R. *J. Am. Chem. Soc.* **1965**, *87*, 395.

(16) Zinato, E.; Lindholm, R. D.; Adamson, A. *J. Am. Chem. Soc.* **1969**, *91*, 1076.

(17) Atkins, P. *A Handbook of Concepts*; Clarendon Press: Oxford, 1974.

(18) Kasha, M. *Discussion Faraday Soc.* **1950**, *9*, 14.

(19) Ermolaev, V. L.; Sveshnikova, E. B. *Acta Phys. Pol., B* **1968**, *34*, 771.

(20) Jablonski, A. Z. *Z. Physik* **1935**, *94*, 38.

(21) Lower, S. K.; El-Sayed, M. A. *Chem. Rev. (Washington, DC, U. S.)* **1966**, *66*, 199.

(22) El-Sayed, M. A. *Acc. Chem. Res.* **1968**, *1*, 8.

(23) Vavilov, S. I. *Z. Physik* **1927**, *42*, 311.

(24) Lewis, G. N.; Kasha, M. *J. Am. Chem. Soc.* **1944**, *66*, 2100.

(25) Smoluchowski, M. v. *Ann. Phys. (San Diego, CA, U. S.)* **1915**, *48*, 1103.

(26) Smoluchowski, M. v. *Z. Phys. Chem.* **1917**, *92*, 129.

(27) Flannery, M. R. *Phys. Rev. A* **1982**, *25*, 3403.

(28) Debye, P. *J. Electrochem. Soc.* **1942**, *82*, 265.

(29) Hong, K. M.; Noolandi, J. *J. Chem. Phys.* **1978**, *68*, 5163.

(30) Eigen, M. *Z. Phys. Chem. (Leipzig)* **1954**, *203*, 176.

(31) Hoffman, M. Z.; Bolleta, F.; Moggi, L.; Hug, G. L. *J. Phys. Chem. Ref. Data* **1989**, *18*, 219.

(32) Lakowicz, J. R. *Principles of Fluorescence Spectroscopy*; Plenum Press: New York, 1983.

(33) Juris, A.; Balzani, V.; Barigelletti, F.; Campagna, S.; Belser, P.; Von Zelewsky, A. *Coord. Chem. Rev.* **1988**, *84*, 85.

(34) Marcus, R. A. *Angew. Chem., Int. Ed. Engl.* **1993**, *32*, 1111.

(35) Verhoeven, J. W. *Pure Appl. Chem.* **1996**, *68*, 2223.

(36) Rehm, D.; Weller, A. *Isr. J. Chem.* **1970**, *8*, 259.

(37) Gafney, H. D.; Adamson, A. *J. Am. Chem. Soc.* **1972**, *94*, 8238.

(38) Ireland, J. F.; Wyatt, P. A. H. *Advances in Physical Organic Chemistry* **1976**, *12*, 131.

(39) Domcke, W.; Sobolewski, A. L. *Science (Washington, D. C., 1883-)* **2003**, *302*, 1693.

(40) Förster, T. *Z. Electrochem.* **1950**, *54*, 531.

(41) Henderson, L. J. *Am. J. Physiol.* **1908**, *21*, 173.

(42) Hasselbach, K. *Biochemische Z.* **1916**, *78*, 112.

(43) Le Chatelier, H. L. *Annales des Mines* **1888**, *13*, 157.

(44) Förster, T. *Angew. Chem., Int. Ed. Engl.* **1969**, *8*, 333.

(45) Beens, H.; Weller, A. *Excited molecular p-complexes in solution*; Wiley: New York, 1975; Vol. 2.

(46) Birks, J. B. *Photophysics of Aromatic Compounds*; Wiley: New York, 1970.

(47) Beens, H.; Knibbe, H.; Weller, A. *J. Chem. Phys.* **1967**, *47*, 1183.

(48) Horváth, A.; Stevenson, K. L. *Coord. Chem. Rev.* **1996**, *153*, 57.

(49) Demas, J. N. *Excited State Lifetime Measurements*; Academic Press: New York, 1983.

(50) Balzani, V.; Moggi, L.; Bolleta, F.; Laurence, G. S. *Coord. Chem. Rev.* **1975**, *15*, 321.

(51) Clodfelter, S. A.; Doede, T. M.; Brennan, B. A.; Nagle, J. K.; Bender, D. P.; Turner, W. A.; LaPunzina, P. M. *J. Am. Chem. Soc.* **1994**, *116*, 11379.

(52) Nagle, J. K.; Brennan, B. A. *J. Am. Chem. Soc.* **1988**, *110*, 5931.

(53) Pettijohn, C. N.; Jochnowitz, E. B.; Chuong, B.; Nagle, J. K.; Vogler, A. *Coord. Chem. Rev.* **1998**, *171*, 85.

(54) Vogler, A.; Kunkely, H. *Inorg. Chim. Acta* **1980**, *45*, L265.

(55) Kinnaird, M. G.; Whitten, D. G. *Chem. Phys. Lett.* **1982**, *88*, 275.

(56) Foreman, T. K.; Bonllha, J. B. S.; Whitten, D. G. *J. Phys. Chem.* **1982**, *86*, 3436.

(57) Ayala, N. P.; Demas, J. N.; DeGraff, B. A. *J. Am. Chem. Soc.* **1988**, *110*, 1523.

(58) Tsubomura, T.; Igarashi, O.; Morita, M. *Chem. Lett.* **1992**, *21*, 385.

(59) Lever, A. B. P.; Seymour, P.; Auburn, P. R. *Inorg. Chim. Acta* **1988**, *145*, 43.

(60) Kapinus, E. I.; Aleksankina, M. M.; Staryi, V. P.; Boghillo, V. I.; Dilung, I. I. *J. Chem. Soc., Faraday Trans. 2* **1985**, *81*, 631.

(61) Hoshino, M.; Seki, H.; Shizula, H. *J. Phys. Chem.* **1985**, *89*, 470.

(62) Winstein, W.; Lucas, H. J. *J. Am. Chem. Soc.* **1938**, *60*, 836.

(63) Andrews, L. J.; Keefer, R. M. *J. Am. Chem. Soc.* **1949**, *71*, 3644.

(64) Mulliken, R. S. *J. Am. Chem. Soc.* **1952**, *74*, 811.

(65) Eliezer, I. *J. Chem. Phys.* **1965**, *42*, 3625.

(66) Ayala, N. P.; Flynn, J., C.M.; Saksteder, L.; Demas, J. N.; DeGraff, B. A. *J. Am. Chem. Soc.* **1990**, *112*, 3837.

(67) Paris, T. P.; Brandt, W. W. *J. Am. Chem. Soc.* **1959**, *81*.

(68) Crosby, G. A.; Perkins, W. G.; Klassen, D. M. *J. Chem. Phys.* **1965**, *43*, 1498.

(69) Fleischauer, P. D.; Fleischauer, P. *Chem. Rev. (Washington, DC, U. S.)* **1970**, *70*, 199.

(70) Morgan, G. T.; Burstall, F. H. *J. Chem. Soc.* **1936**, 41.

(71) Demas, J. N.; Diemente, D.; Harris, E. W. *J. Am. Chem. Soc.* **1973**, *95*, 6864.

(72) Laurence, G. S.; Balzani, V. *Inorg. Chem.* **1974**, *13*, 2976.

(73) Navon, G.; Sutin, N. *Inorg. Chem.* **1974**, *13*, 2159.

(74) Bock, C. R.; Meyer, T. J.; Whitten, D. G. *J. Am. Chem. Soc.* **1974**, *96*, 4710.

(75) Young, R. C.; Meyer, T. J.; Whitten, D. G. *J. Am. Chem. Soc.* **1975**, *97*, 4781.

(76) Anderson, C. P.; Salmon, D. J.; Meyer, T. J.; Young, R. C. *J. Am. Chem. Soc.* **1977**, *99*, 1980.

(77) Maestri, M.; Grätzel, M. *Ber. Bunsen-Ges. Phys. Chem.* **1977**, *81*, 504.

(78) DeGraff, B. A.; Demas, J. N. *J. Am. Chem. Soc.* **1980**, *102*, 6169.

(79) Demas, J. N.; Adamson, A. *J. Am. Chem. Soc.* **1971**, *93*, 1800.

(80) Demas, J. N.; Addington, J. W. *J. Am. Chem. Soc.* **1974**, *96*, 3663.

(81) Demas, J. N.; Crosby, G. A. *J. Am. Chem. Soc.* **1971**, *93*, 2841.

(82) Balzani, V.; Bolleta, F.; Gandolfi, M. T.; Maestri, M. *Top. Curr. Chem.* **1978**, *75*, 1.

(83) Meyer, T. J. *Acc. Chem. Res.* **1978**, *11*, 94.

(84) Sutin, N.; Creutz, C. *Advances in Chemistry Series* **1978**, *No. 168*, 1.

(85) Kalyanasundaram, K. *Coord. Chem. Rev.* **1982**, *46*, 159.

(86) Meyer, T. J. *Pure Appl. Chem.* **1986**, *58*, 1193.

(87) Demas, J. N.; Addington, J. W. *J. Am. Chem. Soc.* **1976**, *98*, 5800.

(88) Demas, J. N.; Harris, E. W.; McBride, R. P. *J. Am. Chem. Soc.* **1977**, *99*, 3547.

(89) Durham, B.; Caspar, J. V.; Nagle, J. K.; Meyer, T. J. *J. Am. Chem. Soc.* **1982**, *104*, 4803.

(90) Dose, E. V.; Wilson, L. J. *Inorg. Chem.* **1978**, *17*, 2660.

(91) Hunziker, M.; Ludi, A. *J. Am. Chem. Soc.* **1977**, *99*, 7370.

(92) Tinnemans, A. H.; Timmer, K.; Reinten, M.; Kraaijkamp, J. G.; Alberts, A. H.; Van der Linden, J. G. M.; Schmitz, J. E. J.; Saaman, A. A. *Inorg. Chem.* **1981**, *20*, 3698.

(93) Braunstein, C. H.; Baker, A. D.; Strekas, T. C.; Gafney, H. D.

Inorg. Chem. **1984**, *23*, 857.

(94) Goodwin, H. A.; Lions, F. *J. Am. Chem. Soc.* **1959**, *81*, 6415.

(95) Murphy, J., W. Rorer; Brewer, K. J.; Gettliffe, G.; Petersen, J. D. *Inorg. Chem.* **1989**, *28*, 81.

(96) Campagna, S.; Denti, G.; Serroni, S.; Ciano, M.; Balzani, V. *Inorg. Chem.* **1991**, *30*, 3728.

(97) Denti, G.; Campagna, S.; Sabatino, L.; Serroni, S.; Ciano, M.; Balzani, V. *Inorg. Chem.* **1990**, *29*, 4750.

(98) Ruminski, R. R.; Cockroft, T.; Shoup, M. *Inorg. Chem.* **1988**, *27*, 4026.

(99) Wallace, A. W.; Murphy, J., W. Rorer; Petersen, J. D. *Inorg. Chim. Acta* **1989**, *166*, 47.

(100) Campagna, S.; Denti, G.; Serroni, S.; Ciano, M.; Juris, A.; Balzani, V. *Inorg. Chem.* **1992**, *31*, 2982.

(101) Marcaccio, M.; Paolucci, F.; Paradisi, C.; Roffia, S.; Fontanesi, C.; Yellowlees, L. J.; Serroni, S.; Campagna, S.; Denti, G.; Balzani, V. *J. Am. Chem. Soc.* **1999**, *121*, 10081.

(102) Brauns, E.; Jones, S. W.; Clark, J. A.; Molnar, S. M.; Kawanishi, Y.; Brewer, K. J. *Inorg. Chem.* **1997**, *36*, 2161.

(103) Baudin, H. B.; Davidsson, J.; Serroni, S.; Juris, A.; Balzani, V.; Campagna, S.; Hammarström, L. *J. Phys. Chem. A.* **2002**, *106*, 4312.

(104) Serroni, S.; Denti, G. *Inorg. Chem.* **1992**, *31*, 4251.

(105) Juris, A.; Balzani, V.; Campagna, S.; Denti, G.; Serroni, S.; Frei, G.; Güdel, H. U. *Inorg. Chem.* **1994**, *33*, 1491.

(106) Brewer, K. J.; Murphy, J., W. Rorer; Petersen, J. D. *Inorg. Chem.* **1987**, *26*, 3376.

(107) McMillin, D. R.; Stacy, E. M. *Inorg. Chem.* **1990**, *29*, 393.

(108) Scott, S. M.; Gordeon, K. C.; Burrell, A. K. *J. Chem. Soc., Dalton Trans.* **1999**.

(109) Kalyanasundaram, K.; Grätzel, M.; Nazeeruddin, M. K. *J. Phys. Chem.* **1992**, *96*, 5865.

(110) Rasmussen, S. C.; Richter, M. M.; Yi, E.; Place, H.; Brewer, K. J. *Inorg. Chem.* **1990**, *29*, 3926.

(111) Ruminski, R. R.; Cambron, R. T. *Inorg. Chem.* **1990**, *29*, 1575.
(112) Baiano, J. A.; Murphy, J., W. Rorer *Inorg. Chem.* **1991**, *30*, 4594.

(113) Balzani, V.; Juris, A.; Venturi, M.; Campagna, S.; Serroni, S. *Chem. Rev. (Washington, DC, U. S.)* **1996**, *96*, 759.

(114) Brewer, K. J.; Murphy, J., W. Rorer; Spurlin, S. R.; Petersen, J. D. *Inorg. Chem.* **1986**, *25*, 882.

(115) Balzani, V.; Denti, G.; Juris, A.; Serroni, S.; Venturi, M. *Acc. Chem. Res.* **1998**, *31*, 26.

(116) Sommovigo, M.; Denti; Serroni, S.; Campagna, S.; Mingazzini, C.; Mariotti, C.; Juris, A. *Inorg. Chem.* **2001**, *40*, 3318.

(117) Cerroni, P.; Paolucci, F.; Paradisi, C.; Juris, A.; Roffia, S.; Serroni, S.; Campagna, S.; Bard, A. J. *Inorg. Chem.* **1998**, *120*, 5480.

(118) Hosek, W.; Tysoe, S. A.; Gafney, H. D.; Baker, A. D.; Strekas, T. C. *Inorg. Chem.* **1989**, *28*, 1228.

(119) Kalyanasundaram, K.; Nazeeruddin, M. K. *Inorg. Chem.* **1990**, *29*, 1888.

(120) Kirchhoff, J. R.; Kirschbaum, K. *Polyhedron* **1998**, *17*, 4033.

(121) Dougherty, T.; Hicks, C.; Maletta, A.; Fan, J.; Rutenberg, I.; Gafney, H. D. *J. Am. Chem. Soc.* **1998**, *120*, 4226.

(122) Hicks, C.; Fan, J.; Rutenberg, I.; Gafney, H. D. *Coord. Chem. Rev.* **1998**, *171*, 71.

(123) Hicks, C.; Ye, G.; Levi, C.; Gonzales, M.; Rutenberg, I.; Fan, J.; Helmy, R.; Kassis, A.; Gafney, H. D. *Coord. Chem. Rev.* **2001**, *211*, 207.

(124) Thomas, T. J.; Nandi, U. W. *AAIA Journal* **1976**, *14*, 1334.

(125) Nakabayashi, Y.; Omayu, A.; Yagi, S.; Nakamura, K.; Motonaka, J. *Anal. Sci.* **2001**, *17*, 945.

(126) Parker, C. A. *Photoluminescence of Solutions*; Elsevier Publishing Company: Amsterdam, 1968.

(127) Hammett, L. P.; Deyrup, A. J. *J. Am. Chem. Soc.* **1932**, 2721.

(128) Bridges, J. W. in *Standards of Fluorescence Spectrometry,* J.N. Miller, ed.Chapman and Hall: London, 1981.

(129) Demas, J. N.; Crosky, G. A. *J. Phys. Chem.* **1971**, *75*, 991.

(130) Favaro, G. *J. Photochem.* **1986**, *35*, 375.

(131) Dhami, S.; de Mello, A. J.; Rumbles, G.; Bishop, S. M.; Phillips, D.; Beeby, A. *Photochem. Photobiol.* **1995**, *61*, 341.

(132) Williams, A. T. R.; Wenfield, S. A.; Miller, J. N. *Analyst* **1983**, *108*, 1067.

(133) Johnson, S. R.; Westmoreland, T. D.; Caspar, J. V.; Barqawi, K. R.; Meyer, T. J. *Inorg. Chem.* **1988**, *27*, 3195.

(134) Damrauer, N. H.; Cerullo, G.; Yeh, A.; Boussie, T. R.; Shank, C. V.; McCusker, J. K. *Science (Washington, D. C., 1883-)* **1997**, *275*, 54.

(135) Yeh, A. T.; Shank, C. V.; McCusker, J. K. *Science (Washington, D. C., 1883-)* **2000**, *289*, 935.

(136) Ferrari, M. B.; Fava, G. G.; Pelssi, G.; Predieri, G.; Vignali, C.; Denti, G.; Serroni, S. *Inorg. Chim. Acta* **1998**, *275-276*, 320.

(137) Castellano, S.; Ginther, H.; Eberaole, S. *J. Phys. Chem.* **1965**, *69*, 4166.

(138) Lytle, F. E.; Petrosky, L. M.; Carlson, L. R. *Anal. Chim. Acta* **1971**, *57*, 239.

(139) Nazeeruddin, M. K.; Kalyanasundaram, K. *Inorg. Chem.* **1989**, *28*, 4251.

(140) Hanna, M. W.; Ashbaugh, A. L. *J. Phys. Chem.* **1964**, *68*, 811.

(141) Sahai, R.; Loper, G. L.; Lin, S. H.; Eyring, H. *Proc. Natl. Acad. Sci. U. S. A.* **1974**, *71*, 1499.

(142) Hunter, C. A.; Bisson, A. P.; Morales, J. C.; Young, K. *Chem.--Eur. J.* **1998**, *4*, 845.

(143) Barrans, J., Richard E.; Dougherty, D. A. *Supramolecular Chemistry* **1994**, *4*, 121.

(144) Cohen, J. I.; Castro, S.; Han, J.-a.; Behaj, V.; Engel, R. *Heteroat. Chem.* **2000**, *11*, 546.

(145) Fielding, L. *Tetrahedron* **2000**, *56*, 6151.

(146) Mathur, R.; Becker, E. D.; Bradley, R. B.; Li, N. C. *J. Phys. Chem.* **1963**, *67*, 2190.

(147) Benesi, H. A.; Hildebrand, J. H. *J. Am. Chem. Soc.* **1949**, *71*, 2703.

(148) Diem, M. *Introduction to Vibrational Spectroscopy*; Wiley Publishers: New York, 1993.

(149) Van Houten, J.; Watts, R. J. *J. Am. Chem. Soc.* **1976**, *98*, 4853.

(150) Nakamaru, K. *Bull. Chem. Soc. Jpn.* **1982**, *55*, 2697.

(151) Johansen, O.; Launikonis, A.; Mau, A. W. H.; Sasse, W. H. F. *Aust. J. Chem.* **1980**, *33*, 1643.

(152) McClanahan, S. F.; Dallinger, R. F.; Holler, F. J.; Kincaid, J. R. *J. Am. Chem. Soc.* **1985**, *107*, 4853.

(153) Kawanishi, Y.; Kitamura, N.; Kim, Y.; Tazuke, S. *Riken Q.* **1984**, *78*, 212.

(154) Bhuiyan, A. A.; Kincaid, J. R. *Inorg. Chem.* **1999**, *38*, 4759.

(155) Su, H.; Kincaid, J. R. *J. Raman Spectrosc.* **2003**, *34*, 907.

(156) Lytle, F. E.; Hercules, D. M. *J. Am. Chem. Soc.* **1969**, *91*.

(157) Demas, J. N.; Taylor, D. G. *Inorg. Chem.* **1979**, *18*, 3177.

(158) Bhasikuttan, A. C.; Suzuki, M.; Nakashima, S.; Okada, T. *J. Am. Chem. Soc.* **2002**, *124*, 8398.

(159) Abdel-Shafi, A. A.; Worrall, D. R.; Ershov, A. Y. *Dalton Trans.* **2004**, 30.

(160) Kober, E. M.; Sullivan, B. P.; Meyer, T. J. *Inorg. Chem.* **1984**, *23*, 2398.

(161) Birchall, J. D.; O'Donoghue, T. D.; Wood, J. R. *Inorg. Chim. Acta* **1979**, *37*, L461.

(162) Cumper, C. W. N.; Ginman, R. F. A.; Vogel, A. I. *J. Chem. Soc.* **1962**, 1188.

(163) Fielding, P. E.; Le Fèvre, R. J. W. *J. Chem. Soc.* **1951**, 1811.

(164) Goethals, C.A. *Recl. Trav. Chim. Pays-Bas* **1935**, *54*, 299.

(165) Goethals, C.A.; Wibaut, J.P. *Recl. Trav. Chim. Pays-Bas* **1954**, *73*, 35.

(166) Raczynska, E. D. *J. Mol. Struct.* **1998**, *427*, 87.

(167) Cagle, J., F. W. *Acta Crystallogr.* **1948**, *1*, 158.

(168) Merritt, J., Lynne L.; Schoroeder, E. D. *Acta Crystallogr., Sect. A: Found. Crystallogr.* **1956**, *9*, 801.

(169) Kramer, J., F. Axtell; West, R. *J. Phys. Chem.* **1965**, *69*, 673.

(170) Constable, E. C.; Lewis, J. *Inorg. Chim. Acta* **1983**, *70*, 251.

(171) Predieri, G.; Vignali, C.; Denti, G.; Serroni, S. *Inorg. Chim. Acta* **1993**, *205*, 145.

(172) Huang, N.-T.; Pennington, W. T.; Peterson, J. D. *Acta Crystallogr., Sect. A: Found. Crystallogr.* **1991**, *C47*, 2011.

(173) Lipkowski, J. **1976**, *5*, 931.

(174) Westheimer, F. H.; Benfey, O. T. *J. Am. Chem. Soc.* **1956**, *8*, 5309.

(175) Nakamoto, K. *J. Am. Chem. Soc.* **1960**, *64*, 1420.

(176) Anderson, P. A.; Anderson, R. F.; Masaoki, F.; Junk, P. C.; Keene, F. R.; Patterson, B. T.; Yeomans, B. D. *Inorg. Chem.* **2000**, *39*, 2731.

(177) Szulbinski, W. S.; Kincaid, J. R. *Inorg. Chem.* **1998**, *37*, 859.

(178) Crutchley, R. J.; Kress, N.; Lever, A. B. P. *J. Am. Chem. Soc.* **1983**, *105*, 1170.

(179) Shinozaki, K.; Kaizu, Y.; Hirai, H.; Kobayashi, H. *Inorg. Chem.* **1989**, *28*, 3675.

(180) Lasser, N.; Feitelson, J. *J. Phys. Chem.* **1973**, *77*, 1011.

(181) Giordano, P. J.; Bock, C. R.; Wrighton, M. S.; Interrante, L. V.; Williams, R. F. X. *J. Am. Chem. Soc.* **1977**, *99*, 3187.

(182) Lay, P. A.; Sasse, W. H. F. *Inorg. Chem.* **1984**, *23*, 4123.

(183) Shimidzu, T.; Iyoda, T.; Izaki, K. *J. Phys. Chem.* **1985**, *89*, 642.

(184) Glazer, E. C.; Magde, D.; Tor, Y. *J. Am. Chem. Soc.* **2005**, *127*, 4190.

(185) Song, L.; Feng., J.; Wang., X.; Yu, J.; Hou, Y.; Xie, P.; Zhang, B.; Xiang, J.; Ai, X.; Zhang, J. *Inorg. Chem.* **2003**, *42*, 3393.

(186) Andersson, J.; Puntoriero, F.; Serroni, S.; Yartsev, A.; Torbjörn, P.; Polívka, T.; Campagna, S.; Sundström, V. *Chem. Phys. Lett.* **2004**, *386*, 336.

(187) Taffarel, E.; Chirayil, S.; Kim, W. Y.; Thummel, R. P.; Schmehl, R. H. *Inorg. Chem.* **1996**, *35*, 2127.

(188) Shaw, J. R.; Webb, R. T.; Schmehl, R. H. *J. Am. Chem. Soc.* **1990**, *112*, 1117.

(189) Vos, J. G.; Nieuwenhuis, H. A.; Reedijk, J.; Haasnoot, J. G.; Snoeck, T. L.; Stufkens, D. J. *Inorg. Chem.* **1991**, *30*, 48.

(190) Keyes, T. E.; O'Connor, C. M.; O'Dwyer, U.; Coates, C. G.; Callagan, P.; McGarvey, J. J.; Vos, J. G. *J. Phys. Chem. A.* **1999**, *103*, 8915.

(191) Fuchs, Y.; Lofters, S.; Dieter, T.; Shi, W.; Morgan, R.; Strekas, T. C.; Gafney, H. D.; Baker, A. D. *J. Am. Chem. Soc.* **1987**, *109*, 2691.

(192) Ballardini, R.; Gandolfi, M. T.; Balzani, V. *Chem. Phys. Lett.* **1985**, *119*, 459.

(193) Lei, Y.; Buranda, T.; Endicott, J. F. *J. Am. Chem. Soc.* **1990**, *112*, 8820.

(194) Bignozzi, C. A.; Indelli, M. T.; Scandola, F. *J. Am. Chem. Soc.* **1989**, *111*, 5192.

(195) Housecroft, C. E.; Sharpe, A. G. *Inorganic Chemistry*; 1st ed.; Pearson Education: Edinburgh, 2001.

(196) Chandrasekaran, K.; Foreman, T. K.; Whitten, D. G. *Nouveau Journal de Chimie* **1981**, *5*, 275.

(197) Hauenstein, J., B.L.; Dressick, W. J.; Demas, J. N.; DeGraff, B. A. *J. Phys. Chem.* **1984**, *88*, 2418.

(198) Bryant, G. M.; Fergusson, J. E. *Aust. J. Chem.* **1971**, *24*, 441.

(199) Cotton, F. A.; Wilkonson, G.; Murillo, C. A.; Bochmann, M. *Advanced Inorganic Chemistry*; 6th ed.; John Wiley & Sons: New York, 1999.

(200) Banks, C. V.; Bystroff, R. I. **1959**, 6153.

(201) Horváth, A.; Stevenson, K. L. *Inorg. Chem.* **1993**, *32*, 2225.

(202) Fan, J.; Helmy, R.; Kassis, A.; Grunseich, A.; Mangubat, P.; Hicks, C.; Stevens, N.; Gafney, H. D. *Inorg. Chem.* **2003**, *42*, 2486.

(203) Matsui, K.; Nazeeruddin, M. K.; Humphry-Baker, R.; Grätzel, M.; Kalyanasundaram, K. *J. Phys. Chem.* **1992**, *96*, 10587.

(204) Peterson, S. H.; Demas, J. N. *J. Am. Chem. Soc.* **1976**, *98*, 7880.

(205) Demas, J. N.; Addington, J. W.; Peterson, S. H.; Harris, E. W. *J. Phys. Chem.* **1977**, *81*, 1039.